Decays At The Edge

Probing Light Proton-Rich Nuclei at State-Of-The-Art Rare Ion Beam Facilities

Dissertation for the Degree of Doctor of Philosophy

Erik Asbjørn Mikkelsen Jensen

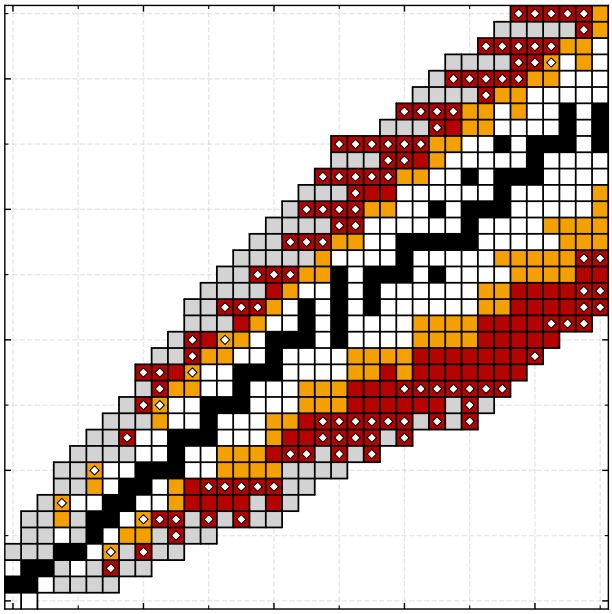

Institut for Fysik & Astronomi

Aarhus Universitet, Denmark

Erik A. M. Jensen

Decays At The Edge

Erik Asbjørn Mikkelsen Jensen
Institut for Fysik & Astronomi
Aarhus Universitet
Ny Munkegade 120
8000 Århus C
Denmark
Email: erik@tenku.dk / ej@phys.au.dk

1st revised edition; 19 March 2023

Minor typographical changes have been made following the submission of the thesis to the Graduate School of Natural Sciences at Aarhus University on the 10th of March 2024. A section in chapter 6 on gamma detection efficiencies was omitted from the thesis, but reference was still made to this section in the beginning of chapter 6; the reference has been removed. Although exciting, the conclusion that the population of an excited state in ^{21}Na at excitation energy $E_{ex}^{^{21}Na} \sim 12.10$ MeV was seen in figure 8.8 was wrong. This excitation energy was wrongly calculated relative to the ground state of ^{22}Mg, not ^{21}Na. The correct energy is $E_{ex}^{^{21}Na} \sim 6.59$ MeV; figure 8.8 and the text relating to it has been corrected.

Cover image based on data from AME2020 and
NUBASE2020 – refs. [Hua+21; Wan+21; Kon+21].

Typeset with `Vollkorn` [Alt18], `Merriweather Sans` [Sor16] and `Aozora Mincho` [Unk12].
Figures from publications included in this thesis typeset with `Linux Libertine` [Pol12].
Figures made with `Matplotlib` [Hun07] and `Inkscape` [The23].
Compiled with `Xe(La)TeX` [Kew+18] and `Biber` [CK23].

Contents

Part II FRIB

Part III Taking stock

Appendices

Abstract

Our current understanding of the nuclear landscape is best challenged by studying the evolution of nuclear structure as we progress from the valley of stability towards the edges of stability, which are defined by the proton and neutron drip lines.

This thesis studies the mechanisms of beta-delayed charged particle emission of a sample of light proton-rich nuclei at state-of-the-art rare ion beam facilities at the ISOLDE facility at CERN and at the Facility for Rare Isotope Beams in the United States. The Q-values of beta decay of these light proton-rich nuclei are of such magnitude that one or several charged particles can be emitted, following the initial beta decay. By observing these charged particles, nuclear structure information of the intermediate states of high excitation energies populated in the decay can be extracted. For the detection of the charged particles, highly segmented silicon detectors are employed in so-called telescope configurations in order to reliably identify the nature of the complex multi-particle breakups.

The decay of ^{21}Mg is studied in great detail based on data from an experiment carried out at the ISOLDE facility at CERN. Refined methods for the extraction of charged particle spectra from detector telescopes result in the revelation of new details regarding the decay of ^{21}Mg.

The decays of ^{22}Al and ^{26}P are also studied, based on data recorded in the 10th experiment to be carried out at the newly commissioned Facility for Rare Isotope Beams. The beam time of this experiment was in July 2023, and the experiment was very successful. There is, in the data from the experiment, a staggering amount of new insights to be gained on the decays of ^{22}Al and ^{26}P. The results of the data analyses thus far carried out on the data are presented, and plans for the further development of the data analyses are outlined.

Resumé

Den bedste måde, hvorpå vi kan udfordre og udvide vores nuværende forståelse af det kernefysiske landskab, er ved at studere de ændringer i kernestruktur, som opstår langt fra kernekortets stabilitetslinje – tæt på kernekortets ydre grænser, som er proton- og neutron-dryplinjerne.

Denne afhandling undersøger de bagvedliggende mekanismer i beta-forsinket udsendelse af ladede partikler fra et udpluk af lette protonrige kerner ved nogle af verdens mest avancerede faciliteter indenfor fremstilling af stråler af radioaktive kerner, såkaldte *rare ion beam facilities*. Disse stråler af radioaktive kerner fremstilles henholdsvis ved ISOLDE-faciliteten på CERN og ved *Facility for Rare Isotope Beams* i USA. Q-værdierne for beta-henfald af de lette protonrige kerner, som undersøges, er så høje, at én eller flere ladede partikler kan udsendes efter beta-henfaldet. Ved at observere disse ladede partikler kan information om kernestruktur ekstraheres fra de kvantetilstande, som populeres i henfaldene. Segmenterede siliciumdetektorer i såkaldte teleskop-konfigurationer anvendes til pålideligt at identificere de ladede partikler og måden, hvorpå de komplekse opbrud med udsendelse af adskillige partikler foregår.

Henfaldet af ^{21}Mg undersøges meget detaljeret med udgangspunkt i et eksperiment udført ved ISOLDE-faciliten på CERN. Forfinede metoder til ekstrahering af spektre for ladede partikler leder til nye indsigter i henfaldet.

Henfaldene af ^{22}Al og ^{26}P undersøges også med udgangspunkt i det tiende eksperiment, som er blevet udført, ved den nyligt indviede *Facility for Rare Isotope Beams*. Dette eksperiment blev udført i juli 2023, og eksperimentet var en stor succes. I de data, som er kommet ud af eksperimentet, er der en overvældende mængde nye indsigter at finde i henfaldene af ^{22}Al og ^{26}P. Resultaterne fra de dataanalyser, som indtil videre er blevet udført, bliver præsenteret, og planerne for de videre dataanalyser skitseres.

Acknowledgments

In the research field of nuclear physics, the experimental projects are large, they have to be planned many years in advance, and they, necessarily, require the combined efforts of many people who contribute a variety of skill sets in order for the projects to succeed. Therefore, I have many people to thank for their help in making my PhD studies rewarding, both professionally and socially. To those of you who are mentioned here specifically, it has been a true pleasure – let's keep it up! And to those of you whom I forget to mention here, do not hesitate to chide and harass me for my mistake.

First and foremost, I would like to thank my supervisor Karsten Riisager for his masterful guidance and for his unwavering pleasant and calm demeanour. My co-supervisor Hans Fynbo deserves the exact same kind of praise; as a bachelor's student, I dipped my toes in the field of experimental nuclear physics for the first time with Hans as my supervisor. I have had two top-notch supervisors looking out for me through my years of studies at the Department, and I hope that we can keep up the good work and the even better chats for years to come.

My thanks also go to all the students in our research group whom I have had the pleasure to get to know throughout my studies. In particular, I wish to thank Hans' newest PhD student, Jeppe Schultz Nielsen, for being an invaluable member of the "Danish team" in the main experiment of my PhD project at FRIB, and I also wish to thank Jeppe for being an excellent (impromptu) city guide on our one-day trip to Chicago and for his hilarious reaction to us missing the train out of Chicago just before nightfall; the trip was an excellent way of marking the end of the experiment. A special shoutout goes also to Justus Matthies Eder, a master's student in our group, who has been making a lot of excellent progress in the consistency checks and analyses of the FRIB data,

while I, myself, have been too busy writing my thesis. Justus has graciously provided me with his latest germanium efficiency calibrations for use in this thesis; however, in the end I did not find the time to include any gamma-related spectra in this thesis and, hence, I have omitted the section which would otherwise detail the current state of the gamma efficiency calibrations.

Expanding beyond the yellow walls of the Department of Physics and Astronomy, I also wish to thank all members of our MAGISOL Collaboration, a small but dedicated research collaboration with decades upon decades of expertise in the field, with members primarily based in Madrid, Göteborg and Århus; it has been a pleasure to get to know all of you throughout the years of experiments, conferences and research exchanges.

In particular, I wish to thank Olof Tengblad for joining me during my second week at FRIB, where we set up for the experiment of my PhD project. The days got quite long, and it was very exhausting, but it was also some of the most rewarding work I have ever carried out. It was a true pleasure to experience how we had learned, through our previous collaborations on experimental setups, to bounce off of each other, both in the lab, in the FRIB food hall and at the Pizza House where we would usually end up some time after midnight!

Both Olof and María José García Borge have effectively acted as my second pair of supervisors. I have had the pleasure of being hosted by both María and Olof in Madrid, and at the Euroschool on Exotic Beams in La Rábida in 2022, María was one of the lecturers with whom I had many insightful discussions about my analyses of the ^{21}Mg data from ISOLDE.

Daniel Fernández Ruiz and Vicente García Távora, PhD students of Olof and María, also deserve a shoutout for all the night shifts we have done together, in the lab and elsewhere.

Thanks also to Zixuan Yue and Chris Page, who have doubled as very handy "people on the inside" at IDS at ISOLDE as well as dinner companions at Ô Brasseur.

To Chris Wrede at FRIB and the members of his research group, Lijie Sun, Lexie Weghorn, Alex Adams, Joe Dopfer and Tyler Wheeler, thank you all so much for your immense help, hospitality and research input on ^{22}Al and ^{26}P during the experiment at FRIB – here's to more excellent experiments like this one!

A special thanks also goes to the members of the Gas Stopping Group at FRIB, Chandana Sumithrarachchi, Stefan Schwarz and their students, for doing everything they could to deliver us a beam of unprecedented intensity and purity. Especially Chandana deserves a huge thanks for tolerating my constant bugging of him after the experiment was over, as I was looking to include in this thesis some figures which he had shown me during the experiment at FRIB. Finally, I wish to thank my parents and my family for always standing up for me.

List of publications

Publications included in this thesis

1. **E. A. M. Jensen**, K. Riisager and H. O. U. Fynbo: *Extracting clean low-energy spectra from silicon strip detector telescopes around punch through energies*, Nucl. Instrum. Methods Phys. Res. A **1055**, 168531 (2023).

2. **E. A. M. Jensen**, S. T. Nielsen, A. Andreyev, M. J. G. Borge, J. Cederkäll, L. M. Fraile, H. O. U. Fynbo, L. J. Harkness-Brennan, B. Jonson, D. S. Judson, O. S. Kirsebom, R. Lică, M. V. Lund, M. Madurga, N. Marginean, C. Mihai, M. Munch, R. D. Page, A. Perea, J. Refsgaard, K. Riisager and O. Tengblad: *Detailed study of the decay of ^{21}Mg*, Submitted to Eur. Phys. J. A (2024).

Additional publications

1. M. Kuhlwein, K. Lytje, H. O. U. Fynbo, A. Gad, **E. A. M. Jensen**, O. S. Kirsebom, M. Munch, J. Refsgaard and K. Riisager: *Exclusive decay study of the 16.62 MeV (2^-, T=1) resonance in ^{12}C*, Phys. Lett. B **825**, 136857 (2022).

2. V. G. Távora, O. Tengblad, M. J. G. Borge, J. A. Briz, D. Fernández Ruiz, **E. A. M. Jensen**, A. N. Nerio and A. Perea: *Populating α-unbound states in ^{16}O via ^{19}F(p,αγ)^{16}O reactions*, EPJ Web of Conf. **290**, 03003 (2023).

Chapter 1

Introduction

As we look to the stars that light up the night sky, we look to nuclear physics to realise what makes the stars shine. The star nearest and dearest to us, our own Sun, emits light which has travelled for a bit more than 8 minutes when it reaches us, while the star nearest to our Sun emits light which is almost one year old when it finally reaches our Solar System. These select few stellar objects, which are among billions upon trillions of stars in the observable Universe, are unfathomably large and unfathomably far away from us, and yet, the interactions that fuel the burning of the stars happen on a length scale which may seem even more unfathomable, at less than a billionth of a hair's width, way beyond human perception. On these minuscule length scales, inside atomic nuclei which consist of nucleons (i.e. protons and neutrons), nuclear interactions – governed by the electromagnetic, the weak and the strong fundamental forces – prevail. There are 253 [Som18] known stable combinations of nucleons which make up *the stable nuclei*. The stable nuclei are at the cores of the atoms that make up the matter we see around us, and it is the nuclear interactions that bind the cores of the individual atoms together. The nuclear interactions also govern the decays of all other combinations of nucleons, *the unstable nuclei*, as they journey spontaneously towards *the valley of stability* where the stable nuclei reside. In the laboratory, stable nuclei can be forced out of the valley of stability, towards *the edges of stability*, by wedging one or several nucleons into the otherwise stable nuclei. Our current understanding of the nuclear landscape is best challenged by studying the evolution of nuclear structure as we progress from the valley of stability towards the edges of stabil-

ity, which are defined by the *proton and neutron drip lines*, where, upon wedging another proton into a proton-rich nuclide or another neutron into a neutron-rich nuclide, the additional nucleon simply drips off the given nuclide.

The theme of this thesis is the decays of light, proton-rich nuclides which lie close to the proton drip line, at the edge of stability. These light, proton-rich nuclides, which undergo complex multi-particle breakups as they decay, are produced at state-of-the-art rare ion beam facilities. Specifically, the nuclides to be studied in this thesis are the nuclides ^{21}Mg, ^{22}Al, ^{25}Si and ^{26}P. A rare ion beam of the first of these nuclides, ^{21}Mg, has been produced at the ISOLDE facility at CERN in Switzerland, and the decay of ^{21}Mg has then been studied extensively; this is the topic of part I of this thesis. All four nuclides have, in turn, been produced at the newly commissioned Facility for Rare Isotope Beams (FRIB) in the United States, with the main aim of studying the decays of ^{22}Al and ^{26}P; this is the topic of part II of this thesis.

Just as our own Sun is one tiny piece of a much larger puzzle, these four light, proton-rich nuclides play but a tiny role in the whole nuclear landscape and their study is a small part in the vast research area of nuclear physics. In nuclear physics, we seek insight into the nuclear landscape and propose models that explain the phenomena we observe. We probe the fundamental forces of nature, and we learn about such topics as stellar evolution and the deaths of stars, the more violent of which are the reason we are all here today. Nuclear physics also has many societal applications; it sees use in the medical examinations and treatments of patients, discussions of its application for the production of (relatively) clean energy has been revitalised in recent years, and it is utilised both in the foods and goods industries[1]. Nuclear physics also acts as a tool of the trade in other research fields where, for example, dating or tracer techniques are employed. The research area of nuclear physics is an ever-growing field, and our studies of light, proton-rich nuclei shall contribute to this growth.

[1] In 2022, NuPECC (the Nuclear Physics European Collaboration Committee) published a brochure titled “Nuclear Physics in Everyday Life” in which an interesting account of the applications of nuclear physics is given; I highly recommend giving it a look.

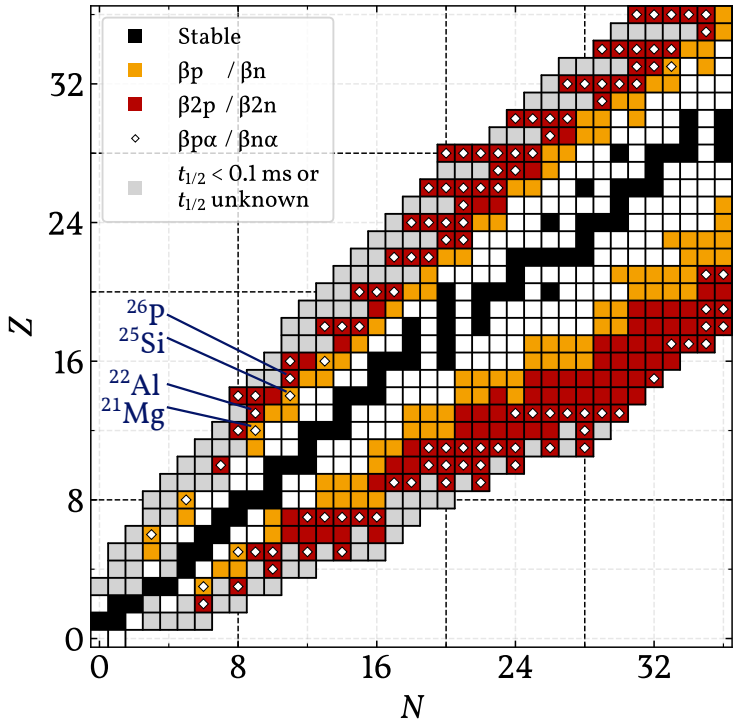

Figure 1.1: Cutout of the low-mass region of the chart of nuclides with the nuclides of interest to this thesis highlighted. Different combinations of neutron number N and proton number Z define the different nuclides. The stable nuclei are indicated, as are the nuclides for which it is kinematically possible to undergo beta-delayed nucleon emission (βp/βn), beta-delayed two-nucleon emission (β2p/β2n) and beta-delayed nucleon-alpha emission (βpα/βnα). Relatively long half-lives are indicative of beta decay. A cutoff in half-lives at 0.1 milliseconds has been chosen to distinguish beta decaying nuclei from nuclei decaying via direct nucleon emission. The figure is drawn based on data from AME and NUBASE 2020 [Hua+21; Wan+21; Kon+21].

1.1 The light proton-rich landscape

Figure 1.1 shows a cutout of the low-mass region of the chart of nuclides. Above the valley of stability, defined by the black squares, lies the proton-rich region of the chart of nuclides, and below the valley of stability lies the neutron-rich region. The four nuclides ^{21}Mg, ^{22}Al, ^{25}Si and ^{26}P are highlighted in the figure. These four nuclides all lie just above the shell closures of the proton and neutron magic numbers $Z = N = 8$. In the shell model framework, the protons and neutrons which are filled on top of these shell closures populate the proton and neutron sd-shells of the nuclei. We shall employ arguments based on this shell

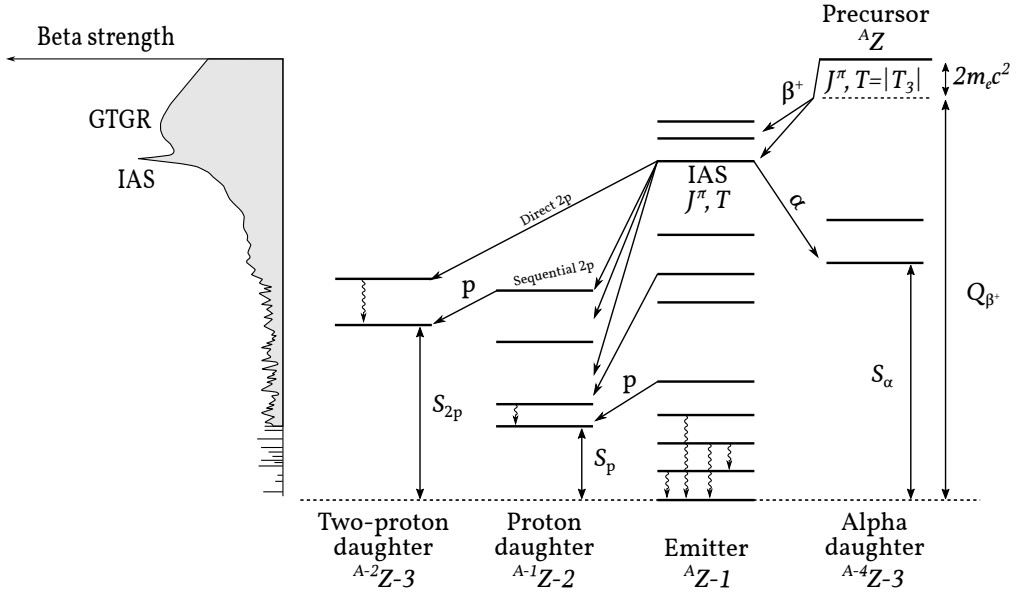

Figure 1.2: Schematic decay scheme of proton-rich nuclei. Beta-delayed charged particle emission can proceed via the emission of one or two protons or of an alpha particle from excited states in the emitter, which are populated as the precursor undergoes beta decay. The beta strength, related to the relative intensity of the population of excited states in the emitter, is depicted schematically to the left.

model picture in our detailed studies of the decay of ^{21}Mg recorded at ISOLDE at CERN.

The distinction is sometimes made between the one-proton (one-neutron) and two-proton (two-neutron) drip lines [BB08; PGR12], as pairing effects influence the one- and two-nucleon separation energies differently, and, hence, these two types of separation energy do not necessarily become negative for the same nuclides as one proceeds towards the edges of stability. The one-proton drip line has been reached experimentally up to the mass region of lead and beyond [BB08]. This has primarily been accomplished by producing proton-rich nuclei at rare ion beam facilities and by observing the protons emitted from states of high excitation energy, which are populated as the proton-rich nuclei undergo beta decay.

Figure 1.2 illustrates various kinds of beta-delayed charged particle emission from proton-rich nuclei. In the level diagram of the figure, the mass difference between the *precursor* and the *emitter* is so large that the population of

excited states in the emitter allows for the emission of one or two protons or for the emission of an alpha particle; the Q-value of beta decay Q_{β^+} less the particle separation energies, S_p, S_{2p} or S_α, is positive and of several MeV in magnitude, and thus states in the *one- and two-proton daughters* as well as states in the *alpha daughter* can be populated by the emission of protons and alpha particles. The ground state of the precursor has a definite isospin quantum number T and isospin projection $T = |T_3|$. From the ground state of the precursor, the Fermi transition, which changes only the isospin projection, populates the Isobaric Analogue State (IAS) of the emitter, which belongs to the same isospin multiplet as the ground state of the precursor. A schematic representation of the beta strength as a function of excitation energy in the emitter is also drawn in figure 1.2. The IAS, in particular, is fed by the Fermi transition of beta decay, but the Gamow-Teller transition also populates various other states. The broad Gamow-Teller Giant Resonance (GTGR) is situated above the IAS and is also within reach of the energy window of the Q-value, but the phase space at very high excitation energy is limited, and the Gamow-Teller transitions of beta decay are primarily seen towards lower excitation energies.

Across the entire chart of nuclides, the general trend is that the lower the mass of a given nuclide, the smaller is its density of states, while the individual states are quite broad; at the other extreme of nuclear mass, the density of states is very large, while the individual states are very narrow. We note that for the particular cases of proton-rich nuclei of relatively small masses, ^{21}Mg, ^{22}Al, ^{25}Si and ^{26}P, the density of states is still relatively small, while the individual states are relatively broad. It is also interesting to note, in relation to figure 1.2, that in the case of beta-delayed particle emission from neutron-rich nuclei, the Q-value of beta decay is typically smaller than the excitation energy of the IAS in the emitter, and, hence, the signature of beta-delayed neutrons is markedly different.

1.2 Production of light proton-rich nuclei

Light proton-rich nuclei are produced at rare ion beam facilities. These facilities do not only specialise in producing light proton-rich nuclei, but produce

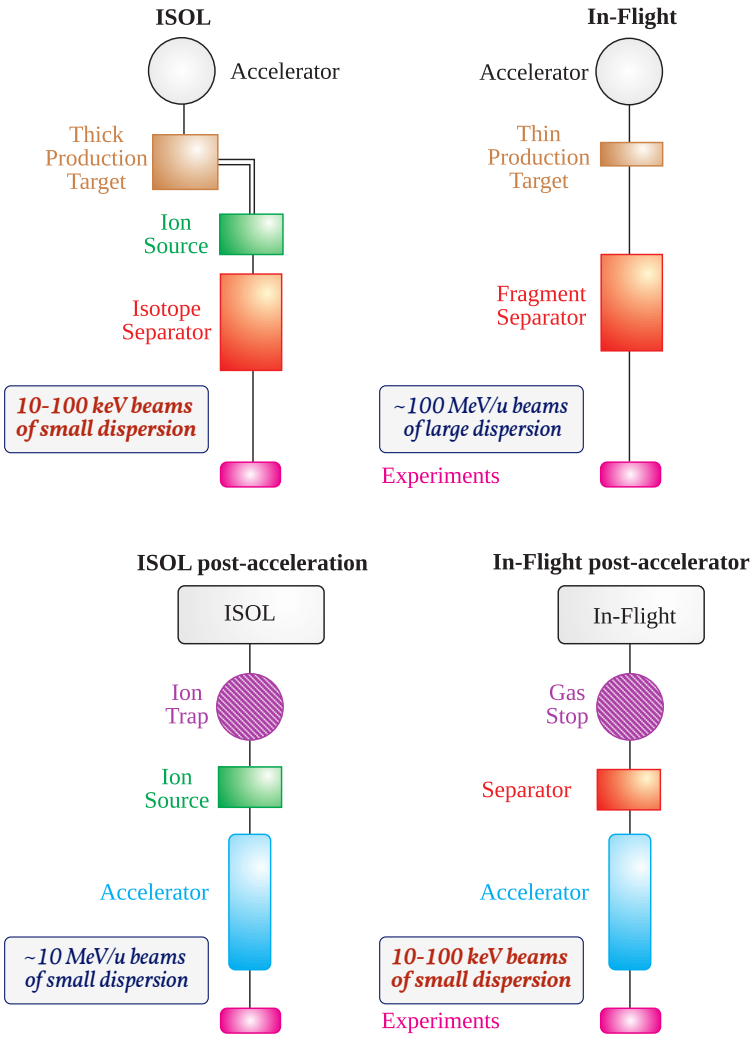

Figure 1.3: Schematic comparison of the ISOL and in-flight beam production methods. Following, respectively, isotope separation of ISOL beams and fragment separation of in-flight beams, the resulting rare ion beams can either be delivered to the relevant experimental setup (the top half of the diagram) or they can be post-accelerated before being delivered to the relevant experimental setup (the bottom half of the diagram). In our decay experiments, we employ low-energy beams of small dispersion, i.e. the top left and bottom right parts of the diagram. Figure adapted from [Ben+00].

rare ions of all kinds of masses and neutron-to-proton ratios across the entire chart of nuclides. Rare ion beam facilities generally fall into two categories: One type of rare ion beam facility employs the *ISOL*[2] technique and the other type employs the *in-flight* fragment separation technique. These two types of rare ion beam facilities are referred to as ISOL facilities and in-flight facilities,

[2]Ion Separation OnLine.

respectively.

A schematic drawing of the working principles of the two types of rare ion beam facilities is shown in figure 1.3. ISOL facilities implant high energy primary beams into thick production targets and extract, as secondary beams, a multitude of rare ion beam particles from an ion source; the rare ion beam particles are subsequently mass-separated. The resulting rare ion beam particles of interest are of low and well-defined energy. In-flight facilities, on the other hand, have high energy primary beams impinging on thin production targets, from which secondary beams of high energy, consisting of rare ion beam particles, emerge; the rare ion beam particles are subsequently fragment-separated in-flight. The resulting rare ion beam particles of interest are of high energy and of rather large dispersion. For the types of decay experiments we typically perform, we prefer beams of low and well-defined energy. Fragment-separated in-flight beams can be slowed down to lower energies e.g. by utilising a gas stopper, as is indicated in figure 1.3.

We shall go into more detail on the aspects of beam production, in particular regarding the in-flight facility FRIB, and we shall also justify the preference of rare ion beams of low and well-defined energy later in the thesis. In terms of beam production, both ISOL and in-flight facilities have their strengths as well as weaknesses; we shall return to this point in the outlook of the thesis.

1.3 Beta-delayed charged particle emission

Beta-delayed charged particle emission is, at the very least, a two-step process. First the precursor (figure 1.2) undergoes beta decay, and subsequently one or several charged particles are emitted from the emitter. In the following two sections we give a brief description of the two, fundamentally, very different processes, starting with that of beta decay.

1.3.1 Beta decay

The rate λ of beta decay, the mechanism of which is a weak perturbation of the nuclear potential, can be calculated using Fermi's golden rule,

$$\mathrm{d}\lambda(E_\mathrm{e}) = \frac{2\pi}{\hbar}\left|M_{fi}^{\pm}\right|^2 \frac{\mathrm{d}\rho(E_\mathrm{e})}{\mathrm{d}E_\mathrm{e}} \tag{1.1}$$

which here expresses the probability per unit time of a positron (electron) of energy between E_e and $E_\mathrm{e} + \mathrm{d}E_\mathrm{e}$ to be emitted along with an (anti-)electron neutrino as a proton (neutron) is transformed into its isospin-conjugate counterpart as it undergoes β^+ (β^-) decay. $\mathrm{d}\rho/\mathrm{d}E_\mathrm{e}$ is the density of final states per unit energy, and $M_{fi}^{\pm} = (g^2/2)V_{ud}\int \Psi_f^*\hat{\mathrm{Q}}_\pm\Psi_i\mathrm{d}V = (g^2/2)V_{ud}\int \psi_f^*\psi_e^*\psi_\nu^*\hat{\mathrm{Q}}_\pm\psi_i\mathrm{d}V$ is the transition matrix element from initial state $\Psi_i = \psi_i$ to final state $\Psi_f = \psi_f\psi_\mathrm{e}\psi_\nu$, where $\psi_{i,f}$ are the initial and final state wave functions of the entire atomic nucleus under consideration, and ψ_e and ψ_ν are the positron (electron) and (anti-)electron neutrino wave functions; g is the weak coupling constant, V_{ud} is the up-down quark-mixing element of the Cabibbo-Kobayashi-Maskawa matrix and $\hat{\mathrm{Q}}_\pm = \tilde{g}_V T_\pm + \tilde{g}_A T_\pm\vec{\sigma}$ acts on the initial state ψ_i, and the resulting overlap of wave functions is integrated over the volume V. In $\hat{\mathrm{Q}}_\pm$, $T_\pm$ is the isospin raising/lowering operator, $\vec{\sigma}$ is the spin operator and $\tilde{g}_V$ and $\tilde{g}_A$ are semileptonic weak interaction vector and axial vector coupling constants, to be re-parametrised shortly.

The appearances of g and V_{ud} in orders of 2 and 1 respectively in $M_{fi}^{\pm}$ are due to the weak interaction vertices of the leading order Feynman diagram(s) describing beta decay in the framework of electroweak theory (see e.g. [AH13]). Analogously to the strength of the electromagnetic interaction – the fine structure constant $\alpha = e^2/4\pi\varepsilon_0\hbar c \simeq 1/137$ – the strength of the weak interaction can, in the low-energy limit, be expressed as

$$\alpha_w = \frac{g^2}{4\pi\hbar c} = \frac{G_F}{(\hbar c)^3}\frac{m_W^2c^4}{4\sqrt{2}\pi} \simeq \frac{1}{235} \tag{1.2}$$

where $G_F/(\hbar c)^3 = 1.1663788(6)\times10^{-5}\,\mathrm{GeV}^{-2}$ is the Fermi constant and $m_W = 80.377(12)\,\mathrm{GeV}/c^2$ is the mass of the mediator of charged current weak interactions, the W boson [Wor+22]. The former is determined to very high precision from the study of muon decays, in which the weak interaction is purely leptonic, and the latter is estimated from $p\bar{p}$ and e^-e^+ interaction studies from various experimental high-energy physics facilities around the world.

By approximating, in $M_{fi}^{\pm}$, the lepton wave functions as plane waves and expanding,

$$\psi_{e,\nu} = \frac{1}{\sqrt{V}} e^{-i\vec{p}\cdot\vec{r}/\hbar} \simeq \frac{1}{\sqrt{V}} \left(1 + \frac{i\vec{p}\cdot\vec{r}}{\hbar} + \cdots\right) \tag{1.3}$$

they each merely contribute $1/\sqrt{V}$ in $M_{fi}^{\pm}$ to first order. Furthermore, by employing the fact (see e.g. [Pov+14, chapter 16]) that conservation of angular momentum prevents interference between vector and axial vector transitions in the total rate of beta decay, we then have $\left|M_{fi}^{\pm}\right|^2 = (g_V^2 B_F + g_A^2 B_{GT})/V^2$, where g_V and g_A are re-parametrised semileptonic weak vector and axial vector coupling constants, absorbing g^2 and $V_{ud} = g_V/G_F$ from earlier[3]; $B_F^{\pm} = |\langle f|T_{\pm}|i\rangle|^2 = \left|\int \psi_f^* T_{\pm} \psi_i \mathrm{d}V\right|^2$ is the Fermi strength of beta decay and $B_{GT}^{\pm} = |\langle f|T_{\pm}\vec{\sigma}|i\rangle|^2 = \left|\int \psi_f^* T_{\pm}\vec{\sigma}\psi_i \mathrm{d}V\right|^2$ is the Gamow-Teller strength of beta decay. Integrating both sides of equation (1.1), while substituting λ for the half-life $t_{1/2} = \ln 2/\lambda$ and incorporating the Fermi function (see e.g. [ZV17, chapter 24][4]) in the integral of the density of states, yields the familiar *ft*-relation for allowed beta decay,

$$\begin{aligned} ft_{1/2} &= \frac{K/g_V^2}{B_F^{\pm} + (g_A/g_V)^2 B_{GT}^{\pm}}; K = \frac{2\pi^3\hbar^7 \ln 2}{m_e^5 c^4} \\ &= \frac{\mathcal{T}_{1/2}}{B_F^{\pm} + (g_A/g_V)^2 B_{GT}^{\pm}}; \mathcal{T}_{1/2} = 6144.48 \pm 3.70\,\mathrm{s} \end{aligned} \tag{1.4}$$

where the value for $\mathcal{T}_{1/2}$ is obtained by adopting the *effective* semileptonic weak interaction vector coupling constant g_V based on the recent survey in [HT20]. This effective constant primarily accounts for the radiative decay processes which add to the bare beta decays in beta decay studies.

In going from equation (1.1) to equation (1.4), an implicit sum over final states has been introduced in the Fermi and Gamow-Teller strengths. For a Fermi transition from an initial state of isospin T and isospin projection T_3, $|i\rangle = |T; T_3\rangle$, to a final state of isospin T and isospin projection $T_3' = T_3 \pm 1$, $|f\rangle = |T; T_3'\rangle$, the Fermi strength is then

$$B_F^{\pm} = \sum_f |\langle f|T_{\pm}|i\rangle|^2 = \langle i|\, T_{\pm}T_{\mp}\, |i\rangle = T(T+1) - T_3 T_3' \tag{1.5}$$

[3] $|V_{ud}| = 0.97373(31)$ based on the recent survey in [HT20].

[4] For allowed beta decay, and in the limit $Q \ll m_e c^2$ where the Q-value of beta decay is much less than the electron rest mass, the Fermi function is approximately $F = 2\pi\eta/(\exp(2\pi\eta) - 1)$, where $\eta = Z_1 Z_2 \alpha c/v$ is the *Sommerfeld parameter*; Z_1 is the charge of the daughter nucleus, Z_2 is the charge of the emitted electron/positron (both charges in units of e), v is the speed of the emitted electron/positron, α is the fine structure constant and c is the speed of light.

by the same algebra as for the angular momentum ladder operators. In particular, when $T = |T_3|$, then $B_{\mathrm{F}}^{\pm} = 2T_3 = N - Z$ for transitions towards $N = Z$ (in the opposite direction $B_{\mathrm{F}}^{\pm}$ is zero), where N is the neutron number, Z is the proton number, and the nuclear physics custom of having neutrons contribute positively to the total isospin projection is employed[5]. Assuming, without loss of generality, that $Z > N$, the *Fermi sum rule* states

$$B_{\mathrm{F}}^{+} - B_{\mathrm{F}}^{-} = 2T_3 - 0 = N - Z \tag{1.6}$$

and the *Gamow-Teller sum rule* can equivalently be shown to be given by

$$B_{\mathrm{GT}}^{+} - B_{\mathrm{GT}}^{-} = 6T_3 = 3(N - Z) \tag{1.7}$$

which is three times the Fermi sum rule, reflective of the three possible spin projections of the Gamow-Teller matrix elements.

1.3.2 Emission of charged particles

The emission of charged particles from the interiors of nuclei necessarily involves the concept of quantum tunnelling; the charged particles in question are to penetrate out of the attractive nuclear potential, through the Coulomb barrier manifested by the protons of the nuclear interior and, possibly, through a centrifugal barrier. The emission of charged particles to the continuum is described by the free-particle solutions of the radial part of the 3-dimensional Schrödinger equation in the presence of a Coulomb and angular momentum potential

$$\frac{\mathrm{d}u_l^2(r)}{\mathrm{d}\rho^2} + \left(1 - \frac{l(l+1)}{\rho^2} - \frac{2\eta}{\rho}\right) u_l(r) = 0 \tag{1.8}$$

where the distance r of the charged particle from the nuclear potential is greater than the nuclear radius R_0; $r > R_0$. Here, $u(r) = rR(r)$, where $R(r)$ is the radial equation of the spherical coordinate representation of the wave function, $\rho = kr$, where $k = p/\hbar$ is the wave number, l is the angular momentum of the charged particle, and η is the Sommerfeld parameter introduced in footnote 4.

[5] This custom unites the two notations $\beta^{\pm}$ and $T^{\pm}$ in blissful harmony.

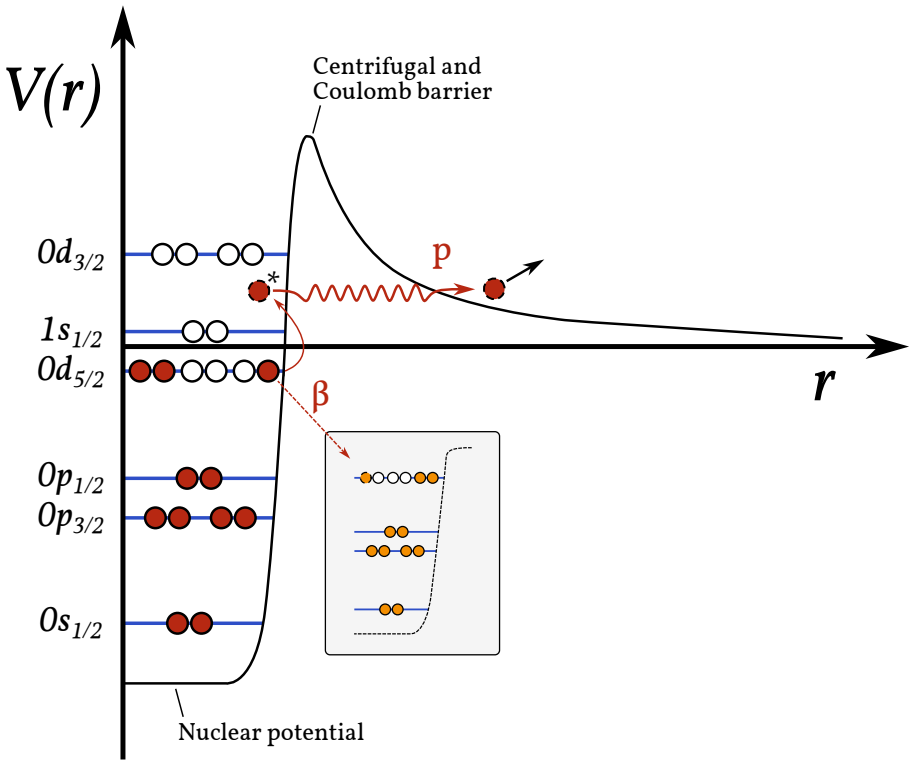

Figure 1.4: Schematic illustration of the tunnelling of a proton out of a nuclear interior, through the centrifugal and Coulomb barriers. The potential V varies with the distance to the centre r of the nucleus. The specific number of protons and neutrons, placed in shell model orbits for illustrative purposes, corresponds to the nuclide ^{21}Na. ^{21}Na is beta-unstable, and its proton separation energy is roughly 2.4 MeV [Hua+21; Wan+21]; the protons that penetrate out of the nuclear potential of ^{21}Na are, for example, those that result from the population of excited states in ^{21}Na due to the beta decay of ^{21}Mg.

An illustration of a proton tunnelling through the Coulomb and centrifugal barrier from a nuclear interior is shown in figure 1.4.

The general solutions to equation (1.8) are the *regular* and *irregular Coulomb wave functions*, $F_l(\eta,\rho)$ and $G_l(\eta,\rho)$ (see e.g. [Ili15]). By matching the solutions at R_0 to the interior wave function of the nucleus at $r < R_0$, one can find, independently of the interior wave function, the *penetrability* of charged particles, from the nuclear interior to the continuum, to be given by

$$P_l = \frac{kR_0}{F_l^2 + G_l^2} \tag{1.9}$$

where F_l and G_l are understood to be evaluated at R_0. The penetrability P_l is an

expression of the relative probability of a given charged particle to penetrate out of the nucleus in which it is confined, and it is but one of many ingredients in the framework of *R-matrix theory*, which is used to describe resonance behaviour in nuclear physics by modelling the nuclear interiors as resonant cavities and the nuclear exteriors by the description of equation (1.8); see e.g. [Vog68].

In the current chapter, broad overviews of the light proton-rich landscape, production methods and the fundamental models through which we understand beta-delayed charged particle emission have been presented. In the following chapter, the subject matter will become more specialised, as we describe, in fairly broad terms, the specific experimental methods which we employ in order to study the decays of light proton-rich nuclei. Most of the remainder of this thesis then becomes highly specialised, as specific experiments carried out at the specific rare ion beam facilities of ISOLDE and FRIB become the two main topics throughout. In the outlook of the thesis, we shall take a couple of steps back and relate the specific experiments at ISOLDE and FRIB to the more general considerations presented in this chapter.

Chapter 2

Experimental methods

2.1 Quick rundown

In a nutshell, our experimental methods consist in the following. We take, as input, proton-rich rare ion beams of well-defined low energy, and we stop the radioactive beam particles in a thin catcher foil from which they can decay. The thin catcher foil is surrounded by our small segmented silicon detectors[1] for the detection of charged beta-delayed particles, and we tend to borrow, if possible, germanium detectors local to a given rare ion beam facility, for the detection of gamma rays also emitted in the decay. Thus, we can detect all the types of particles emitted in the beta decay of proton-rich nuclei (figure 1.2). The lower the energies of the beam particles, the thinner our catcher foil can be made (but decreasing the beam energy and/or the foil thickness has practical limitations). The thinner the catcher foil, the smaller are the energy losses endured by the charged particles emitted from the foil. Although there is a spread ΔE_{loss} in these energy losses around some mean value of energy loss E_{loss} (due to the random nature of the interactions between the charged particles and the foil), this spread decreases with the foil thickness. As the energies of the beam particles can, in principle, also have some spread ΔE_{b} around the mean beam energy E_{b}, this uncertainty in E_{b} will propagate into the uncertainty in E_{loss}. When we speak of rare ion beams of *well-defined* low energy, the spread

[1] The silicon detectors can be held in one hand, and they can be operated at room temperature. They are hence easy to ship from our home institution to any rare ion beam facility in the world.

in the beam energy ΔE_b is negligible, i.e. the dispersion in momentum of the beam particles is small. The payoff in stopping rare ion beams of well-defined low energy in a thin foil and observing the decay products of the stopped beam particles in segmented detectors surrounding the thin foil is:

- High-resolution particle spectra which are primarily limited in resolution by the resolutions of the individual detector segments.
- The ability to identify individual decay products of multi-particle decays such as beta-delayed two-proton emission.

We shall return to these points and compare them to other prevalent experimental methods employed in the field of rare ion beam studies in the outlook of this thesis.

The following sections delve a bit deeper into the technicalities of the ideas introduced in this section, establishing them in a more quantitative fashion. First, some general considerations in the stopping of charged particles – specifically, the stopping of atomic nuclei in matter – are presented. It is customary, when describing the stopping of atomic nuclei in matter, to refer to the atomic nuclei as ions, whether the atomic nuclei are at the cores of unionised neutral atoms, or whether they are part of partially or entirely ionised atoms; we shall employ this terminology in the entirety of this thesis. The upcoming section on the stopping of ions in matter is followed by a section describing the detection of charged particles in our silicon detectors, and, in the final section of this chapter, some general considerations in relation to the acquisition of data from our detectors are presented.

2.2 Stopping of ions in matter

In figure 2.1 the results of TRIM[2] simulations [ZZB10] of the passage of ^{21}Mg, ^{22}Al, ^{25}Si and ^{26}P through a thin carbon foil[3] are shown. The ions initially have kinetic energies $E_{\text{kin}} = 30$ keV, and each interaction with the atomic electrons

[2] TRansport of Ions in Matter.

[3] Nuclear charge number $Z = 6$, ionization potential $I \simeq 1$ keV and density $\rho = NM/N_A = 2.26$ g/cm^3, where M is the molar mass and N_A is the Avogadro constant; see equation (2.1).

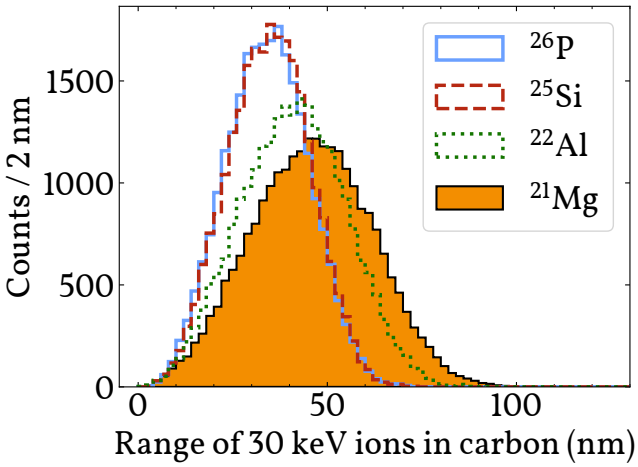

Figure 2.1: Ranges of low-energy ions with initial kinetic energies $E_{\text{kin}} = 30$ keV in carbon. TRIM, a subprogram of the SRIM program [ZZB10], has been used to simulate the passage of 25,000 of each of the ions ^{21}Mg, ^{22}Al, ^{25}Si and ^{26}P through carbon.

	^{26}P	^{25}Si	^{22}Al	^{21}Mg
Mean range (nm)	34.1	34.6	40.1	45.9
Median range (nm)	34.1	34.8	41.2	46.0
Central 95 % confidence interval (nm)	[13.2, 55.3]	[13.7, 55.3]	[14.5, 67.8]	[15.7, 76.6]

Table 2.1: Various statistics of ranges of low-energy ions with initial kinetic energies $E_{\text{kin}} = 30$ keV in carbon. The statistics are derived from the distributions of figure 2.1. The statistical uncertainty in the listed values is 0.1 nm.

of the carbon foil causes the ions to lose some of their kinetic energy, until they are completely stopped in the foil. In this chain of interactions, each individual interaction is random in nature, and so is the distance between the points of interaction within the carbon foil. At each point of interaction, the ions may be deflected away from their current path through the foil. It is due to these mechanisms that the distributions of ranges R – i.e. the longitudinal distances the ions traverse before they are completely stopped – are as shown in figure 2.1.

Table 2.1 lists the means, medians and central 95% confidence intervals of the ranges depicted in figure 2.1. It is evident that the lighter the ion, the more

spread there is in the range. Also, due to the asymmetric nature of the range distributions, the mean and median values are not entirely the same, although they are close. It is worth noting that all analyses involving energy loss corrections and range extrapolations of ions in this thesis employ *mean values* in the same sense as presented in table 2.1. These values are extracted from the stopping and range tabulations of SRIM[4] [ZZB10].

In the limit of a large number of interactions between a given ion traversing a material consisting of a given type of absorber atoms, the stopping power $S(E) \equiv -\mathrm{d}E/\mathrm{d}x$ describes the average change in energy of the ion $\mathrm{d}E$ per path length $\mathrm{d}x$ in the material. The stopping power depends (explicitly) on the energy E of the ion as well as the type of ion and the type of material. For non-relativistic ions [Kno10; Sal22], the stopping power can be approximated as

$$S(E) = -\frac{\mathrm{d}E}{\mathrm{d}x} \simeq \frac{4\pi e^4 z^2}{m_e v^2} NZ \ln \frac{2m_e v^2}{I} \tag{2.1}$$

where z is the nuclear charge number of the ion and v is its velocity, Z is the atomic charge number of the absorber atoms, m_e is the corresponding electron masses of the absorber atoms, N is the number density of the absorbing material and I is its ionization potential.

Assuming that a given ion does not veer significantly from its initial path through a given absorber material, and assuming that the absorber material has a thickness t sufficiently large to stop the ion completely, the range R of the ion is given by

$$R(E_i) = \int_0^R \mathrm{d}x = -\int_{E_i}^0 \frac{\mathrm{d}E}{-\mathrm{d}E/\mathrm{d}x} = \int_0^{E_i} \frac{\mathrm{d}E}{S(E)} \tag{2.2}$$

where E_i is the initial energy of the ion. If, on the other hand, the ion is sufficiently energetic to *punch through* the absorber material of thickness t, it merely endures an energy loss E_{loss}, which is given by

$$E_{\mathrm{loss}}(t) = -\int_{E_i}^{E_f} \mathrm{d}E = \int_0^t -\frac{\mathrm{d}E}{\mathrm{d}x}\mathrm{d}x = \int_0^t S(E)\mathrm{d}x \tag{2.3}$$

[4] Stopping and Range of Ions in Matter.

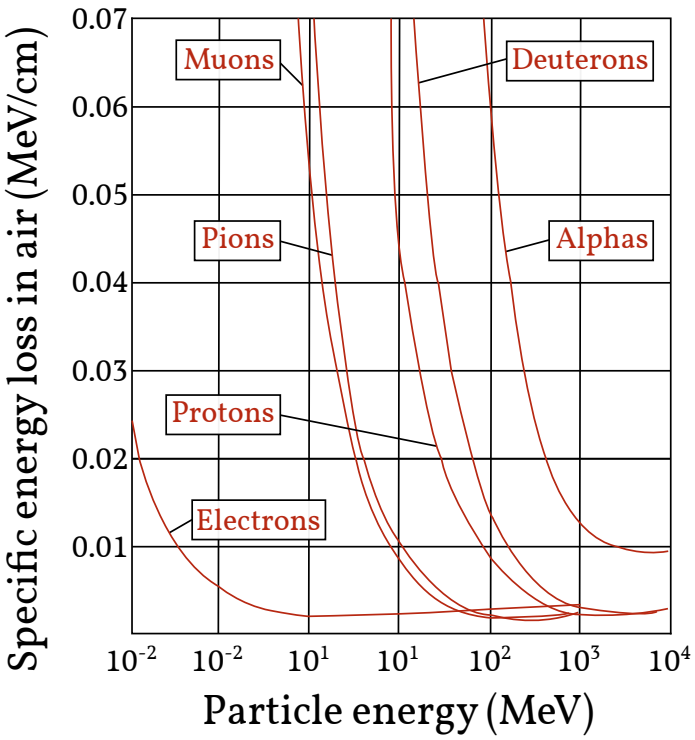

Figure 2.2: Variation of energy loss for charged particles of various kinds and energies. When the particles are sufficiently energetic, they reach a broad near-constant minimum in energy loss. Figure adapted from [Bei52].

where E_f is the remaining energy of the ion as it punches through the absorber material. Finally, for two different species of ions of equal initial speeds v_i traversing the same absorber material, the range R_a of species a with nuclear charge z_a and mass m_a is approximately related [Kno10] to the range R_b of species b with nuclear charge z_b and mass m_b via the relation

$$R_a = \frac{m_a z_b^2}{m_b z_a^2} R_b \tag{2.4}$$

The relation is most accurate when the involved charges and masses are not too different. Using this relation, we can understand, qualitatively, the variation in the mean ranges of figure 2.1, keeping in mind that the initial energies E_i of the various ions in the figure are all equal, and, hence, the initial velocities v_i vary slightly (compare equations (2.1) and (2.4)).

For increasing charged particle kinetic energies, it is observed experimentally [Kno10] that the energy losses of charged particles in light materials eventually reach a near-constant, broadly universal, minimum in the energy losses

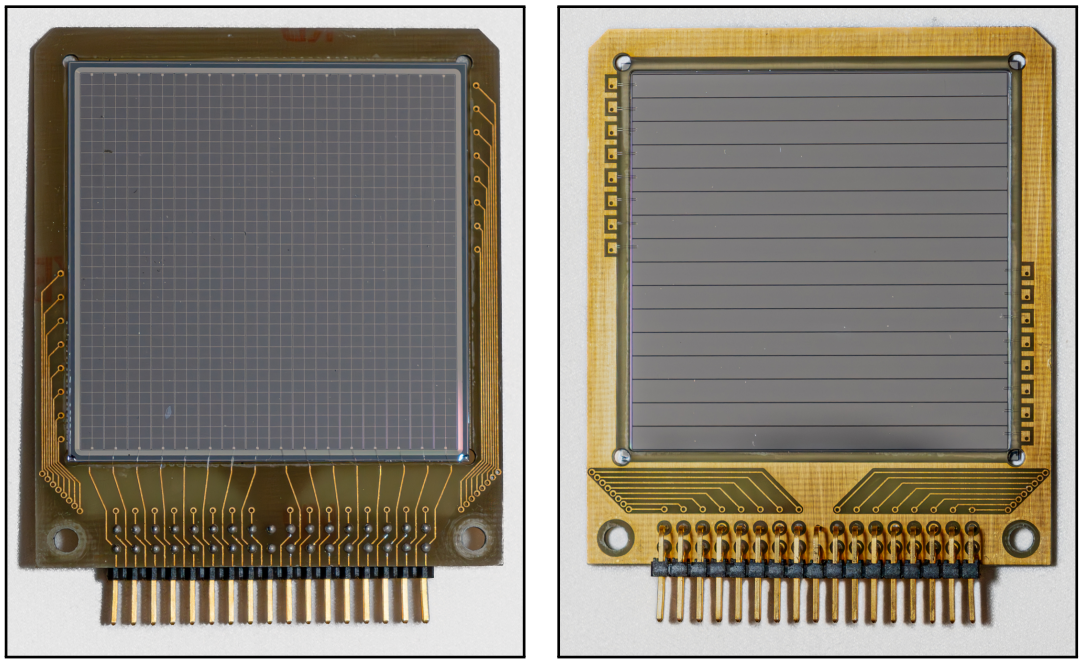

Figure 2.3: p^+- and n^+-side of one of our Micron Semiconductor DSSSDs of W1 design [Mic18]. The photo on the left shows the p^+-side of the detector, and the photo on the right shows the n^+-side of the detector. The p^+-side has 16 vertical strips, and the n^+-side has 16 horizontal strips.

they endure. When charged particles are sufficiently energetic to reach this specific energy loss of approximately $2\,\mathrm{MeV}/(\mathrm{g}/\mathrm{cm}^2)$ they are referred to as *minimum ionising particles*. Generally, the lighter the charged particle, the lower the kinetic energy necessary for it to become minimum ionising. The onset of minimum ionisation for various charged particles is illustrated in figure 2.2. The charged particle kinetic energies which we observe in our studies of the beta decays of proton-rich nuclei (beta particles, protons, alpha particles; figure 1.2) are of order 0.1-10 MeV. We conclude, based on the data of figure 2.2, that the beta particles in our experiments are minimum ionising. We shall return to this point, when the relevant length scales of our silicon detectors have been established in the next section.

2.3 Detection of charged particles

The centrepieces of our experimental setups are our DSSSDs[5]; these detectors are n-type semiconductor detectors of high purity with p^+ rectifying contacts

[5] Double-Sided Silicon Strip Detectors.

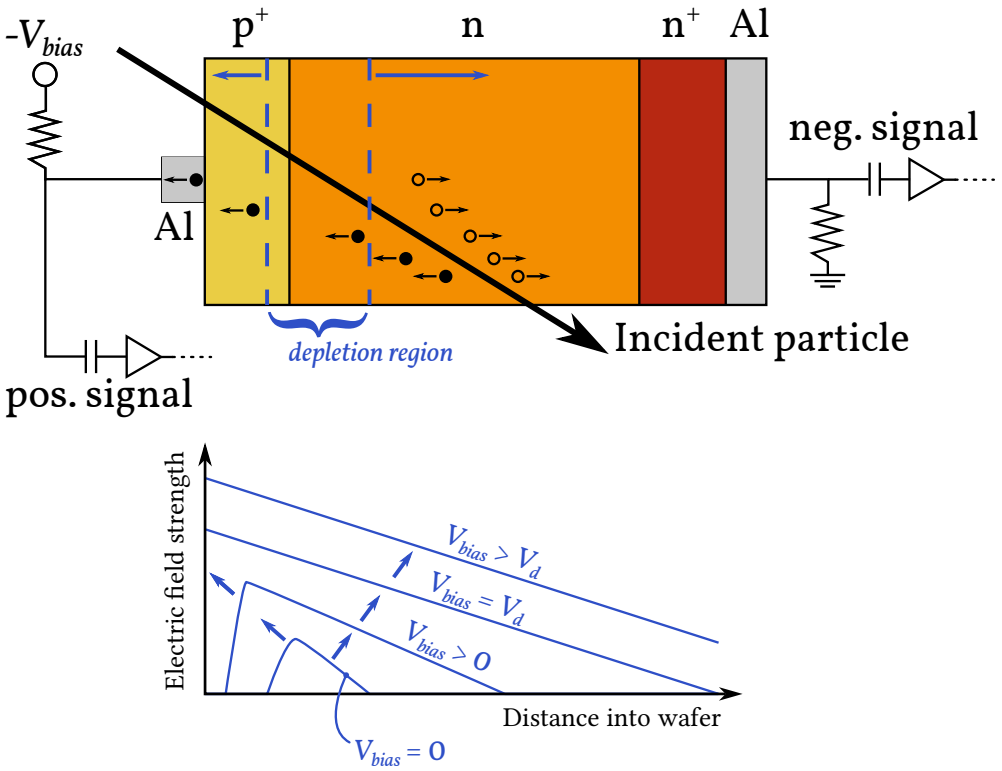

Figure 2.4: Schematic cross section of silicon detector pixel. A negative bias voltage $-V_{bias}$ is applied to the aluminium grid on the p^+-side with respect to the aluminium strip on the n^+-side. As V_{bias} is increased, the depletion region expands from covering the intrinsic depletion region of the pixel to cover the entire wafer as V_{bias} reaches the depletion voltage V_d. The evolution of the electric field strength with respect to distance into the wafer is sketched. As an incident charged particle traverses the wafer, electron-hole pairs are created and driven to opposite sides of the detector; a positive signal is generated at the p^+-side, while a negative signal of equal magnitude is generated at the n^+-side. The various heights and thicknesses in the drawing are not to scale.

of 0.1 µm thickness on the front side and n^+ rectifying contacts of 0.4 µm thickness on the back side. 16 such p^+-n-n^+ isolated vertical segments form 16 vertical *strips* on the p^+-side of the detectors, and on the n^+-side of the detectors a similar isolation of segments defines 16 horizontal strips. Each strip is 3000.0 µm wide and the active area of the DSSSDs spans 50.0×50.0 mm^2 [Mic18]. Overlaying the 16 strips on one side with the 16 orthogonal strips of the other side defines a detector matrix of $16 \times 16 = 256$ silicon detector *pixels*. Photos of the p^+- and n^+-sides of one of our DSSSDs are presented in figure 2.3.

On the p^+-side, a thin aluminium grid of thickness 0.2 µm covers only 3–4 %

of the surface area, while each strip on the n^+-side is completely covered by aluminium of thickness 0.2 µm. The aluminium is etched onto the surfaces of the p^+- and n^+-sides and is used to establish electrical contact with the silicon wafer: A reverse bias is applied to the electrical contact on the p^+-side across the silicon wafer, and the electrical contacts are simultaneously used for readout of the signals generated in the active n-type bulk of the detector. When charged particles traverse the active detector medium, electron-hole pairs are generated due to the ionisation of the electrons of the absorber material; see figure 2.4. The number of generated electron-hole pairs corresponds to the energy losses endured by the incident charged particles.

Most charged particles incident on the detector will only encounter the p^+ rectifying contact of thickness 0.1 µm before reaching the active n-type medium. This means that the energy losses endured by these particles are quite small. In the ideal case, then, a charged particle incident on the detector does not encounter the detector's aluminium grid; also, in the ideal case, various *interstrip effects* (see e.g. [Tor+13]) do not influence the response of the detector. When this is the case, the electrons of the generated electron-hole pairs are driven to the p^+-side of the detector, and the holes are driven to the n^+-side, generating, respectively, a positive signal in one of the p^+-side strips and a negative signal of equal magnitude in one of the n^+-side strips. Both signals are characteristic of the incident particle energy, and the overlaying of the two strips defines a detector pixel of 3000.0×3000.0 µm^2 on which the particle was incident. If the source point of emission and the type of the particle is known, the direction from source point of emission to pixel, the mass of the incident particle and its deposited energy can be used to calculate the momentum of the particle.

The design of the detectors with a thin aluminium grid of 3–4 % surface coverage was developed in a collaboration between Micron Semiconductor Ltd. and our MAGISOL[6] collaboration, with Olof Tengblad of our collaboration as *primus motor* [Ten+04]. During these developments the thickness of the p^+ rectifying contact of the detectors was also brought down from 0.4 µm to the 0.1 µm mentioned above. This was, again, in order to minimise the energy losses of

[6] Madrid-Århus-Göteborg-ISOL.

	DSSSD	Pad
p^+-side electrical contact	Al (grid), 0.2 µm	Al, 0.2 µm
p^+ rectifying contact	Si, 0.1 µm	Si, 0.4 µm
n-type bulk	Si, 50–1000 µm	Si, 500–1500 µm
n^+ rectifying contact	Si, 0.4 µm	Si, 0.4 µm
n^+-side electrical contact	Al, 0.2 µm	Al, 0.2 µm

Table 2.2: Material layer types and thicknesses of our silicon detectors. The orderering of rows in the left column is the order in which an incident particle will encounter the layers. Depending on the needs of the experiment, we employ various active layer (n-type bulk) thicknesses of both DSSSDs and Pads. The electrical and rectifying contact thicknesses are not precisely known; they are, in fact, known to have changed over time in Micron's product catalogue (see [AUS24]). As such, these thicknesses might vary between detectors from different batches by up to a factor of two.

the incident ions and, hence, the low energy thresholds of the dynamic ranges of the detectors. The detectors are of Micron's W1 design [Mic18]. The response of the detectors, including that of the aluminium grid, has been studied in [Viñ+21].

The various layer thicknesses of our silicon detectors are listed in table 2.2. Apart from the DSSSDs of W1 design, we also employ SSSDs[7] of the same active area as that of the DSSSDs ($50.0 \times 50.0\ \mathrm{mm}^2$). These detectors consist of a single p^+-n-n^+ semiconductor with a complete surface coverage of 0.2 µm aluminium on both the p^+- and the n^+-side. We tend also to refer to this type of detector as a "Pad detector". The layer thicknesses of our Pad detectors are also given in table 2.2. For the remainder of the thesis, we shall drop the "+" superscript when referring to the contacts of the silicon detectors, and simply refer to the two sides of our silicon detectors as the p-sides and the n-sides.

Now that the relevant length scales of our silicon detectors have been established, we return to the point of minimum ionising beta particles from the previous section. Our silicon detectors are by no means of sufficiently large thickness to completely stop beta particles of energies 1–10 MeV, when one considers the thicknesses listed in table 2.2 and compares them with the trend

[7] Singled-Sided Silicon Detectors.

of figure 2.2, the specific energy loss $2\,\mathrm{MeV}/(\mathrm{g/cm^2})$, quoted in the previous section, and the density of silicon $\rho = 2.33\,\mathrm{g/cm^3}$ [WA82, page B-37]: Taking the energy losses endured by the beta particles to be constant, the minimum ionising stopping power in silicon is

$$S_{mi}^{Si} = 2\,\mathrm{MeV}/(\mathrm{g/cm^2}) \times 2.33\,\mathrm{g/cm^3} \simeq 0.5\,\mathrm{keV/\mu m} \tag{2.5}$$

which amounts to a deposited energy of roughly 750 keV in our thickest Pad detectors of 1500 µm active thickness[8]. While we do not expect to stop beta particles in our silicon detectors, we can instead, by proper choice of detector thicknesses, stop the heavier charged particles emitted in the beta decays of proton-rich nuclei in our detectors. The consequence of the approximate result of equation (2.5) is that the larger the silicon detector thickness, the more energy the minimum ionising beta particles deposit in the detector. In the charged particle spectra of our silicon detectors this manifests itself as a background in the spectra of interest; those of protons and alpha particles. The background reaches further up in energy and is more intense, the larger the detector thickness. On the other hand, keeping the detector thicknesses small means that protons, for example, might not be completely stopped in the detectors.

A simple but clever way of minimising the beta background without compromising on the sensitivity to e.g. protons of higher energy is to employ the so-called ΔE-E technique, in which a thin detector is placed in front of a thick detector: A proton of relatively high energy might punch through the thin detector and deposit a fraction of its energy, ΔE, and then be completely stopped in the thick detector where it deposits its remaining energy, E. The sum $\Delta E + E$ is, neglecting energy losses, the initial proton energy. Below punch through, the beta background is kept minimal due to the small thickness of the "ΔE detector", and above punch through, the fraction of deposited energies in the "ΔE detector" and the "E detector" is characteristic of the type of ion, i.e. the ΔE-E technique provides a particle identification method. For many more details see e.g. [PR76; Bad+22] or section 4.1 of this thesis.

[8] It should be noted that beta particles of energies 1–10 MeV generally have much more erratic paths through matter (see e.g. [Kno10]), so a fraction of the beta particles of lower energy could conceivably be stopped in our thickest Pad detectors.

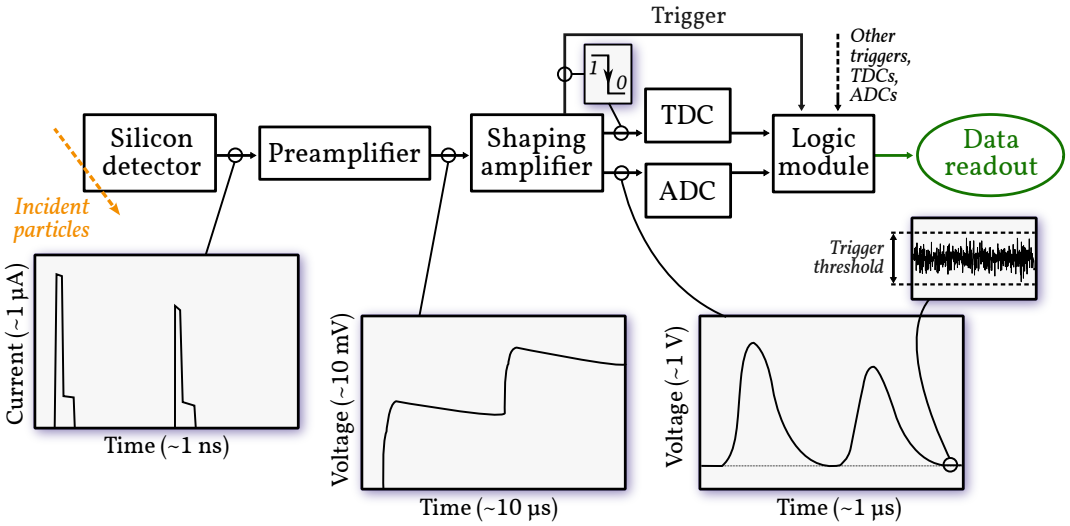

Figure 2.5: Schematic representation of the signal transmission and analogue signal processing pipeline of our experimental setups. Charged particles are, here, incident on one of our silicon detectors, and the signals thus produced are amplified and shaped before being recorded in digital form. The same pipeline applies to germanium detectors integrated into our data acquisition system.

With our specialised DSSSDs and Pad detectors, we have the means to identify the energies, momenta and spatial distributions of the charged particles emitted in the beta decay of proton-rich nuclei. In order to carry out these identifications, we first require the recording of the signals produced by the electrical contacts of the semiconductor detectors. Recording of the signals is handled by our DAQ[9], which is the topic of the next section.

2.4 Data acquisition

Although the transition from the analogue data acquisition systems of old to the digital data acquisition systems of new is well underway in all branches of experimental nuclear physics, the two experiments described in this thesis were both carried out with an analogue data acquisition system; an analogue, as opposed to a digital, DAQ. Newer experiments e.g. at the IDS setup at ISOLDE at CERN employ the XIA Pixie-16 digital data acquisition system [XIA24], and the experiment on ^{22}Al and ^{26}P at FRIB was also meant to employ a XIA Pixie-

[9] Data AcQuisition system.

16-based DAQ available at FRIB, although, due to time constraints, we ended up shipping our own analogue DAQ to FRIB and using that for the experiment instead.

A schematic drawing of the signal transmission and analogue signal processing pipeline from silicon detector to data readout is presented in figure 2.5. As charged particles impinge on the silicon detector, currents of size proportional to the charged particle energies are immediately fed to a preamplifier, as the currents are both small and short in time (i.e. their time distributions contain high-frequency components) and, hence, the longer the transmission lengths of these currents, the more noise they will inevitably pick up (e.g. due to so-called "$1/f$ noise"). The preamplifier produces (through a *CR*-equivalent circuit [Kno10]) step-like voltages with step sizes proportional to the input currents; after the step-up in voltage, the signal decays on a time scale of order 10 µs. These preamplified signals are much less noise-prone, and the signals can be transported several metres before reaching the shaping amplifier. In the shaping amplifier, the preamplified signals are further amplified and shaped (in a *CR*-*RC*-equivalent circuit) to curves of the shapes depicted in figure 2.5; the shaped signals have widths of order 1 µs. The individual integrals of these curves are directly proportional to the initial signal amplitudes produced in the silicon detector. It is the job of the ADC[10] to carry out the integration of the shaped signals and deliver, for each shaped signal, a digital representation of the signal amplitude to the logic module.

The shaping amplifiers of our experimental setups also deliver trigger signals (logical on/off signals) separately to our TDCs[11] and to our logic module. The TDCs provide the arrival of trigger signals with high-precision timestamps (resolution of order 100 ps) and deliver them to the logic module. The trigger signals, from all the various shaping amplifiers of a given experimental setup, are used in some combination to define when a combination of detector signals is potentially interesting. When such a trigger combination is encountered, the logic module's response is to signal the readout of the values from all TDCs and ADCs of the setup.

Finally, as is illustrated in figure 2.5, there is some (ideally, only random)

[10] Analogue-to-Digital Converter.
[11] Time-to-Digital Converters.

noise of finite size on top of which the shaped signals appear. This noise is the result of all the random electrical fluctuations in the entire electrical system schematically depicted in the figure. Minimising the noise allows for the detection of low-amplitude true events in the silicon detectors, which would otherwise be indistinguishable from noise. The *trigger threshold* indicated in the figure is configurable on each shaping amplifier, and only signals of amplitude larger than this threshold generate a trigger. We generally try to set our trigger thresholds as low as possible, in order not to miss low-amplitude true events, but our DAQ is limited in data throughput, and setting the thresholds too low would result either in the recording of a lot of uninteresting random events or the non-functioning of our DAQ.

We shall refer back to the signal transmission and data acquisition ideas encapsulated in figure 2.5 when describing the experimental setup employed at FRIB in part II of this thesis. The software facilitating the data acquisition of our analogue DAQ is described in [Mun18]. Now, armed with our general theoretical understanding presented in chapter 1 and the experimental methodology presented in this chapter, we shall proceed to specific experiments studying the beta decay of proton-rich nuclei. The first of the two experiments, relevant to the work presented in this thesis, was carried out at the rare ion beam facility ISOLDE at CERN, studying the beta decay of ^{21}Mg.

Part I

ISOLDE

Chapter 3

The ISOLDE Facility at CERN

The legacy of the ISOLDE facility at CERN is almost as long as the legacy of CERN itself. Only 10 years after CERN's first accelerator, the Synchrocyclotron (SC), was commissioned in 1957, the first experiment at the first iteration of the ISOLDE facility took place [BJ17]. Since then, the ISOLDE facility has been continually upgraded. Most significant, in the past decade, is the commissioning of HIE-ISOLDE[1] which allows for the post-acceleration of ISOL beams as is sketched in figure 1.3. The SC was decommissioned in 1990, and, today, ISOLDE takes protons of 1.4 GeV kinetic energy as its primary beam from the PSB[2] which, in turn, receives hydrogen anions from LINAC 4 at 160 MeV; see figure 3.1. LINAC 4 was commissioned quite recently, in 2020.

The PSB at CERN consists of four synchrotron rings with radii of 25 metres, stacked on top of each other. The 160 MeV hydrogen anions from LINAC 4 are split between the four rings of the PSB, where they are stripped of their two electrons, bunched and accelerated to 1.4 GeV. The bunches are then recombined into a single pulse, and the pulse is either sent to the ISOLDE facility or to the PS[3] from which the rest of the CERN accelerator complex gets its protons. This process takes place every 1.2 seconds and defines what is called a *cycle*. Every 12 cycles defines a *super cycle*, and it is based on these super cycles that the bunches of 1.4 GeV protons are distributed across the CERN accelerator complex. In the near future, the kinetic energies of the protons delivered

[1] High Intensity and Energy-ISOLDE.
[2] Proton Synchrotron Booster.
[3] Proton Synchrotron.

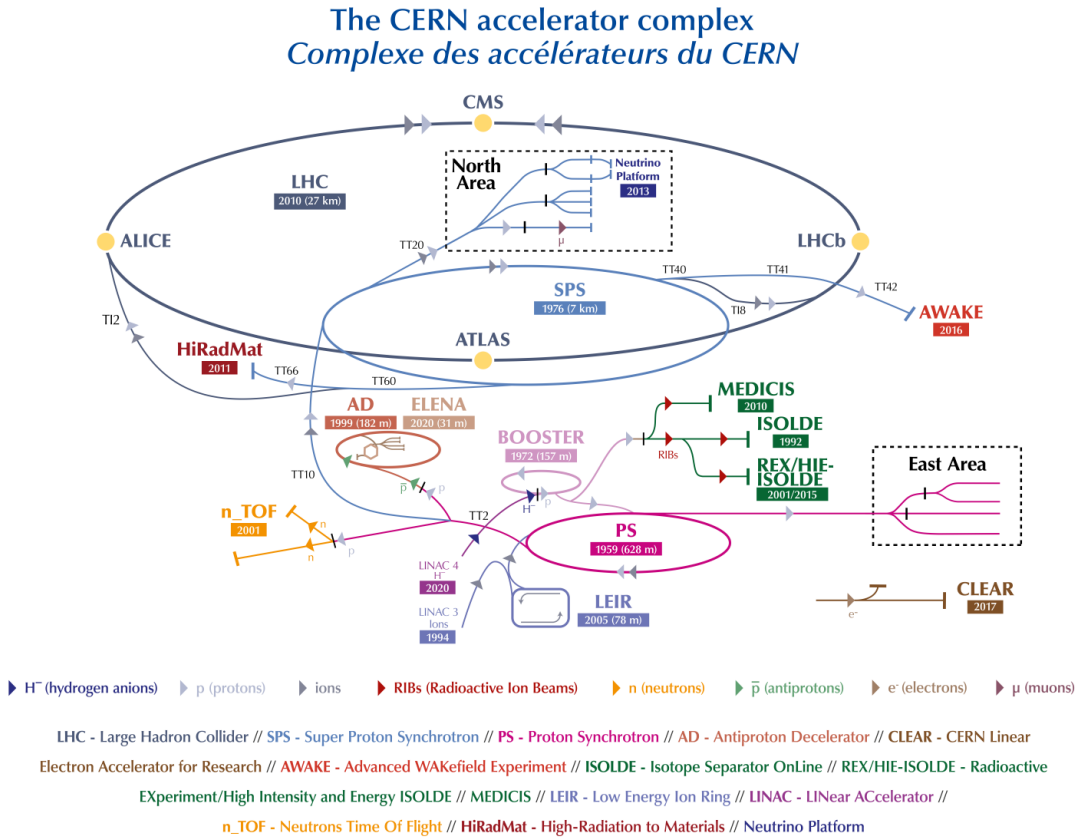

Figure 3.1: Sketch of the CERN accelerator complex, adopted from [CER22].

from the PSB to ISOLDE are to be increased to 2 GeV [Asv+22], and with this increase in primary beam energy comes also a possibility of increased intensities of the delivered protons. This will require major upgrades of, respectively, the proton transfer lines and the beam dumps at ISOLDE, while the benefit of these upgrades will be increased production cross sections at the production targets at ISOLDE (figure 1.3), which are estimated to increase, at the very least, by an order of magnitude.

As the pulses of 1.4 GeV protons, the primary beam, arrive at ISOLDE, they are implanted in a thick production target in which spallation, fission and fragmentation reactions between primary beam and target nuclei occur. The range of these high-energy protons in the typical production targets employed at ISOLDE is in the order of tens of centimetres; as the protons traverse the production target, a multitude of rare ions are produced. The trick is then to extract the rare ions from the production target. As the proton pulses impinge on

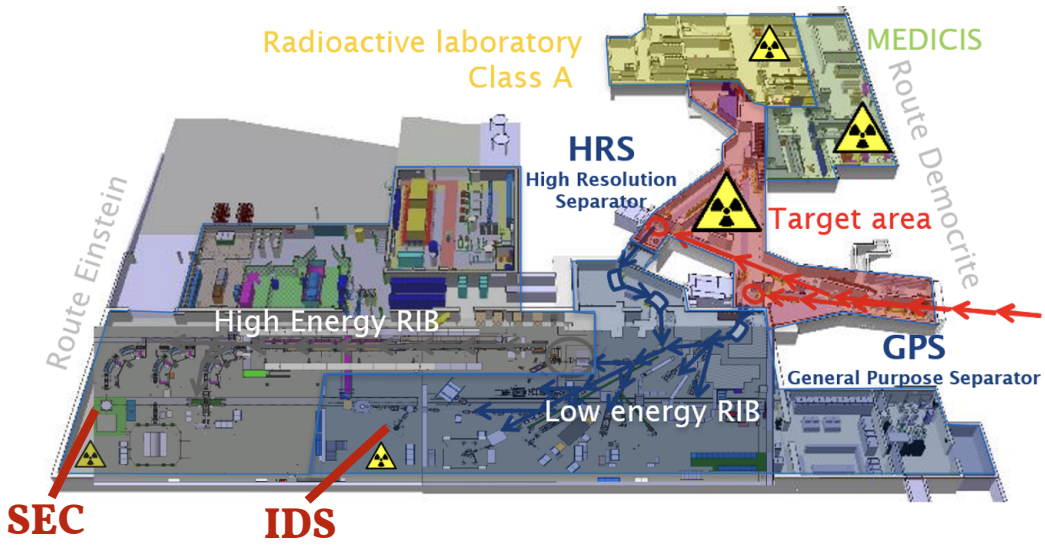

Figure 3.2: Sketch of the ISOLDE facility at CERN, adapted from [Kow21].

the production target, large electrical currents[4] are run through the tantalum cylinder, in which the production target is kept. This brings the temperature of the production target up to thousands of Kelvin, such that the diffusion of rare ions towards the transfer line to the ion source (figure 1.3) is fostered. Finally, as the rare ions reach the ion source, they are accelerated to 30–60 keV and subsequently mass-separated.

An overview of the ISOLDE facility is shown in figure 3.2. The target area (indicated in the centre right of the figure), from which the rare ion beams emerge, are mass-separated either in the General Purpose Separator (GPS) or the High Resolution Separator (HRS). As the name implies, the HRS has a larger mass-separating resolution as compared to the GPS at $M/\Delta M \sim 7000$; more details on the target areas and mass separation areas can be found in [BJ17] and the references listed therein. The rare ion beams emerging from GPS and HRS are of low and well-defined energy. In figure 3.2, IDS[5] is highlighted. This is where the MAGISOL Collaboration, in cooperation with the broader IDS Collaboration, carries out the majority of its rare ion beam experiments. In the figure, SEC[6] is also highlighted. This is another experimental

[4] Separate from those generated by the protons.
[5] The ISOLDE Decay Station.
[6] The Scattering Experiment Chamber.

setup with which the MAGISOL Collaboration is closely associated. In the following chapter, we describe the experiment on ^{21}Mg carried out at IDS in 2015 by the MAGISOL and IDS Collaborations.

Chapter 4

The beta decay of ^{21}Mg

nokorimono ni wa fuku ga aru
残り物には福がある。

Meaning: There is fortune in leftovers.

Japanese proverb from the Edo period, ca. 1700.

Note: This chapter starts on a slightly personal (to the author) diversion, utilising the first-person "I" quite extensively. We shall soon return to the conventional form of scientific prose in which the "I" has no place, the "we", when employed appropriately, can do wonders for one's relations with colleagues, and the omnipresent "one" is predisposed to see, know and understand all (however, only when invoked).

In the year 2015 (the year I started my undergraduate studies in physics), the IDS Collaboration carried out an experiment with the main aim of studying the beta decay of ^{20}Mg. A radioactive beam of ^{20}Mg with a kinetic energy of 30 keV was produced at the ISOLDE facility at CERN, and the beam was then guided to the experimental setup at IDS where it was stopped, allowing for the study of the decay of ^{20}Mg. During this experiment, mostly for calibration purposes, a 30 keV beam of ^{21}Mg was also produced, allowing measurements on the beta decay of ^{21}Mg to be carried out as well. Little did I know, at the time, how important these data on ^{21}Mg would turn out to be for me many years down the line. Although the data are nearing a decade in age, and although several papers have been published by our collaboration on the beta decays of ^{20}Mg [Lun+16] and ^{21}Mg [Lun+15a; Lun+15b][1], the ^{21}Mg data from 2015 re-

[1] The papers published on ^{21}Mg concern an even earlier experiment.

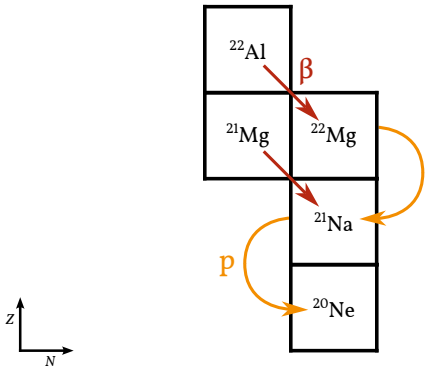

Figure 4.1: Illustration of overlap in beta-delayed sequential two-proton emission of ^{22}Al and beta-delayed one-proton emission of ^{21}Mg from the point of view of the chart of nuclides.

veal, as I can attest to, many previously unseen details in the beta decay of this proton-rich nucleus.

Apart from my supervisors' suspicions that there would be more details to dig out of the data, my analysis on ^{21}Mg was, at first, also motivated by the fact that there would be many similarities between the analysis methods to be used on the ^{21}Mg data and those to be used on the upcoming data from the main experiment of my PhD project. The main experiment of my PhD project was to be carried out at the NSCL[2] at the Michigan State University campus in the United States, studying the beta decays of ^{22}Al and ^{26}P. With the aim of studying, at some point during my PhD, the decay of ^{22}Al came also a very fitting nuclear physics parallel to the study of ^{21}Mg: ^{22}Al is the precursor of the two-proton emitting nucleus ^{22}Mg which, if the two-proton emission is sequential, decays first to ^{21}Na and then to ^{20}Ne. On the other hand, ^{21}Mg is the precursor of the one-proton emitting nucleus ^{21}Na which, again, decays to ^{20}Ne – see figure 4.1. The specific physics case of the beta decay of ^{21}Mg thus has a broad overlap with that of ^{22}Al; the feeding of the various levels in ^{21}Na and ^{20}Ne might in principle be completely different for the two cases, but the mechanisms of one-proton emission from ^{21}Na and sequential two-proton emission from ^{22}Mg are, in any case, dictated by the same intermediate states in ^{21}Na and the same final states in ^{20}Ne.

[2]National Superconducting Cyclotron Laboratory.

So – at the beginning of my PhD, in early 2020 – I started digging into the data on ^{21}Mg, taken at IDS at ISOLDE back in 2015, with the aim of revealing new details in the beta decay of ^{21}Mg, motivated also by the upcoming experiment on ^{22}Al and ^{26}P to be carried out at the NSCL within the coming year or so. Then Covid-19 came about. What was initially delay upon delay of my PhD project's experiment at the NSCL turned into an outright cancellation, as the NSCL was decommissioned due to the upgrade of the very same facility to the FRIB coming closer and closer to completion, while my European collaborators and I were prevented from going to the United States and carrying out the experiment. (Remarkably, the upgrade from NSCL to FRIB continued, seemingly unhampered, during lockdown.) As our experiment had been approved to run at the NSCL, but there was no longer any NSCL to speak of, the experiment could no longer be carried out. The whole situation was quite the letdown for all of us, and especially for me.

In the end, during the following years, we got an approval on my supervisor's, Hans Fynbo's, proposal to run the previously accepted, but cancelled, experiment at the newly commissioned FRIB instead, and we managed to carry out the experiment in July 2023, just barely leaving enough time for me to scratch the surface of these fresh new data and to present some of the preliminary results later in this thesis. It was very, very, *very* lucky that the experiment on ^{22}Al and ^{26}P ended up actually being feasible and then carried out. The fact that this experiment became among the first ten experiments to run at FRIB – and the very first to utilise the Gas Stopping Area at FRIB – is quite humbling, but it was also completely unplanned.

While this thesis would have been something else entirely, had the experiment at FRIB not been carried out in the end, I believe that this thesis would still have been a fruitful one. Because, as it turns out, sometimes there really is fortune in leftovers.

The following two sections introduce and summarise each of the two papers that have resulted from my analyses of the ^{21}Mg data from 2015. The two introductory and summarising sections are immediately followed by their corresponding manuscripts, in their entirety. The first paper was published in Nuclear Instruments and Methods in Physics Research Section A in 2023. This pa-

per details the silicon detector telescope methodologies that I have developed and systematised during my analyses of the charged particle spectra from the decay of ^{21}Mg. The methods are presented utilising particle spectra from the experiment as an example, but the methods are generally applicable in low-energy decay and reaction experiments. The second paper has been submitted to the European Physical Journal A in 2024. This paper presents the nuclear physics results of the analyses of the data on ^{21}Mg.

4.1 Refined silicon detector telescope analyses

One thing that became apparent in the study of the ^{21}Mg data was the high level of care neccesary in extracting particle spectra below the punch through thresholds of the ΔE detectors in the ΔE-E silicon detector telescopes employed in the experiment. The crux of it all is the interplay of various phenomena that are all encapsulated in figure 4.2.

As an ion is incident on and traverses a ΔE silicon detector which we employ in our experiments, it continuously deposits parts of its initial kinetic energy E_p as it interacts with the atomic electrons of the material (section 2.2) until it is either stopped in the detector or it *punches through* the detector and emerges on the opposite side. The sum of deposited energies is denoted E_dep, and this is the observable that we extract from the detector, apart, possibly, from the relative position of the energy deposition and its timestamp. If the ion is energetic enough to punch through the detector, it will have deposited only a fraction of its initial energy, and it might then proceed into the bulk of a backing E silicon detector. There is, however, a series of obstacles between the emerging ion and the active layer of the backing E detector, and if the ion has already lost most of its initial kinetic energy by traversing the ΔE detector, it may not reach the active layer of the E detector after all. In practice, the inactive, or "dead", layers of the detectors as well as the lower signal threshold of the backing E detector cause an energy interval of *unresolvable* initial particle energies E_p to appear. The various layer thicknesses preceding the active layer of the backing E detector as well as the signal threshold of the backing E detector determine the extent of this energy interval. As the various layer thicknesses,

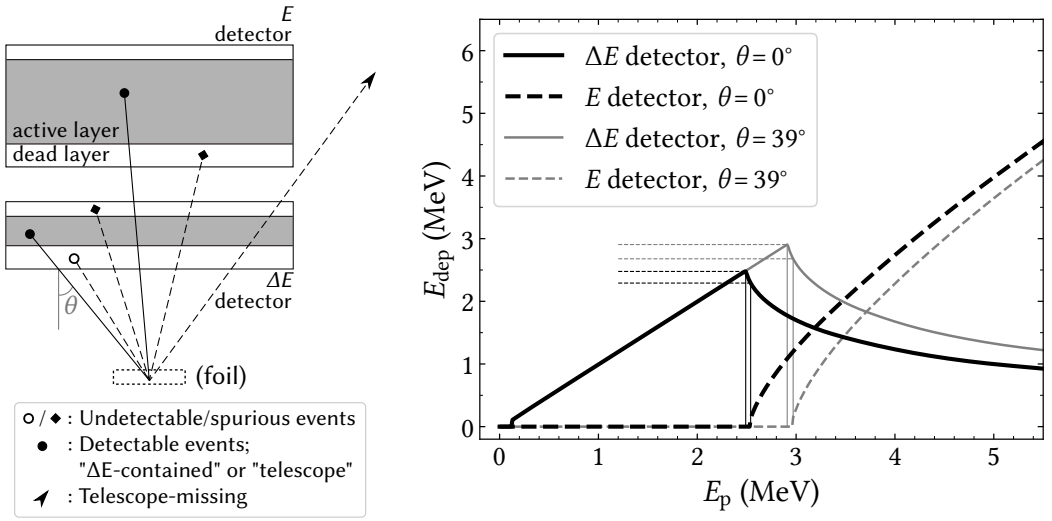

Figure 4.2: Types of events in ΔE-E silicon detector telescopes and their relation to initial particle energies and observed deposited energies. **Left:** Illustration of different types of stopping of a charged particle in a detector telescope as it is emitted from a point with various kinetic energies. The layer thicknesses are not meaningfully scaled. **Right:** Example of energy deposition E_{dep} vs. kinetic energy E_{p} of a proton in the active silicon detector layers of a telescope at two extremes of angles of incidence θ. The ΔE detector has a thickness of 67 µm and the E detector has a signal threshold of 100 keV. SRIM [ZZB10] has been employed to tabulate the deposited energies. The figure is from [JRF23] in which it is explained in more detail.

as they are depicted in figure 4.2, are effectively greater at larger angles of incidence θ, there is a continuous set of such energy intervals across the solid angle extended by the silicon detector telescope as a whole. For each of these *spurious* energy intervals, there is in general no way to uniquely assign an initial particle kinetic energy E_{p} to the observed deposited energy E_{dep}, as the particle in question could either be of initial energy below *punch through threshold* of the ΔE detector, or it could be of initial energy above punch through threshold. The dashed horizontal lines in the right part of figure 4.2 indicate the beginning and end of these types of spurious energy intervals at minimal and maximal angle of incidence allowed by one of our detector telescopes in the experiment on the decay of ^{21}Mg at IDS from 2015. From smallest to largest angle of incidence, the combination of all spurious energy intervals in this example amounts to an interval of 600 keV.

If one wishes to extract charged particle energy spectra from silicon detector telescopes below punch through threshold, one should recognise this

kind of effect and accommodate it in the data analysis. In effect, if one does not do this, the particle energy spectra below punch through threshold will be distorted by events from above threshold. In our paper describing this issue, we present ways to characterise silicon detector telescopes and, based on these characterisations, we then show how to accommodate the issue. The outcome of the methodologies and analyses presented in the paper is an energy-dependent solid angle coverage of the silicon detector telescopes surrounding the point of particle emission in a given experiment.

Another important consequence of the studies for our particular arrangement of silicon detector telescopes is the fact that we cannot use the outermost strips of our ΔE DSSSDs, as a punch through particle incident on any of these strips (if our detectors are otherwise aligned as we intend them to) can miss the backing E detector (figure 4.2). This is due to the, otherwise convenient, fact that both of our ΔE and E detectors have the same surface dimensions, 5 centimetres by 5 centimetres. For our typical experimental setups with a ΔE detector situated roughly 40 mm from the point of particle emission and a backing E detector 3 mm behind the ΔE detector, this results in a reduction in the solid angle coverage from approximately 8.5 % of 4π down to approximately 7 % of 4π. As we tend to employ 4 to 6 of such silicon detector telescopes in our experiments, we lose 6-9 % of 4π solid angle coverage. This is definitely something that is worth accommodating in future designs of our experimental setups.

All analyses, figures and text in the following paper are produced by me. During analyses and writing of the manuscript, my co-authors Karsten Riisager and Hans Fynbo provided useful feedback to the structuring, wording and contents of the paper.

Nuclear Inst. and Methods in Physics Research, A 1055 (2023) 168531

Contents lists available at ScienceDirect

Nuclear Inst. and Methods in Physics Research, A

journal homepage: www.elsevier.com/locate/nima

Full Length Article

Extracting clean low-energy spectra from silicon strip detector telescopes around punch through energies

E.A.M. Jensen *, K. Riisager, H.O.U. Fynbo

Institut for Fysik & Astronomi, Aarhus Universitet, DK-8000, Aarhus C, Denmark

ARTICLE INFO

Keywords:
Silicon strip detector
Detector telescope
Punch through
Energy loss
Stopping
^{21}Mg

ABSTRACT

The response of detector telescopes becomes complex around their relevant punch through energies: For some deposited energies the corresponding particle kinetic energies cannot be uniquely assigned, and these spurious energy regions can span several hundreds of keV if the telescopes are employed in close geometry. We present methods for producing clean low-energy spectra of light ions from detector telescopes consisting of thin double-sided silicon strip detectors (DSSSDs) backed by thick silicon pad detectors. By following these methods, the spectra of several such detector telescopes can be combined to span the entire relevant particle energy spectrum, above as well as below the punch through thresholds of the individual telescopes. The total energy spectrum resulting from the combination of all telescope spectra thus encompass the entire particle energy distribution in conjunction with the energy-dependent, setup-specific solid angle coverage. Energy spectra of beta-delayed proton emission from ^{21}Mg are used to illustrate the methods.

1. Introduction

The utilisation of detector telescopes to distinguish types of atomic nuclei and determine their initial kinetic energies in nuclear reaction and decay experiments with the so-called *ΔE-E technique* is well-established [1,2], and the technique is continuously being refined and adapted for specialised detection designs at low, intermediate and high energies — see e.g. Ref. [3] for a recent review. The correlated energy depositions in a thin ΔE detector and the thicker E detector are characteristic of the type of particle which first deposits a fraction of its initial energy in the ΔE detector, then *punches through* to the E detector and, finally, deposits the remainder of its energy in the E detector. Depending on the needs of the experiment, the correlated signals for various telescope events can be compared e.g. by the *power law scheme* described in [1], or the energy depositions can be compared to energy loss tabulations provided e.g. by *SRIM* [4] or *ICRU* [5,6], thus providing a particle identification (PID) method.

While the PID provided by utilising detector telescopes is an invaluable feature, in this paper the focus is on how energy spectra of detector telescopes can be properly extended below the *punch through thresholds* of the individual ΔE detectors. By extending the energy spectra below the punch through thresholds, the dynamic ranges of the detector telescopes becomes not only that of the combined $\Delta E - E$ configuration but also that of the ΔE detector on its own. Employing the entire dynamic range of a given detector telescope in this way can be very attractive for some nuclear physics cases. There are, however, inherent problems involved in extending the energy spectra below the punch through thresholds, and, depending on the data at hand, the problems might not be immediately obvious from the resulting combined spectra alone. In this paper, the problems inherent in extending the energy spectra below the punch through thresholds of detector telescopes will be described and their proper handling demonstrated.

The small thicknesses of the ΔE detectors employed in detector telescopes has the advantage of suppressing the beta response of the telescope as a whole. PID cannot be carried out with a given ΔE detector, by itself, below its punch through thresholds (which will vary for different types of particles). This means that prior knowledge or other PID methods must be employed to interpret the particle energy spectra below the relevant punch through thresholds. If the particle spectra, in this sense, can be meaningfully extended below the relevant punch through thresholds, care must still be taken to eliminate various types of distortions at intermediate energies. The distortions primarily appear due to the signal thresholds of the employed E detectors, and the effect will be enhanced if the geometry of the detection setup is close — an otherwise desirable feature. The distortions can potentially span many hundreds of keV of the full energy spectrum at hand.

In experiments where beta-delayed particle emission is studied, properly extending the energy range below the punch through threshold can in principle reveal the entire particle energy spectra — from the characteristically low-lying single-nucleon separation energies of the *emitter* up to the large Q-value of β-decay from the *precursor*; see e.g. Refs. [7,8]. Recent data [9] on beta-delayed proton emission from

* Corresponding author.
E-mail address: ej@phys.au.dk (E.A.M. Jensen).

https://doi.org/10.1016/j.nima.2023.168531
Received 3 June 2023; Accepted 6 July 2023
Available online 9 July 2023

^{21}Mg [10] is used to illustrate the methods which will be developed in this paper. The physics case of ^{21}Mg is quite ideal for these illustration purposes, due both to the beta-delayed proton branch dominating the decay scheme and due to the wide distribution of energy levels across the entire dynamic range of the utilised silicon detector telescopes. While the methods developed here are framed around nuclear decay experiments, the methods should easily extend to low-energy nuclear reaction experiments as well.

The utilised ΔE detectors are double-sided silicon strip detectors (DSSSDs) with 16 × 16 strips spanning an area of 50 × 50 mm^2 with ultra-thin entrance windows [11]. The active layer thicknesses of these detectors are in the range 30–70 μm. The ΔE detectors are situated roughly 40 mm from (and facing) the point of particle emission and are backed by 50 × 50 mm^2 single-sided silicon pad detectors of thicknesses around 500 μm. These E detectors are situated 5 mm behind their corresponding ΔE detectors. A complete description of the experimental setup is given in Ref. [12]. The segmentation of the ΔE detectors provides accurate information of a given particle's trajectory and, in turn, allows for accurate determination of the initial particle energies through energy loss corrections of the particles in the effective dead layers of both ΔE and E detectors. The energy calibrations of the detectors take various dead layer energy losses into account. The response functions of the utilised silicon detectors, while not taken into account here, are well understood [13].

In the following, we start by presenting an overview of the passage of particles through detector telescopes. From this overview it will become clear that care must be taken in extending the energy spectra below the punch through thresholds of ΔE detectors. We will then demonstrate how this can be done with the aid of energy loss tabulations, developing a repertoire of methods. The end result of utilising these methods is the ability to produce full-range particle energy spectra accompanied by energy-dependent, setup-specific solid angle coverages. Data from an experiment studying beta-delayed proton emission from ^{21}Mg will exemplify the development of the methods.

2. Particle passage of detector telescopes

2.1. Stopping

In the following, the stopping of charged particles shall principally concern what is commonly referred to as the *stopping of ions* [4], i.e. the stopping of atomic nuclei — the "ions" may or may not be electrically neutral due to the ionisation of the atoms in question.

As a charged particle impinges on the surface of a slab of material of thickness L_0 at an angle of incidence θ, the length of material traversable by the particle (if the particle energy is sufficiently large) is the effective length of material

$$L_{\text{eff}} = \frac{L_0}{\cos\theta} = L_0 + \Delta L = L_0 + (L_{\text{eff}} - L_0) \tag{1}$$

The effective length L_{eff} is here explicitly split into the minimal length of material L_0 at $\theta = 0$ and the additional component ΔL which contributes at $\theta > 0$. The energy loss E_{loss} experienced by a particle which traverses the entire material is given by

$$E_{\text{loss}} = \int_0^{L_{\text{eff}}} S(E)\mathrm{d}x \simeq S_0 \int_0^{L_{\text{eff}}} \mathrm{d}x = S_0(L_0 + \Delta L) = S_0 L_0 \left(1 + \frac{1-\cos\theta}{\cos\theta}\right) \tag{2}$$

where the stopping power S, which explicitly depends on the particle energy E and implicitly depends on the properties of the particle and the material, is approximated as being a constant S_0 during the particle's entire traversal of the material. While this approximation is generally poor, the functional form of the right-hand side of Eq. (2) will prove useful later on; the expression relates a given energy loss E_{loss} to a given angle of incidence θ for fixed S_0 and L_0. Note that the particle in question is supposed not to veer (measurably) from its initial direction of motion as it traverses the material.

2.2. Electronics

The electronic signals read out from the *active layers* of charged-particle detectors are converted, via energy calibrations, to deposited particle energies. These must be corrected for the energy losses in the detector *dead layers* and any other inactive media the particles might traverse before reaching the active layer of the detector; see e.g. Ref. [14]. Energy loss corrections are made employing energy loss tabulations.

Charged-particle detectors inevitably have some signal threshold under which charged particles cannot meaningfully be separated from electrical noise inherent in the detector. This can be considered an effective (energy-dependent) contribution to the actual physical thickness of the dead layer of the detector. Of course, this effective part of the dead layer does not require energy loss corrections, but it does, effectively, act as a significant obstacle for any particle incident on a given detector.

Here we stress an important point: For modern silicon detectors with low-Z entrance window thicknesses on the sub-micrometer level, the dynamic range towards zero energy (assuming otherwise perfect detector calibrations) for a given silicon detector is primarily constrained by its signal threshold, and *not* by the thickness of its entrance window. Consider, for instance, a proton with an initial kinetic energy of 2.0 MeV which punches through a ΔE silicon detector of 40 μm active layer thickness at normal incidence. The proton deposits roughly 1.4 MeV [4] in the ΔE detector and emerges on the opposite side with 0.6 MeV kinetic energy remaining, bound for impact with a backing E detector. The remaining 0.6 MeV of the proton will be reduced further in the dead layers of the E detector before reaching its active layer — for example by roughly 33 keV in a combined aluminium and silicon dead layer of 0.6 μm. The E detector could, however, conceivably have a signal threshold of 100 keV (at room temperature) which is three times the energy lost in its dead layers. Taking the 33 keV reduction in the dead layer into account, this 100 keV signal threshold corresponds to an additional 1.7 μm dead layer thickness. Based on this example, we state here that the two main parameters of interest for a modern $\Delta E - E$ detector telescope are (1) the signal threshold of the E detector, and (2) the active layer thickness of the ΔE detector. These two parameters characterise, more than anything else, the data extracted from detector telescopes above and below punch through.

The ΔE detectors used as examples in this paper are equipped with 0.1 μm p-doped silicon dead layers (only 3%–4% of the detector surface is covered by electrical contacts) and had signal thresholds around 100 keV. The E detectors are equipped with metallisation on top of p-doped silicon dead layers corresponding to approximately 0.6 μm silicon — their signal thresholds are also roughly 100 keV. Evidently, the example of a proton punching through a ΔE detector of 40 μm active layer thickness and having to overcome the dead layer and signal threshold of the backing E detector is highly relevant. If the angle of incidence between detector surface and the point of particle emission is allowed to vary, a significant portion of the particle energy spectrum will be affected, as we shall now see.

2.3. Types of events

The left part of Fig. 1 schematically depicts the various types of events a charged particle of varying kinetic energy can cause in a charged-particle detector telescope, and the right part of Fig. 1 shows an example of a particle's energy deposition E_{dep} in the active layers of a telescope against its actual kinetic energy E_{p}. The charged particle is emitted – e.g. from a foil with possible spread in source position – towards the detector telescope at some angle of incidence with a given energy. With reference to both the left and right parts of Fig. 1, the following scenarios can occur:

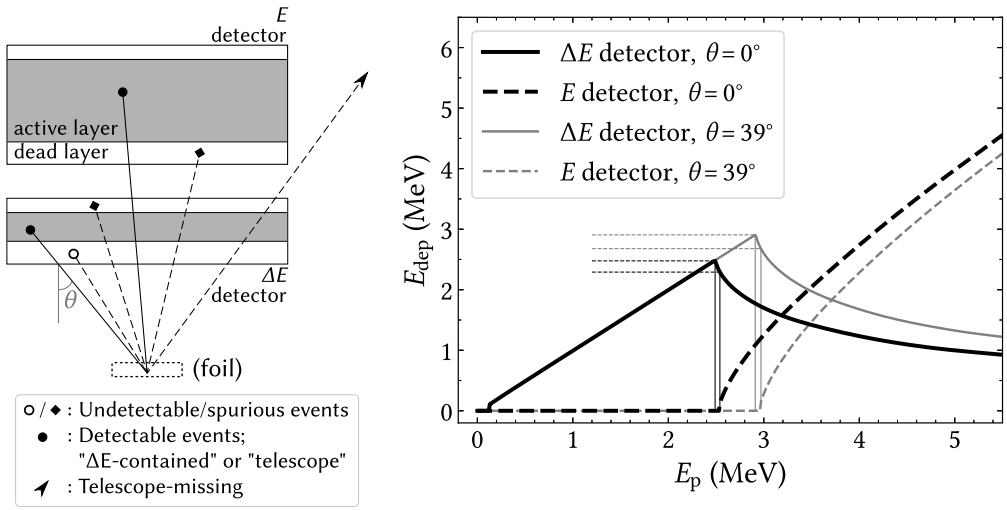

Fig. 1. Left: Illustration of different types of stopping of a charged particle in a detector telescope as it is emitted from a point with various kinetic energies. The layer thicknesses are not meaningfully scaled. **Right:** Example of energy deposition E_{dep} vs. kinetic energy E_p of a proton in the active silicon detector layers of a telescope at two extremes of angles of incidence θ. The ΔE detector has a thickness of 67 μm and the E detector has a signal threshold of 100 keV. SRIM [4] has been employed to tabulate the deposited energies. See the text for a discussion of the different types of events.

- Open circle, $E_p \lesssim 0.1$ MeV: The particle is emitted with such low energy that it is stopped in the (effective) dead layer before it reaches the active layer of the ΔE detector. The telescope is blind to this kind of event, which effectively sets the lower limit on the dynamic range of the telescope. We shall denote this type of event an *undetectable event*.
- Closed circle, E_{dep} is increasing with E_p: The particle initially has a kinetic energy which allows it to reach one of the two active layers of the telescope before it is completely stopped. These are the ideal types of events. The particle is either stopped in the active layer of the ΔE detector, or it is considerably more energetic and *punches through* the ΔE detector and is then stopped in the active layer of the E detector. Starting from the deposited energy in a given active layer, one can find the original particle energy by employing energy loss tabulations to iteratively calculate the particle's energy prior to its traversal of the effective thicknesses of the preceding layers. Events in which the particle is stopped in the active layer of the ΔE detector we shall denote *ΔE-contained events*, while events in which the particle is stopped in the active layer of the E detector we shall denote *telescope events*.
- Square, E_{dep} is decreasing with E_p in the ΔE detector and E_{dep} in the E detector is zero: The particle is sufficiently energetic to *punch through* the active layer of the ΔE detector, but it lacks the necessary energy to *reach through* to the active layer of the E detector. Hence it is stopped in the dead layer of either of the two detectors, between their active layers. As the particle loses more energy in the larger effective layer thicknesses at larger angles of incidence θ (Eq. (2)), the beginning and end of this energy region is inherently dependent on θ. We shall denote the entire θ-dependent region in which the particle is stopped in the dead layers between the two active layers the *dead zone* of the detector telescope. The two black vertical lines in the right part of Fig. 1 exemplifies the boundaries of the dead zone at small θ and the two grey vertical lines at large θ — in this example the entire dead zone, from smallest to largest θ, spans 400 keV. We shall denote events lying within the dead zone *undetectable events*, similarly to the case where a given particle has such low energy that it is stopped in the entrance window of the ΔE detector. While these types of events are undetectable in the detector telescope as a whole, the particle still deposits some energy in the ΔE detector. The range of deposited energies E_{dep} corresponding to kinetic energies E_p within the dead zone is *not* unique. There exists a range of kinetic energies E_p below punch through with the same range of deposited energies E_{dep}, and we shall hence denote this range of deposited energies E_{dep} the *spurious zone* of the detector telescope. Dashed horizontal lines outlining the spurious zone at small and large θ are drawn in the right part of Fig. 1 — from smallest to largest θ, the entire spurious zone spans 600 keV in this example.
- Arrowhead: The particle punches through the ΔE detector, but it *misses* the E detector. As we shall see, the spectra of ΔE-contained events can be severely distorted by this effect. The effect can be avoided if the solid angle coverage of the E detector at least matches that of the ΔE detector, as seen from the particle's point of emission. An event in which a particle deposits some of its energy in the ΔE detector, punches through it and then misses the backing E detector we shall denote a *telescope-missing event*.

Finally, relevant to the characterisation of the dead zone of detector telescopes, we shall from hence forth specifically use the term *punch through* to refer to the scenario in which a particle has sufficient energy to punch through all material layers up to and including the active layer of a ΔE detector (Fig. 1) at a given angle of incidence θ. We shall define the *punch through threshold* as the lowest possible initial particle energy at which punch through can occur for a given θ. Similarly, we shall use the terms *reach through* and *reach through threshold* to refer to the cases where the particle's initial energies are, respectively, sufficient and barely sufficient to reach the active layer of the E detector for a given θ. We shall also, as a useful shorthand, define the term *x μm telescope* to refer to a detector telescope in which the ΔE detector has an active layer thickness of x in units of micrometers. Unless otherwise specified, in all of the following, the employed E detectors have a signal threshold of 100 keV.

3. Distortion from non-backed telescope areas

The final item in the above list, telescope-missing events, comes about when the E detector of a telescope covers a smaller solid angle than the ΔE detector as seen from the point of particle emission. The extents of the detectors and their placement relative to each other and the point of particle emission are ideally such that this scenario cannot occur. In practice, this is not always possible to achieve, and, even if it is, the scenario nicely illustrates some features which are shared with the *inescapable* existence of dead zones between ΔE and E detectors; this latter issue will be covered in Section 4.

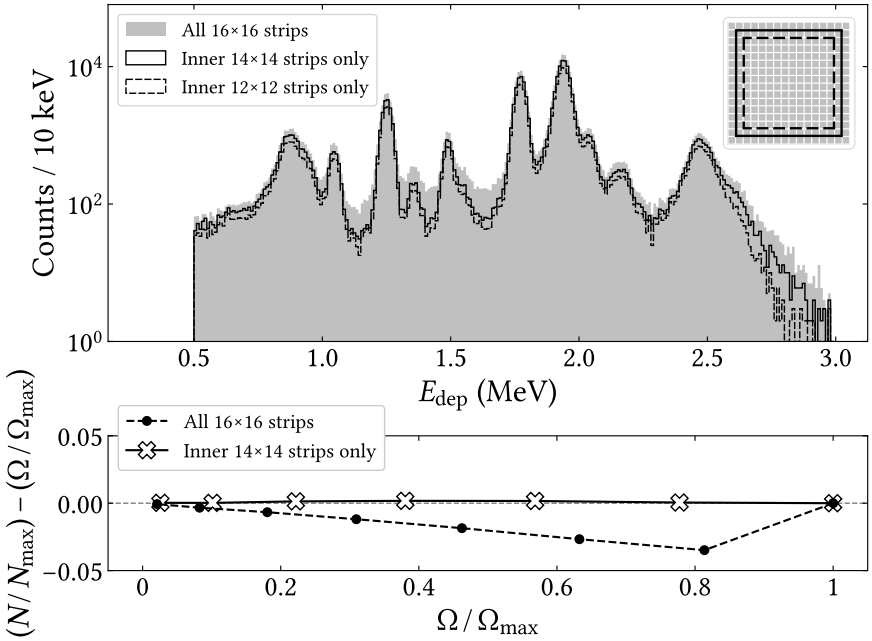

Fig. 2. Top: Energy deposition E_{dep} in 67 μm thick ΔE detector in anti-coincidence with its backing E detector (*ΔE-contained events*). The upper right inset illustrates which strips of the ΔE detector are utilised to produce the spectra. When all 16 × 16 strips are utilised, especially the 1.1 to 1.7 MeV region is heavily distorted. The data are from a decay experiment on ^{21}Mg [9] and are mainly produced by protons emitted from excited states in ^{21}Na. **Bottom:** Deviation from linear relation between number of observed ΔE-contained events N and solid angle coverage Ω, each respectively normalised to the maximum number of observed ΔE-contained events N_{max} and the maximum solid angle coverage Ω_{max}. For the points starting at $\Omega/\Omega_{\mathrm{max}} = 1$ and moving towards 0, the current outermost strips are progressively excluded; as in the top part of the figure.

3.1. Example of the problem

The *non-backed areas* of a given ΔE detector can significantly distort the intermediate energy region of the observed particle spectra. More specifically, the ΔE-contained spectra below the punch through threshold can have regions of significant smearing, obscuring the nuclear structure information otherwise contained there. This is illustrated in the spectra of Fig. 2: The spectra consist of events from different subsets of ΔE strips in which the events are anti-coincident with the corresponding E detector. Based on the definitions of the previous section, we here expect to see ΔE-contained events and, possibly, telescope-missing events. It is crucial to be able to separate telescope-missing events from all other types of events. In the areas of the telescope where the ΔE detector is properly backed by the E detector, telescope events can be identified and, logically, telescope-missing events are not a concern, but in the non-backed areas of the ΔE detector, there is generally no way to distinguish telescope-missing events from ΔE-contained events. The conclusion is that the non-backed areas of the detector telescope must be excluded from the analysis of the particle spectra, reducing the solid angle coverage of the telescope from the otherwise larger solid angle coverage of the ΔE detector to that of the E detector. The recourse, as illustrated in Fig. 2, is more well-defined peaks in the intermediate energy region of the particle spectrum where the telescope-missing events were otherwise responsible for a heavy distortion of the spectrum. The extent and severity of distortion is entirely determined by the relative intensity of particle energies above punch through.

3.2. Validation of ΔE-backing

A simple test to identify the non-backed areas of a detector telescope can be made from the following considerations. For an isotropically emitting source, one expects a linear relation between a certain solid angle and the number of events observed in the solid angle in question; twice the events for a doubling of the solid angle, etc. The true events observable by a detector telescope can be split into the two types of events which we have already defined – ΔE-contained events and telescope events – and these subtypes of events should each obey the same principle. But if one includes the non-backed area of the telescope, the telescope-missing events will add to the true ΔE-contained events. The registered number of ΔE-contained events will thus be erroneously larger in the non-backed areas of the telescope. This is illustrated in the bottom part of Fig. 2 where the normalised deviation from a linear relation between the number of observed ΔE-contained events N and the solid angle coverage Ω is plotted against the normalised solid angle coverage. By only including the innermost 14 × 14 strips, the maximum deviation is roughly 1 per mille instead of 4 percent.

The sort of treatment just outlined can be extended to situations where a symmetric exclusion of detector strips is too simple. By systematically including and excluding certain strips or pixels of a given ΔE detector, the non-backed areas of a given telescope can be accurately mapped. In principle, this allows for the determination of the telescope's position relative to the point of particle emission and offers insight on the spread of the emission point as well. Especially if several detector telescopes are utilised in an experiment, this method offers some constraints on the point of particle emission. If the positioning of the E detector relative to the ΔE detector is uncertain within some bounds, the same method can be used to elucidate that issue.

4. Identifying dead and spurious zones of telescopes

We continue by discussing the issues related to stopping in the dead layers between a detector telescopes' two active layers — the undetectable and spurious events defined in Section 2.3. In that section it was pointed out how the dead and spurious zones of a telescope vary

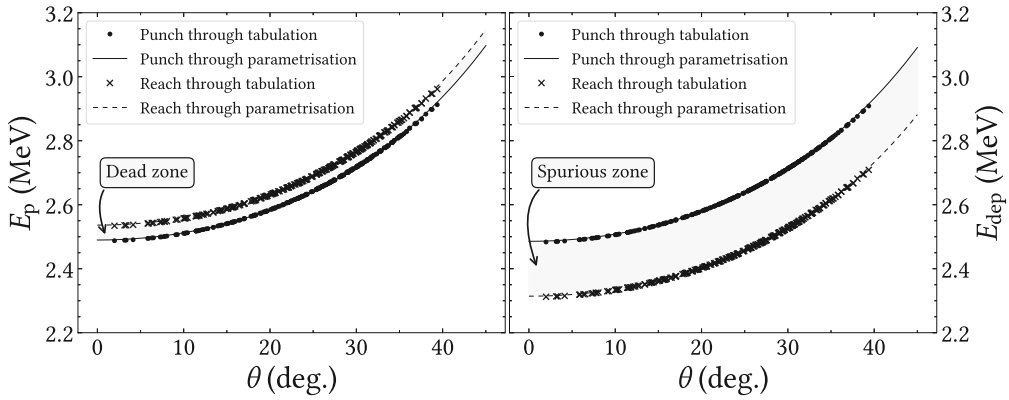

Fig. 3. Left: Example of proton kinetic energies E_p against angle of incidence θ between the point of particle emission and detector surface. These specific proton energies outline the *dead zone* for a telescope with a ΔE detector thickness of 67 μm and a signal threshold of 100 keV on the E detector. Protons with E_p within the dead zone are undetectable (as defined in Section 2.3). **Right:** Corresponding deposited proton energies E_{dep} in the ΔE detector against θ. At and above punch through, E_{dep} will decrease towards the reach through threshold and beyond. For E_{dep} between the punch through and reach through thresholds, the corresponding kinetic energy E_p cannot be uniquely assigned (see Fig. 1). This region of events is hence a *spurious zone* of events. Energy loss tabulations [4] have been utilised to calculate the relevant proton energies for all 256 pixels of the detector and have then been fitted to Eq. (3).

with angle of incidence θ between detector surface and a particle's point of emission. In other words, a θ-dependent gap in the dynamic range of a given detector telescope emerges.

4.1. Parametrisation of dead and spurious zones

Fig. 3 shows an example of the dead and spurious zones for protons outlined by the punch through and reach through thresholds of a telescope consisting of a 67 μm ΔE detector with an effective total dead layer thickness between ΔE and E detector consisting of 0.4 μm silicon, 0.8 μm aluminium and a signal threshold of 100 keV. Energy loss tabulations from SRIM [4] have been utilised to tabulate the punch through and reach through thresholds of the centre of each individual pixel of the ΔE detector. With guidance from the approximation in Eq. (2), a parametrisation of the two angle-dependent thresholds have then been carried out by fitting the tabulations to the expression

$$E(\theta) = E_0\left(1 + a\frac{1-\cos\theta}{\cos\theta}\right) \tag{3}$$

with $E_0 = S_0 L_0$ the approximate energy loss at $\theta = 0$ and a being a factor which mostly corrects for the otherwise poor approximation in Eq. (2).

A closer visual inspection of Fig. 3 reveals that the parametrisation is not perfect; the residuals between tabulation and parametrisation are as large as 10 keV at the extremes of θ. This deviation can be reduced by adding more terms to Eq. (3). In the end, the simpler form of Eq. (3) was settled upon as deviations of 10 keV near the edges of the dynamic ranges of the individual ΔE and E detectors are insignificant compared to the extents of the dead and spurious zones, the detectors' resolutions, etc. The simple form of Eq. (3) is convenient, as it ensures fast convergence for fits with initial guesses $a = 1$ and $E_0 = \min(\mathbf{E})$, where $\mathbf{E}$ are the dependent variables of the data to be fitted.

4.2. ΔE Thickness estimation from punch through

Fig. 4 shows data for energy depositions E_{dep} against angles of incidence θ in the same 67 μm telescope[1] as in Fig. 3. The data are conditioned on the presence of a signal in the E detector. The maximally possible energy depositions in the ΔE detector for various possible active layer thicknesses have been calculated and then fitted and drawn in Fig. 4 with the same method as in Fig. 3. Comparing these maximally possible energy deposition curves with real data can help to determine the thickness of a detector, as there should be no true events above these curves for the correct detector thickness. Conversely, by drawing these energy deposition curves and confirming the thickness specifications of the ΔE detector, as they may have been given by the manufacturer, one is reassured in the correctness of the range of the dead zone of the telescope in question.

In comparing Figs. 3 and 4, it is important to distinguish the initial particle energy E_p and the deposited energy E_{dep}: Due to the dead layers preceding the active layer of the detector, $E_p(\theta)$ will generally be larger than $E_{dep}(\theta)$. Consider, for instance, the lowest-lying punch through events in Fig. 4, identified by their dependence on θ. These events are due to the largest initial particle energies E_p of the data. Peaks in the E_{dep} spectrum which are independent of θ, on the other hand, stem from particles which deposit all of their energy in the ΔE detector — these are the ΔE-contained events discussed at length in Section 3.

The peak near 2.5 MeV in Fig. 2 is only seen above $\theta \sim 10°$ in Fig. 4 where the effective thickness of the ΔE detector allows for the appearance of the peak in the spectrum. Checking whether peaks appear and disappear above and below the expected angles of incidence like this can, again, serve as a consistency check. This is, however, entirely dependent on the particle spectrum being sufficiently intense around the punch through threshold. It should be noted that the telescope-missing events of Fig. 2 are also present in Fig. 4 at large θ. All punch through events can be removed from the E_{dep} vs. θ spectrum via an anti-coincidence gate with the E detector, as was done in order to produce Fig. 2.

On the subject of thickness estimation of a given ΔE detector, if one draws the same kinds of tabulations as in the right part of Fig. 1 on top of a $\Delta E - E$ spectrum for various assumed thicknesses of the ΔE detector, yet another method of checking the detector thickness presents itself. This is illustrated in Fig. 5 for the same 67 μm ΔE telescope. If the detector geometry is close, and hence the possible angles of incidence θ between detector surface and point of particle emission are large, one can constrain the data on various subintervals of θ and verify the correct displacements and varying curvatures of the curves describing telescope events. Similarly, one can verify the larger possible energy depositions in the ΔE detector for larger θ. In Fig. 5, the telescope event curves are drawn at the lower and upper extremes of angles of incidence θ for the selected data, and since the placement of the curve for $2° \leq \theta \leq 5°$ does not vary much, while the placement of the curve for $33° \leq \theta \leq 39°$ does (Fig. 3), the placement of the curves are as expected within the detector resolutions, etc. The two thin horizontal lines drawn in Fig. 5, where the telescope event curves and ΔE-contained event regions meet, highlight regions

[1] *x μm telescope* defined at the end of Section 2.3.

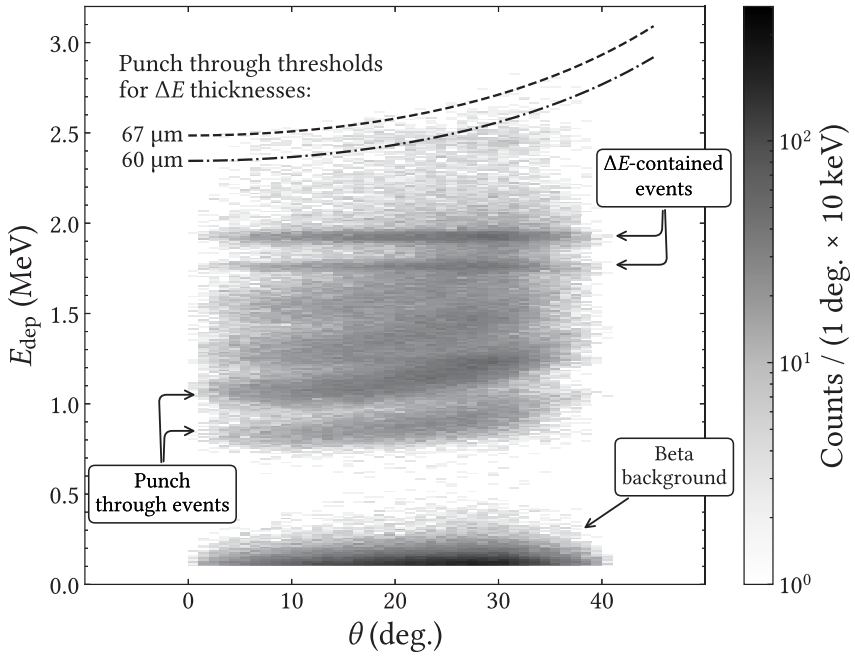

Fig. 4. Energy deposition E_{dep} against angle of incidence θ between the point of particle emission and detector surface in ΔE detector with a thickness of 67 μm. Energy loss tabulations [4] have been utilised to draw the punch through threshold curves using the same fitting procedure as exemplified in Fig. 3. The data are from the same experiment as referenced in Fig. 2 where beta particles and protons are primarily observed in the detector telescopes. In order to be able to illustrate the presence of punch through events, events in anti-coincidence with the E detector (pure *ΔE-contained* events) are not shown here. The ΔE-contained events hence stem from random coincidences with the E detector or from true coincidences where the beta particles are detected in the E detector.

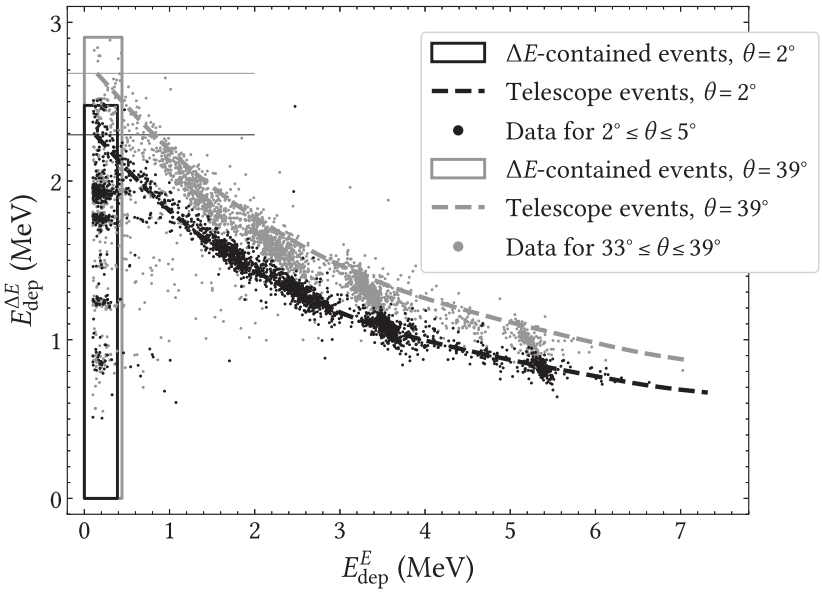

Fig. 5. Energy deposition in ΔE detector $E^{\Delta E}_{dep}$ against energy deposition in E detector E^{E}_{dep} for detector telescope at different angles of incidence θ between the point of particle emission and detector surface. The ΔE detector has a thickness of 67 μm and the E detector has a signal threshold of 100 keV. The boxes outlining the ΔE-contained events and the curves defining the telescope events have been drawn solely based on energy loss tabulations from SRIM [4] and knowledge of the dead layer thicknesses and signal thresholds, assuming an active layer thickness of 67 μm in the ΔE detector. The data are from the same experiment as referenced in Fig. 2 where protons can be identified by the $\Delta E - E$ technique. The constraints on θ are chosen such that there are roughly the same number of events (around 3000) in both intervals.

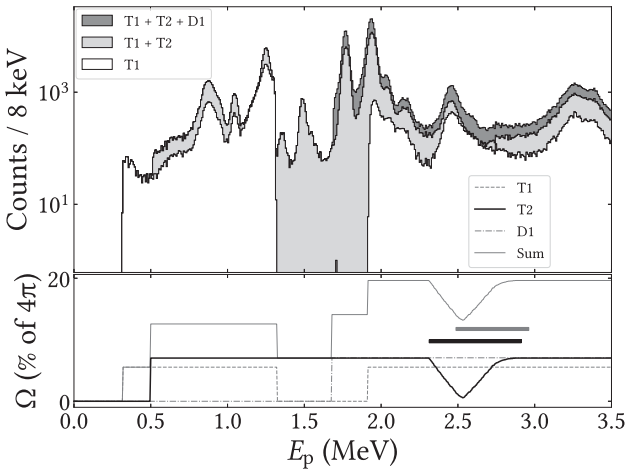

Fig. 6. Top: Beta-delayed proton energy spectrum of ^{21}Mg at low to intermediate proton kinetic energies E_p as observed by two detector telescopes and one thick DSSSD. The data are from the same experiment as referenced in Fig. 2 where protons emitted from excited states in ^{21}Na are primarily observed. In the figure legends, *T1* is short for *42 μm telescope*, *T2* is short for *67 μm telescope*, and *D1* is short for *1000 μm DSSSD*. **Bottom:** The corresponding energy-dependent solid angle coverage Ω of the detector telescopes and the thick DSSSD. The extents of the spurious zone (black) and the dead zone (grey) are indicated for the 67 μm telescope with the thick lines lying between 2.3 and 3.0 MeV. Taken as a whole, the top and bottom panels illustrate the results of properly accounting for all challenges, as described in this paper, associated with extending the energy spectra of detector telescopes below their punch through thresholds. The variations in solid angle coverage with energy can, if they are not taken into consideration, give a misrepresentation of the underlying nuclear structure. See text for a more detailed discussion.

of energy deposition in the ΔE detector that can never coincide with a true signal in the backing E detector — this is merely yet another way of visualising the spurious zone between the two detectors as in Figs. 1 and 3.

5. Combining telescope spectra

After telescope- and ΔE-contained events have been properly separated and when dead zones and spurious zones of the detector telescopes have been identified, the groundwork has been laid for combining the observed energy spectra into one complete spectrum, where above- and below-punch through events can be treated on an equal footing. By mapping the energy-dependent solid angle coverage of each detector configuration,[2] one can combine the energy spectra of the detector configurations into an all-encompassing spectrum like the one shown in Fig. 6. The figure shows the combined beta-delayed proton energy spectrum of ^{21}Mg as observed by two detector telescopes and one thick DSSSD all situated near the point of particle emission. The solid angle coverage Ω of the entire setup varies with the kinetic energies E_p of the protons. The total spectrum ranges up to roughly 9 MeV, but here we wish to highlight the varying solid angle coverage at low to intermediate energies.

In Fig. 6, the solid angle coverage for all detector configurations are initially zero, as an energy cutoff has been set in order to separate betas from protons (Fig. 4). The detectors then become active above their energy cutoffs. The cutoff for the thick DSSSD is larger than what would be necessitated by minimum ionising beta particles alone; it is due to the positioning of the detector directly below the target frame on which particles scattered during the experiment. The reduction in solid angle coverage of the thick DSSSD due to the shadow generated by the target frame is taken into account.

[2] Detector configuration in this case refers either to a detector telescope or to a DSSSD which is not backed by any detector.

In Fig. 6, the varying solid angle coverage for the 67 μm telescope is nicely illustrated for particle energies spanning the dead and spurious zones depicted in Fig. 3, ranging from $E_p \sim 2.3$ MeV up to $E_p \sim 3.0$ MeV. Note that although the solid angle coverage does approach zero in this region, at least a small fraction of the detector telescope is active throughout. Having properly characterised this 67 μm telescope, the proton energies lying in the telescope's dead and spurious zones do not have to be neglected entirely. Rather, the proton energies which remain detectable at certain angles of incidence θ (Fig. 3) also remain part of the combined energy spectra, but only under consideration of the energy-dependent solid angle coverage additionally present in this region. Note also in Fig. 6 that the dead and spurious zones of the 67 μm telescope broadly overlap. This is the case for the telescope as a whole, but for an individual pixel of the ΔE detector, the dead and spurious zones are disjoint sets with the upper end of the spurious zone barely touching the lower end of the dead zone — see Fig. 3. The two zones are complementary, but the spurious zone spans a larger range due to the inability to uniquely assign a particle energy E_p to any given deposited energy E_{dep} between punch through and reach through, as is evident from Fig. 1.

The solid angle coverage of the 42 μm[3] telescope in Fig. 6 should have seen a similar kind of variation with energy, but it was decided to entirely exclude deposited energies in the ΔE detector above 1.3 MeV — hence the drop of solid angle coverage to zero. The reason for excluding the energy region is a seemingly non-uniform thickness across the detector surface. Identification of punch through events seem indicative of an active layer thickness as small as 30–35 μm in the centre of the detector, but approaching the 42 μm, stated by the manufacturer, near the edges of the detector. The limit of 1.3 MeV has been set based on the extremes of the dead and spurious zones tabulated for a 30 μm telescope. Whether the apparent variation in thickness of the ΔE detector is in fact due to a ~20% variation of the detector thickness, or if it is perhaps due to incomplete depletion of the active medium is not known, as the detector has not been readily available when the present analyses were carried out. While the solid angle coverage of the 42 μm telescope is not exactly illustrative of the methods developed in this paper, the method of combining energy spectra of several detector telescopes should still be clear from the ideal example presented via the 67 μm telescope and from the prerequisite methods outlined earlier in this paper. For the purposes of the nuclear physics results published separately [9], all events are internally consistent within the 42 μm telescope when the spurious energy region is excluded, and the resulting energy spectra are consistent with those of the other detector configurations as well.

Finally we note, with reference to Fig. 6, that when all detectors are active and when the punch through thresholds of all detector telescopes have been overcome, the solid angle coverage remains constant. In principle, the solid angle coverage will taper off as the particles begin to punch through the E detectors of the telescope, but this is irrelevant under most practical circumstances.

6. Summary and outlook

The problems involved in extending the energy spectra of silicon strip detector telescopes below punch through of the involved ΔE detectors have been investigated and methods to overcome these problems have been presented. This was done in the context of beta-delayed proton emission from ^{21}Mg, which has a wide distribution of energy levels across the entire dynamic range both of the $\Delta E - E$ telescope and of the ΔE detector by itself. It was argued that the two parameters which, more than anything else, characterise the data extracted from modern detector telescopes employed in close geometry are (1) the active layer thicknesses of the ΔE detectors, and (2) the signal thresholds of the E detectors. The potential distortion of the below-punch through

[3] Stated thickness.

energy spectrum of detector telescopes from telescope-missing events was illustrated, and it was shown how, in such a case, the non-backed areas of a given ΔE detector can be mapped by systematically including and excluding events from its strips and comparing the number of ΔE-contained events to the resulting varying solid angle coverage.

The closer the detector geometry of a given setup, the greater the range of angles of incidence θ between point of particle emission and detector surfaces. The θ-dependent active layer thickness of a given ΔE detector in combination with the signal threshold of its backing E detector can, for sufficiently close detector geometries, result in the appearance of dead and spurious zones spanning several hundreds of keV. Within the dead zone of a detector telescope, certain particle energies E_p are undetectable. The spurious zone, an accompaniment to the dead zone, defines a range of deposited energies E_{dep} in a given ΔE detector in which the corresponding particle energies E_p cannot be uniquely assigned. For a given detector telescope as a whole, the spurious zone generally spans a broader range of particle energies E_p than does the dead zone.

It was shown how the θ-dependent dead and spurious zones can be parametrised, and the parametrisation procedure was extended to allow for the determination of the active layer thicknesses of ΔE detectors through comparison with observed data. The separation of true ΔE-contained events and true telescope events as well as the identification of θ-dependent undetectable and spurious events in telescope dead and spurious zones ensures the integrity of data extracted from detector telescopes. As a result of this, it was shown how the particle energy spectra of several detector telescopes can be combined into one complete particle energy spectrum where the energy-dependent variation in solid angle coverage must be – and can be, due to the developed methods – taken into consideration. For the example of beta-delayed proton emission from ^{21}Mg the entire particle energy spectrum from the proton separation threshold of ^{21}Na to the Q-value of the decay can be investigated only by extending the telescope spectra below their punch through thresholds.

6.1. List of recommendations

In summary, we recommend the following steps when setting out to extend the particle spectra of $\Delta E - E$ detector telescopes below their punch through thresholds:

1. Map the non-backed areas of the ΔE detectors of each telescope, thus potentially filtering out telescope-missing events from the ΔE-contained events.
2. Estimate the thicknesses of the employed ΔE detectors by:
   (a) Tabulating maximally possible energy depositions for various active layer thicknesses of the ΔE detectors and comparing with real data.
   (b) Tabulating the expected energy depositions in the E detectors for various active layer thicknesses of the ΔE detectors and comparing with real data.
3. Tabulate the dead zones and spurious zones of each detector telescope.
4. Reject events lying within these zones and estimate the resulting energy-dependent reduction in solid angle coverage.

By following these steps, one is assured in the correctness of the particle energy spectra extracted below punch through threshold, and further analyses of the data in question can be carried out.

6.2. Thickness non-uniformity of thin silicon strip detectors

As was mentioned towards the end of Section 5, there were indications of a non-uniform active layer thickness of one of the employed ΔE detectors. Thickness non-uniformity of thin silicon strip detectors has recently been investigated e.g. in Ref. [15]. The methods developed in the present paper generally assume a uniform active layer thickness where the effective variation in thickness stems from the variation in angle of incidence θ between point of particle emission and detector surface. The methods can, however, in principle be extended to map the active layer thickness of the individual pixels of a given ΔE detector, given a sufficiently large data set per pixel. The methods' dependence on the distribution of particle energies following the decay of a given radioisotope could be avoided entirely, for example, by devising investigative experiments similar to the ones in Ref. [15]. There, the authors scatter 40 and 55 MeV ^{12}C on a gold foil, which, from a simple elastic scattering calculation, yields scattered particle energies in the range 32–40 (44–55) MeV for scattering angles between 0 and 180 degrees for projectile energies of 40 (55) MeV. For a lighter projectile, such as a proton, on gold, the variation in scattered particle energies can be brought to the order of typical silicon detector energy resolutions. In principle any combination of projectile, projectile energy and target can be utilised, provided that the punch through threshold can be exceeded. By varying the projectile energy around the relevant punch through thresholds of detector telescopes, the pixels at varying angles of incidence will be characteristically active or inactive given the active layer thickness of each pixel, and hence the individual pixel thicknesses can be mapped.

As a final remark we note that while the methods presented in this paper allow the entire dynamic ranges of detector telescopes, including the telescope dead and spurious zones, to be utilised, setups in which several detector telescopes are employed might still benefit from containing ΔE detectors of active layer thicknesses which differ to such an extent that the dead and spurious zones of the individual telescopes do not overlap. In that case, an additional assurance of data integrity of a detector telescope can be attained by comparison with another telescope where the relevant particle energies are not within each others' dead and spurious zones.

Declaration of competing interest

The authors declare that they have no known competing financial interests or personal relationships that could have appeared to influence the work reported in this paper.

Data availability

Data will be made available on request.

Acknowledgements

We acknowledge funding from the Independent Research Fund Denmark (9040-00076B and 2032-00066B). We thank our colleagues from the ISOLDE IS507 experiment from where the ^{21}Mg data originated.

References

[1] F.S. Goulding, D.A. Landis, Ann. Rev. Nucl. Sci. 25 (1975) 167.
[2] D.G. Perry, L.P. Remsberg, Nucl. Instrum. Methods 135 (1976) 103.
[3] A. Badalà, et al., Riv. Nuovo Cimento 45 (2022) 189.
[4] J.F. Ziegler, et al., Nucl. Instrum. Methods Phys. Res. B 268 (2010) 1818.
[5] Stopping powers and ranges for protons and alpha particles, ICRU report 49, J. ICRU (1993).
[6] Stopping of ions heavier than helium, ICRU Report 73, J. ICRU (2005).
[7] B. Blank, M.J.G. Borge, Prog. Part. Nucl. Phys. 60 (2008) 403.
[8] M. Pfützner, et al., Rev. Modern Phys. 84 (2012) 567.
[9] E.A.M. Jensen, et al., The beta decay of ^{21}Mg, 2023, Manuscript, (in preparation).
[10] M.V. Lund, et al., Eur. Phys. J. A 51 (2015) 113.
[11] O. Tengblad, et al., Nucl. Instrum. Methods Phys. Res. A 525 (2004) 458.
[12] M.V. Lund, et al., Eur. Phys. J. A 52 (2016) 304.
[13] S. Viñals, et al., Eur. Phys. J. A 57 (2021) 49.
[14] U.C. Bergmann, et al., Nucl. Instrum. Methods Phys. Res. A 515 (2003) 657.
[15] Q. Liu, et al., Nucl. Instrum. Methods Phys. Res. A 897 (2018) 100.

4.2 New insights into the beta decay of ^{21}Mg

Using the methods outlined in the preceding paper lends us confidence in the charged particle spectra which we extract from the measurements taken on ^{21}Mg at IDS at ISOLDE. Furthermore, it also informs us of some of our limitations: As was highlighted in sections 5 and 6 in the preceding paper, one of our ΔE detectors seemingly had a highly non-uniform active volume thickness. This led us to discard the intermediate energy region of our 42 µm detector telescope. As a result, we have only one detector telescope covering this energy region which means that we do not resolve this energy region particularly well; specifically, our statistics in this energy region is at least an order of magnitude less than that of [Lun+15a]. We therefore refrain from extracting nuclear structure information from this energy region, but we do use the region to extract the beta strength of the decay of ^{21}Mg, as, when extracting the beta strength, we are merely integrating the observed spectrum, and this we can correct by the reduced solid angle coverage.

Apart from utilising silicon detectors for the detection of charged particles in the decay of ^{21}Mg, we also employed High-Purity Germanium Clover detectors for the detection of gamma rays. This allows us to produce the spectra shown in figure 4.3, in which proton singles spectra are shown with and without a gate on the most intense gamma line from the deexcitation of the proton daughter ^{20}Ne from the first excited 2^+ state to the 0^+ ground state. The gamma-gated proton spectrum is scaled up by 50.7, corresponding to an overall efficiency of roughly 2 % for the add-back-corrected, 4-fold segmented Clover detectors, of which there were four during the experiment. The bottom panel in figure 4.3 illustrates the energy-dependent solid angle coverage of our silicon detectors, based on the results presented in the preceding paper.

While the study of ^{21}Mg at IDS is not the first to combine the detection of charged particles with the detection of photons emitted in the beta decay of ^{21}Mg [Tho03; Wan+18], the improved resolution of our charged particle spectra, in particular, allows us to provide further clarifications to the complex decay scheme. Figure 4.4, adapted from the upcoming manuscript, provides a qualitative illustration of the input to our derived decay scheme as the popu-

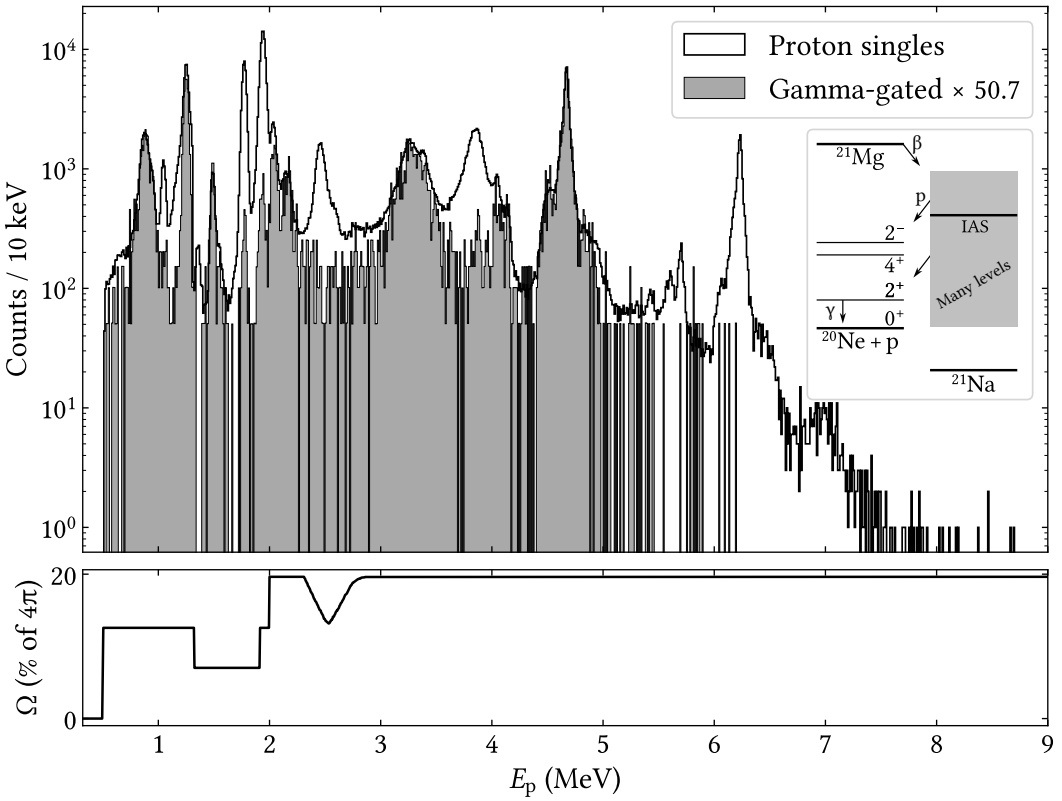

Figure 4.3: Combined charged particle spectrum recorded in the silicon detectors in the IDS experiment on ^{21}Mg. Singles spectra of kinetic energies of protons E_p (corrected for energy losses) emitted from excited states in ^{21}Na are depicted. The shaded histogram shows which parts of the spectrum are in coincidence with the 1634 keV gamma line emitted in the 2^+ to 0^+ transition in ^{20}Ne; the histogram is rescaled to match the ungated spectrum. The inset level diagram shows the partial decay scheme of ^{21}Mg. The lower panel shows the effective solid angle Ω of the setup at a given energy, as outlined in [JRF23]. Figure adapted from [Jen+24].

lation of various intermediate states in ^{21}Na which decay either to the ground state or to excited states in ^{20}Ne by the emission of a proton. If excited states in ^{20}Ne are populated in the decay, one or several photons are emitted. In this adaptation of the figure, the repeated structure which we denote the *IAS complex* is highlighted in red: In the proton singles spectrum, around an excitation energy in ^{21}Na $E_{ex}^{^{21}Na} \sim 8.9$ MeV, the most prominent peak is the state which is the isobaric analogue to the ground state of ^{21}Mg. This state, the IAS, is very narrow, having a width around $\Gamma = 650$ eV [Wil+92], which is far smaller than

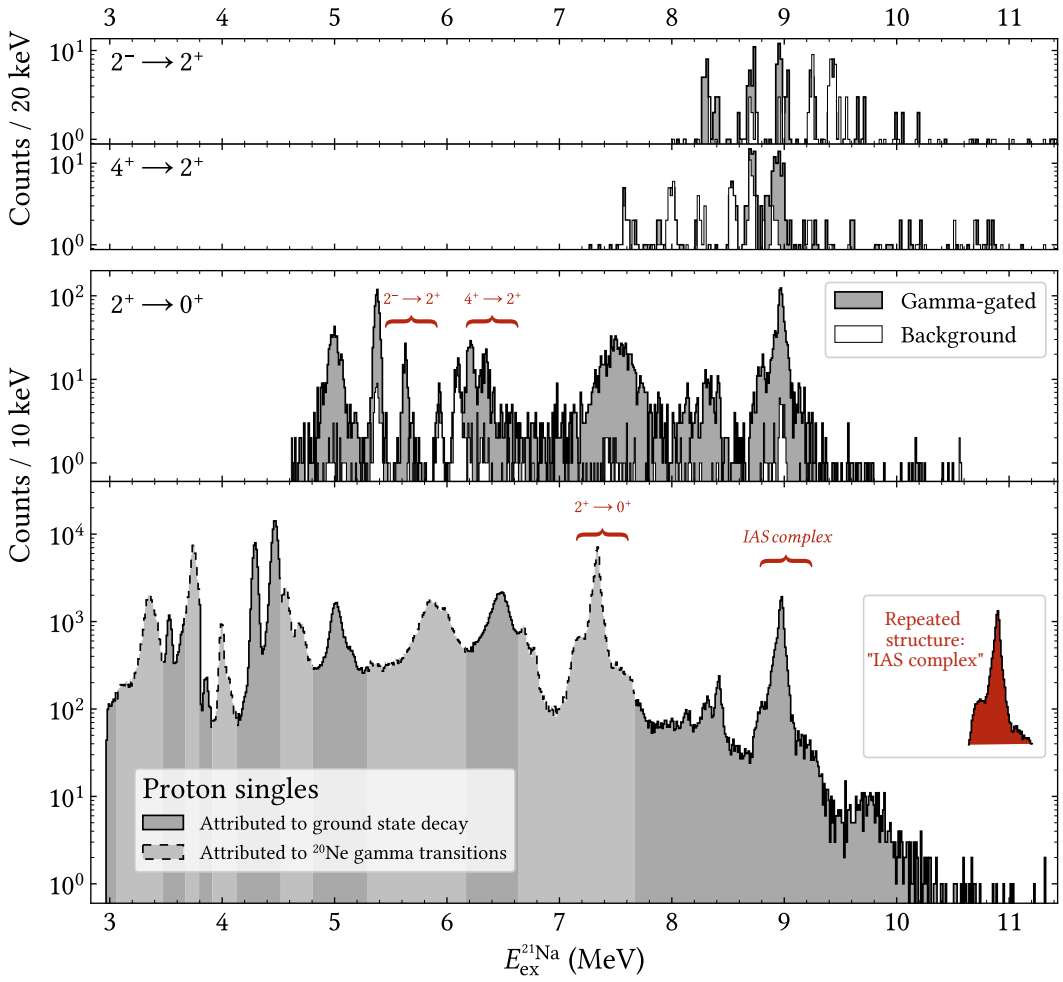

Figure 4.4: The beta-delayed proton spectra from the decay of ^{21}Mg observed in singles (lowest panel) and with gates on the γ rays emitted in the $2^+ \rightarrow 0^+$, $4^+ \rightarrow 2^+$ and $2^- \rightarrow 2^+$ transitions (upper panels) are shown displaced in energy so that all features appear at the appropriate excitation energy in ^{21}Na, $E_{ex}^{^{21}Na}$. The white histograms in the upper panels are spectra obtained with a shifted gate in γ ray energy and correspond to random coincidences. The curly brackets mark regions where decays from the IAS (and states close to it) occur. Note the repeated "IAS complex" structure in the lower panel. Figure adapted from [Jen+24].

our combined spectral resolution of around 50 keV FWHM[3]. Just above and just below this peak, two seemingly broader peaks are also seen. These three states in ^{21}Na are already known in the literature (the states just above and just below the IAS actually have several candidates [Fir15]), but what is striking is that this group of states seems to decay in more or less identical proportion to the

[3] Full Width at Half Maximum.

ground state of ^{20}Ne ($E_{\mathrm{ex}}^{^{21}\mathrm{Na}} \sim 8.9$ MeV in the figure) and to the first excited state of ^{20}Ne ($E_{\mathrm{ex}}^{^{21}\mathrm{Na}} \sim 7.4$ MeV in the figure). We shall return to a possible interpretation of this feature in the outlook of this thesis.

For this IAS complex as well as for other regions in our charged particle spectra, we observe interference effects which, in combination with our gamma-gated spectra and comparison with expected penetrabilities to the 0^+ and 2^+ states in ^{20}Ne, allow us to suggest spin and parity assignments for hitherto unsettled states in ^{21}Na. These assignments are iterative in the sense that the spin and parity of at least one of the interfering states should already be settled in the literature, which then allows us to extend the same assignment to the remaining interfering state or states. The fact that we can use this method to settle spin and parity assignments is partly due to the sufficiently large sample size and sufficiently high resolution of our spectra, but it is also due to the general considerations outlined in section 1.1: The relatively small mass of ^{21}Na and the selectivity of allowed beta decay yield an observed charged particle spectrum with a relatively small density of states where the individual states are fairly broad, and, hence, when states of equal quantum numbers overlap, interference effects will appear. The new results of our studies illustrate very well the strengths of utilising beta-delayed particle emission to reveal nuclear structure information that is otherwise difficult to extract in reaction experiments; it is, for example, difficult to populate $7/2^+$ states in ^{21}Na by adding a proton onto the 0^+ nucleus ^{20}Ne in reaction experiments, while beta decay from the $5/2^+$ ground state of ^{21}Mg naturally allows this.

Apart from the highlights thus far mentioned, in the upcoming manuscript we also extract, utilising the pulsing of the PSB at CERN, a half-life for ^{21}Mg of $t_{1/2} = 120.5(4)$ milliseconds, and we identify a first-forbidden branch to a state of excitation energy 3.859(10) MeV with spin and parity $5/2^-$. We calculate $\log(ft)$ values for the decay of ^{21}Mg to low-lying states in ^{21}Na and compare with corresponding values from the mirror decay of ^{21}F to ^{21}Ne; we see rather large differences in $\log(ft)_{\pm}$ values to the two lowest-lying states just above the relevant one-nucleon separation thresholds: $\Delta \equiv \log(ft)_+ - \log(ft)_- = -0.90$ to the $5/2^+$ state just above threshold, and $\Delta = -0.36$ to the following $5/2^-$ state. Finally, we also extract an energy-dependent experimental beta strength

for the decay of ^{21}Mg and compare it with theory. In the extraction of the beta strength, we utilise equation (1.4), where the beta strength $B_\beta(E) = B_F(E) + (g_A/g_V)^2 B_{GT}(E)$ is the energy-dependent sum of the energy-dependent Fermi and Gamow-Teller strengths. Neither the notation nor the nomenclature employed here is perfect, but it is fairly common in the literature; what is really meant, is that for a given excitation energy E, the cumulative beta strength up to the given E is reported as

$$\sum B_\beta(E) \equiv \frac{\mathcal{T}_{1/2}}{t_{1/2}} \sum_{E_i} s(E_i) \frac{b_i}{f(E_i)}; s(E_i) = \begin{cases} 0 \text{ for } E < E_i \\ 1 \text{ for } E \geq E_i \end{cases} \tag{4.1}$$

i.e. for discrete states $i = 1, 2, \ldots$ of excitation energy E_i, the energy-dependent f-factor is determined for each state, and their contributions to the beta strength, moderated by their individual branching ratios b_i, are added in a discrete sum to the cumulative beta strength only when $E \geq E_i$ (the step function $s(E_i)$ ensures this behaviour). The principle is the same for continuum states, but here the discrete sum is replaced by an integral. For the specific case of beta decay from ^{21}Mg to states in ^{21}Na, the discrete state picture is to be used for states populated below proton separation threshold, and the continuum state picture is to be used for states populated above proton separation threshold (see also figure 1.2). Abusing notation slightly, we take $\sum B_\beta(E)$ to apply to both pictures, keeping in mind that, experimentally, we are to evaluate the beta strength across states of finite width, bin by bin. In our calculations of the f-factor, we employ the phase space parametrisations of [WM74].

All figures as well as most of the analyses and text in the following paper are produced by me. My co-author Sofie T. Nielsen [Nie16] carried out initial analyses which have inspired the newer analyses. The newer analyses are redone from the ground up and are presented in the paper. My co-author Karsten Riisager has also contributed by preparing parts of the text and the tables and some of the analyses.

Eur. Phys. J. A manuscript No.
(will be inserted by the editor)

Detailed study of the decay of ^{21}Mg

E.A.M. Jensen[a,1], S.T. Nielsen[1], A. Andreyev[2], M.J.G. Borge[3], J. Cederkäll[4], L.M. Fraile[5], H.O.U. Fynbo[1], L.J. Harkness-Brennan[6], B. Jonson[7], D.S. Judson[6], O.S. Kirsebom[1], R. Lică[8], M.V. Lund[1], M. Madurga[9], N. Marginean[8], C. Mihai[8], M. Munch[1], R.D. Page[6], A. Perea[3], J. Refsgaard[1], K. Riisager[1], O. Tengblad[3]

[1]Institut for Fysik & Astronomi, Aarhus Universitet, DK-8000 Aarhus C, Denmark
[2]School of Physics, Engineering and Technology, University of York, York YO10 5DD, N Yorkshire, UK
[3]Instituto de Estructura de la Materia, CSIC, E-28006 Madrid, Spain
[4]Department of Nuclear Physics, Lund University, SE-22100 Lund, Sweden
[5]Facultad de Ciencias Fisicas, Universidad Complutense, 28040 Madrid, Spain
[6]Department of Physics, University of Liverpool, Liverpool L69 7ZE, UK
[7]Department of Physics, Chalmers University of Technology, SE-412 96 Göteborg, Sweden
[8]"Horia Hulubei" National Institute of Physics and Nuclear Engineering, RO-077125 Magurele, Romania
[9]Department of Physics and Astronomy, University of Tennessee, Knoxville, Tennessee 37996, USA
Received: date / Accepted: date

Abstract Beta-delayed proton and gamma emission in the decay of ^{21}Mg has been measured at ISOLDE, CERN with the ISOLDE Decay Station (IDS) set-up. The existing decay scheme is updated, in particular what concerns proton transitions to excited states in ^{20}Ne. Signatures of interference in several places in the spectrum are used to settle spin and parity assignments. The previously reported βpα branch is confirmed. A half-life of 120.5(4) ms is extracted for ^{21}Mg. The beta strength of ^{21}Mg is extracted and compared with theory.

1 Introduction

The mechanism of beta-delayed particle emission provides an attractive means of probing the nuclear structure of neutron- and proton-deficient nuclei. For the case of the neutron-deficient nucleus ^{21}Mg with spin and parity $5/2^+$, the selectivity of beta decay enables the precise study of a subset of the otherwise large density of excited and relatively broad [1] states of ^{21}Na. The preferential population of $3/2^+$, $5/2^+$ and $7/2^+$ levels in ^{21}Na in the decay of ^{21}Mg reveals details of the sd-shell nucleus ^{21}Na which are not easily accessible by other experimental means.

Following the beta decay of ^{21}Mg, the emission of a proton and/or an alpha particle is possible, as is the de-excitation of excited states via gamma emission; see fig. 1. The combined amount of detected particles from the decay of ^{21}Mg has, over time, become increasingly complete. In the first comprehensive study of the decay of ^{21}Mg [2], only beta-delayed protons were observed. The observed spectrum was compared to shell model calculations. Later, an unpublished experiment from GANIL [3] detected both protons and gamma rays in the decay, and branching ratios could be determined on an absolute scale. Our earlier experiment [4] on the decay of ^{21}Mg detected both beta-delayed protons and alpha particles. Based on this experiment, several revisions and extensions of the decay scheme were carried out; in particular, a βpα branch was observed for the first time [5]. The identified proton lines were placed in a decay scheme partly based on energy relations and knowledge of the level scheme of ^{21}Na, albeit without the coincident detection of γ rays. More recently, a measurement [6] with ^{21}Mg ions implanted in a Si-detector recorded the proton spectrum as well as protons coincident with γ rays from the first excited state in ^{20}Ne. Other unpublished experiments of similar type have also been performed [3, 7] where more gamma rays have been recorded. These latter experiments have given important clarifications to the decay scheme, but, due to the implanted source, the proton energy resolution is rather limited.

The aim here is to further test the decay scheme by combining detection of γ rays with charged particle detection in a number of Si-detector telescopes positioned in close geometry. The revised decay scheme will be employed to test mirror symmetry in the decay (following [8]) and to extract the beta strength distribution.

[a]e-mail: ej@phys.au.dk

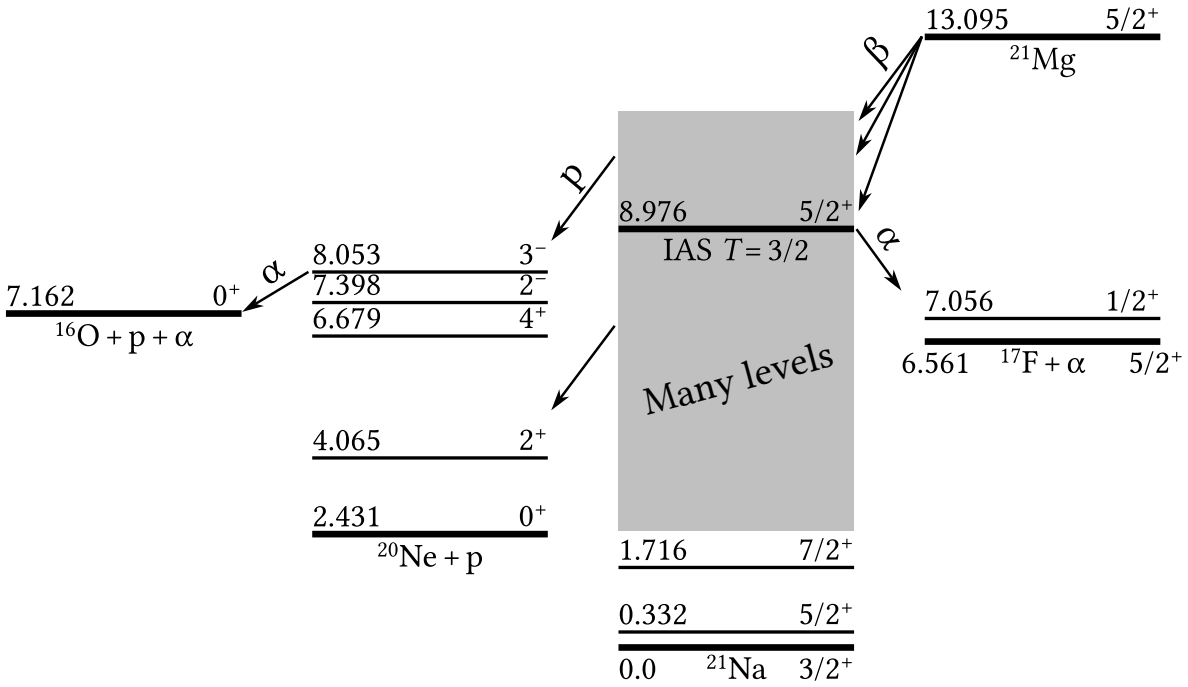

Fig. 1 Decay scheme of ^{21}Mg. Energies are given in MeV relative to the ground state of ^{21}Na. The individual levels in ^{21}Na that take part in proton decay are not shown explicitly; they are listed in table 1.

2 The experiment

The experiment was carried out in 2015 with the main aim of studying the decay of ^{20}Mg. Those results have been published in [9]. As part of the calibration of the setup, data were also taken on the decay of ^{21}Mg; these data are analysed in the present paper.

A complete description of the beam production and experimental setup is given in [9]; here we give a brief summary. A 30 keV ^{21}Mg beam was produced at the ISOLDE facility at CERN [10] and guided to the ISOLDE Decay Station (IDS) [11]. There, the low-energy beam was implanted in a carbon foil of thickness 24.5(5) μg/cm^2 from which the radioactive beam particles decayed. The carbon foil was surrounded by silicon detectors, and, outside the vacuum chamber, by High-Purity Germanium (HPGe) detectors; a sketch of the setup is shown in fig. 2. For the results presented in this paper, data from two of the four ΔE-E silicon detector telescopes as well as the silicon detector below the foil are used. Data from the remaining silicon detectors have been excluded due to technical issues during data taking of ^{21}Mg. The utilised ΔE detectors are double-sided silicon strip detectors (DSSSDs) with 16×16 strips spanning an area of 50×50 mm^2 with ultra-thin entrance windows [12]. The utilised E detectors are 50×50 mm^2

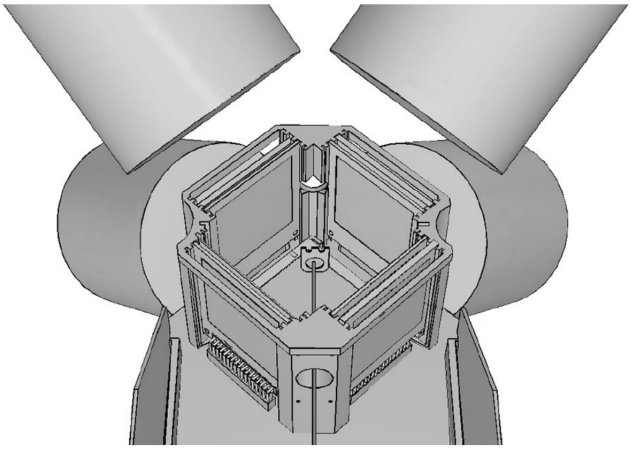

Fig. 2 Schematic drawing of the setup used in the experiment. A 30 keV ^{21}Mg beam goes through the front collimator and is stopped in a carbon foil. In the horizontal plane four ΔE-E silicon detector telescopes are placed and below the foil an additional silicon detector; the ΔE detectors are situated roughly 40 mm from the centre of the carbon foil, and the backing E detectors are situated 5 mm further behind. The four cylinders outside the silicon detector holder represent the 4 High-Purity Germanium detectors which are four-fold segmented and situated roughly 30 cm from the carbon foil. This drawing is a slightly modified version of the one presented in [9].

single-sided pad detectors. Both E detectors have active layer thicknesses of 500 μm and the ΔE detectors have active layer thicknesses of 42 and 67 μm. The silicon detector below the foil is the same type of DSSSD as the two ΔE detectors with an active layer thickness of 1000 μm. The 4 HPGEs situated outside of the chamber are four-fold segmented Clover detectors.

The setup used in this experiment allows for the identification of the protons, alphas and gammas emitted in the complex beta-delayed particle emission of ^{21}Mg; see fig. 1. The segmentation of the DSSSDs provides accurate information on a given particle's trajectory and, in turn, allows for accurate determination of initial particle energies, whilst the small thickness of the ΔE detectors suppresses beta response at low energy. The segmentation of the Clover detectors provides improved detection efficiency via add-back correction of the gammas. The inherent high resolution of the Clover detectors is not utilised to the fullest in proton-gamma coincidences due to the data acquisition system of the experiment being optimised for resolution on the silicon detectors. This is of less importance when the gamma data are used to gate on specific gamma transitions in order to clarify the population and de-population (via proton or alpha emission) from excited states in ^{21}Na.

The ΔE-E *technique* is well-established [13–15], and it is in principle straightforward to unambiguously identify various kinds of charged particles when they deposit characteristic fractions of their initial energies in both the ΔE and the E detectors. When the initial particle energies are less than the punchthrough threshold of a given ΔE detector, however, energy regions in which initial particle energies *cannot* be uniquely assigned will emerge [15]. In close geometry, i.e. when the angle of incidence with respect to the ΔE detector surface can vary significantly, these spurious energy regions can span many hundreds of keV: At zero angle of incidence, $\theta = 0$, one spurious energy region may span the interval $[E_1, E_2]$, while at a larger angle of incidence $\theta > 0$ another spurious energy region may span the interval $[E_3, E_4]$ with $E_1 < E_2 < E_3 < E_4$. The complete set of θ-dependent spurious energy regions for a given ΔE-E telescope corresponds to some interval $[E_{\mathrm{p}}^{\mathrm{min}}, E_{\mathrm{p}}^{\mathrm{max}}]$ of the total particle energy spectra which we wish to extract. The segmentation of our ΔE detectors allows us to selectively exclude the various θ-dependent spurious energy regions in such a way that our extracted particle energy spectra are rid of them, while the interval $[E_{\mathrm{p}}^{\mathrm{min}}, E_{\mathrm{p}}^{\mathrm{max}}]$ still does not have to be excluded entirely. The result is unobscured particle energy spectra, where the solid angle coverage in the interval $[E_{\mathrm{p}}^{\mathrm{min}}, E_{\mathrm{p}}^{\mathrm{max}}]$ is energy-dependent. This has to be accounted for. If the spurious energy regions of ΔE-E telescopes are not identified and excluded, the particle energy spectra below punch through threshold will be distorted by events from above threshold. More details are given in [15].

Based on the ΔE-E analysis methods thus outlined and based on identification from previous measurements [4,5], protons and alpha particles are reliably identified above and below the relevant punchthrough thresholds of our setup.

About 10^6 decays of ^{21}Mg were observed during the measurement time of 5 hours. Correcting for detection efficiencies ($\sim$20 %), there were, on average, 280 decays of ^{21}Mg ions per second within our chamber. 7650 proton pulses impinged on the production target at ISOLDE during the measurement. This corresponds to 650 ^{21}Mg ions being delivered to our chamber per pulse, or, with a proton current at the production target of 1.9 μA, to 150 ions per microcoulomb.

3 Results

The results will be presented as follows. The determination of the half-life of ^{21}Mg is described first. Accounts are then given of the observed gamma lines, of the singles and gamma-coincident proton spectra and, finally, of the proton-α particle coincidences. The derived decay scheme is then discussed in detail.

3.1 Half-life

The half-life of the precursor ^{21}Mg is determined by identifying and counting protons emitted from excited states in the emitter ^{21}Na at various times after production of the radioactive ^{21}Mg beam at ISOLDE. The proton events are gathered from two of the setup's detector telescopes and from one thick DSSSD.

The number of proton counts detected at various times after production is shown in fig. 3. During the first 350 milliseconds the activity is led into the chamber and there is a build-up of (decaying) ^{21}Mg within the chamber. The subsequent exponential decay is characteristic of the half-life of ^{21}Mg. The discontinuity at 1.2 seconds is due to the cycling of the Proton Synchrotron Booster at CERN, which resets the clock at integer multiples of 1.2 seconds. The bump just before 1.2 seconds is due to neutrons produced when the proton beam hits the production target, the reset of the clock only takes place after the separator high voltage is stable, see sect. 2.5 in [10]. In the fit of the half-life we avoid this spurious region and we did not include the region of lower statistics after 1.2 seconds.

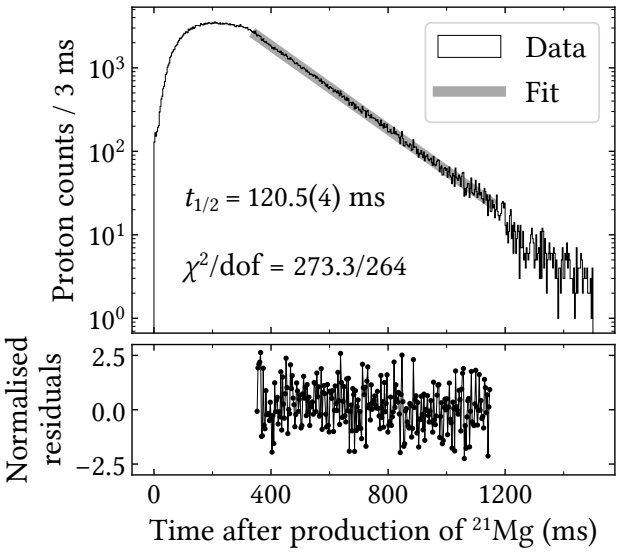

Fig. 3 Time distribution of protons recorded from the decay of ^{21}Mg. The shaded region marks the time interval used to deduce the halflife of ^{21}Mg.

The data in the region 350 to 1150 milliseconds are fitted to a simple exponential decay using unbinned maximum likelihood as the cost function. For our Poisson-distributed data, the binned χ^2 variable

$$\chi^2_{\mathrm{P}} = 2\sum_i^N n_i \ln \frac{n_i}{\hat{m}_i} + \hat{m}_i - n_i \qquad (1)$$

follows, in the limit of a large sample size N, a χ^2 distribution with $N-2$ degrees of freedom (see e.g. [16]). In the expression, n_i is the observed number of counts in bin i and $\hat{m}_i$ is the expected number of counts in bin i estimated by the fit. The result of the fit is a half-life $t_{1/2} = 120.5(4)$ milliseconds of ^{21}Mg, and, with the chosen binning shown in the figure, we extract a chi-square value of $\chi^2 = 273.3$ with dof = 264 degrees of freedom. Varying the end points of the fitting range with up to 50 milliseconds has no influence on the result at the given precision. Our result is consistent with the current adopted value [17] of 120.0(4) ms.

3.2 The gamma spectrum

The combined gamma spectrum from all detectors including add-back is shown in fig. 4. As seen from fig. 1 it may contain gamma rays from particle-bound states in ^{21}Na and from states in ^{20}Ne fed through proton-emission as well as from ^{21}Ne (from the beta decay of ^{21}Na; not indicated in fig. 1). The low-lying spectrum in ^{21}Na is well-established and we observe, as has been done previously [3], three gamma lines from the de-excitation of the 2 lowest-lying states in ^{21}Na, below the proton separation energy: a 332 keV line from the first excited $5/2^+$ level to the $3/2^+$ ground state, a 1384 keV line from the second excited $7/2^+$ level to the first excited $5/2^+$ level, and a 1716 keV line from the second excited $7/2^+$ level to the $3/2^+$ ground state; see fig. 1. We observe a quite strong 351 keV line from the beta decay of ^{21}Na; it has only a 5% branch in the decay, which indicates that we have direct production of ^{21}Na from our target, as also observed earlier at ISOLDE [4]. We are therefore not able to extract the intensity of the ground state branch. Several transitions in ^{20}Ne are also observed and are marked with arrows in fig. 4.

With a gate in the time distribution the transitions from the decay of ^{21}Mg can be enhanced further above background. The following relative intensities of gamma transitions are derived:

- 1716 keV line to 1384 keV line, i.e. the decay paths from the $7/2^+$ level: the ratio is 0.067(3), consistent with but more accurate than the previous value [1] of 0.075(22)
- 1384 keV line to 332 keV line: the ratio is 0.30(2), indicating that the ratio of feeding to the $7/2^+$ and $5/2^+$ levels is 0.46(4) (the previous estimate of the ratio of 0.27(6) came from the mirror decay of ^{21}F)
- 1634 keV line to 1384 keV line: the ratio is 0.42(2), it will be used below to relate the feedings to levels above and below the proton threshold

The transitions in ^{20}Ne are enhanced in fig. 4 in the spectrum of gamma rays coincident with a proton recorded in the Si detectors. The background level is clearly reduced and three transitions in ^{20}Ne are observed in agreement with [7], the inset in the figure gives the relevant partial level diagram. Earlier experiments [3,6] have only observed proton spectra coincident with the 1634 keV line, our results will be shown in the next section. Note that the majority of the feeding to the 4^+ and 2^- states as well as some feeding to the 3^- state will give a 1634 keV line as the de-excitations proceed through the 2^+ state.

In the proton-gated spectrum one clearly observes the recoil-broadening of the 1.634 MeV line due to the preceeding proton emisison. Similar broadening occurs for the other ^{20}Ne lines, but the statistics are less for these cases, the branching ratios relative to that of the 1.634 MeV line are at most 0.10(3) and 0.07(2) for the 2.614 MeV and 3.333 MeV lines, respectively. (A background line is also present at 2.614 MeV, so that only an upper limit can be given here.) As explained below the 3^- state is also populated by beta-delayed protons and gamma rays from its deexcitation are expected. However, the 3^- state mainly decays via alpha particle emission and the most intense gamma line at 3.987

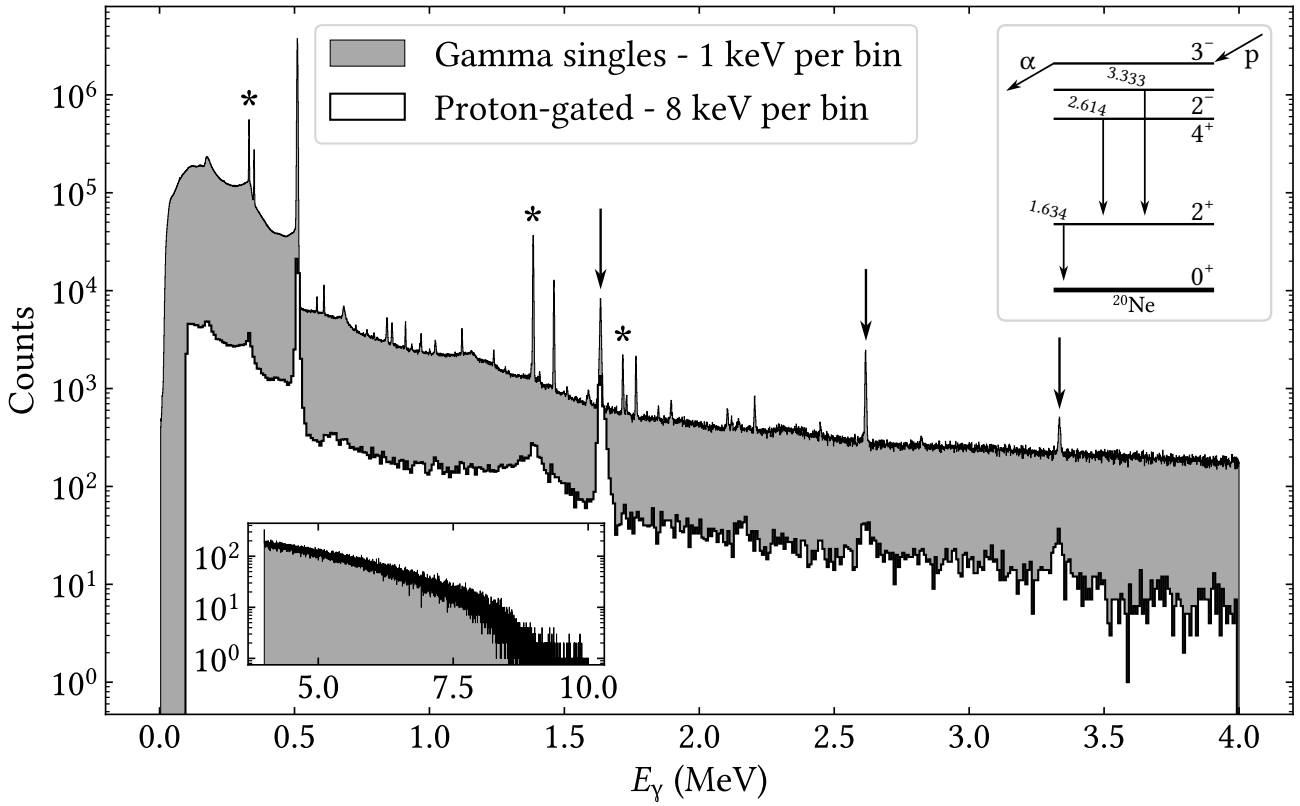

Fig. 4 Combined gamma spectra of gamma energies E_γ recorded in the four 4-fold segmented HPGe detectors, the high-energy part is shown in the lower inset. Both the singles and the proton-gated spectra are addback-corrected. The upper inset shows the observed gamma transitions in ^{20}Ne that are marked with arrows. Note that the 2.614 MeV line coincides in energy with a background line from ^{208}Tl. The gamma lines from bound state transitions in ^{21}Na are marked by asterisks. See the text for further discussion.

MeV has a branching of about 7%, so that only a few coincidences would have been expected.

3.3 The particle spectrum

The events registered in the Si detector telescopes will mainly be β particles at low energy and protons at higher energy. There are also small contributions from the $\beta\alpha$ and βpα branches, however, protons will dominate the charged particle spectra where the $\beta\alpha$ and βpα branches contribute [5]. The strongest α line at 1954 keV is situated where the two most intense proton lines of the decay appear (fig. 5), and the other α lines of smaller energies are too weak to be disentangled from the proton spectrum without particle identification. Overall, the contribution of the $\beta\alpha$ and βpα branches to the extracted βp spectra is negligible.

The final particle spectrum, obtained by combining the best spectra from the Si detectors, is shown in fig. 5. We discard the two telescopes that have a 20 μm and 300 μm front strip detector (the first has too low resolution, the last appears to have not been fully depleted). The regions in the other detectors where punch-through protons or beta particles may contribute are also left out. The bottom panel in fig. 5 shows what the combined solid angle of the reliable detectors is at a given energy. The sharp drop in the solid angle coverage around a proton energy E_p of 1.3 MeV, for example, results in a correspondingly sharp drop in the number of counts at the high-energy tail of the proton peak in the vicinity of this energy. Details of the analysis procedure which lead to the illustrated variation in solid angle coverage are given in [15].

The earlier experiments [3,4,6] have made clear that there is substantial proton feeding to excited states in ^{20}Ne, as confirmed by our gamma spectrum shown in fig. 4. The parts of the proton spectrum that correspond to excited state transitions are identified with a gate on the 1634 keV $2^+ \rightarrow 0^+$ γ transition, the spectrum obtained in this way is also displayed in fig. 5 and is rescaled by the γ-ray detection efficiency. This spectrum is significantly improved in resolution compared to the earlier experiments.

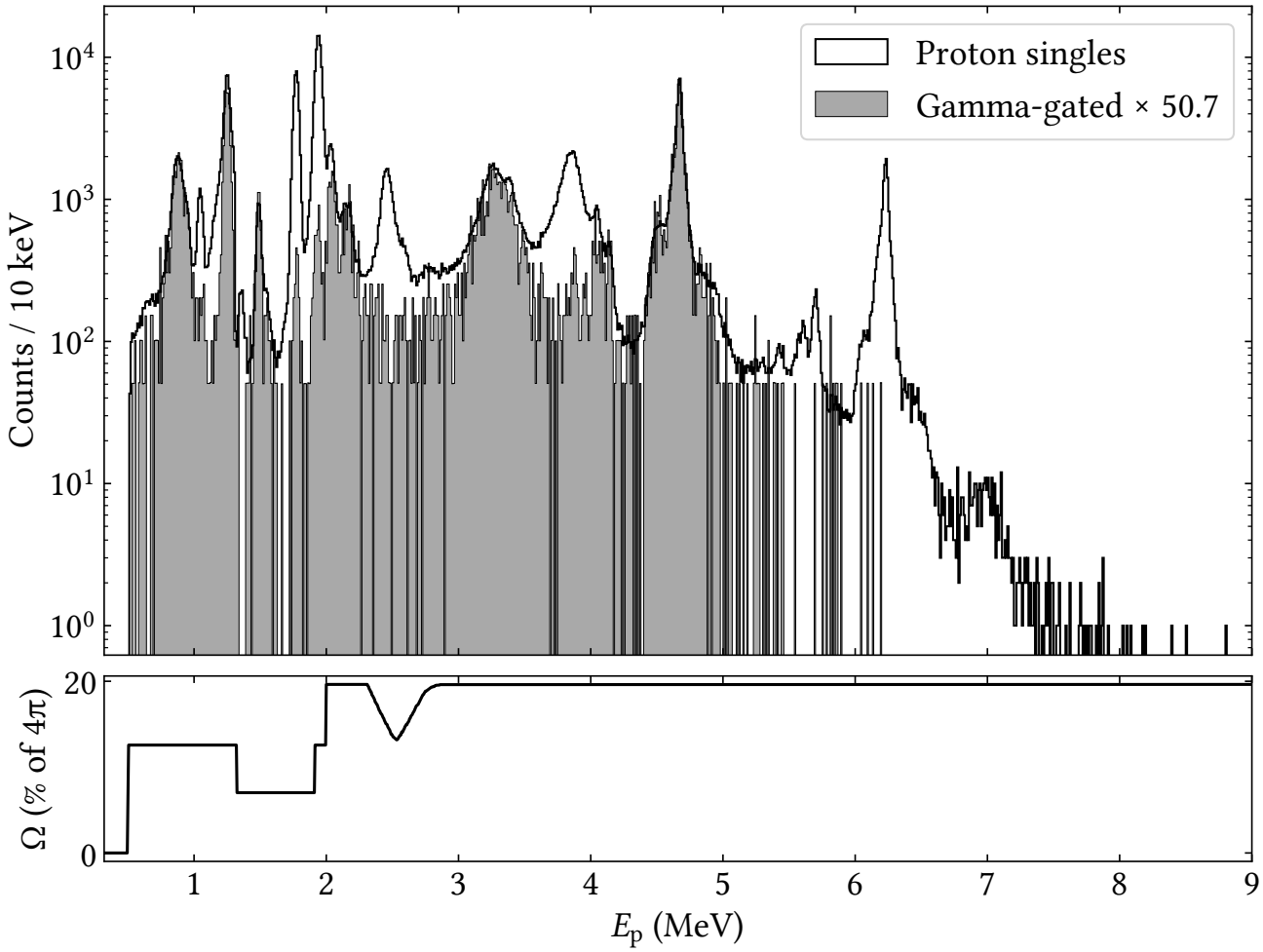

Fig. 5 Combined charged particle spectrum recorded in the Si detectors is shown versus the proton energy (corrected for energy loss) E_p. The shaded histogram shows which parts of the spectrum are in coincidence with the 1634 keV gamma line; it is rescaled to match the singles spectrum. The lower panel shows the effective solid angle Ω of the setup at a given energy, as outlined in [15].

The proton spectra found with gates on all three observed lines, as well as background spectra found with a displaced gate in the gamma ray energy, are shown as a function of the deduced excitation energy in ^{21}Na in fig. 6. A more detailed account of this coincidence analysis can be found in [18]. The only clear feeding of the 4^+ state is from the IAS in ^{21}Na, but there seems to be an excess of coincidences from the unresolved region above the IAS. In contrast, the 2^- state is fed both from the IAS and a state around 8.3 MeV, and the 2^+ state is fed by quite a few states in ^{21}Na. The random coincidences seen with the displaced gates mainly occur for the most intense peaks in the singles proton spectrum.

Due to the low statistics in the coincidence data and the increase in uncertainty of our gamma ray efficiency at high gamma energy, we use the coincidence spectra mainly to place transitions correctly in the decay scheme and evaluate the intensity of the peaks from the singles spectrum.

3.4 The proton-α particle coincidences

Our earlier experiment [5] gave evidence for a βpα branch from ^{21}Mg that was interpreted as proceeding through the 3^- state in ^{20}Ne. The energies of the α events pointed to this interpretation, but only a few coincidence events were recorded. In order to verify this observation and interpretation, we show in fig. 7 the low-energy coincidence events recorded between the two opposing double-sided Si strip detectors with thicknesses of 42 μm and 67 μm. The β particles deposit only a few tens of keV in these detectors so we mainly see coincidences between heavy charged particles. The only true coincidence events expected are from the βpα decays,

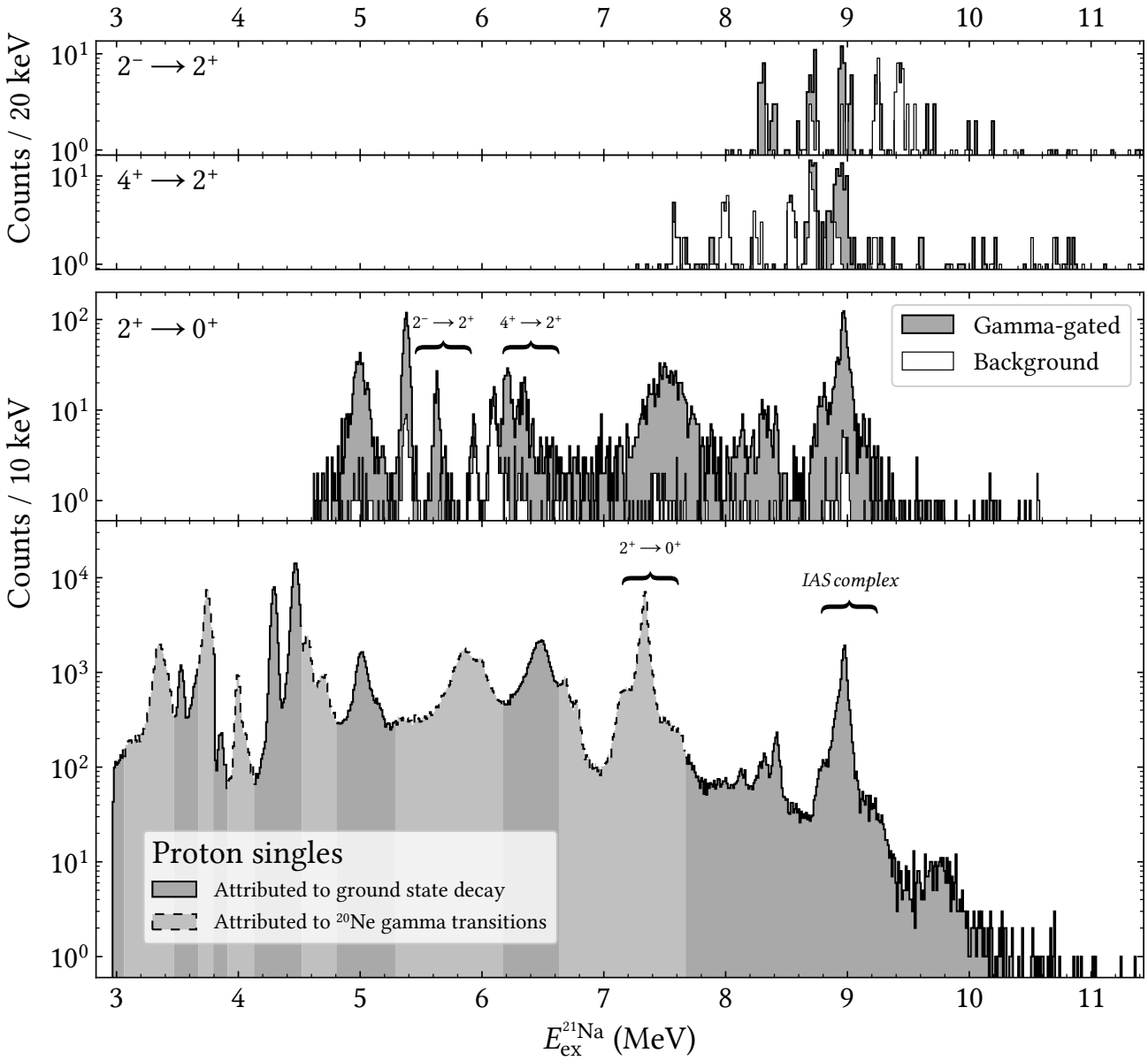

Fig. 6 The beta-delayed proton spectra from the decay of ^{21}Mg observed in singles (lowest panel) and with gates on the γ rays at 1634 keV, 2614 keV and 3333 keV (upper panels) are shown displaced in energy so that all features appear at the appropriate excitation energy in ^{21}Na, $E_{\rm ex}^{^{21}{\rm Na}}$. (Note that the 2^+ gated spectrum will also contain lines from the 4^+ and 2^- spectra as the gamma decays of these levels proceed through the 2^+ level.) The white histograms in the upper panels are spectra obtained with a shifted gate in γ-ray energy and correspond to random coincidences. The curly brackets mark regions where decays from the IAS (and states close to it) occur.

but random coincidences with the strongest proton lines will also occur.

We observe about 150 low-energy events, close to the dotted lines in the figure. Both detectors give the same projected energies (not corrected for energy losses in the collection foil and detector deadlayers), namely a sharp line around 850 keV and a broad distribution from a bit above 500 keV to just below 800 keV. This fits perfectely with the interpretation: A proton emitted from the IAS in ^{21}Mg to the 3^- state in ^{20}Ne will have a laboratory energy of 877 keV, the α particle emitted to the ^{16}O ground state a laboratory energy of 714 keV, and the maximum recoil shift of the α energy will be 158 keV. This is all consistent with our data. One can in principle determine in which order two different particles are emitted from the amount of recoil broadening, but the final difference for different orderings is small

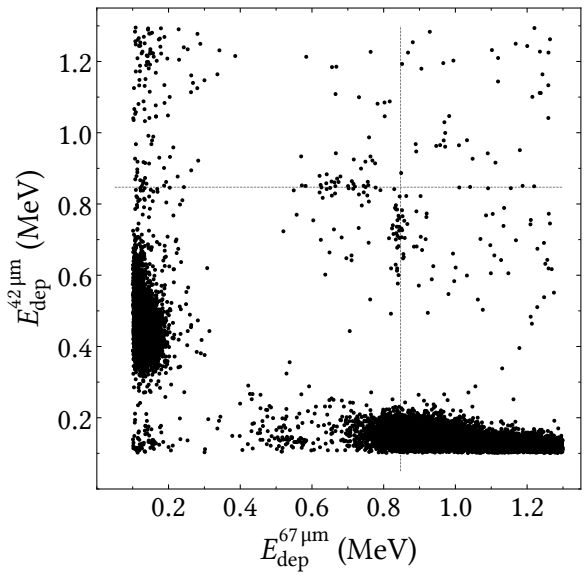

Fig. 7 Coincidence spectrum of deposited energies $E_{\rm dep}$ between the two thin (42 μm and 67 μm) Si strip detectors. Apart from beta-proton coincidences along the energy axes, the main feature is the events along the dotted lines that are interpreted as proton-alpha coincidences. See the text.

and the smearing from energy losses will here be more important.

We conclude that the βpα observation in [5] is confirmed.

3.5 Derived decay scheme

The interpretation of the proton spectrum has evolved since the first published data [2], in particular what concerns broad features in the spectrum. Before describing the changes due to our data, it may be useful to outline which complementary information can be used.

Allowed beta decay will populate levels in ^{21}Na with spin-parity $3/2^+$, $5/2^+$ and $7/2^+$. It is likely that the decay in a first approximation can be described within the sd-shell and we may therefore compare to the shell-model predictions given in [19]. In the region up to the position of the IAS they predict 7, 7 and 6 levels for the three possible spin values (excluding the IAS itself). We shall compare to the theoretical strength distribution later.

Several reaction experiments have given a quite extensive knowledge of the level structure of ^{21}Na, mainly by adding a proton to ^{20}Ne via e.g. (p,p), (p,γ) and (d,n), but also from more complex reactions such as ^{23}Na(p,t). The latest compilation can be found in [1] where also information on the mirror nucleus ^{21}Ne is available. In the region up to the IAS (excluding levels mainly seen in earlier ^{21}Mg decay experiments) the number of identified $3/2^+$, $5/2^+$ and $7/2^+$ levels in ^{21}Ne and ^{21}Na are 9, 6 and 3 (with 3–4 more tentative $7/2^+$ levels), and 8, 6 and 1, respectively. We can therefore to a large extent base our interpretation on previous experiments for $3/2^+$ and $5/2^+$ levels, but not for $7/2^+$ levels which are difficult to populate in a one-step reaction from ^{20}Ne.

3.5.1 The proton spectrum

In fig. 5, the singles spectrum shows all of the observed proton groups from the decay, and the gamma gated spectrum reveals which proton groups are due to decays to excited states in ^{20}Ne. This information is compiled into fig. 6, in which the population of the various excited states in ^{21}Na is depicted, and the various proton groups are attributed to decays either to the ground state or to excited states in ^{20}Ne. We first go through the energy spectrum and note differences to earlier work as well as the regions where contributions from excited state transitions reduce the sensitivity to ground state transitions.

Of the four peaks in the region up to 1.7 MeV (laboratory proton energy), only the peak at 1 MeV goes to the ground state. The 1.5 MeV peak goes to the 2^- state in ^{20}Ne and the other two to the 2^+ state, except that the (slightly asymmetric) 0.9 MeV peak has contributions also from transitions to the 2^- and 3^- states. Our solid angle coverage changes in the region from 1.3 MeV to 1.7 MeV and we do not completely resolve the small extra peaks in this region observed in [4,6].

The two strongest peaks, at 1.8-2 MeV go to the ground state, while the two following peaks go to the 2^+ and 4^+ states. The broad slightly asymmetric peak at 2.5 MeV goes again to the ground state, there is unresolved ground state strength up to 3 MeV followed by a quite broad complex between 3 MeV and 3.5 MeV that earlier [2] has been fitted with up to four peaks, but now (as in [4]) is interpreted as a broad peak leading to the 2^+ state and a smaller narrow peak on the high energy side that presumably goes to the ground state.

The region 3.5–4.3 MeV again features a broad peak that goes to the ground state, with two peaks at higher energy (and one slightly lower only seen in the coincidence spectrum) that go to the 2^+ state, again more consistent with [4] than with [2,6]. The strength in the 4.3–5.0 MeV region goes mainly to the 2^+ state and shows structure both below and above the main peak, as in [4,6]. The 5.2–6 MeV region contains in the middle three peaks going to the ground state with indications below and above for strength to the 2^+ state; this is a region where the interpretation has differed earlier [2,

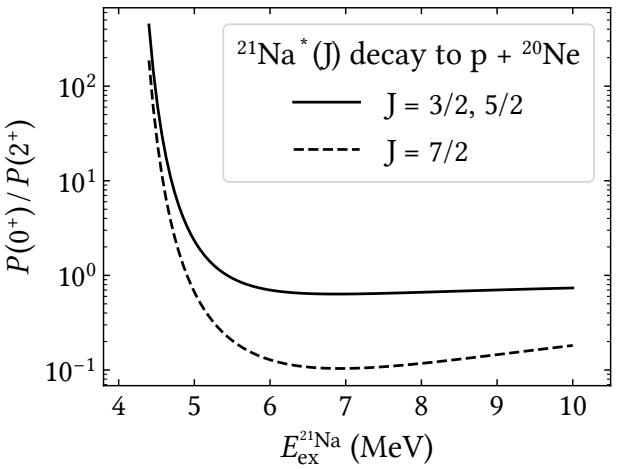

Fig. 8 The ratio of penetrabilities for transitions into the 0^+ ground state, $P(0^+)$, and 2^+ first excited state, $P(2^+)$, in ^{20}Ne as a function of excitation energy in ^{21}Na, $E_{ex}^{^{21}Na}$, and for different spin values, J.

6,21]. The spectrum above 6 MeV contains decays to the ground state.

In the regions 3–3.5 MeV and 4.3–5 MeV we are not sensitive to weak peaks going to the ground state.

3.5.2 The excitation energy spectrum

The next step is to systematically go through the experimental excitation energy spectrum in fig. 6. When transitions to several states in ^{20}Ne are observed (typically the ground state and the 2^+ state) the relative decay rates can be extracted. Finally, the observed peaks can be compared to the existing level schemes [1] and spin values may be assigned. Some assignments are necessarily tentative, for example for the energy region above the IAS where the statistics is low.

The proton penetrabilities enter in the relative decay rates to states in ^{20}Ne. For $3/2^+$ and $5/2^+$ levels the protons will be in d-waves to the ground state and 4^+ state and in s-waves to the 2^+ state. For $7/2^+$ levels the protons are in g-waves to the ground state, d-waves to the 2^+ and s-waves to the 4^+ state. For both negative parity states and all levels p-wave emission suffices. Figure 8 shows the ratio of penetrabilities to the two lowest states, the 2^+ feeding is seen to start around 5 MeV and is then quickly favoured for all spin values.

The observed proton lines are collected in table 1 as a function of deduced level energy. The estimated width and branching ratios to the ground state and 2^+ state in ^{20}Ne are listed and preferred spins are given. In several cases, including the levels at 3544 keV, 4294 keV, 4468 keV and the IAS at 8976 keV, the identification with levels in the literature [1] (also given) is unambiguous and the spin can be safely taken over. Comments are given below on other cases.

Recently, in a ^{24}Mg(p,α) experiment [20], the broad level at 5 MeV has been observed at 5.036 MeV with a spin assignment of $(3/2{,}5/2)^+$. It had about equal intensity for the two branches as also observed here. The peak is slightly asymmetric on the high-energy side which could indicate the presence of a weakly fed level, it is listed in parentheses in the table.

The level at 5.37 MeV is mainly seen to proceed to the 2^+ state, with at most a small ground state branch. This and the fact that it has not been observed in proton scattering on ^{20}Ne is compatible with a spin value of 7/2. Note that the level at 5.6 MeV in the 2^+-gated proton spectrum is from the IAS decay to the 2^- state and appears here due to the gamma cascade in ^{20}Ne. Note also that there is an indication for unresolved strength to the ground state from the 5 MeV level up to around 5.6 MeV excitation energy. Furthermore, there is a weak peak at 5.98 MeV that appears to proceed only to the ground state.

In a similar way the peak in the 2^+-gated proton spectrum at 6.4 MeV is due the IAS decays to the 4^+ state. The level at 6.20 MeV mainly decays to the excited state and cannot have spin 3/2 since it does not interfere with the broad 6.47 MeV state, as for the 5.37 MeV level a spin value of 7/2 is likely. The 6468 keV state is well-established and has spin-parity $3/2^+$. A ^{20}Ne(p,p) experiment with polarized protons [21] that measured elastic to total widths showed that the level decays mainly to the ground state, in agreement with our results; the proton branching ratio of levels to the ^{20}Ne ground state are also displayed in the table.

The broad level seen clearly at 7.5 MeV in the 2^+-gated proton spectrum may also have a ground state transition that in the singles spectrum lies below the IAS complex decaying to the 2^+ state. However, only the upper tail between 7.6 MeV and 7.8 MeV seems visible, so a proper extraction is not feasible. The properties of the level seem close to the ones of the 7609 keV level in [21], but the assignment is not firm. The ^{20}Ne(p,p) experiment [21] reported 8 levels with spin-parity $3/2^+$ or $5/2^+$ in the region 8–9 MeV. We tentatively see the first three of these and observe essentially featureless strength around 8.6 MeV that cannot be attributed easily to any (combination of) level(s), but clearly see much strength in connection with the IAS. The interpretation of the decay of the IAS and the closely surrounding levels will be done in the following subsection.

The spectral shape above 9.2 MeV differs from the one reported in [4,6]. We see a clear indication for a peak at 9.8 MeV that tentatively is identified as the

Table 1 Beta-delayed protons from ^{21}Mg listed by their corresponding intermediate level excitation energies in ^{21}Na, $E_{ex}^{^{21}Na}$, and their widths Γ. Results from the current experiment are listed in the left block along with deduced branching ratios b_p to the 0^+ ground state and 2^+ first excited state of ^{20}Ne as well as spin J assignments of the intermediate levels in ^{21}Na. Literature values from [1] are listed in the middle block along with their spin and parity J^π assignments. Branching ratios to the 0^+ ground state of ^{20}Ne, b_0, from [21] are listed in the right block.

Current experiment					Literature, [1]			Literature, [21]
$E_{ex}^{^{21}Na}$ (MeV)	Γ^a (keV)	b_p (%)^b 0^+	2^+	J^c	$E_{ex}^{^{21}Na}$ (keV)	Γ (keV)	J^π	b_0 (%)
3.52(2)	S	1.5(2)	n.a.	L	3544.3(4)	0.0155(14)	$5/2^+$	
3.86(1)^d	S	0.66(3)	n.a.	L	3862.2(5)	0.0026(3)	$5/2^-$	
4.29(2)	S	16.5(3)	–	L	4294.3(6)	0.0039(1)	$5/2^+$	
4.46(2)	S	23.2(5)	–	L	4467.9(7)	0.021(3)	$3/2^+$	
5.02(1)	110(15)	4.6(3)	4.4(4)	3/2, 5/2				
(5.15(2))	S	0.3(2)	0.3(2)	(3/2,5/2)				
5.37(1)	S	< 0.4	10.8(4)	(7/2)				
5.98(2)	S	0.15(5)		3/2				
6.20(1)	S		1.5(4)	(7/2)				
6.47(2)	130(25)	6.5(6)	0.5(3)	L	6468(20)	145(15)	$3/2^+$	90(12)
7.49(2)	200(50)	< 1.4	7.2(6)	(L)^d	7609(15)	112(20)	$3/2^+$	11(3)
8.13(2)	S	0.16(3)	0.5(3)	L	8135(15)	32(9)	$5/2^+$	18(5)
8.31(2)	S	0.20(2)	0.6(2)	L	8397(15)	30(13)	$3/2^+$	11(6)
8.42(2)	S	0.23(2)	0.4(2)	L	8464(15)	25(9)	$3/2^+$	13(3)
8.55	^{d}							
8.8	^{d}				8827(15)	138(16)	$5/2^+$	28(5)
8.97(1)	S	2.10(3)	8.4(3)	L	8976(2)	0.65(5)	$5/2^+$	
9.0	^{d}				8981(15)	23(16)	$5/2^+$	8(4)
9.8(1)	300(100)	0.06(1)	0.15(2)	(L)	9725(25)	256(29)	$3/2^+$	53(7)
10.2	S	0.008(3)	0.07(2)					
10.70(2)	S	0.002(1)		(3/2)^d				

[a] S denotes a width up to our combined resolution of 50 keV.
[b] The fraction of the total beta-delayed proton spectrum.
[c] L denotes that the spin is taken from the literature.
[d] See the discussion in the text.

9725 keV $3/2^+$ level seen earlier. The only partially resolved strength between 10 MeV and 11 MeV that is present in both ground state and excited state spectra is here attributed to two levels. The lower one is assumed narrow due to the signature in the 2^+-gated spectrum and would then preferentially decay into the 2^+ channel. The upper one could be the, so far missing, $3/2^+$ level of isospin $T = 3/2$ known [1] to exist in the other members of the multiplet, but this assignment is tentative and is mainly based on its small apparent width and its position about 1.7 MeV above the lowest $T = 3/2$ level.

3.5.3 The IAS decay and interference effects

The $5/2^+$ IAS at 9876 keV is the lowest isospin 3/2 state and is known [22] to be narrow, $\Gamma = 650(50)$ eV with a width for decays to the ^{20}Ne ground state of $\Gamma_p = 117(10)$ eV corresponding to a partial branching ratio of $b_0 = 18(2)\%$. By combining our data with the results in [4,5], we have the most extensive overview of the decay channels of the IAS. Our results are shown in Table 2, but we first present a few observations.

It is striking from figure 6 that the levels close to the IAS appear to decay in about the same proportion to the ^{20}Ne ground state and first excited state. Even though the statistics is limited, the decays to the 4^+ and 2^- states could also proceed in the same way. We further reinterpret the α-particle spectrum shown in [5] as consisting of decays only to the ^{17}F ground state, and then see the same pattern appearing also for α decays. (Our upper limit on the intensity of the 495 keV gamma ray in ^{17}F of 1.4% of the total proton intensity is not sufficiently strong to distinguish the two interpretations.) Assuming this is a correct interpretation, and acknowledging that we cannot experimentally separate the IAS decays from the ones of the closely lying neighbouring levels, we will look at the combined decay of these levels, called "the IAS complex".

The relative branching intensities in table 2 are taken from table 1 except for the α and the 3^- branch that is rescaled from the results in [4,5], the latter further being corrected for the known 93(3)% α decay probability of the 3^- state. Our extracted b_0 of 14(3)% is slightly lower than the one from [22] which could be due to an underestimation of the background under the IAS com-

Table 2 Decay channels of the IAS complex. Protons decay to states in ^{20}Ne; alpha particles decay to states in ^{17}F. Relative intensities are from table 1 and [4,5] (see text).

Particle	Final state	Rel. intensity (%)	Penetrability
p	0^+ (g.s.)	2.10(3)	1.22
	2^+	8.4(3)	1.74
	4^+	1.4(3)	0.088
	2^-	2.4(2)	0.13
	3^-	0.07(1)	0.015
α	$5/2^+$ (g.s.)	0.23(2)	0.11

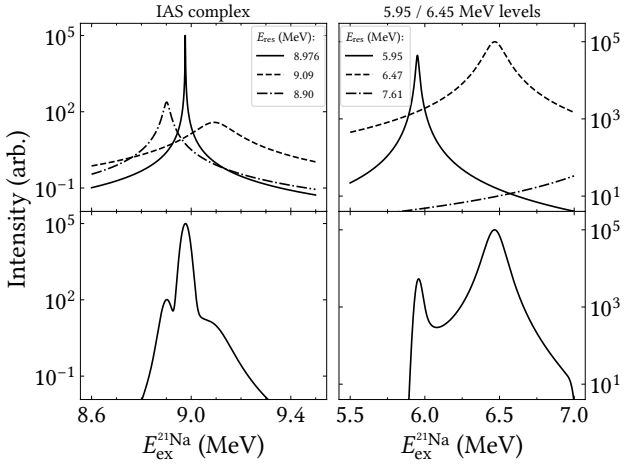

Fig. 9 Sketches of the spectral shapes against excitation energy in ^{21}Na, $E_{ex}^{^{21}Na}$, of the IAS complex (left panels) and the 5.95 MeV and 6.45 MeV levels (right panels) for the non-interferring resonances of resonance energies E_{res} (top panels) and the interferring (bottom panels) cases.

plex to the 2^+ state. We follow [2] and quote also the penetrabilities for the different channels, but do not see any obvious pattern in the results.

There are at least two more $5/2^+$ levels that according to literature [1] lie closer than one halfwidth to the IAS, so one must expect pronounced interference effects. We note further the remark in [22] that it was not possible to make a unique phase-shift analysis of the $T = 1/2$ states in the region and therefore may not be able to trust the previous positions of the other $5/2^+$ levels. However, it is clear that several $5/2^+$ levels occur in close vicinity to the IAS. A complete elucidation would require fitting with the multi-level, multi-channel R-matrix theory as outlined e.g. in [23]. Our statistics for the excited state channels do not allow a detailed investigation to be carried out, but we can illustrate the effects in a simple one-channel model. (Technically, the energy dependence of the penetrability and shift factor will be neglected.)

Figure 9 shows in the left hand side the results for the IAS complex for the case without and with interference, respectively, where the literature widths (see table 1) are used. The IAS is so narrow that any interference effects will be very close to its position, and the interference dip is here placed at its lower side, in accordance with the pattern observed in [4]. The other two levels have to interfere constructively between their positions and destructively outside in order that the outer edges of the IAS complex become as sharply defined as seen expetimentally. To reproduce the observation that the lower edge is sharpest, we have put the widest level above the IAS, opposite to the literature. In the simulations, the IAS is at 8.976 MeV, the 23 keV wide level at 8.90 MeV and the 138 keV wide level at 9.09 MeV. The strengths are adjusted to roughly correspond to the ground state IAS complex.

The second example to the right in figure 9 is concerned with the 6.45 MeV level and the 5.95 MeV level. Constructive interference between these two levels can naturally explain the asymmetric shape of the 6.45 MeV level, leading to the conclusion that their spins are the same. Note also that the upper edge of the 6.45 MeV level is decreasing rapidly (more than an order of magnitude before 7 MeV) which must be due to destructive interference in this region with decays through the 7.49 MeV level, an effect also included in the figure. Interference should be visible several other places in our spectra, such as for the two $3/2^+$ levels at 8.31 and 8.42 MeV. The non-observation of interference effects can also be significant, so the tentative 5.15 MeV level is most likely of a different spin than the 5.02 MeV level.

4 Discussion

We observe that 41(2)% of the proton decays go to excited states in ^{20}Ne. Out of this roughly 2% and 4% of the protons go to the 4^+ and 2^- states with the rest proceeding directly to the 2^+ state, this is in reasonable agreement with the intensity ratios derived from the gamma spectrum. A reason for the high feeding to the 2^+ state must be the penetrabilities that as discussed above in connection with figure 8 favour transitions to it. It is well established that ^{20}Ne is deformed and that the mentioned states belong to the two lowest rotational bands in the nucleus.

We reinterpret peak p_7 in [4] as proceeding to the ground state in ^{20}Ne. The derived excitation energy is then 3859(10) keV in perfect agreement with the position of the $5/2^-$ level at 3862.2(5) keV. Its observed intensity is 0.66(3)% of all proton decays. This first-forbidden branch has earlier been observed in the mirror decay of ^{21}F [24].

We were not able to measure the feeding to the ^{21}Na ground state and therefore cannot put the branching

Table 3 Branching ratios, b, and $\log(ft)$ values for the lowest ^{21}Mg transitions ordered by increasing energy, and compared to the mirror ^{21}F transitions. $\Delta = \log(ft)_+ - \log(ft)_-$ is also listed for the different levels. In order to test the sensitivity to the ground state branching, two $\log(ft)_+$ values of the $3/2^+$ ground state are employed: In one case, the $\log(ft)_+$ value is taken to be the same as for the mirror decay of ^{21}F, 5.67, and, in the other case, it is taken to be one unit larger, 6.67. This, in turn, corresponds to branching ratios of 6.1 % and 0.6 % to which the remaining levels' branching ratios and $\log(ft)_+$ values are adjusted. See the text for further details.

level	b (%)	$\log(ft)_+$	$\log(ft)_-$	Δ
$3/2^+$	6.1/0.6	5.67/6.67	5.67(16)	0/−1
$5/2^+$	49.5/52.5	4.71/4.68	4.65(1)	0.06/0.03
$7/2^+$	22.7/24.0	4.78/4.76	4.72(3)	0.06/0.04
proton	21.7/22.9	n.a.		
$5/2^+$	0.33/0.34	6.21(6)	7.11(5)	−0.90
$5/2^-$	0.14/0.15	6.49(3)	6.85(4)	−0.36
$5/2^+$	3.57/3.78	4.99/4.97	5.02(3)	−0.03/−0.05
$3/2^+$	5.03/5.32	4.80/4.77	4.5(3)	0.3/0.3

ratios on an experimentally founded absolute scale. To show the sensitivity to the ground state branching two evaluations will be made, one where its $\log(ft)$ value is equal to that of the mirror decay of ^{21}F and one where the branching is an order of magnitude lower. All branching ratios can then be put on an absolute scale and table 3 gives the resulting branching ratios, the deduced $\log(ft)$ values along with those of the mirror decay (here taken from [1]) and the resulting difference $\Delta = \log(ft)_+ - \log(ft)_-$, as used in the recent overview [8]. For the two first unbound levels ($5/2^+$ and $5/2^-$) the uncertainty in the branching ratio from table 1 is larger than the uncertainty induced from the ground state branching. The overall uncertainty of the normalization procedure is of order 5–10 %, within that most transitions agree with the mirror transitions, except for the two weakest ones. Note that the transitions to the bound states could not be included in earlier comparisons [8].

The beta strength $\mathrm{B}_\beta = \mathrm{B}_F + (g_A/g_V)^2\mathrm{B}_{GT}$ can now be extracted from $\mathrm{B}_\beta = 6144\,\mathrm{s}/ft$. Since the f-factor can vary noticably across the broadest levels, it is safer to perform the conversion bin by bin in the proton spectrum (see [25] for further arguments why this procedure is appropriate). Adding the intensity from the bound states and the tiny contribution from the $\beta\alpha$ decays gives the total cumulative beta strength distribution shown in fig. 10. This is compared to the theoretical calculations of the Gamow-Teller strength from [19] to which a Fermi strength of 3 units is added at the position of the IAS[1]. The theoretical Gamow-Teller strength to the IAS is 0.33 and the total experimental strength of the IAS complex from 8.8 MeV to 9.3 MeV (adding all decay channels) is 3.35 units. This agreement is quite good, so there are no indications for significant spread of the Fermi strength beyond the IAS complex. The experimental and theoretical strength distributions agree well up to around 8 MeV, above this more strength is predicted than observed. This could be due to a small displacement in the position of the Gamow-Teller Giant Resonance in the calculations or to wrongly assigned strength (in particular strength attributed to ground state rather than excited state transitions) in the experiment.

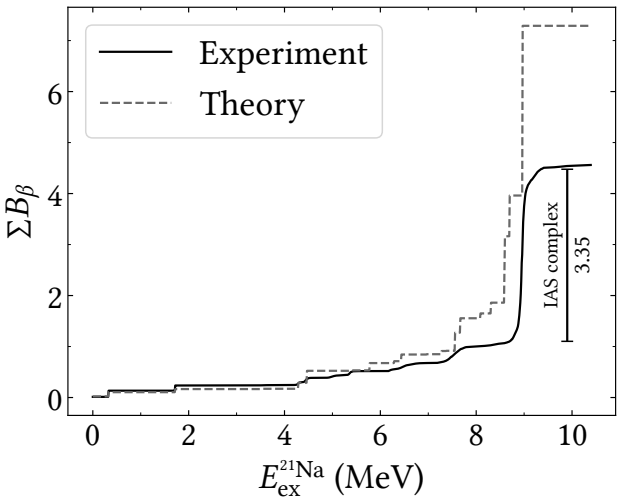

Fig. 10 Deduced cumulated beta strength $\sum B_\beta$ of the current experiment as a function of excitation energy in ^{21}Na, $E_{\mathrm{ex}}^{^{21}\mathrm{Na}}$. The experimental result is compared to theory: A Fermi strength of 3 units is added to the theoretical Gamow-Teller strength from [19] at the position of the IAS (8.976 MeV).

5 Conclusion

The experiment has improved significantly on our knowledge of the decay scheme of ^{21}Mg. Beta-delayed proton emission to excited states in ^{20}Ne was confirmed to be an important decay route through explicit gamma-proton coincidences, but the fact that these decays amount to around 40% of the total particle emission masks proton transitions to the ground state in several energy regions. A further characteristic of the decay is that several levels in ^{21}Na with width more than 100 keV are populated. This leads in several cases to clear interference effects that helps in assigning spin-parity to the

[1]The theoretical calculations in [19] are based on complete $(0d_{5/2}, 1s_{1/2}, 0d_{3/2})$-space shell model calculations utilising shell model wave functions from [26] with an isospin-conserving Hamiltonian containing one- and two-body interactions.

levels. (Some earlier experiments wrongly interpreted the broad levels in terms of several narrow proton lines.) A detailed fitting of these effects was hampered by the low statistics in the gamma-gated spectra. The earlier observed βpα branch was confirmed and a precise half-life value was extracted.

The ground state transition could not be extracted due to the presence of directly produced ^{21}Na in our beam. To further progress on the decay scheme, it would be very valuable to get experimental values for this transition. It would e.g. allow a more precise comparison to the mirror decay of ^{21}F to be made.

Much of the interpretation of the decay could be based on existing reaction experiment studies, in particular of ^{20}Ne+p scattering. However, there is a lack of information on (p,p') reactions that could be useful for exploring our observation that proton emission to the 2^+ state in ^{20}Ne in many cases are favoured to emission to the ground state. We note finally that it would be interesting to test our tentative assignment of a new 10.70 MeV level as having T=3/2, as well as our tentative assignments of several new $7/2^+$ levels.

Acknowledgements We acknowledge the support of the ISOLDE Collaboration and technical teams. We acknowledge the support of the IDS Collaboration. We acknowledge funding from the Independent Research Fund Denmark, project numbers 9040-00076B and 2032-00066B. We acknowledge funding from the Romanian IFA grant CERN/ISOLDE and Nucleu project No. PN 23 21 01 02. This work was also supported by the United Kingdom Science and Technology Facilities Council through the grant numbers ST/P004598/1 and ST/V001027/1.

References

1. R.B. Firestone, Nuclear Data Sheets **127**, 1 (2015)
2. R. G. Sextro, R. A. Gough, J. Cerny, Phys. Rev. C **8**, 258 (1973)
3. J. C. Thomas, PhD thesis, University of Bordeaux (2003), unpublished.
4. M. V. Lund et al., Eur. Phys. J. A **51**: 113 (2015)
5. M. V. Lund et al., Phys. Lett. B **750**, 356 (2015)
6. Y.-T. Wang et al., Eur. Phys. J. A **54**: 107 (2018)
7. P. Ruotsalainen, private communication to H.O.U. Fynbo (2020)
8. K. Riisager, Eur. Phys. J. A 59: 35 (2023)
9. M. V. Lund et al., Eur. Phys. J. A **52**, 304 (2016)
10. R. Catherall et al., J. Phys. G **44**, 094002 (2017)
11. H. Fynbo et al., J. Phys. G **44**, 044005 (2017)
12. O. Tengblad et al., Nucl. Instrum. Methods Phys. Res. A **525**, 458 (2004)
13. F.S. Goulding and D.A. Landis, Ann. Rev. Nucl. Sci. **25**, 167 (1975).
14. D.G. Perry and L.P. Remsberg, Nucl. Instrum. Methods **135**, 103 (1976).
15. E. A. M. Jensen et al., Nucl. Instrum. Methods Phys. Res. A **1055**, 168531 (2023)
16. S. Baker, R.D. Cousins, Nucl. Instrum. Methods. Phys. Res. **221**, 437 (1984)
17. F.G. Kondev et al., Chinese Phys. C **45**, 030001 (2021)
18. S.T. Nielsen, Master thesis, Aarhus University, unpublished (2016)
19. B.A. Brown and B.H. Wildenthal, Atomic Data and Nuclear Data Tables **33**, 347 (1985)
20. M.J. Kim et al., Phys. Rev. C **104**, 014323 (2021)
21. M. Fernandez et al., Nucl. Phys. A **369**, 425 (1981)
22. J.F. Wilkerson et al., Nucl. Phys. A **549**, 223 (1992)
23. F.C. Barker and E.K. Warburton, Nucl. Phys. A **487**, 269 (1988)
24. E.K. Warburton and D.E. Alburger, Phys. Rev. C **23**, 1234 (1981)
25. K. Riisager, Nucl. Phys. A **925**, 112 (2014); ibid 298 (2014)
26. B.H. Wildenthal, Prog. Part. Nucl. Phys. **11**, 5 (1984)

Part II

FRIB

Chapter 5

FRIB in the USA

The Facility for Rare Isotope Beams (FRIB) is located at the Michigan State University's (MSU's) campus grounds in East Lansing in the State of Michigan in the United States. FRIB is a scientific user facility funded by the U.S. Department of Energy Office of Science (DOE-SC), MSU and the State of Michigan [Fac24b]. The facility is devoted to the studies of nuclear physics and its relation to the properties and fundamental interactions of rare isotopes, to nuclear astrophysics and to its impact on medicine, homeland security and industry. While FRIB is an all new state-of-the-art rare ion beam facility, its foundation is a legacy of advancements in the acceleration of charged particles and of in-flight beam developments dating back to the 1960s. While FRIB's predecessor, the National Superconducting Cyclotron Laboratory (NSCL), employed superconducting cyclotrons to provide the experimental halls of the facility with rare ion beams, the newly commissioned FRIB provides the very same experimental halls with rare ion beams produced by a superconducting linear accelerator, a superconducting "linac", which is poised to accelerate primary beams up to energies of 200 MeV/u at a beam power of 400 kW [She18]. FRIB was commissioned in January 2022 and delivered its first rare ion beam to scientific users in May 2022 [Wei+22; Cra+22].

For our beta decay studies of ^{22}Al and ^{26}P at FRIB, we are not interested in beam particles with energies of order 100 MeV/u. Rather, we prefer to implant low-energy beams of these nuclides in a thin catcher foil and detect their decay products, as per the general experimental methods outlined in chapter 2. Our MAGISOL Collaboration has many years of experience carrying out low-

energy decay experiments at ISOL facilities such as ISOLDE at CERN (part I) and IGISOL at the University of Jyväskylä in Finland. At FRIB, it is possible to bring the high-energy in-flight separated beams down to energies of order 10 keV e.g. by thermalising the beam particles in one of the two gas cells of the Gas Stopping Area. This fact enables us to transfer the experimental designs and methods, which we have developed and refined at ISOL facilities throughout the years, directly to our collaboration's very first experiment in the United States, at the in-flight Facility for Rare Isotope Beams.

In this chapter, an introduction to the Facility for Rare Isotope Beams is given, while the next chapter will describe the experimental setup which our MAGISOL Collaboration[1] shipped to FRIB in order to carry out the experiment. In the sections that follow in this chapter, we first give an overview of the layout of FRIB, introducing some central concepts of the equipment as they become relevant. Then, we summarise the working conditions at FRIB during the experiment on ^{22}Al and ^{26}P, and we present a selection of beam diagnostics carried out by the ARIS and Gas Stopping Groups at FRIB while the beams were making their way to our setup.

5.1 Layout of FRIB

The layout of FRIB is illustrated in figure 5.1, where the beam path relevant to the experiment on ^{22}Al and ^{26}P is highlighted. From the Front End, beams of stable ions are accelerated up to a maximum of 200 MeV/u via the paperclip-shaped linac, consisting of 3 linac segments and two folding segments, as indicated in the schematic. The high-energy stable beam is then delivered from the Beam Delivery System to the Production Target Systems; here, the beam impinges on a relatively thin fragmentation target, causing the beam particles to undergo projectile fragmentation and projectile fission [MS04]. Out of the fragmentation target comes a "cocktail beam" of a multitude of beam particles – all of nearly the same energy as the primary beam energy – with nucleon numbers from 1 up to that of the stable beam projectiles: Virtually all (bound system) combinations of neutrons and protons within this mass region are pos-

[1] With me as *primus motor*.

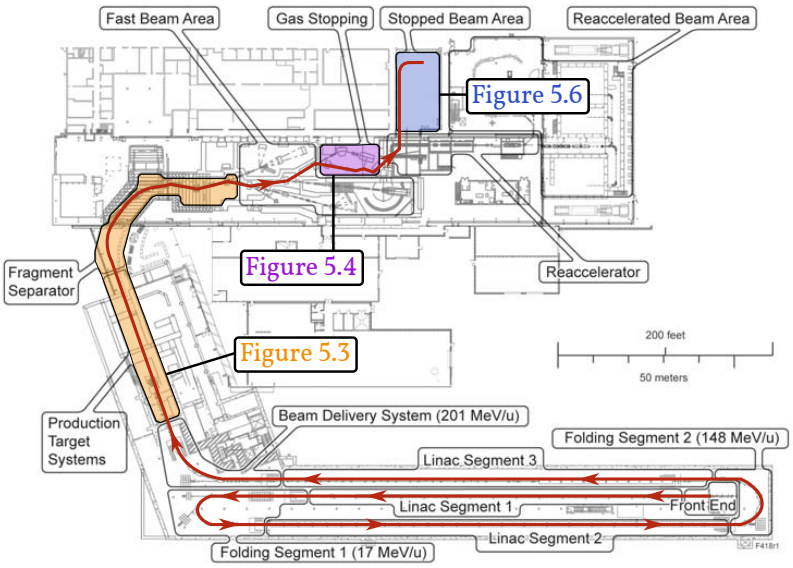

Figure 5.1: Layout of the Facility for Rare Isotope Beams. Some elements of the facility are shown in more detail in the indicated figures. Schematic adapted from [Wei+12].

sible, although the production cross sections are maximal for fragments of masses somewhat less than those of the stable beam projectiles; and from this given plateau in cross section magnitudes, the cross sections then decrease exponentially with mass. In the subsequent Fragment Separator, the rare ion beam particle(s) of interest to a given experiment are separated out of the cocktail beam, and they are then directed to the experimental setup that requires them.

We will return to the remainder of the beam path after a short diversion on the Fragment Separator. The two main tools of the Fragment Separator at FRIB are momentum-to-charge selection and isotonic separation. Momentum-to-charge selection is achieved utilising dipole magnets of rigidity

$$BR = \frac{p}{q} \tag{5.1}$$

with B the magnetic field strength of the dipole magnet, R its bending radius, and p the relativistic momentum of a given charged particle of charge q travelling perpendicularly to the magnetic field of the dipole. As the particles emerging from the production target have nearly the same velocities, the momentum-to-charge selection, p/q, can equally be described as mass-to-charge selection,

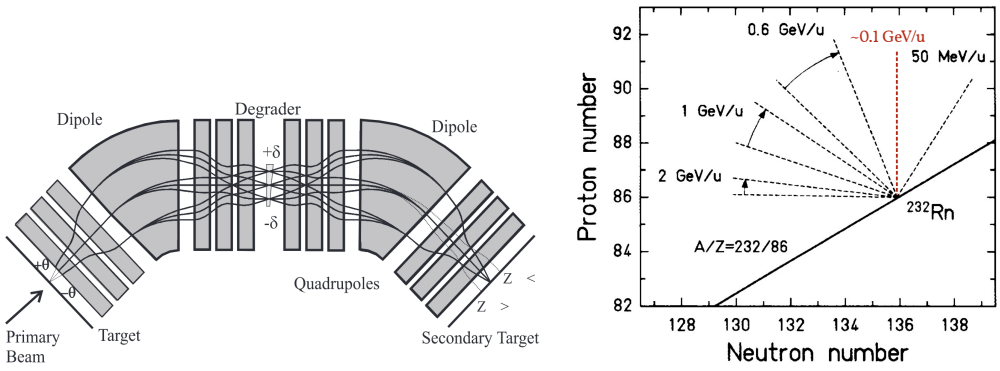

Figure 5.2: Beam optics in dipole-wedge-dipole fragment separation. **Left:** Envelope of cocktail beam as it emerges from a production target and undergoes mass-to-charge selection in a dipole magnet, followed by stopping in a *monokinetic degrader* (commonly referred to as a "wedge"), before the beam again undergoes mass-to-charge selection. The wedge has some minimum thickness t (not indicated) plus an additional thickness from bottom to top of $[0, 2\delta]$. **Right:** Illustration of the effects of the first dipole magnet followed by the wedge on the selection of nuclides. The solid line represents a given mass-to-charge selection, performed by the dipole magnet, and the dashed lines represent the selectivity of the employed wedge for various beam energies. For the beam energies around 100 MeV/u, which we employ, the effect of the wedge is that of isotonic selection. Figures adapted from [MS04; Sch+87].

m/q. Isotonic separation is achieved by employing *monokinetic degraders*, also commonly referred to as "wedges". The working principle of degraders in relation to beam optics is illustrated in figure 5.2. A degrader is simply a piece of material of some thickness which is inserted in the beam path in order to lower the energies of the beam particles (at the cost of dispersion of the beam). Because the energy losses through the degrader experienced by the beam particles of equal mass-to-charge ratios, m/q, will vary approximately as $-\mathrm{d}E/\mathrm{d}x = z^2/v^2$ (equation (2.1)), the corresponding losses in momenta will vary approximately as $-\mathrm{d}p/\mathrm{d}x = z^2/v^3$ (here, $q = z$). Hence, a variation in the *momentum-to-charge* ratios has been introduced, and the subsequent dipole magnet can carry out a momentum-to-charge selection on the degraded beam particles. As is highlighted in figure 5.2 a momentum-to-charge selection on degraded beam particles of energies around 100 MeV/u correspond to isotonic selection. The reason for using a monokinetic degrader, i.e. a wedge, where the degrader thickness varies, as depicted in figure 5.2, is to reduce the dispersion of beam particles emerging from the degrader: For two specific ions in the beam which

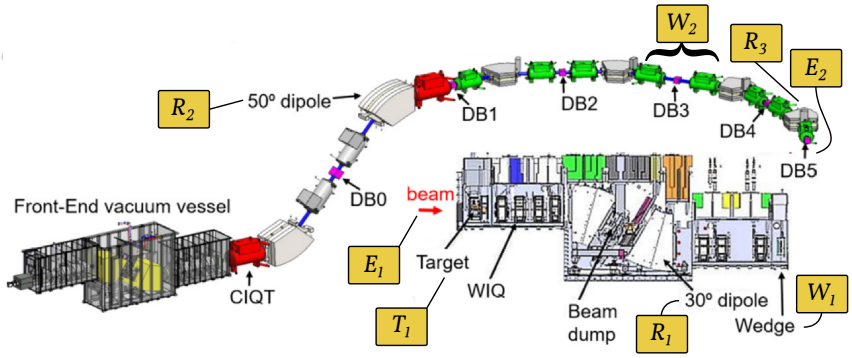

Figure 5.3: Technical drawing of the Advanced Rare Isotope Separator (ARIS) at FRIB. The labels with yellow background indicate operating conditions during the experiment on ^{22}Al and ^{26}P which are summarised in table 5.1. Drawing adapted from [Por+23].

are completely identical except that one is of higher energy than the other, the ion of higher energy travels a longer distance through the wedge compared to the other. The resulting energies of the two ions, as they emerge from the degrader, are approximately equal – this applies to all ions in the cocktail beam.

A technical drawing of the Advanced Rare Isotope Separator (ARIS) at FRIB is shown in figure 5.3. In the figure, a more detailed view of the beam's path through the Production Target Systems and the Fragment Separator of figure 5.1 is shown. The beam is fragment separated in various dipole magnets and wedges. The labels with yellow background indicate operating conditions during the experiment on ^{22}Al and ^{26}P, which are summarised in table 5.1. As the beam emerges from the Fragment Separator at "DB5" ("DB" is short for "Diagnostic Box") in figure 5.3, a fraction of all the ions produced at the fragmentation target remain. Next, in the case of our experiment, the beam from ARIS is bound for the Gas Stopping Area at FRIB.

A schematic of the Gas Stopping Area is shown in figure 5.4. In our experiment, the beam is guided towards the Advanced Cryogenic Gas Stopper (ACGS) of the Gas Stopping Area. On its path to the ACGS, the beam first passes through a degrader, a wedge and yet another degrader. The thicknesses and angles of these components are chosen such that the beam particles of interest are slowed down to speeds which preferentially favour their passing of the gas cell and such that the beam optical dispersion is mathced upon entry of the gas

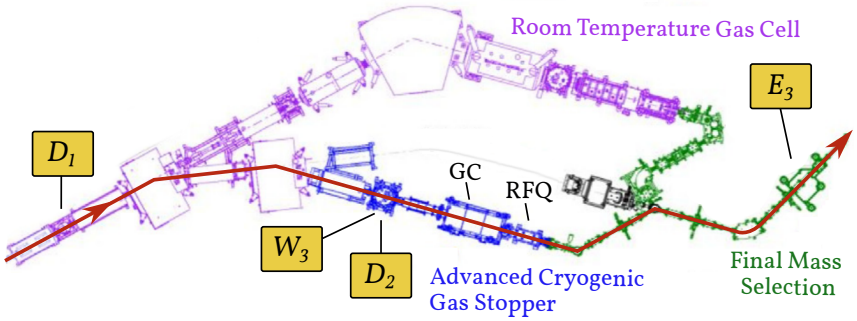

Figure 5.4: Schematic of the Gas Stopping Area at FRIB. The labels with yellow background indicate operating conditions during the experiment on ^{22}Al and ^{26}P which are summarised in table 5.1. The label "GC" is short for "Gas Cell", and the label "RFQ" is short for "Radio Frequency Quadrupole". Schematic adapted from [Vil+23].

cell.

A photo of the Advanced Cryogenic Gas Stopper is shown in figure 5.5. The Gas Cell is, in itself, 1.4 metres long. In the gas cell is a helium gas at a temperature of 50 K and a pressure of 40 mbar [Lun+20]. As beam particles impinge on the helium atoms of the gas, the beam particles lose roughly 40 eV per ionised helium atom. A naïve estimate (which is not too far from the truth [Lun+20]) is, then, that a couple of million such ionisations per atomic mass unit are necessary in order to stop the incoming beam particles of energies around 100 MeV/u. The low temperature of the gas reduces molecular recombination, and the combined gas flow as well as DC and RF electric fields in the gas cell are devised such that the beam particles tend towards the other end of the gas cell, while the ionised helium is neutralised in a "wire carpet" at the center of the cell. Under optimal conditions, the beam particles are completely stopped in the gas cell and are then guided, from the end of the gas cell, to a subsequent Radio Frequency Quadrupole ion guide, which finally leads the beam particles to an acceleration column in which the beam particles are re-accelerated to 30 keV. A low-energy beam of quality comparable to that which can be achieved e.g. at ISOLDE (part I) has thus been produced, not at an ISOL facility, but at an in-flight facility.

The low-energy, high-quality beam is then guided from the Gas Stopping

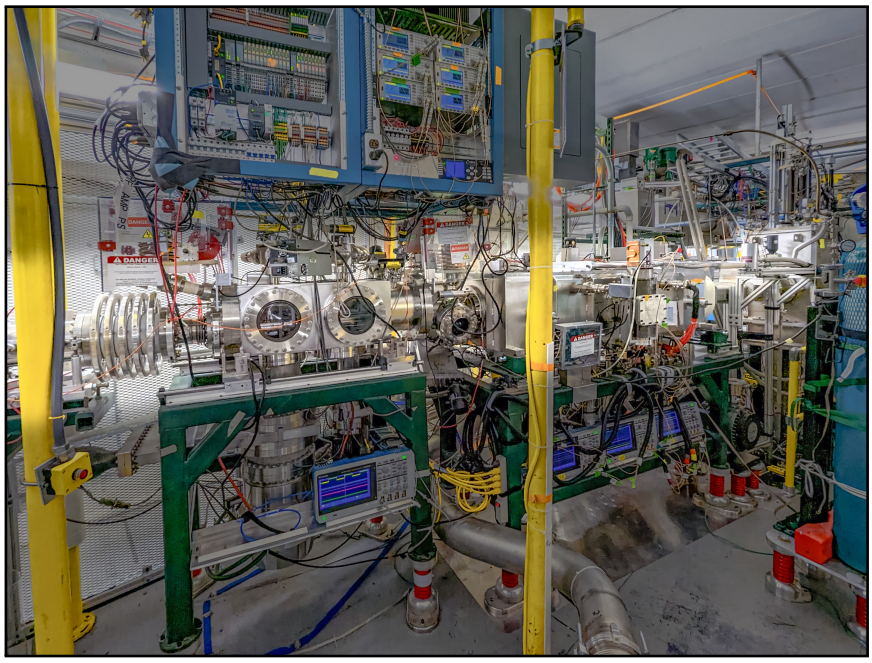

Figure 5.5: Advanced Gryogenic Gas Stopper (ACGS) at FRIB. The beam enters the gas cell at the right side of the photo and exits through the acceleration column on the left. Photo courtesy of Chandana Sumithrarachchi.

Area at FRIB to the Stopped Beam Area, subject to a final mass-to-charge selection in a dipole magnet before it reaches our experimental setup. The layout of the Stopped Beam Area at FRIB is depicted in figure 5.6, where a photo of our experimental setup is also shown. A description of our experimental setup is given in the next chapter.

In the following section, we present the working conditions at the Facility for Rare Isotope Beams during the experiment on ^{22}Al and ^{26}P, and we also present some of the beam diagnostics recorded at the facility along the paths of the beam particles.

5.2 Working conditions during the experiment

The working conditions during the experiment on ^{22}Al and ^{26}P at FRIB are summarised in table 5.1. The labels in the table refer to those indicated in figures 5.3-5.4. The primary beam and production target were the same throughout the experiment; a primary beam of ^{36}Ar of energy 210 MeV/u at a beam

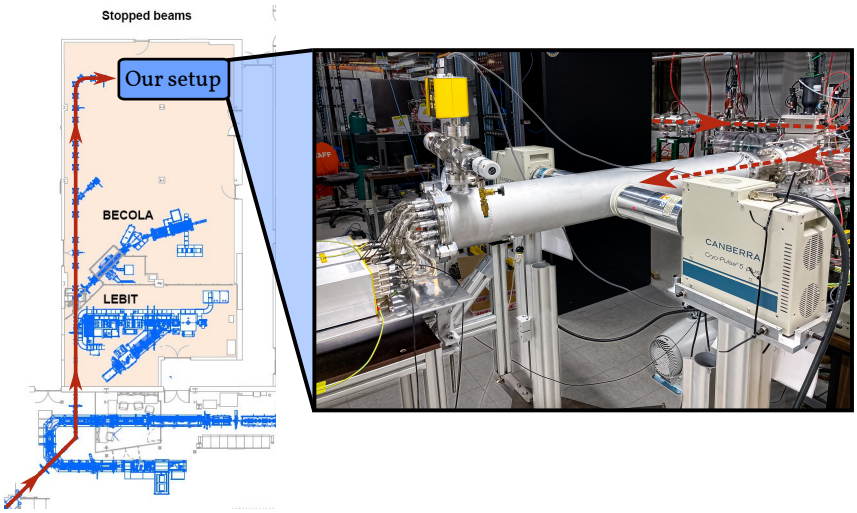

Figure 5.6: Stopped Beam Area at FRIB. Our experimental setup is attached to the General Purpose Line (GPL) at the point where the rightmost arrowhead in the photo is drawn. The experimental setup shared space with the Beam Cooler and Laser Spectroscopy (BECOLA) setup during the experiment. Schematic on the left adapted from [Fac24a].

power of 5 kW impinged on a 8.07 mm thick target of ^{12}C. The rigidities of the dipole magnets were the same for both beam developments, while the wedge angles and thicknesses were varied in order to preferentially select the beam particles of interest.

The combined beam diagnostics of DB3 and DB5 (figure 5.3) produced the ΔE vs. time-of-flight plots seen in figure 5.7. These plots illustrate the contents of the secondary beams delivered from ARIS after beam development on ^{22}Al (the left panel in the figure) and after beam development on ^{26}P (the right panel in the figure). The secondary beam delivered from ARIS contained, for the case of ^{22}Al, two isotonic chains:

1. From ^{17}O to ^{23}Si; including ^{21}Mg and ^{22}Al.
2. From ^{19}F to ^{23}Al.

while, for the case of ^{26}P, the secondary beam contained just one isotonic chain:

1. From ^{22}Na to ^{27}S; including ^{25}Si and ^{26}P.

The presence of a neighbouring, unwanted, heavier isotonic chain in the first of the two beam developments is a potential contamination of the beam particles

	^{22}Al	^{26}P
E_1	210 MeV/u ^{36}Ar at 5 kW	210 MeV/u ^{36}Ar at 5 kW
T_1	8.07 mm ^{12}C	8.07 mm ^{12}C
R_1	3.1172 Tm	3.1172 Tm
W_1	-9.531 mrad; 2.271 mm	-8.124 mrad; 2.294 mm
R_2	2.8725 Tm	2.8725 Tm
W_2	4.574 mrad; 2.217 mm	3.762 mrad; 1.849 mm
R_3	2.5827 Tm	2.5827 Tm
E_2	106 MeV/u; 2 isotonic chains	106 MeV/u; 1 isotonic chain
D_1	3.168 mm	2.327 mm
W_3	2.61 mrad; 1004 µm	3.06 mrad; 1004 µm
D_2	$1.000\,\text{mm}/\cos(23^\circ) = 1.086\,\text{mm}$	$1.000\,\text{mm}/\cos(34^\circ) = 1.206\,\text{mm}$
E_3	30 keV ^{21}Mg$^+$, ^{22}Al$^+$	30 keV ^{25}SiO$_2^+$, ^{26}PO$^+$(^{25}SiOH$^+$)

Table 5.1: Sets of working conditions during FRIB experiment. The two sets of working conditions during the experiment were those developed for the study of ^{22}Al (first column) and those for the study of ^{26}P (second column). The parameters given in each row are those of figures 5.3-5.4. "E" is short for "energy", "T" is short for target, "R" is short for "rigidity", "W" is short for "wedge", and "D" is short for degrader. All wedges and degraders are made of aluminium. For the wedges, the tabulated angles are the opening angles at the short end of the wedge in question, and the tabulated lengths are through the middle of the wedge (see figure 5.2).

of interest. For instance, ^{22}Al, which is part of the lighter of the two isotonic chains, beta decays to ^{22}Mg, which is part of the heavier of the two isotonic chains. If the beam delivered to our experimental setup e.g. contains a mixture of ^{22}Al and ^{22}Mg, then the particle spectra we observe are not only those characteristic of the decay of ^{22}Al, which is what we are interested in, but also those characteristic of the decay of ^{22}Mg alone. In the analyses of the experimental data we ought to look for indications of contaminated beams.

As mentioned in the previous section, the paths through the degraders and wedges just before the gas cell are chosen such that the beam particles of interest are exactly stopped in the gas cell. In practice, coarse beam stopping is accomplished with the first degrader, D_1 in table 5.1, and fine-tuning of the

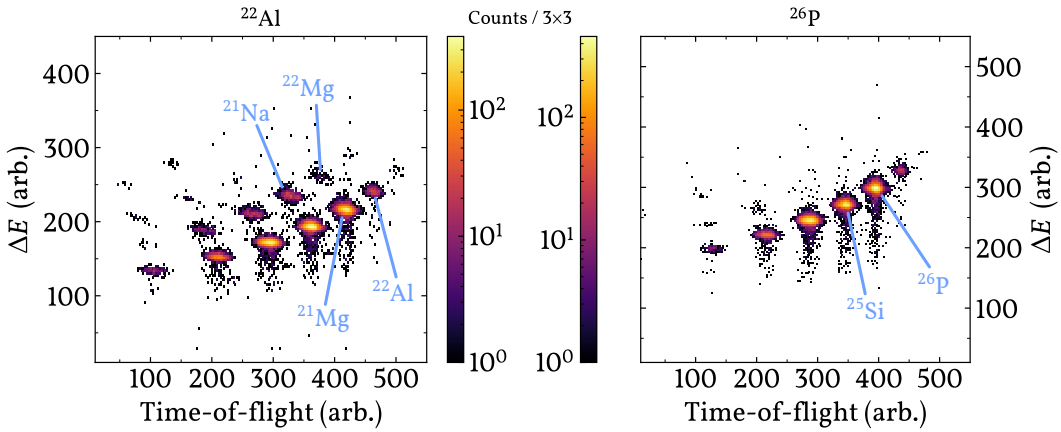

Figure 5.7: ΔE vs. time-of-flight of rare ion beam delivered from ARIS. The left panel illustrates the various beam contents delivered to the gas cell during development of the beam of ^{22}Al, and the right panel illustrates the corresponding contents for ^{26}P. Data in figures courtesy of Chandana Sumithrarachchi from the Gas Stopping Group.

beam stopping is accomplished by varying the angle of incidence θ between the beam and the normal to the surface of the second degrader, D_2 in table 5.1. The results of these *angle scans* are shown in figure 5.8. Variations of θ were carried out as the beams of ^{22}Al and ^{26}P were developed in the gas cell, and the resulting beta activity in a detector just after the gas cell was monitored – these are the black data points of the figure. Near the "Bragg peak" [Lun+20] in the variation of degrader angle, the variation in gas cell ionisation (measured on push plates at the edges of the gas cell) shows a characteristic dip, as does the observed current in a Faraday cup placed just after the gas cell. The two red curves in the figure show the variation of these two currents when θ is varied. These currents are of order nA, while the radioactive ions of interest contribute currents of order less than fA; the changes in these currents are, in other words, characteristic of the response of the entire system of the gas cell to the optimal stopping of the radioactive ions of interest.

Following the gas cell, the final mass-to-charge selection is to be carried out, and the radioactive beam of interest is then sent to our experimental setup in the Stopped Beam Area. In order to carry out the correct mass-to-charge selection, beam development in the gas cell was first carried out on radioactive beams of higher yields (but similar chemistry), before the switch was made to

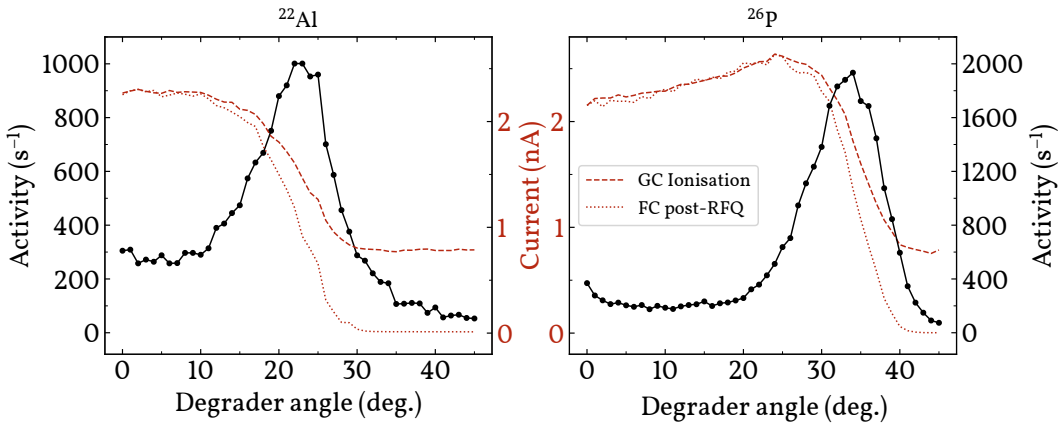

Figure 5.8: Angle scans of degrader just before gas cell. The angle of incidence between incoming beam and normal to the surface of a degrader is varied, thus varying the effective distance travelled through the degrader by the beam particles. The left panel shows the angle scan for the development of the beam of ^{22}Al, and the right panel shows the angle scan for the development of the beam of ^{26}P. "GC" is short for "Gas Cell", and "FC" is short for "Faraday Cup". Data in figures courtesy of Chandana Sumithrarachchi from the Gas Stopping Group.

the beams of ^{22}Al and ^{26}P, of interest to the experiment. Following the development of these beams of higher yield, *mass-to-charge scans* (or, simply, mass scans) were carried out just after the gas cell. The results of this are shown in figure 5.9. Even though the helium gas employed in the Gas Stopping Area is more than 99 % pure, small impurities e.g. of hydrogen and oxygen present in the gas cell will, in some fraction, bind to the radioactive beam particles leaving the gas cell, thus forming radioactive beam molecules. The chemical properties of the beam particles, as well as the impurity concentration, determines the fraction of beam molecules leaving the gas cell as compared to the *atomic* beam particles. Analyses of the mass scans shown in figure 5.9 have been carried out by the Gas Stopping Group, identifying beam particles as well as beam molecules. The analyses of the mass scans are not yet fully complete, but nuclides of interest to our experiment are highlighted in the figure. For the mass scan relevant to the measurements on ^{22}Al, a developed ^{24}Al beam was employed, and for the mass scan relevant to the measurements on ^{26}P, a developed ^{28}P beam was employed. In order to obtain sufficient points of reference in the mass scan on ^{24}Al, an offset voltage was applied between the gas cell and the

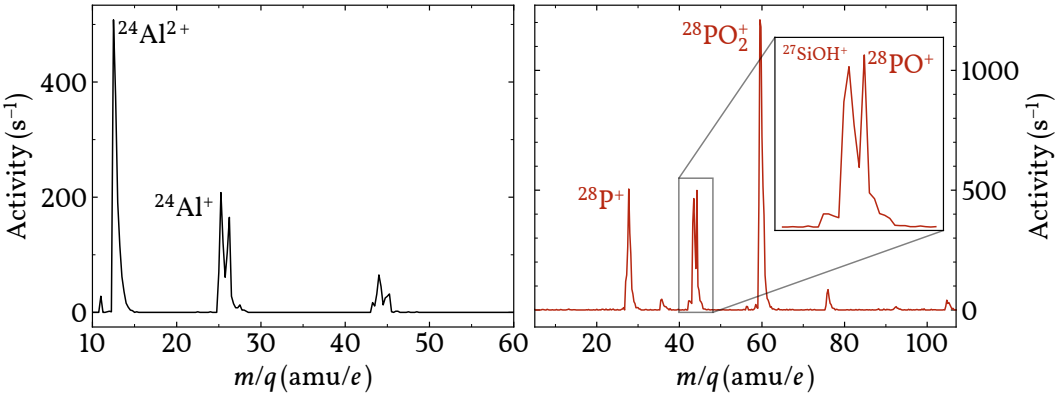

Figure 5.9: Mass-to-charge scans after gas cell. The magnetic field strength in the dipole magnet following the gas cell is varied (the bending radius R is fixed, equation (5.1)), and the beta activity in a detector following the magnet is monitored. The left panel shows the mass-to-charge scan for the development of the beam of ^{24}Al, and the right panel shows the masss-to-charge scan for the development of the beam of ^{28}P. Data in figures courtesy of Chandana Sumithrarachchi from the Gas Stopping Group.

RFQ. The collision-induced dissociation of the radioactive beam particles thus provoked is the explanation for the intense peak of $^{24}Al^{2+}$ at the lower end of the mass scan. The mass scan on ^{28}P reveals, on the other hand, an unfortunate coincidence of nature: The masses of $^{27}Si(O_x)H$ and $^{28}P(O_x)$ are very nearly equal; and the same is true of $^{25}Si(O_x)H$ and $^{26}P(O_x)$. The resolution of the dipole magnet following the gas cell is not sufficiently large to separate ^{25}SiH from ^{26}P and, as such, we have to expect contamination from ^{25}Si in the measurements on ^{26}P.

Based on the mass scans, the magnetic field strength was adjusted to pick beams of ^{22}Al and ^{26}P to send to our experimental setup. Beams of ^{21}Mg and ^{25}Si were also sent to our setup during the experiment. Measurements on ^{21}Mg were performed early in the experiment for energy calibration purposes, while some improvements on the yield of ^{22}Al were yet to be carried out. During the latter part of the experiment, when a sufficient amount of data had been recorded on ^{26}P, dedicated measurements on the contaminant ^{25}Si were also carried out, in order to characterise the contamination of the ^{26}P data. The concern of contamination from ^{25}Si was brought up well in advance by the Gas Stopping Group and, when the beam of ^{26}P had been prepared, measurements were

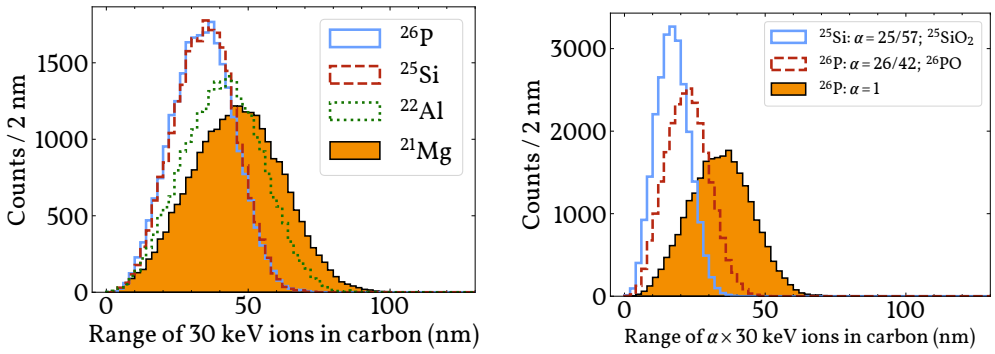

Figure 5.10: Ranges of low-energy ions with initial kinetic energies $E_{\text{kin}} = \alpha \times 30$ keV in carbon with $\alpha \leq 1$. **Left:** The distributions from figure 2.1 are redrawn for comparison with the right part of this figure ($\alpha = 1$ for all of the shown distributions). **Right:** The range of a 30 keV beam of ^{26}P is illustrated compared to the ranges of an 18.6 keV beam of ^{26}P and a 13.1 keV beam of ^{25}Si. These latter two beam energies were effectively the beam energies of the two nuclides, as the ions $^{26}PO^{+}$ and $^{25}SiO_2^{+}$ were mass-selected just after the gas cell and then sent to our setup. When the ionised molecules impinge on our carbon foil, the molecular binding energy of, at most, a couple of eV [WA82, pages F180-200] is broken, and the atoms advance into the foil with reduced kinetic energies given by their mass fractions. As in figure 2.1, TRIM has been used to generate the distributions.

carried out with our experimental setup on the masses 26, 42 and 58 corresponding to beams of ^{26}P, ^{26}PO and $^{26}PO_2$. Based on these measurements, it was decided to stick with the beam of ^{26}PO, the argument being that this beam seemed to be more pure than the two other options. Finally, when the dedicated measurement on ^{25}Si was later carried out, a molecular beam of $^{25}SiO_2$ was employed.

All radioactive beams were delivered to our setup with 30 keV kinetic energy. The ranges of 30 keV beams of ^{21}Mg, ^{22}Al, ^{25}Si and ^{26}P in carbon were illustrated in figure 2.1, but, effectively, the beams of ^{25}Si and ^{26}P delivered to our experimental setup had kinetic energies less than 30 keV, given by the mass fractions of the relevant beam molecule. The ranges of the beam particles of reduced kinetic energies in carbon are illustrated in figure 5.10. The reduced ranges of ^{25}Si and ^{26}P are to be taken into account in the data analyses.

Chapter 6

Experimental setup at FRIB

The experimental setup shipped to FRIB from Århus in Denmark by our MAGISOL Collaboration was designed with the experimental ideas presented in chapter 2 in mind; the same ideas as those utilised in the experiment on ^{21}Mg at ISOLDE, presented in chapter 4. For the experiment at FRIB, a new chamber was designed by our collaboration. The aim of the design was to maximise the solid angle coverage of the germanium detectors of the Segmented Germanium Array (SeGA) at FRIB [Mue+01]. SeGA was to be used for the detection of gamma rays in conjunction with the detection of charged particles provided by our own silicon detectors. The chamber design is a long, hollow aluminium tube, which can be slid into the so-called β-SeGA configuration of SeGA, where the detectors of SeGA will surround the aluminium tube with a distance of a few millimetres between the detectors and the tube. The inner diameter of the tube is only just large enough to fit a detector holder for our silicon detectors and their necessary cabling, and the thickness of the aluminium wall of the tube is kept as small as mechanically feasible in order to minimise the attenuation of gamma rays leaving the chamber.

As it turned out, our experiment was not carried out utilising SeGA. When the opportunity to carry out our experiment finally presented itself after the series of delays and cancellations mentioned at the beginning of chapter 4, SeGA was being refurbished. Instead, Christopher (Chris) Wrede's research group at FRIB very helpfully provided us with their newly acquired germanium detectors for the duration of the experiment. Thus, SeGA was replaced by the germanium detectors to be used in Chris Wrede's group for a setup employing the

Particle X-Ray Coincidence Technique (PXCT) [Sun+22].

This chapter is structured as follows. First, the design of the vacuum chamber of our experimental setup is described, and then the detector geometry of our setup is described. Finally, the working conditions of the signal processing and of our data acquisition system are described. Chapter 7 is dedicated entirely to the calibration of our silicon detectors.

6.1 Vacuum chamber

As described in the introduction to this chapter, our vacuum chamber consists of a long tube made of aluminium. This 1.3 metre long aluminium tube was connected at the end of the General Purpose Line (GPL), as already shown in figure 5.6. The inner diameter of the tube is 155 mm and the outer diameter is 159 mm, separating the vacuum inside our vacuum chamber from the atmospheric pressure of the surrounding Stopped Beam Area by an aluminium wall of 2 mm thickness. In figure 5.6, the metal cylinders flanking the tube contain the germanium detectors mentioned in the introduction. The cables emerging from the feedthrough flange at the left end of the tube contain all silicon detector channels which are immediately fed to preamplifiers. The cross on top of the tube just before the feedthrough flange consists of pressure-monitoring equipment and a valve for ventilation of the chamber.

The photo in figure 6.1 depicts the silicon detector holder of the setup. This detector holder, a 3D-printed aluminium cube, is fixed at the end of a rod which has a length that places the cube at the center of the tube when the rod is pushed all the way in and the vacuum chamber is sealed. The rod is fixed to the feedthrough flange which in turn is fixed to a metal plate which can slide in and out of the tube via the rail which is fixed on top of the stand at the bottom of the photo. The cube has an aperture with a diameter of 12 mm on the edge of the cube facing upstream, and there is a similar aperture on the edge of the cube facing downstream. Situated between this downstream aperture of the cube and the rod, is a segmented Faraday Cup, which has been detached from the rod for closer inspection in the photo on the left in figure 6.2. This Faraday Cup was utilised early in the FRIB experiment in order to verify the transmis-

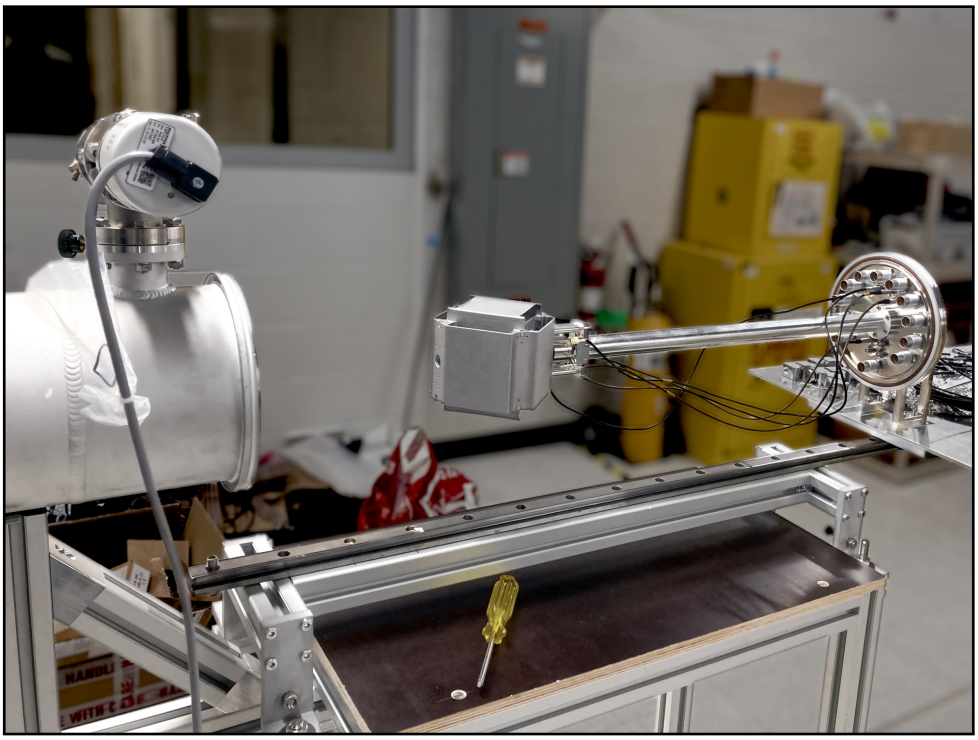

Figure 6.1: Silicon detector holder employed in the experiment at FRIB. The holder is a 3D-printed aluminium cube which is fixed to a rod and has been slid out of its vacuum chamber in this photo.

sion of stable beam from the Gas Stopping Area, through the aluminium cube and into the Faraday Cup.

Inside the rod in the photo of figure 6.1, which is actually hollow, it is possible to attach a thin rod at the end of which calibration sources can be mounted. A photo of this thin rod with an alpha emitting calibration source attached is shown on the right in figure 6.2. The rod enters the cube through the downstream aperture. From outside the vacuum chamber, on the feedthrough flange, is a knob which, when rotated, in turn rotates the thin rod with the calibration source attached. This significantly reduced the number of times the chamber had to be ventilated when reorienting the calibration sources in order to carry out the calibrations of all silicon detectors.

At the GPL, where our vacuum chamber was attached during the experiment, the pressure inside the vacuum chamber was required by the facility to be 1×10^{-6} Torr $\simeq 1 \times 10^{-6}$ mbar or lower. The initial design of the chamber had, instead of a 3D-printed aluminium silicon detector holder, a detector

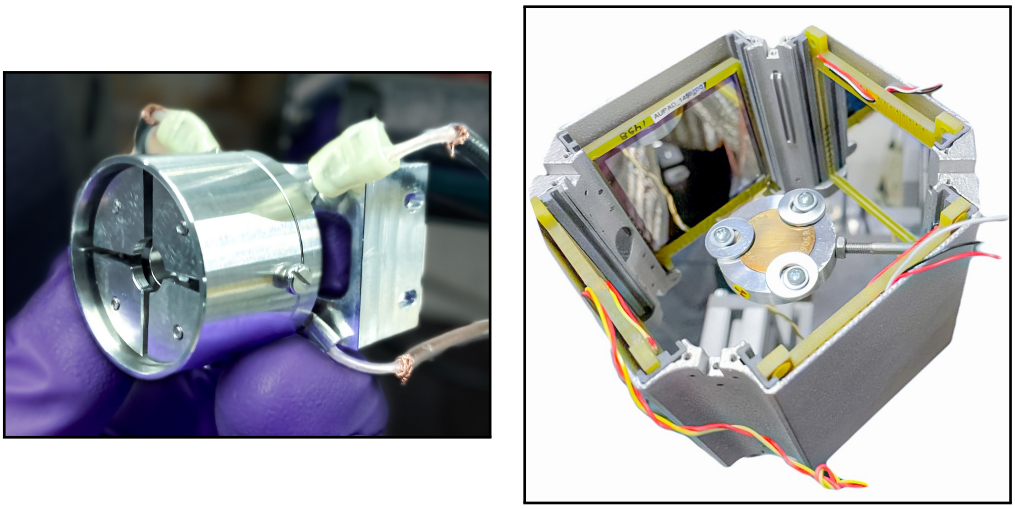

Figure 6.2: Faraday Cup and calibration source holder of the FRIB experimental setup. **Left:** A four-fold-segmented Faraday Cup used to verify the arrival of stable beam at our setup early in the experiment. **Right:** A calibration source is mounted on a thin metal rod, here, in order to calibrate the Pads of the experimental setup. The thin metal rod can be rotated from outside of the vacuum chamber, while the vacuum chamber is closed and at low pressure.

holder of similar design, but made of 3D-printed plastic. Furthermore, in order to connect the signals of the silicon detectors to the feedthroughs of the chamber, 12 ribbon cables of rather large surface areas are also to run approximately 50 cm from the cube to the feedthroughs. Initially, the insulation of the ribbon cables were also made of plastic. Plastic tends to slowly outgas under low-pressure conditions, which causes the pressure of the enclosing volume to rise, while metals and materials such as teflon do not have this issue. In preparing for the experiment at FRIB, it quickly became evident that we could not meet the low-pressure requirements at FRIB with all the plastic inside our vacuum chamber. (It should be noted that the chamber, with all of these plastic components inside, was used to carry out a successful experiment on the beta decay of ^{12}B at the IGISOL facility in Jyväskylä, Finland, in 2020.)

With the aid of the workshop and the electronics pool at the Department of Physics and Astronomy in Århus, these vacuum challenges were overcome. Revised designs of the silicon detector holder were made and sent to the Danish Technological Institute in Århus, where very recent developments had been made in the 3D-printing of metals, and there was an interest in receiving print jobs for the new 3D-printing equipment at the institute. In addition, plastic in-

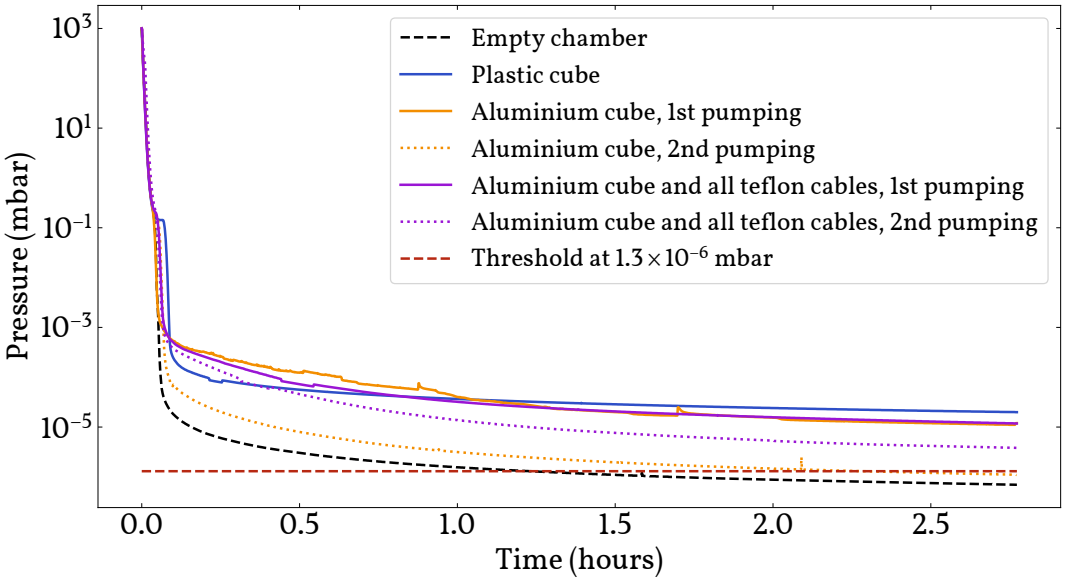

Figure 6.3: Improvements in vacuum conditions of vacuum chamber achieved by replacing plastic components in the chamber with aluminium and teflon. The variation in pressure in the vacuum chamber is shown for all test cases from the moment the roughing pump was turned on. The turbo pump was turned on when the pressure reached 1×10^{-1} mbar. "1st pumping" signifies the first time the indicated items were placed in the vacuum chamber and pumping on the chamber was carried out. "2nd pumping" signifies a ventilation of the chamber followed by a 1 minute opening of the chamber (detaching the feedthrough flange of figure 6.1) whereupon the chamber was immediately closed and pumping on the chamber was recommenced.

sulation in the cables to be placed in the vacuum chamber was replaced with teflon insulation wherever possible. Figure 6.3 shows the test results of attempting to improve the vacuum conditions of the vacuum chamber by replacing, as much as possible, the plastic inside the vacuum chamber with aluminium and teflon. After pumping on the plastic cube for 17 hours, the pressure saturated at 7×10^{-6} mbar. On the other hand, the threshold is seen to be crossed after roughly 1.5 hours, when the chamber is empty. For the remaining pressure curves of the figure, from highest-lying to lowest-lying, threshold was crossed after 2 days, 1.5 days, 11 hours and 2.5 hours. The first pumping on the aluminium cube continued for 18 days down to 2.5×10^{-7} mbar, before the chamber was briefly ventilated, and pumping on the chamber was then recommenced. Similarly, the first pumping on the aluminium cube and all te-

flon cables continued for 2 days down to 9.3×10^{-7} mbar, before the chamber was briefly ventilated and pumping on the chamber was recommenced. The vacuum tests showed improvements on the vacuum conditions by replacing the plastic cube with an aluminium cube. The tests presented here do not directly compare the effects on the pressure of plastic-insulated and teflon-insulated cables, but separate tests also showed an improvement when replacing the plastic with teflon. Another important take-away from the tests is that the good vacuum conditions which were established on the first pumpings can be partially retained, if the vacuum chamber is only ventilated briefly before pumping on the chamber recommences. The initial test pumping on the aluminium cube by itself went on for approximately 2 weeks before the threshold of 1×10^{-6} Torr was crossed; this told us that it was necessary to assemble the vacuum chamber and pump on it constantly several weeks in advance of the beam time of our experiment, if we were to cross the threshold in due time.

6.2 Detector geometry

A photo of the silicon detector holder with the top lid removed is shown in figure 6.4. In this photo, all silicon detectors have been placed in the silicon cube and a target frame (made of aluminium) has been mounted in the centre of the cube. A thin carbon foil of thickness $32\,\mu g/cm^2 / 2.253\,g/cm^3 = 142$ nm has been floated onto the target frame[1]. This carbon foil thickness was a conservative choice which ensured that beam particles of ^{21}Mg, ^{22}Al, ^{25}Si and ^{26}P with kinetic energies of 30 keV would all be stopped, on average, in (or a bit before) the centre of the carbon foil. By making this choice of thickness, virtually no beam particle will be able to penetrate the carbon foil due to range straggling (figure 5.10). The beam particles are to enter through the upstream aperture. We note that the diameter of the carbon foil is the same as that of the upstream aperture – 12 mm. In the photo in figure 6.4, each of the five inward-facing sides of the cube holds a ΔE-E silicon detector telescope. The ΔE detectors are the DSSSDs described in section 2.3, and the E detectors are

[1] TRIM uses $2.253\,g/cm^3$ as the density of carbon, but the reported densities of amorphous carbon vary between 1.8 and $2.3\,g/cm^3$ [WA82, page B-10]. A picture guide of the floating of carbon foils can be found on our group's wiki page [Jen21].

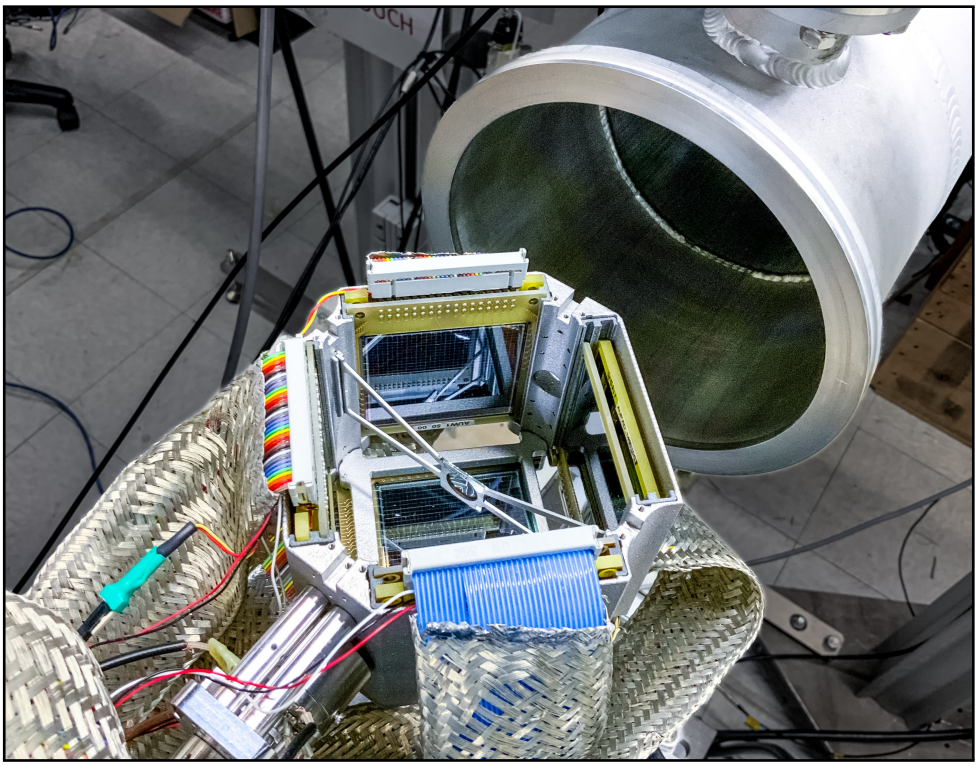

Figure 6.4: Silicon detector holder with all detectors and target frame installed. The top lid has been removed from the holder in order to take the photo.

the Pads also described in that section. The lid of the cube, which has been removed in the photo, only has a DSSSD installed due to the failing of the Pad that was otherwise to have been installed behind it.

The geometry of the silicon detectors is as follows. In the horizontal plane, the distances from the centre of the cube to the centres of the n-side surfaces of all DSSSDs is 42.5 mm, and the n-side surfaces of the backing Pads are situated 5.8 mm behind the n-side surfaces of the DSSSDs; for a 0.5 mm thick Pad, the distance from n-side surface of DSSSD to p-side surface of Pad is then 5.3 mm. These distances can be surmised from the technical drawings of the silicon detector cube included in appendix A, where the relevant dimensions of the silicon detectors are also given, including the recess depths of the printed circuit boards on which the silicon chips are mounted. The distances to the detectors in the top and bottom lids are the same as in the horizontal plane, except for the fact that the distances from the centre of the cube to the n-side surfaces of the

DSSSDs are, instead, 41.5 mm. As already mentioned in section 4.1, the solid angle coverage of each DSSSD is roughly 8.5 % of 4π (neglecting the shadow caused by the target frame in the top and bottom DSSSDs), but the solid angle coverage of each backing Pad and, hence, of each detector telescope as a whole is only roughly 7 % of 4π.

The two germanium detectors also employed in the experiment were facing the carbon foil and placed as close to it as possible just outside the chamber, as can be seen in figure 5.6. The faces of these detectors were placed roughly 5 mm from the surface of the vacuum chamber, and they were thus positioned roughly 85 mm from the centre of the silicon detector cube. The germanium detectors are Canberra[2] Extended Range (XtRa) Coaxial Germanium Detectors of model number GX10020 [Mir24]. These germanium detectors boast a thin carbon composite window and a thin-window contact, extending the useful energy range down to 3 keV. The resolution of these detectors are of order 1-2 keV FWHM or less from 122 keV to 1332 keV, while the detection efficiencies of these detectors increase with decreasing gamma energy down to roughly 100 keV, and only below 30 keV is there a significant onset of decreasing detection efficiency. Unfortunately, neither the high resolution nor the high efficiencies at low energies could be utilised during the experiment, as we had to employ our own analogue DAQ (described in the next section), which is optimised for the shaping of silicon detector signals, but is less than ideal for the shaping of germanium detector signals.

In figure 6.5 a diagram of the placement and naming of the detectors employed during the experiment is shown. In the diagram, the observer is looking down at the silicon detector holder from above. DSSSDs are labelled with prefix “U”, Pads are labelled with prefix “P” and germanium detectors are labelled with prefix “G”. The beam enters from the top of the diagram. Beneath U5 is the target frame with catcher foil, followed by U6 and followed, finally, by P6.

Relevant characteristics of the silicon and germanium detectors employed in the experiment are summarised in tables 6.1-6.2.

[2] Part of Mirion Technologies as per 2016.

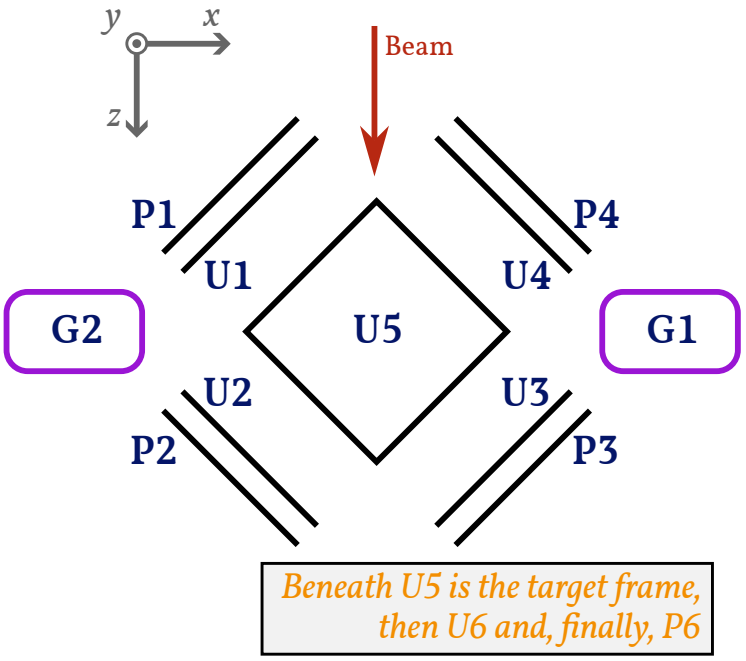

Figure 6.5: Diagram of the placement and naming of the detectors employed during the FRIB experiment. DSSSDs are labelled with prefix "U", Pads are labelled with prefix "P" and germanium detectors are labelled with prefix "G".

6.3 Signal processing and data acquisition

The signal processing and transmission pipeline of the FRIB experiment is illustrated schematically in figure 6.6. The structuring of the diagram is based on that of figure 2.5. In the majority of the analogue signal processing, we employ hardware from Mesytec GmbH [Mes23]. For the preamplification of signals from U1–U6, we employ three Mesytec MPR-64 preamplifiers; each DSSSD has 32 output channels, and each MPR-64 preamplifier has 64 input channels, so each preamplifier takes the signals of two whole DSSSDs as input. For the preamplification of signals from P1–P6, we employ five[3] Mesytec MPR-1 preamplifiers; each Pad has 1 output channel, and each MPR-1 has one input channel. The germanium detectors G1 and G2 have their own built-in preamplifiers; each detector has 1 output channel. After preamplification, the signals from each p- and n-side of each DSSSD are delivered to a corresponding 16-channel Mesytec MSCF-16 F shaping amplifier. Each shaping amplifier

[3] P5 was not functional during the experiment.

	Serial number	Thickness (µm)	Bias voltage (V)	Threshold (keV)
U1	3189-3	55	−12.2	200–300
U2	2887-4	65	−14.2	150–250
U3	3188-5	55	−20.0	150–200
U4	3102-13	296	−56.6	~100
U5	2541-7	1002	−66.0	~150
U6	2881-1	67	−14.2	~100
P1	2331-5	500	−62.2	280
P2	3143-25	500	−61.8	340
P3	3143-26	505	−61.2	180
P4	"E11"	1498	−150	350
P6	2712-11	500	−59.8	220

Table 6.1: Characteristics of silicon detectors employed during the FRIB experiment. Detectors U1-U6 and P1-P6 are those indicated in figure 6.5. The given thicknesses are the active layer thicknesses and are those stated by the manufacturer, Micron Semiconductor Ltd; for U1-U4 these are all different from what we deduce in section 7.4. Dead layer and contact thicknesses are described in section 2.3. Data sheets of the employed silicon detectors can be found on our group's wiki page [AUS24]. The listed thresholds are the low-energy limits of the detector dynamic ranges resulting from the trigger and ADC thresholds of figures B.1–B.2 shown in appendix B.

provides a trigger signal; i.e. we have one trigger signal per DSSSD side – 12 in total. The five preamplified Pad signals are all delivered to one Mesytec MSCF-16 F shaping amplifier, and the two preamplified germanium detector signals are delivered to another such shaping amplifier. Hence, we also have one separate trigger signal for the Pads and one separate trigger signal for the germanium detectors. The shaped p- and n-side signals of each DSSSD are recombined into a 32-channel Mesytec MADC-32 ADC, and the shaped Pad signals are combined into a separate MADC-32, as are the germanium detector signals. For the experiment, we had only one functional CAEN V1190A [CAE24] 128-channel TDC. The timing output signals of the n-side shapers as well the timing output signals of the Pad and Germanium shapers were delivered to the TDC during the experiment. The ADCs provide one 12-bit word for each

	G1	G2
Serial number	5593	5596
Crystal diameter (mm)	84.8	79.8
Crystal length (mm)	65.2	80.0
Carbon window thickness (mm)	0.60	0.60
Crystal distance from window (mm)	6.8	6.3
Bias voltage (V)	+4500	+4500

Table 6.2: Characteristics of germanium detectors employed during the FRIB experiment. Detectors G1 and G2 are those indicated in figure 6.5. Data sheets of the employed germanium detectors can be found on the PXCT Collaboration's wiki page [PXC24].

detector channel, yielding a dynamic range of 4096 discrete bins per detector channel. The TDC provides one 19-bit word for each detector channel with a timing resolution of 100 ps.

Each p- and n-side trigger of each DSSSD is combined into a new logical `AND` trigger between p- and n-side of the relevant DSSSD; e.g. (using the notation of figure 6.6) $pA \wedge nA \equiv A$. Throughout the experiment, whenever radioactive beam was in our chamber, data readout was triggered by a logical `OR` between all six such triggers ($A = \mathrm{U1}, \mathrm{U2}, \ldots, \mathrm{U6}$) in combination with a logical `OR` between the Pads and the Germaniums:

$$\text{trigger} = \mathrm{U1} \vee \mathrm{U2} \vee \mathrm{U3} \vee \mathrm{U4} \vee \mathrm{U5} \vee \mathrm{U6} \vee \text{Pads} \vee \text{Germaniums} \tag{6.1}$$

Combining p- and n-side triggers into the triggers $A = \mathrm{U1}, \mathrm{U2}, \ldots, \mathrm{U6}$ ensures a significant reduction in data readout due to random noise, as true events will generate signals above trigger threshold on both the p-side and the n-side (chapter 2).

The trigger thresholds of each individual detector channel (configured on the shaping amplifiers) of the FRIB experiment are illustrated graphically in figure B.1 of appendix B[4]. In the worst case, the trigger thresholds are set just

[4] In the appendix, a link to a data archive containing all the relevant configuration files of the experiment – including the configuration file containing trigger threshold values and the configuration file containing ADC threshold values, to be described briefly – is given.

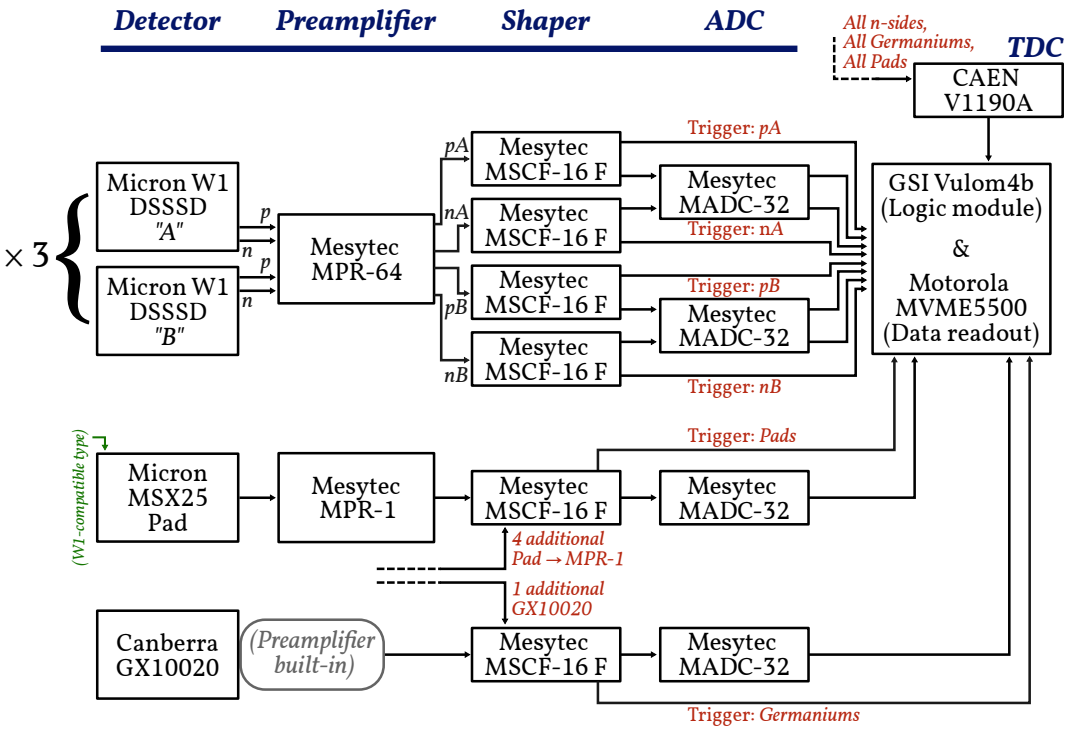

Figure 6.6: Flowchart diagram of signal processing and transmission pipeline of the FRIB experiment. The diagram is structured similarly to the more general diagram presented in figure 2.5.

below 3 % of the dynamic range of the relevant channel, and more than three quarters of the channels are set below 1.5 % of the dynamic range. As mentioned in section 2.4, the trigger thresholds are set as low as possible, but such that random electrical noise does not contribute significantly to the amount of generated triggers. The same idea applies to the *ADC thresholds* of each individual detector channel (configured on the ADCs), which are illustrated in figure B.2 of appendix B. When a trigger signals the readout of data, the signal amplitudes of all channels of all ADCs are read out, but signals with amplitude below the individual ADC thresholds are rejected. The ADC thresholds on U1 range between 3 and 5 % of the dynamic range of the relevant channels, while those of U2 range between 1 and 3 %, and those of U3-U6 range between 1 and 1.5 %. The ADC thresholds of the Pads range between 3.5 and 5 % of the dynamic range, while those of the Germaniums are set just below 3 %.

The combination of trigger thresholds and ADC thresholds defines the low-energy thresholds of the dynamic ranges of each detector channel; the res-

ults of the combination of thresholds employed in the FRIB experiment are those listed in the right-most column of table 6.1. The listed thresholds are given in keV, based on the silicon detector calibrations presented in the next chapter. For the observation, in our proton spectra, of beta-delayed proton emission from the astrophysically important 3^+ resonance at 5.93 MeV in ^{26}Si, the thresholds on our thin DSSSDs should be set comfortably below 400 keV, which is the kinetic energy of protons emitted from this state [Tho+04]. This requirement is generally met, although the thresholds on U1 and U2 are at relatively large threshold energies compared to the remaining DSSSDs. The thresholds on the Pads are set rather high, perhaps a bit too high, as a larger rate of data readout of random noise on only 5 of the 200 detector channels of the setup would probably not have over-encumbered the DAQ. High thresholds on the Pads result in wider dead and spurious zones (section 4.1) of our detector telescopes. This shall become apparent when we present the energy-dependent solid angle coverages of the detector telescopes in the next chapter.

6.3.1 Configuration management and reproducibility

The concrete performance and characteristics of the transmission pipeline and the DAQ is very much dependent on the configuration of its corresponding hardware and software. In fact, this is a vital part of the experimental setup. The concept of *configuration* in this context also includes the specific pieces of software necessary to interface with the hardware, i.e. the configuration for a given experiment comprises the configuration files of the hardware and software as well as the specifically employed software revisions. This notion of an all-comprising configuration for an activity correspond closely to the concept of *configuration management* used in the discipline of *project management*; see e.g. [Ben05] for a short introductory description.

Configuration management is defined as the ability to record and reproduce the state of a system by storing the states (i.e. configurations) of anything that is potentially variable, but necessarily also controllable. The scientific principle of reproducibility for experiments also has the requirement (or at least the ideal) of being able to record and reproduce the state of a given

experimental setup. Hence, there is good reason for applying configuration management practices to the software and hardware of the transmission pipeline and the DAQ.

Traditionally the facts about an experiment are recorded in laboratory journals and log books, which have become digital in the 21st century. These tools are not suited for storing configuration files and software, so the configuration/state of that kind is mostly not stored in an easily retrievable form, if it is stored at all. The concept of configuration management might inspire the idea of employing version control systems[5] in order to not only document the versions of software employed in experimental setups, but in order to document the software and hardware configurations, as well as the software interdependencies.

In preparing for the experiment at FRIB, I made a configuration management system (employing Git) in which all the various pieces of software necessary to run our DAQ, the software's interdependencies and all software and hardware configurations can be unambiguously recorded. The Git *super project* called "ausadaq" [Jen23a] has a tag bearing the name "e21010"[6] which is the definitive configuration of the entire experimental setup. The super project fetches 12 different Git *submodule* [Git24b] repositories, which all undergo independent developments and, hence, will inevitably diverge over time. The super project links together all repositories at definite points in time where all pieces of software have been known to work in unison, and all working software and hardware configurations used for a given experimental setup during a given experiment are also documented for these definite points in time.

The work on the "ausadaq" super project was initiated as various iterations on our DAQ software and hardware had accumulated over the years. These iterations were spread across many different devices and user accounts, small patches and hacks of the individual iterations had been made by merging configurations from one iteration to another, stale development branches were part of each individual software repository, and, overall, the configuration management of the software revisions of the DAQ was a mess, while the configur-

[5] Git [Git24a] is an example of a version control system.

[6] "e21010" is the name of the experiment on ^{22}Al and ^{26}P in the FRIB database of experiments.

ation management of the software and hardware configurations was virtually non-existent. Information on how this is all set up can be found on our group's wiki page [Jen23b]. A link to a data archive of the definitive configuration of the entire experimental setup is given in appendix B, and the same definitive configuration can be *checked out* from the "ausadaq" Git repository.

Chapter 7

Calibration of silicon detectors

In order to see how our experimental data fits into the nuclear landscape, we first need to calibrate our data: We need energy calibrations in order to put the nuclear states which our experiments populate on an absolute scale, and we need efficiency calibrations in order to put the feeding and subsequent decays of these states if not on a absolute scale, then at least on a relative scale. With our experimental equipment, we cannot calibrate our way directly e.g. to spin and parity quantum numbers, but if we can make reasonable assumptions about them or somehow deduce them (e.g. from angular correlations), then we have, in principle, all the ingredients we need to try to understand the underlying fundamental forces governing the phenomena we observe.

This chapter is devoted solely to the topic of silicon detector calibration. Fortunately, when it comes to the silicon detectors we employ in our experiments, the detection efficiency of ions with kinetic energies of order 0.1-10 MeV is unity, provided the kinetic energies are within the dynamic ranges of the silicon detectors (and provided the kinetic energies do not lie within the dead and spurious zones, cf. section 4.1). Determining the detection efficiency of our silicon detectors hence amounts to determining their (energy-dependent) solid angle coverage.

In this chapter, methods for energy calibrating our DSSSDs with beta-delayed protons are presented. It will be shown how these calibrations compare with the simpler and much more prevalent method of carrying out energy calibrations of silicon detectors with a *triple-alpha* (or 3α) source. When appropriate, we will comment on why one might wish to use protons for energy calib-

rations in an experiment such as ours. Both methods require accurate knowledge of the geometry of the detection setup: The positions and orientations of the silicon detectors with respect to the source point of particle emission[1] must be well accounted for, as must the inactive media which a given particle traverses before it reaches a specific point in our active detector media. The reason for this is, of course, that for a given reference kinetic energy E_{kin} of a charged particle, which we wish to use for the calibration of a corresponding signal x produced by some active detector medium, the signal x does not actually represent the reference energy E_{kin}, it rather represents the remaining kinetic energy of the charged particle after it has endured an energy loss E_{loss} in traversing the inactive media preceding the active detector medium. This *deposited energy* $E_{\text{dep}} = E_{\text{kin}} - E_{\text{loss}}$ is what x should be calibrated against. If we know or can determine E_{kin} and E_{loss} to good accuracy (and, preferably, to good precision, as well), then carrying out these types of calibrations is straightforward. In the determination of E_{kin}, we rely on well-known literature values, whereas for the determination of E_{loss}, we characterise the geometry of our detection setup to the best of our abilities and utilise energy loss tabulations in order to calculate E_{loss} based on E_{kin}. Specifically, the energy loss tabulations employed throughout this and the following chapter are from SRIM [ZZB10]. By characterising the geometry of our setup in order to make good energy calibrations, we also obtain the detection efficiency of the silicon detectors as the solid angle coverage of the detectors in the geometry of the setup.

Figure 7.1 illustrates our proposed development of energy calibrations of the silicon detectors employed in the experiment at FRIB. Calibrations with a 3α source were customarily carried out at the very beginning of the experiment in order to ensure, by adjusting the gain on the shaped detector signals, that the dynamic range of the resulting pulse height distribution would contain all particle energies of interest in the experiment. Using these calibrations, many of the data analyses, the results of which are presented in the next chapter, were then developed. Only after significant progress had been made in the data analyses was it then decided to go back and refine the energy calib-

[1] In actuality, the beam which is stopped in our catcher foil has some finite-dimensional distribution in the plane of the foil. Whenever we refer to the source point of particle emission, it is understood to be the location of the mean value of this distribution.

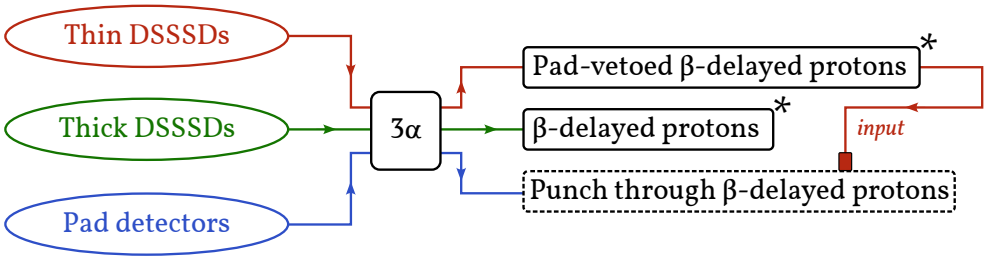

Figure 7.1: Roadmap for the calibration of silicon detectors of the FRIB experiment. Black boxes with solid lines denote types of calibrations which have been carried out. Asterisks indicate that there are some details yet to be accounted for in the calibrations (see section 7.5). Black boxes with dashed lines denote types of calibrations that are yet to be carried out.

rations. As such, the calibrations to reference energies of protons presented in this chapter are very new, and some steps in the refinements are still missing, as is indicated in figure 7.1: The thick and thin DSSSDs have been energy calibrated using protons, but a few details are yet to be accounted for properly; and the Pad detectors have not yet been calibrated using protons. We shall return to these two points later in this chapter. Finally, it should be noted that calibrations with a 3α source were also carried out at the very end of the experiment for consistency checks; these consistency checks also remain to be carried out.

7.1 Source point of particle emission

If we wish to calibrate the silicon detectors with beta-delayed protons, we should first have a rough idea of the source point from which the protons are emitted. In knowing the source point of particle emission of the protons, the energy losses endured by the protons in the inactive media preceding the active detector media can be accounted for. Figure 7.2 shows the hit patterns of the 6 DSSSDs from the measurements on ^{21}Mg from the beginning of the FRIB experiment. The outermost strips of the DSSSDs are excluded whenever analyses based on proton spectra are carried out, as (per section 4.1) we cannot generally tell protons of energies below punch through threshold apart from protons of energies above punch through threshold, as the latter type will miss the backing Pads of our setup. Apart from the exclusion of the outermost strips

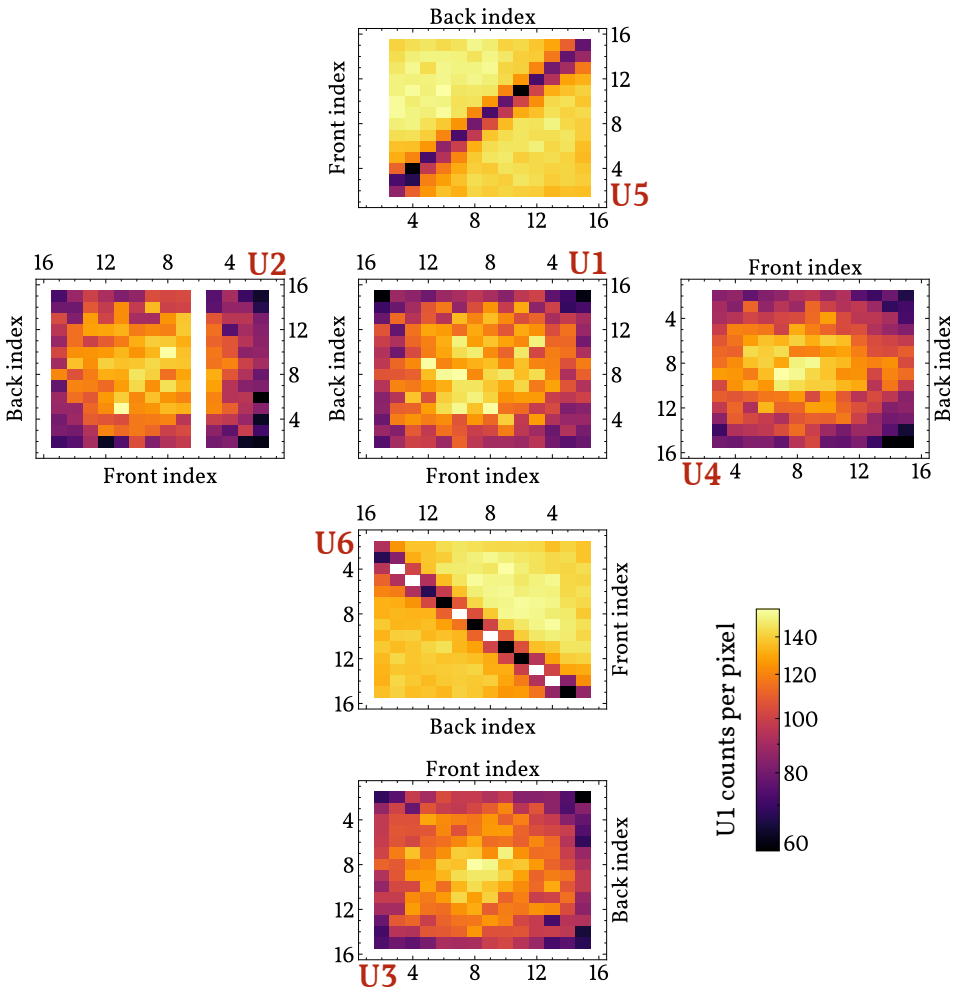

Figure 7.2: Hit patterns of DSSSDs from the measurements on ^{21}Mg at FRIB. In order to have a good sample size of events for the hit patterns, hit patterns of telescope events are drawn for the thin DSSSDs and hit patterns of ΔE-contained events are drawn for the thick DSSSDs. Strips on the front side of the detector here refer to strips on the p-side of the detector, and strips on the back side of the detector refer to strips on the n-side of the detector. The layout of the hit patterns, as it is presented here, is such that one can imagine sitting at the centre of the silicon detector cube, facing U1, and the other sides of the cube have then been folded out to be in the same plane as U1 (see figure 6.5).

of indices 1 and 16, a few additional strips do not contribute to the hit patterns of figure 7.2, as these strips of the DSSSDs were not functioning during the experiment. In the horizontal plane (U1-U4), the hit patterns are most intense close to the centres of the DSSSDs, indicating that the centres of the DSSSDs are closest to the source point of emission of beta-delayed protons. The two DSSSDs above and below the target frame have shadows in their hit patterns

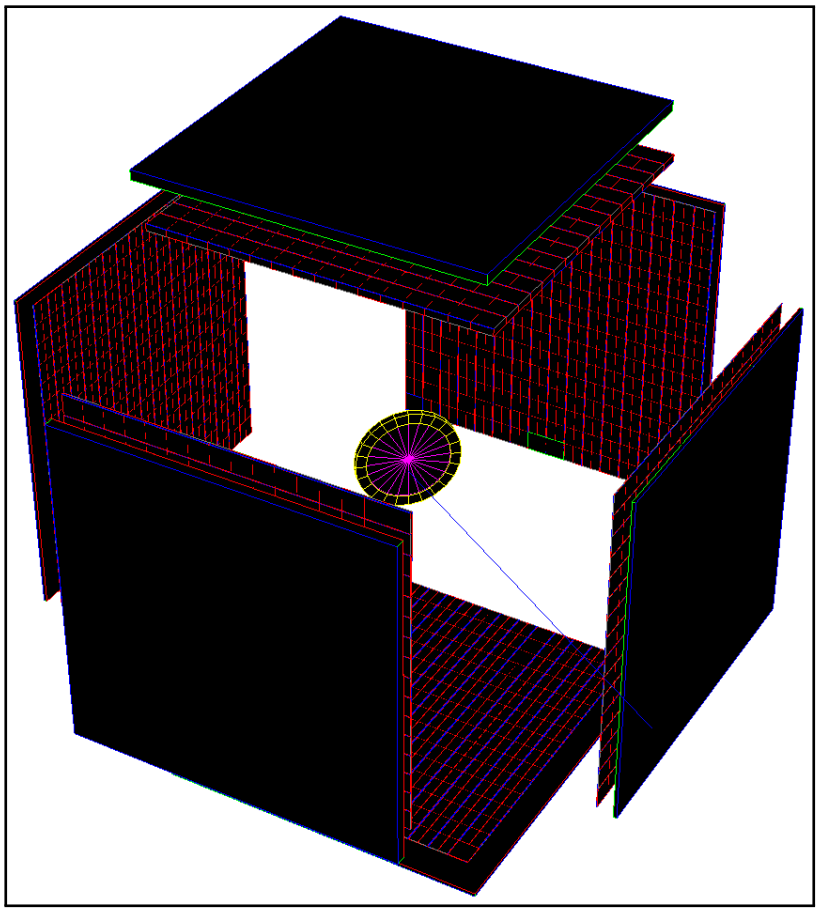

Figure 7.3: Visualisation of detector and target frame geometry in Geant4. The carbon foil (magenta) is displaced 0.3 mm upstream from the centre of the target frame (yellow), placing it 0.2 mm from the face of the target frame.

due to the complete stopping of protons in the target frame. It is noteworthy that the shadow of the target frame is wider in U6 (which is situated below the target frame) than it is in U5. This indicates that the beam of ^{21}Mg is implanted in our carbon foil a bit below the centre of the silicon detector holder, closer to U6 than to U5.

In order to estimate this offset, our detector and target geometry has been described in Geant4 [Ago+03], and simulations have then been carried out in which monoenergetic protons are emitted isotropically from various source points in the carbon foil of our setup. The resulting simulated hit patterns of U5 and U6 have then been compared with those from the actual ^{21}Mg data.

A visualisation of the description of the setup geometry in Geant4 is shown in figure 7.3, and the results of comparing simulated hit patterns to actual hit

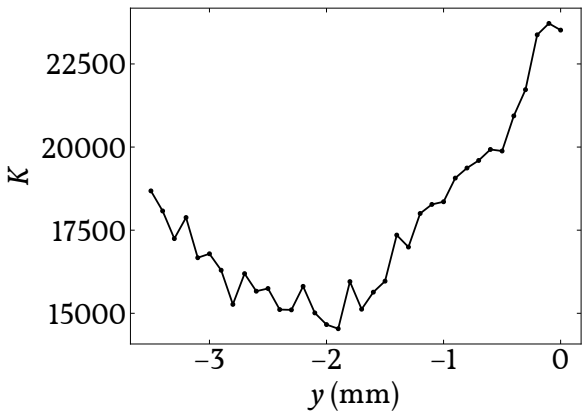

Figure 7.4: Variation in deviation K (see text) between simulated and real hit patterns in U5 and U6. An attempt to replicate the shadows of the target frame (seen in detectors U5 and U6 in figure 7.2) is performed by varying the vertical offset y of the source point of particle emission in the plane of the target foil.

patterns are shown in figure 7.4. In figure 7.4, different values of y (figure 6.5) were sampled in the simulations, while z was based on the expected implantation depth from figure 5.10 and x was fixed at zero. In the comparison of simulations with the real data, the total number of simulated events $M = 1 \times 10^6$ of each simulation is normalised to the total number of real events N, and the difference in normalised number of counts between simulation and data is then calculated for each pixel, $m_i - n_i$; here m_i is the normalised number of counts in pixel i, and n_i is the real number of counts in pixel i. This difference is squared, divided by n_i, and then summed up for all pixels: $K \equiv \sum_i (m_i - n_i)^2 / n_i$. The measure K is inspired by the (Neyman's [Beh+13]) χ^2 test statistic, but by no means do we claim that K actually follows a χ^2 distribution. A minimum in K as a function of y would be an indication of (relatively) good agreement between the simulations and the real data. There are indications that $y \sim -2.0$ mm could be a good guess for the vertical offset of beam implantation.

The hit patterns of U5 and U6 from the real data and from the simulations with $y = -2.0$ mm are shown in figure 7.5. Qualitatively, the locations and widths of the shadows seem to agree pretty well between the simulated and real hit patterns. The shadows of the real data are not completely void of counts and, in addition, there seems to be a variation in the intensities of the hit patterns, where the parts of the hit patterns that are upstream with respect to

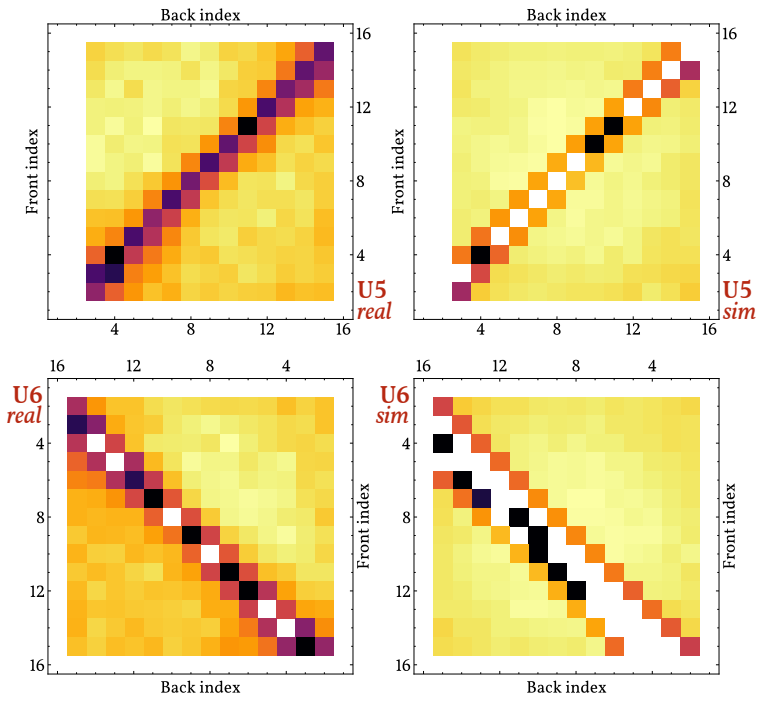

Figure 7.5: Comparison of real and simulated hit patterns of detectors U5 and U6. In the simulations with a point-like source emitting protons from $y = -2.0$ mm in the target foil, the locations and widths of the shadows in the two detectors are similar to those of the real data which are replicated here from figure 7.2.

the target frame are more intense than those that are downstream. These details are not replicated in the simulated data and could be an indication that a broader beam profile is required in order to replicate the real data. Further refinements of these preliminary simulations will aid in characterising the conditions inside the silicon detector cube during the experiment. For now, the values $x = 0, y = -2.0$ mm and z given by the implantation depths simulated by TRIM are employed in the following beta-delayed proton calibrations.

7.2 Pad-vetoed beta-delayed protons

A Pad-vetoed beta-delayed proton spectrum is obtained by inspecting data from a measurement on a reference precursor which undergoes beta-delayed proton decay, and generating, from those data, a pulse height spectrum of a given thin ΔE detector in anti-coincidence with its backing Pad detector. This type

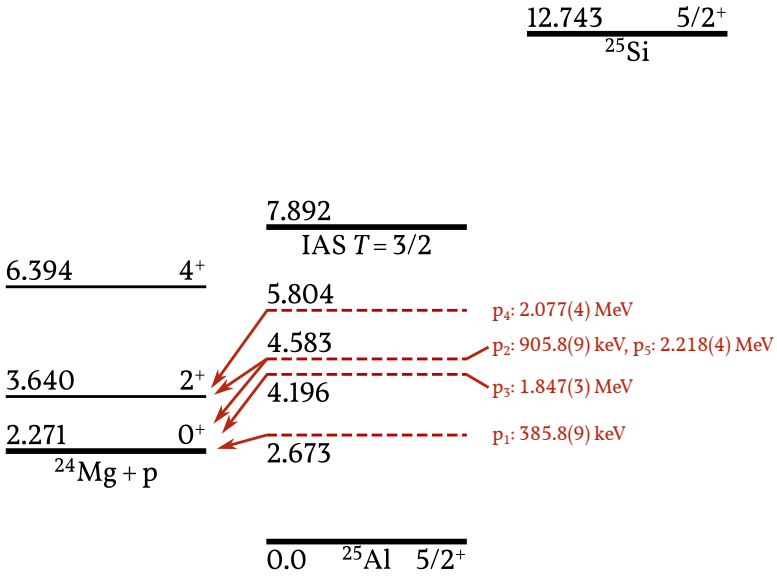

Figure 7.6: Level diagram of beta-delayed protons from ^{25}Al used to calibrate silicon detectors. All energies in black font are in MeV and are adopted from the compilation of known levels in ^{25}Al deduced from ^{24}Mg(p,γ) and ^{24}Mg(p,p'γ) reaction experiments [Fir09]. The dashed red lines indicate from which levels low-energy protons have been used in the Pad-vetoed calibrations of the thin DSSSDs, and the corresponding kinetic energies of the protons are given to the right of the levels.

of spectrum will, provided the reference precursor is well-chosen, predominantly contain low-energy protons from the beta-delayed proton decay; i.e. the protons will be of sufficiently low energy to be completely stopped in the ΔE detector. Although it is, algorithmically, a bit more involved to carry out energy calibrations with Pad-vetoed beta-delayed protons as compared to ungated beta-delayed protons, we start our presentation of the calibrations for this scenario in order to accentuate the promising improvement in going from energy calibrations with alpha particles to energy calibrations with protons on thin ΔE detectors.

^{25}Si is an ideal precursor for these purposes: ^{25}Si has 5 relatively intense proton peaks distributed between 350 keV and 2.1 MeV, while punch through threshold at normal incidence for the thin ΔE detectors we employ is in the 2.2-2.5 MeV range (for 55-65 µm silicon). During the experiment at FRIB, we

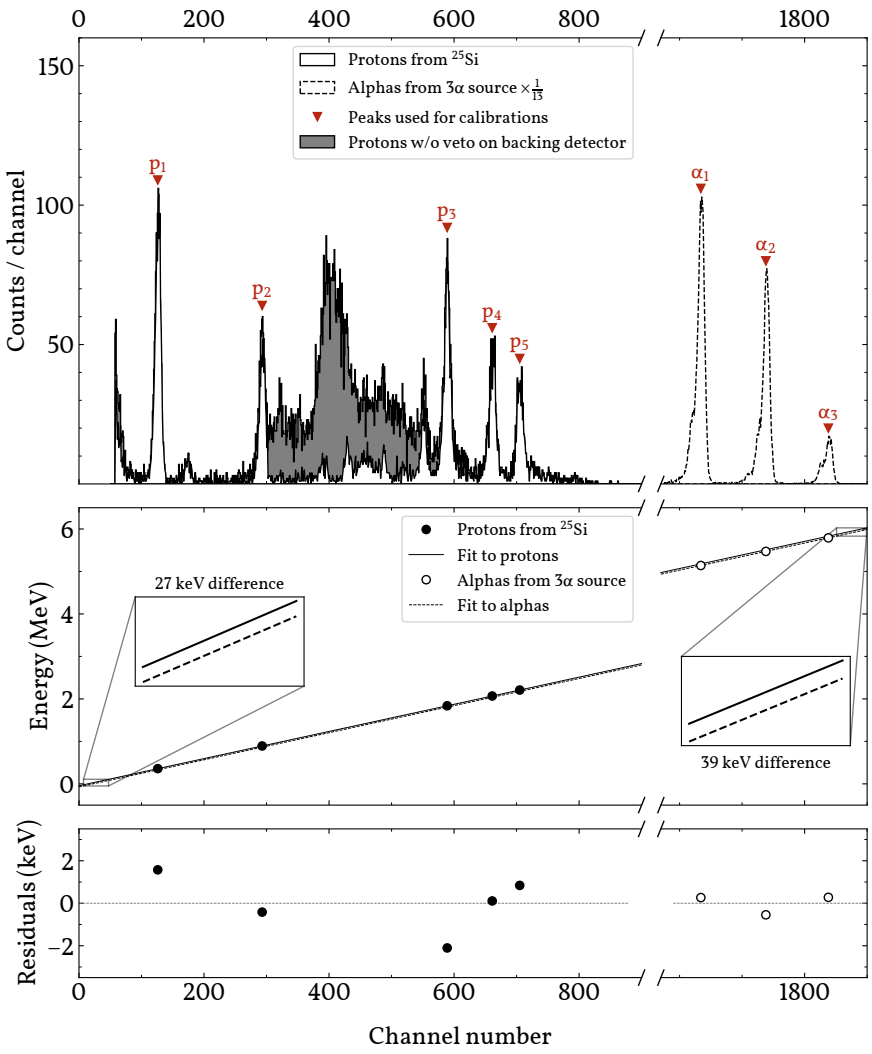

Figure 7.7: Example of Pad-vetoed proton calibration of a single strip of a thin DSSSD. In the top panel, the pulse height spectrum of a single strip is shown with and without an anti-coincidence gate on the backing Pad detector, and the pulse height spectrum of the same strip from a measurement with a 3α source is also shown. The peaks used for the calibration of channel number to corresponding proton/alpha kinetic energy are indicated with the labels $p_i; i = 1, 2, \ldots, 5$ and $\alpha_j; j = 1, 2, 3$. The middle panel shows two straight-line fits to the proton and alpha peaks respectively, and the bottom panel shows the residuals of the fits.

recorded sufficient amounts of data on the decay of this nuclide to make its usage as a calibration source feasible. A level diagram of ^{25}Si and its daughters is shown in figure 7.6 where the proton energies which have been included in the Pad-vetoed beta-delayed proton calibrations are indicated in red with the labels $p_1, p_2, \ldots, p_5$.

Figure 7.7 shows an example of the calibration of a single strip of a thin ΔE DSSSD with Pad-vetoed beta-delayed protons. In the top panel of the figure, the grey histogram shows the spectrum of the relevant strip without vetoing of its corresponding backing Pad-detector, and the white histogram with solid outline shows the spectrum with vetoing. The events that are filtered away by the veto are above-punch through protons which deposit only a fraction of their energy in the strip before proceeding into the backing Pad-detector. For comparison with the energy calibration of the same strip employing, instead, a 3α source, the white histogram of dashed outline is also drawn in the top panel of the figure. The placements of the reference proton energies from the level diagram of figure 7.6 are indicated in figure 7.7, as are the most intense alpha peaks from the alpha decays of ^{239}Pu, ^{241}Am and ^{244}Cm[2]. Less intense alpha peaks from the decays of these three alpha emitters also contribute to the peak shapes in the figure, adding a "fine structure" to the peak shape. These contributions and their relative intensities, which are known in the literature, can be taken into account, adding more reference energies to the calibration. There is, however, a systematic trend in the results of the fits of the three reference energies employed here, and we believe that taking the fine structure of the peak shapes into account does not improve on the quality of the fit, unless this systematic trend is first understood and accounted for. We shall return to this point shortly.

As was motivated in the introduction to this chapter, the reference energies of the protons indicated in figure 7.7 are not precisely those given in figure 7.6; they are, rather, the deposited energies E_{dep} of the protons. The same idea applies, also, to the reference energies of the alpha particles. The deposited energies are calibrated according to the linear relation

$$E_{\text{dep}} = ax + b \tag{7.1}$$

where x is a given channel number, and a and b are fit parameters[3]. The results of the energy calibrations using proton and alpha reference energies for

[2]The kinetic energies of the three alpha particles are, in order, $E_{\alpha_1} = 5156.59(14)$ keV, $E_{\alpha_2} = 5485.56(12)$ keV and $E_{\alpha_3} = 5804.77(5)$ keV [BT14; Bas06; SB08].

[3]The link to the data archive in appendix B, mentioned in the previous chapter, contains files with calibration coefficients for all strips of all detectors; these files will be updated, as the calibrations outlined in this chapter are further refined.

the single strip of figure 7.7 are shown in the middle panel. It is noteworthy how the slopes of the two fits are nearly identical, highlighted by the fact that across 6 MeV of deposited energies, around half of the dynamic range of this particular strip, the change in offset between the two calibrations is only 12 keV, around 0.2 %. Yet, there is an overall offset between the two calibrations of roughly 30 keV throughout; if we were e.g. to use a calibration based on reference energies of alpha particles to deduce the energies of protons, we might suspect that the proton energies would suffer a systematic error. For use later in this chapter, we shall define

$$\Delta E_{\mathrm{dep}} \equiv E^{\mathrm{p}}_{\mathrm{dep}} - E^{\alpha}_{\mathrm{dep}} = (a_{\mathrm{p}} - a_{\alpha})x + (b_{\mathrm{p}} - b_{\alpha}) \tag{7.2}$$

to denote the difference between the calibrations obtained by using protons, $E^{\mathrm{p}}_{\mathrm{dep}}$, and alpha particles, $E^{\alpha}_{\mathrm{dep}}$, with their respective calibration coefficients $a_{\mathrm{p},\alpha}$, $b_{\mathrm{p},\alpha}$ for a given channel number x.

The *pulse height defect* is a term assigned to the empirical observation that ions of differing charge and mass, but of the exact same kinetic energy, do not produce the exact same pulse height in semiconductor detectors. This effect is well-known in the literature [Kno10; Len+86; Kir+14]. It is, then, to be expected that there is a small discrepancy between the two calibrations shown in figure 7.7. On the other hand, what is customarily done in the literature is to correct the deduced deposited energy of equation (7.1) by an empirically founded factor[4], which amounts to modifying the slope and the intercept of the calibration by the same factor. What seems to be the case for the example presented in figure 7.7, however, is that the pulse height defect between protons and alpha particles might instead amount to a small constant offset of order 10 keV across the energy region of order 0.1-10 MeV. Of course, in making this comparison, both calibrations are extrapolated far outside the regions in which they have each been carried out. This, in itself, is reason enough to favour the energy calibration employing protons when extracting proton energies from the low-energy region; and similarly for the energy calibration employing alpha particles when extracting alpha particle energies from the high-

[4]This factor amounts to a few percent, if one wishes to convert from deposited proton energies to deposited alpha energies.

energy region. As it turns out, this is exactly what can be done in the analyses of the FRIB data presented in the next chapter: The distribution of proton energies do indeed lie in the energy region of our proton calibrations, and the distribution of alpha particle energies do indeed lie in the energy region of our alpha particle calibrations.

As a final remark on figure 7.7, the bottom panel shows the residuals of the fits to equation (7.1). The residuals of the proton calibration are markedly larger than those of the alpha calibration. This could be due to the fact that the uncertainties in the energy loss corrections are also markedly larger for the reference energies of the protons as compared to the alpha particles. This difference in energy loss corrections will be illustrated shortly. First, however, we give a brief description of how the peaks of the calibration spectra are found – not only for the single strip of figure 7.7, but for the calibration of all ΔE detector strips, both thick and thin.

Peak finding on the ΔE strips, of which there are over 150, is automated to a significant degree by using the peak finding algorithm `SearchHighRes()` of the C++ class `TSpectrum`[5], which is part of the ROOT data analysis library [BR97]. The peak finding algorithm is based on the following principle: If the peaks in a given spectrum can be approximated by Gaussians, and if the background, on top of which the Gaussians appear, can be locally approximated as a linear function, then the number of counts N in a given channel number x around one such Gaussian will be given by

$$N(x) = G(x) + B + Cx \tag{7.3}$$

where $G(x)$ is the relevant Gaussian, and B and C are constants describing the background local to $G(x)$. For a continuous function $N(x)$, the second derivative of N, $N''(x)$, is then independent of the background, and it is zero far from the relevant peak. One then simply has to find regions where $N''(x) \neq 0$ in order to find the peaks. In practice, the channel numbers x are discrete, and the data at hand may not be as ideal as prescribed by equation (7.3). Still, the discrete second derivative of N is calculated in the peak finding algorithm, and

[5] Although `TSpectrum` has been marked as a legacy interface in ROOT at least since version 6.26, there still does not seem to be an alternative to it in the ROOT library.

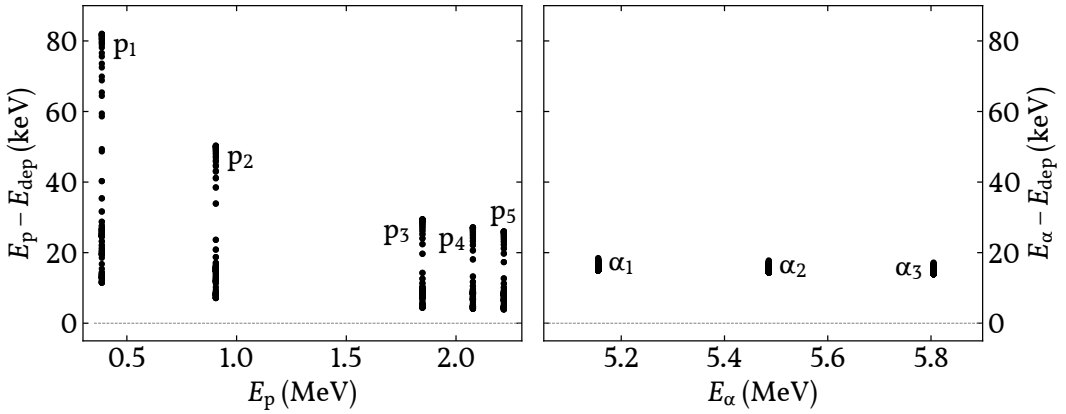

Figure 7.8: Energy losses endured by reference protons and alpha particles before they reach a given thin ΔE strip. Each point (the points can only be told apart for some of the reference protons) represents the energy loss E_{loss} endured by a proton (alpha particle) of initial kinetic energy E_p (E_α) in traversing the inactive media preceding a given ΔE strip, into which the proton (alpha particle) deposits its remaining energy $E_{\text{dep}} = E_p - E_{\text{loss}}$ ($E_{\text{dep}} = E_\alpha - E_{\text{loss}}$). The reference energies $p_i; i = 1, 2, \ldots, 5$ and $\alpha_j; j = 1, 2, 3$ are those of figure 7.6 and of footnote 2, respectively.

some clever choices of constraints on the counts in a moving window across the channel numbers x make the peak finding algorithm quite reliable. More details are given in [Mar67].

Returning now to the energy losses endured by the reference protons as compared to the reference alpha particles employed in the calibrations of the thin ΔE detectors, these energy losses are shown for all strips in figure 7.8. The energy losses are calculated based on estimates of the distances the particles have to traverse in inactive media, before they reach the active detector strips. As can be seen, there is a much larger spread in the calculated energy losses of all proton energies, as compared to the alpha particle energies. Hence, errors in the accounting of the distances traversed in the inactive media will manifest themselves as much larger errors in the proton calibrations as compared to the alpha particle calibrations. Considering the range (and variety) of energy loss corrections that the reference protons require, the range of residuals in the bottom panel of figure 7.7, ranging between -2 and $+2$ keV, does not seem very large.

In figure 7.9, the distribution of residuals from the Pad-vetoed beta-delayed

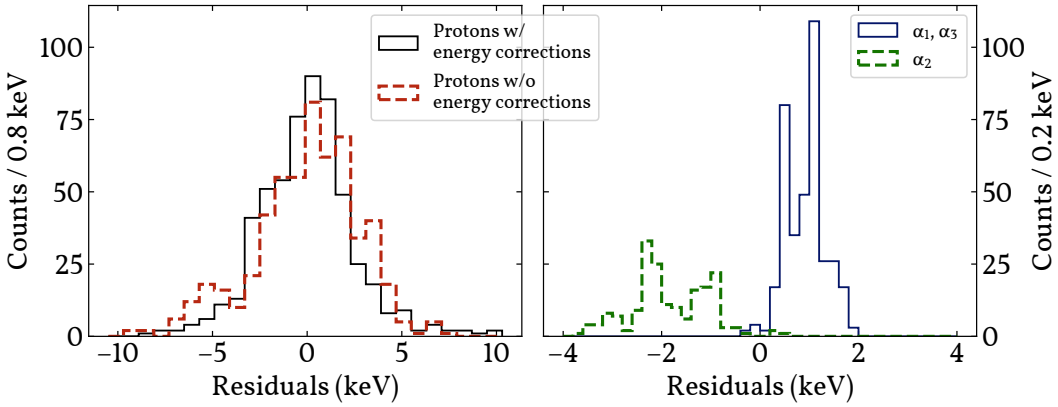

Figure 7.9: Distribution of residuals of reference energies employed in the calibrations of ΔE detector strips. The left panel shows the distribution of residuals of all five reference proton energies of figure 7.6 with and without the energy loss corrections discussed in this section. The right panel shows the distribution of residuals of the three reference alpha particle energies from footnote 2 with energy loss corrections applied; the residuals are divided into two groups of (α_1, α_3) and (α_2), highlighting a systematic trend in their distributions.

proton calibrations of thin ΔE detectors is shown in the left panel, and the distribution of residuals from the 3α calibrations of both thick and thin ΔE detectors is shown in the right panel. The systematic trend in the results of the alpha calibrations, mentioned earlier, are seen here. The fit of the three reference alpha particle energies favours, in all cases, a straight line fit where α_2 is situated a bit below the straight line, and α_1 and α_3 are situated a bit above it. In contrast, a study of the distribution of groups of residuals from the proton calibration does not clearly reveal a similar tendency. In the figure, it is illustrated how a fit to the proton reference energies with and without energy loss corrections affects the distribution of residuals. It seems that the residuals including energy loss corrections are quite well-centered around zero, with the majority of residuals ranging from -5 to $+5$ keV. Visually, the residuals from the alpha calibrations with and without energy loss corrections are indistinguishable, hence only the residuals from the calibrations including energy loss corrections are shown.

In figure 7.10, the residuals of the energy calibrations employing respectively protons and alpha particles are plotted against each other for all pairings

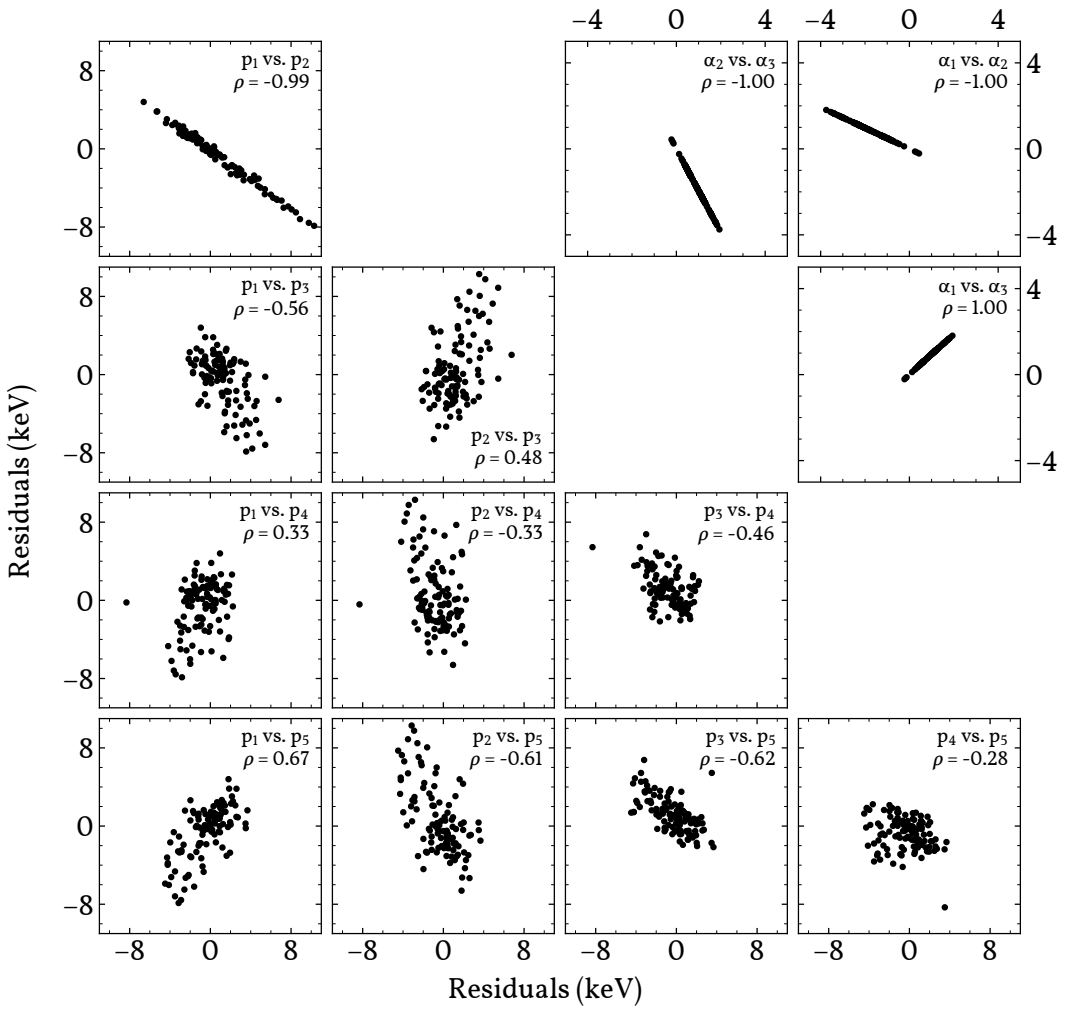

Figure 7.10: Correlation plots of residuals from calibrations employing Pad-vetoed beta-delayed protons and a 3α source. All possible pairings of correlations between fits to p_1, p_2, . . ., p_5 (figure 7.6) and to α_1, α_2 and α_3 (footnote 2) are shown. The strong correlation between the residuals of the alpha calibrations seen in figure 7.9 is also seen here. There is also quite a strong correlation between p_1 and p_2, while the remaining residuals of the proton calibrations are only weakly correlated.

of proton energies and for all pairings of alpha particle energies. The sample correlation ρ is calculated and printed for each individual pairing in the figure. As in figure 7.9, the complete correlation between the three groups of residuals of the alpha calibrations is evident. Here, it is also revealed that there is quite a strong correlation between the reference protons p_1 and p_2, while the remaining residuals are weakly correlated. A possible explanation for the systematic trend in the alpha particle energy residuals could possibly be found in the pre-

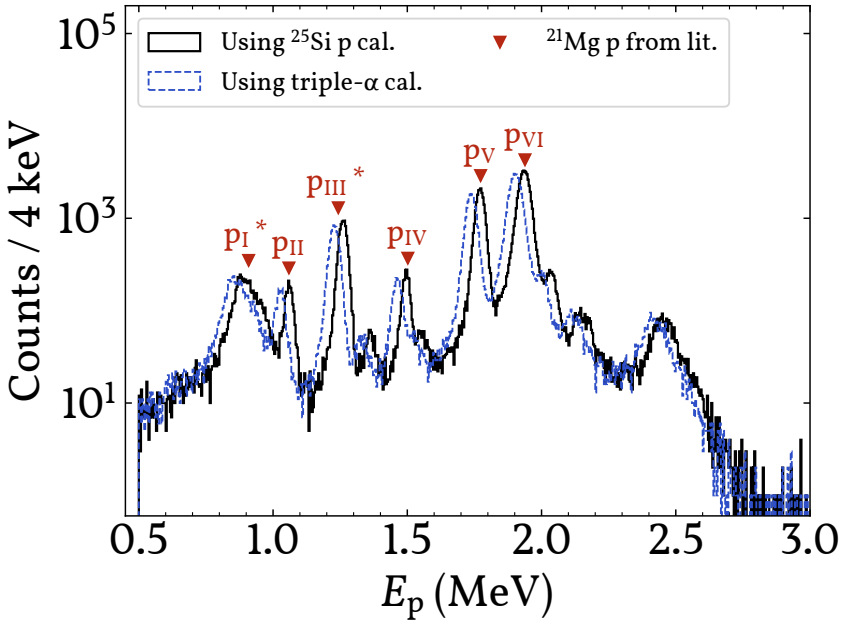

Figure 7.11: Pad-vetoed beta-delayed protons of all thin ΔE detector strips from ^{21}Mg employing proton and alpha calibrations of this section. Literature values [Jen+24; Fir15] of a selection of proton peak positions are indicated in red. The values of the two peaks p_I and p_{III} are from beta-delayed proton emission studies, and the remaining peaks are from ^{20}Ne(p,p) and ^{20}Ne(pol p,p) reaction studies. The agreement between the peak positions taken from reaction studies and the calibrations employing protons from ^{25}Si is quite good.

paration of the 3α source: If the three alpha emitters ^{239}Pu, ^{241}Am and ^{244}Cm are not deposited uniformly onto the source holder during the source production, but instead are deposited in a manner resulting in a layering of the three emitters, then the alpha particles emitted from at least one of the emitters will endure an energy loss as it traverses the layer of (very heavy) emitters on top of its parent.

We conclude this section by illustrating the benefit of employing Pad-vetoed beta-delayed protons for energy calibrations of the data from our experiment at FRIB. Figure 7.11 shows the familiar (from section 4.2) low-energy proton spectrum from the decay of ^{21}Mg; these spectra are Pad-vetoed data from ^{21}Mg, recorded at FRIB, from *all* thin ΔE detector strips. In producing the spectra, calibrations using the reference protons from the decay of ^{25}Si have been employed, and the calibrations based on reference alpha particles from a 3α source have also been employed. A level diagram for the beta decay of ^{21}Mg (with ex-

cited states relevant to this and the following section highlighted) is shown in figure 7.12. The placements of low-energy proton peaks from the level diagram of figure 7.12 are indicated in figure 7.11, in both figures in red. The two peaks p_I and p_{III}, which are also accompanied by asterisks in figure 7.11, are adopted from the studies of the beta decay of ^{21}Mg in [Jen+24]. The energies reported there differ only by, at most, a few keV from the values reported in previous beta decay studies of ^{21}Mg in [SGC73; Lun+15a]. However, when employing the proton calibration on the Pad-vetoed spectrum, the two literature values of the peaks p_I and p_{III} do not coincide with the local maxima in their vicinity. The remaining four peaks are based on the compilation of known levels in ^{21}Na deduced from ^{20}Ne(p,p) and ^{20}Ne(pol p,p) reaction experiments [Fir15]. These four levels are seen to coincide pretty well with the peaks of the spectrum when employing the proton calibration, while the same peaks are systematically at lower energy when employing the alpha calibration. Based on the alignment of these latter four peaks with our proton-calibrated spectrum, and considering the fact that the calibration of the spectrum was independently based on protons emitted in the decay of ^{25}Si, going forward with the proton calibrations presented in this section seems quite encouraging. Finally, we also note a modest improvement in the resolution of the spectrum, as the peak p_{VI} has a FWHM of 50 keV when employing the alpha calibration, while it has a FWHM of 42 keV when employing the proton calibration; this is a relative improvement of 16 %.

7.3 Beta-delayed protons

In moving on to the calibration of the thick DSSSDs of the setup (figure 7.1), the methods outlined in the previous section are broadly re-applicable. The two major differences are the following:

1. Background from minimum ionising beta particles in the silicon detector spectra reach further up in energy.

2. It is not necessary to veto on backing Pad detectors in order to suppress distortions of the spectra due to punch through protons.

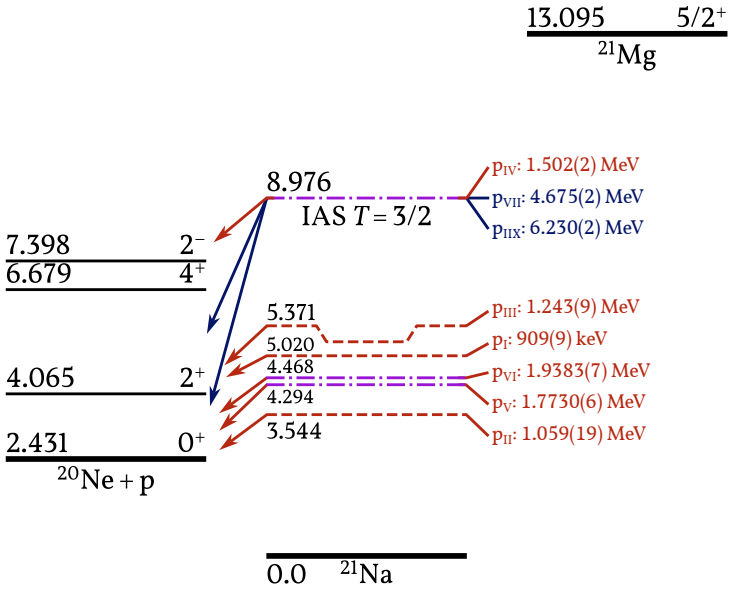

Figure 7.12: Level diagram of beta-delayed protons from ^{21}Mg used to check validity of calibrations of thin ΔE detectors and to calibrate thick ΔE detectors. All energies in black font are in MeV and all level placements, except for the ones at 5.020 MeV and 5.371 MeV, are adopted from the compilation of known levels in ^{21}Na deduced from ^{20}Ne(p,p) and ^{20}Ne(pol p,p) reaction experiments [Fir15]. The placements of the levels at excitation energy of 5.020 MeV and 5.371 MeV are from [Jen+24]. The dashed red lines and dash-dotted magenta lines indicate from which levels low-energy protons have been used to validate the Pad-vetoed calibrations of the thin DSSSDs, and the corresponding kinetic energies of the protons are given to the right of the levels in red font. Protons from the two levels represented by dash-dotted magenta lines at lower excitation energy have also been used to calibrate the thick DSSSDs, as have the two proton energies indicated in blue font.

The first point implies that we require reference protons of larger kinetic energies for the calibrations, and the second point means that the analyses are simpler than in the preceding section.

Figure 7.13 shows an example of the calibration of a single strip of a thick ΔE DSSSD with beta-delayed protons. The layout for this figure is the same as that of figure 7.7. In the top panel of the figure, the white histogram with solid outline is the spectrum of beta-delayed protons. For comparison with the energy calibration of the same strip employing, instead, a 3α source, the white histogram of dashed outline is also drawn in the top panel of the figure.

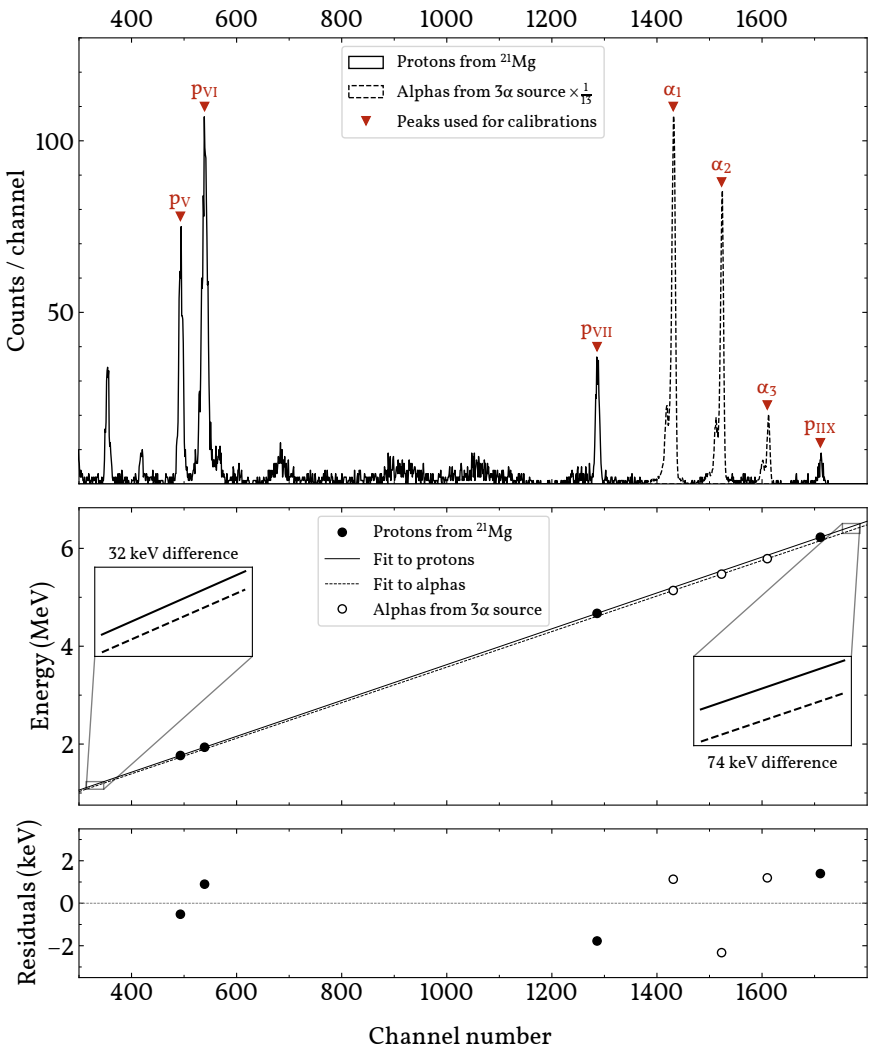

Figure 7.13: Example of beta-delayed proton calibration of a single strip of a thick DSSSD. In the top panel, the pulse height spectrum of beta-delayed protons from a single strip is shown, as is the pulse height spectrum of the same strip from a measurement with a 3α source. The peaks used for the calibration of channel number to corresponding proton/alpha kinetic energy are indicated with the labels $p_i; i = \mathrm{V}, \mathrm{VI}, \mathrm{VII}, \mathrm{IIX}$ and $\alpha_j; j = 1, 2, 3$. The middle panel shows two straight-line fits to the proton and alpha peaks respectively, and the bottom panel shows the residuals of the fits.

The placements of the reference proton energies from the level diagram of figure 7.12 are indicated in figure 7.13, as are the most intense alpha peaks from the alpha decays of ^{239}Pu, ^{241}Am and ^{244}Cm. The peaks have been located using the same method as described in connection with equation (7.3). The results of the energy calibrations using proton and alpha reference energies for the

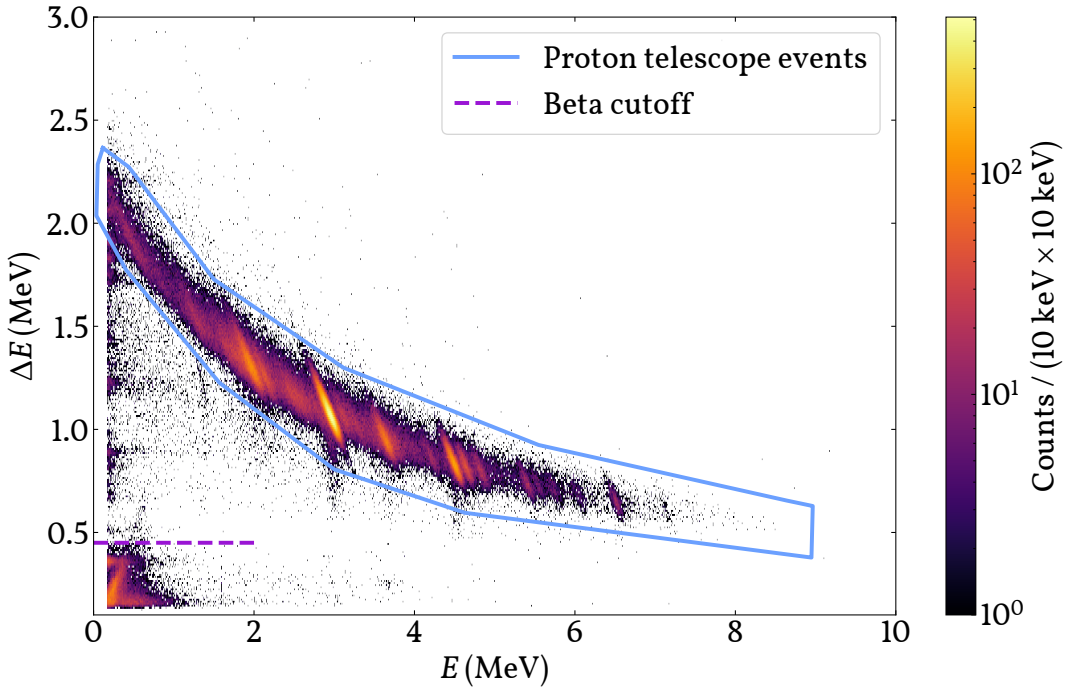

Figure 7.14: ΔE vs. E plot of the detector telescope consisting of the detectors U3 and P3. The ΔE values of U3 are due to proton calibrations and, hence, represent deposited proton energies $E^{\mathrm{p}}_{\mathrm{dep}}$, while the E values of P3 are due to alpha particle calibrations, thus representing deposited alpha particle energies $E^{\alpha}_{\mathrm{dep}}$. The spectrum is the combination of all spectra recorded on ^{21}Mg, ^{22}Al, ^{25}Si and ^{26}P during the experiment at FRIB.

single strip of figure 7.13 are shown in the middle panel. This time, the difference between the two calibrations, equation (7.2), is 32 keV at channel number $x = 350$ and 74 keV at channel number $x = 1800$; this is a larger discrepancy compared to the previous example. The bottom panel shows, again, the residuals of the fits to equation (7.1). Here, the residuals from the two different calibrations are of equal size.

7.4 Detector telescope characterisation

Before the Pad detectors are used to extend the ranges of the charged particle energy spectra to higher energies, the detector telescopes consisting of pairs of DSSSDs and Pads should first be characterised. In particular, the dead and spurious zones of the detector telescopes should be identified. In this section,

we outline the main results of the characterisations of our detector telescopes.

The first step in characterising the detector telescopes is to draw ΔE vs. E plots and defining, from these plots, the ranges in which ΔE-contained events and telescope events lie. An example of such a plot is shown in figure 7.14 for the detector telescope consisting of the detectors U3 and P3. Along the ordinate are deposited energies in U3, the ΔE detector of the telescope configuration, and along the abscissa are deposited energies in P3, the E detector of the telescope configuration. The plot contains, per event, all possible combinations of energy depositions in the ΔE and E detectors. In order to have as large a sample as possible from which to define the region of telescope events, the spectrum is the combination of all spectra recorded on ^{21}Mg, ^{22}Al, ^{25}Si and ^{26}P. In figure 7.14, the region containing proton telescope events is enveloped by the shape of solid outline, and the energies above which beta particles do not contribute to the ΔE-contained events, the beta cutoff, is indicated with the dashed line. Just below beta cutoff is an indication of beta-delayed protons from the astrophysically important 3^+ resonance at 5.93 MeV in ^{26}Si; extracting this signal from the data will require extra care. It should be noted that the Pads of our detection setup are still merely calibrated with a 3α source. As such, the E values of the figure represent deposited alpha particle energies $E^{\alpha}_{\mathrm{dep}}$, while the ΔE values of the figure represent deposited proton energies $E^{\mathrm{p}}_{\mathrm{dep}}$. As a final note, the signal thresholds of the detectors, due to the combination of trigger and ADC thresholds on the detector channels, determine the emergence of detector signals at positive values of ΔE and E in the figure. Information about which of the various trigger signals of equation (6.1) were responsible for signalling data readout for each individual event is available, but this information does not influence the identification of ΔE-contained events and telescope events; only the graphical cuts of figure 7.14 and the characterisation of dead and spurious zones (see below) influence the event identification.

In appendix C, figures similar to figure 7.14 are presented for the detector telescope configurations U1-P1, U2-P2 and U4-P4. Based on our ΔE vs. E plots, we note, for all our detector telescopes, those energy regions which contain ΔE-contained events and those energy regions which contain telescope events. This division of energy regions is one of the main foundations of our data ana-

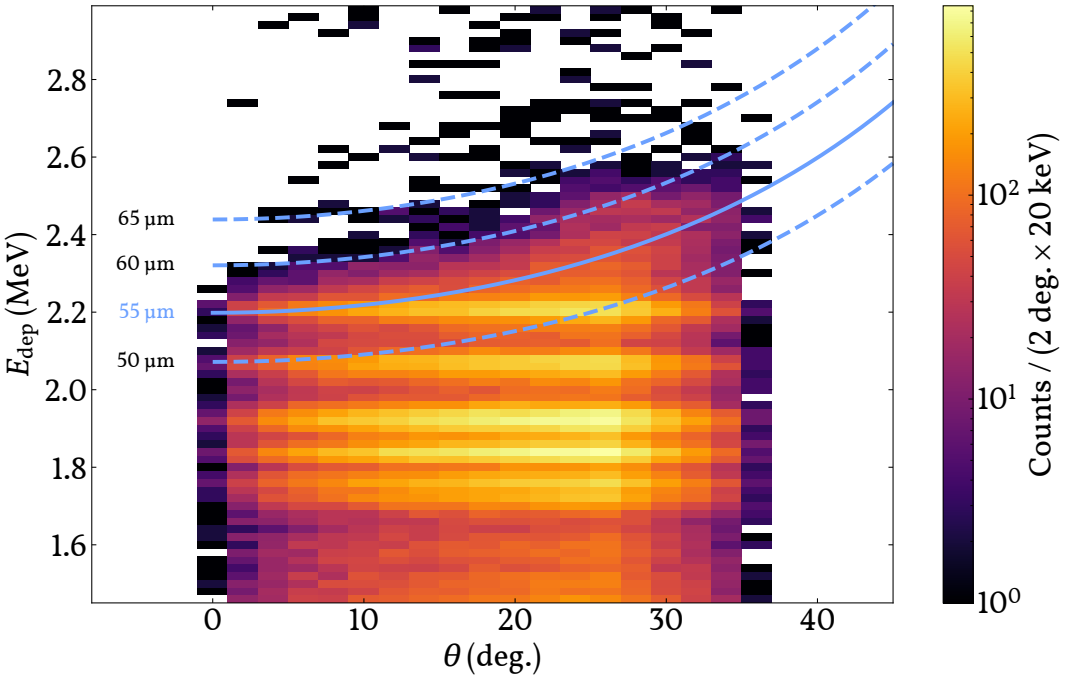

Figure 7.15: Deposited energies E_{dep} against angles of incidence θ between particles and normals to the detector surface of U3. The spectrum consists of ΔE-contained events for all of the data recorded on ^{21}Mg, ^{22}Al, ^{25}Si and ^{26}P during the FRIB experiment. Tabulations of punch through threshold for silicon of thickness 50, 55, 60 and 65 µm are drawn on top of the spectrum. 55 µm (the solid curve) is the thickness of the detector as stated by Micron Semiconductor Ltd. We deduce a thickness around 60 µm from this spectrum.

lyses.

Now, in order to identify the dead and spurious zones of the detector telescopes, we employ one of the methods presented in [JRF23] (section 4.1): We plot deposited energies E_{dep} against angles of incidence θ between particles and normals to detector surfaces of our ΔE detectors, and we compare the resulting spectra with calculated punch through thresholds in the vicinity of the detector thicknesses stated by Micron, the manufacturer of the detectors. An example of such a plot is shown in figure 7.15 for the DSSSD U3. The spectrum consists only of ΔE-contained events; it does not contain events identified as telescope events. In order to have as large a sample as possible from which to estimate the thickness of U3, the spectrum of deposited energies is the combination of all spectra recorded on ^{21}Mg, ^{22}Al, ^{25}Si and ^{26}P. In figure 7.15, the solid curve indicates punch through threshold for 55 µm silicon which is the stated thickness

	U1	U2	U3	U4
Deduced thickness (µm)	58	70	60	310
Stated thickness (µm)	55	65	55	296
Relative difference (%)	6	8	9	5

Table 7.1: Deduced active layer thicknesses of the DSSSDs U1–U4. The deduced thicknesses are active layer thicknesses obtained by comparing punch through tabulations with observed energy depositions as exemplified in figure 7.15. The stated thicknesses are the same as those listed in table 6.1.

of U3. There is an intense θ-independent peak around $E_{\text{dep}} = 2.2$ MeV which crosses the solid curve towards $\theta = 0°$, while for all values of θ, the dashed line corresponding to punch through threshold of 60 µm generally lies above the observed spectrum. From this spectrum, we deduce an active layer thickness of 60 µm for this particular ΔE detector.

In appendix C, figures similar to figure 7.15 are presented for the DSSSDs U1, U2 and U4. In table 7.1, the deduced active layer thicknesses of the DSSSDs U1–U4 are summarised. Our deduced active layer thicknesses are consistently larger than those stated by Micron, and the relative differences range from 5 to 9 %. For now, we employ the active layer thicknesses tabulated in table 7.1, but the systematic tendency of our thickness estimates exceeding those stated by Micron is cause for further investigation.

7.5 Summary and outlook

7.5.1 Summary

With detector telescope characterisations in hand, we are finally able to present the culmination of all the calibration steps outlined in this chapter, presented in figure 7.16: Full energy range charged particle spectra from ^{21}Mg of the detector telescopes U1-P1, U2-P2, U3-P3 and U4-P4. The spectra illustrate initial kinetic energies of protons E_{p} emitted from excited states in ^{21}Na; i.e. the observed deposited energies in the detectors have been corrected for the energy losses endured by protons in the inactive media of the experimental setup. For the detector telescopes with thin ΔE detectors (U1-P1, U2-P2 and U3-P3),

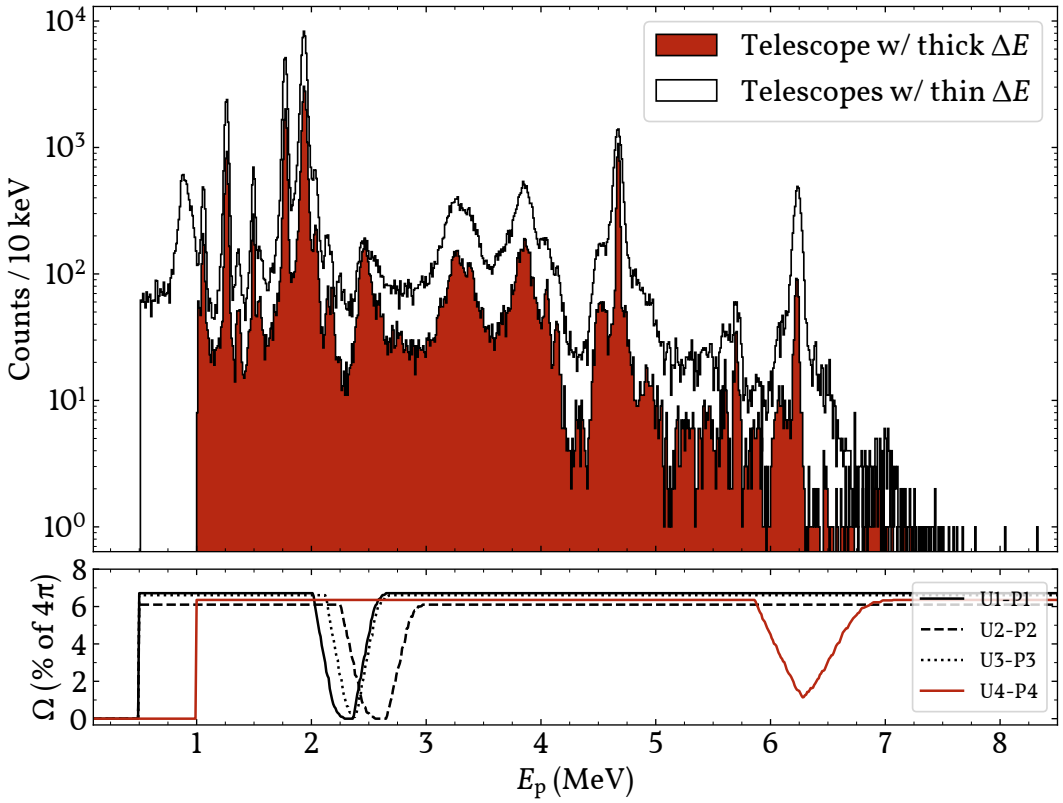

Figure 7.16: Proton singles spectra from the beta decay of ^{21}Mg recorded at FRIB. The distributions of initial kinetic energies of protons E_p from the detector telescopes U1-P1, U2-P2, U3-P3 and U4-P4 are shown in the top panel, and the energy-dependent solid angle coverage Ω of the telescopes are shown in the bottom panel. Compare with the proton singles spectra from the beta decay of ^{21}Mg recorded at IDS, figure 4.3.

the spectrum looks unmistakably like the singles spectrum presented in figure 4.3, although the differing onsets of the dead and spurious zones of the telescopes employed in the present experiment influence the spectrum differently. The spectrum from the detector telescope with a thick ΔE detector (U4-P4) is plotted separately from the other combined spectrum, and these two spectra do differ noticeably. In the lower panel of the figure, the energy-dependent solid angle coverage Ω is depicted. The dips in Ω are characteristic of the onset of the dead and spurious zones of the detector telescopes, and the width of these dips are characteristic of the range of effective thicknesses of the ΔE detectors as well as the signal thresholds of the E detectors. Below punch through threshold, the combined detector resolutions of U1, U2 and U3 are on

par with the resolution of U4, but, as the Pads are included in the extraction of the charged particle energies, the resolutions of the detector telescopes are significantly reduced. Due to the high resolution of U4 all the way up to $E_p = 5.8$ MeV, we see details in the spectrum which we were not able to see in the data recorded at IDS. This is cause for further investigation; however, in the spectrum of higher resolution we do not see indications of features that would dispute any of the conclusions drawn in our study of ^{21}Mg at IDS.

It should be noted that the deposited energies of the Pads are calibrated against alpha particle reference energies, and the pulse height defect then influences the energies of protons extracted from the Pads. In producing figure 7.16, the extracted deposited alpha particle energies of the Pads have been multiplied with an empirically founded constant of 1.016, which was observed to give the agreement between peak positions of the spectra shown in the figure. In the future, when the Pad detectors have also been calibrated by employing proton reference energies, this temporary hack can be discarded.

7.5.2 Outlook

The main intent of this chapter has been to motivate the replacement of energy calibrations employing 3α calibration sources with that of beta-delayed protons. It is very fortunate that the complementary measurements on ^{21}Mg and ^{25}Si were carried out during the experiment on ^{22}Al and ^{26}P at FRIB, as there would otherwise not have been any beta-delayed protons with which to carry out this kind of energy calibration. Long in advance of the experiment, we had thought to inquire about the possibility of measuring on ^{21}Mg for calibration purposes, but the dedicated measurements on ^{25}Si were specifically carried out because this nuclide was a contaminant in the measurements on ^{26}P. As it turned out, the low-energy, beta-delayed protons emitted in the decay of ^{25}Si are highly ideal for the calibration of our thin ΔE detectors, and they provide a means of cross-checking the energy calibrations based on beta-delayed protons from ^{25}Si with those based on beta-delayed protons from ^{21}Mg; and vice versa.

As was mentioned at the beginning of this chapter, the venture of carrying out energy calibrations with beta-delayed protons is not quite finished yet (fig-

ure 7.1). In particular, the following points outline what remains to be done:

- Initial geometry calibrations have been carried out by simulating different source points of particle emission in the target foil and comparing the shape of the shadows generated by the target frame in the DSSSDs above and below the target frame for simulated and real data. Further refinements of the geometry calibrations could be achieved by expanding upon these simulations; in particular, sampling of source points of particle emission in all three dimensions of the target foil seems like a logical next step, as does the simulation of different beam profiles. Additionally, the hit patterns of figure 7.2, can be used to estimate the points of the DSSSDs which are closest to the source point of particle emission, and the combination of several such estimates can be used to estimate the actual source point(s) of particle emission. Finally, the method of localisation using the ratio of square-distances [Chi+08] could also, potentially, be an interesting way of gaining more insight into the geometry of the detection setup.

- The detectors above and below the target frame have been omitted from the calibrations presented in this chapter, and they will also be omitted from the analyses presented in the next chapter. A better understanding of the effective target foil thickness encountered by particles emitted towards the detectors above and below the target frame is required, as is the effects of the shadows generated by the target frame on these detectors. The placement of the beam implantation point(s) also has a greater impact on the spectra extracted from these particular detectors.

- Calibrations employing beta-delayed protons on the Pads are yet to be carried out.

Any change in the understanding of the geometry of the detection setup will, of course, necessitate a retracing of the calibration steps presented in this chapter. The idea for the calibration of the Pads employing punch through beta-delayed protons is to utilise[6], for a given telescope event, the relatively precise know-

[6] As is already done when generating charged particle energy spectra from telescope events.

ledge of the point of incidence with the DSSSD to deduce the point of incidence with the Pad. In doing so, the energy losses endured by a given incident proton can be accurately accounted for. The accuracy of this kind of calibration should be much better compared to the calibrations subjecting the Pads, alone, to a 3α source where each individual alpha particle can be incident anywhere across the entire $5 \times 5\,\mathrm{cm}^2$ surfaces of these unsegmented detectors.

One thing, which has become clear in working with the calibration of the silicon detectors, is the unfortunate fact that we utilise a bit less than half (2048 channels) of the full dynamic range (4096 channels) of our ADCs in all of our silicon detector channels; see figures 7.7 and 7.13. The dynamic ranges on the detector channels were chosen such that they could contain the energies of protons and alpha particles emitted in the beta decays of ^{22}Al and ^{26}P; i.e. the guideline was the Q-value of beta decay less the relevant particle separation energies. In practice, however, protons punch through our thin ΔE detectors when their energies exceed 2–3 MeV, and we do not expect to see alpha particle energies of more than 5–6 MeV; these energies correspond, respectively, to a quarter of the dynamic range and half of the dynamic range e.g. in figure 7.7. The issue is similar for our thick ΔE detectors. If we had doubled the amplification on our shaping amplifiers, our ability to detect the different species of charged particles would not have been diminished, and, naïvely, the detector resolution on our spectra would have been doubled. Furthermore, it might have been easier to fine-tune the trigger and ADC thresholds in order to favour the recording of low-energy true signals while suppressing random signals due to electrical noise, cf. section 6.3.

The differences ΔE_{dep} (equation (7.2)) in extracted energies when employing proton and alpha calibrations for all DSSSD channels of U1-U4 are illustrated in figure 7.17. ΔE_{dep} is calculated at small and large channel numbers, corresponding roughly to energies of 0 and 6 MeV, respectively. These kinds of differences were illustrated in the middle panels of figures 7.7 and 7.13, and the two specific cases of those two figures are highlighted here, in figure 7.17. As it turns out, there is quite a variation in ΔE_{dep}, but the different values of ΔE_{dep} are primarily positive and in the 0-70 keV range. There are a few outliers in the figure, and they, in particular, require further investigation.

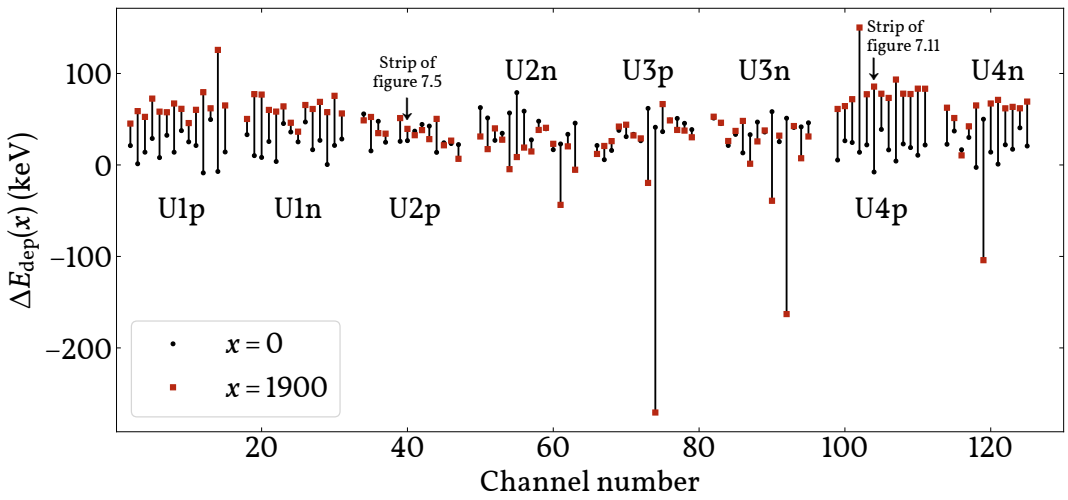

Figure 7.17: Difference between proton and alpha calibrations of various DSSSD detector strips. The difference ΔE_{dep}, equation (7.2), is calculated at small and large channel numbers $x = 0, 1900$, corresponding roughly to 0 and 6 MeV. These two values are, for each strip, connected with a thin black line to guide the eye. There is quite a variation in the differences between the two types of calibrations, and there are some outliers which might require further investigation. The detectors U5 and U6 (figure 6.5) are not included in this plot.

As was suggested by the low-energy proton spectrum from the decay of ^{21}Mg, figure 7.11, switching from energy calibrations employing alpha particles to energy calibrations employing protons both improves on our resolution and seems to correct for systematic errors which are due to employing the former type of calibrations. It might very well turn out to be the case that we are able to significantly refine the decay and level schemes of both ^{21}Mg and ^{25}Si based on the calibration data presented in this chapter.

This concludes the present chapter detailing the current state of the calibrations of the silicon detectors employed in the FRIB experiment. The next chapter is devoted to presenting the data and results from the measurements on ^{22}Al and ^{26}P at FRIB. In all that follows, if nothing else is stated, charged particle spectra are extracted by the means exemplified by figure 7.16: Below punch through threshold, ΔE-contained events are identified, and, above punch through threshold, telescope events are identified; these events are combined into full energy range spectra, while events lying within the dead and spurious zones are discarded. Deposited energies are extracted from the detectors

by employing proton calibrations when proton spectra are under study, and alpha particle calibrations are employed when alpha particle spectra are under study. The deposited energies are converted to initial proton/alpha particle kinetic energies via energy loss tabulations. Finally, if nothing else is stated, only the detector telescopes U1-P1, U2-P2, U3-P3 and U4-P4 are utilised to extract charged particle energy spectra.

Chapter 8

The beta decays of ^{22}Al and ^{26}P

In this chapter, we first consider, in turn, the different types of decay channels in the decays of ^{22}Al and ^{26}P: Beta-delayed α emission (βα), beta-delayed 2-proton emission (β2p) and beta-delayed 1-proton emission (βp). We shall investigate these individual decay channels, in the given order, collectively for ^{22}Al and ^{26}P. We start with βα, as this case is short and simple. We then consider β2p, which is more involved than βp, but by first gaining a good understanding of the specific cases of β2p from ^{22}Al and ^{26}P we will then be much better poised to gain a good understanding of the specific cases of βp.

Overviews of the decay schemes of ^{22}Al and ^{26}P are presented in figures 8.1 and 8.2. Note the overlapping of daughter nuclides in these two decay schemes as well the overlapping with the decay schemes of ^{25}Si and ^{21}Mg; figures 7.6 and 7.12.

8.1 Beta-delayed alpha emission

As was mentioned in the previous chapter, our thin ΔE detectors (58-70 μm silicon) can stop protons with kinetic energies up to 2–3 MeV, depending on the angle of incidence between a given proton and the normal to the detector surface of a given thin ΔE detector. On the other hand, our thin ΔE detectors can stop alpha particles with kinetic energies of 9 MeV or more. Thus, for alpha particles with kinetic energies above punch through threshold for protons in our thin DSSSDs we have the ability to identify beta-delayed α particles emitted in the decays of ^{22}Al and ^{26}P. In figure 8.3, alpha particle energy spectra

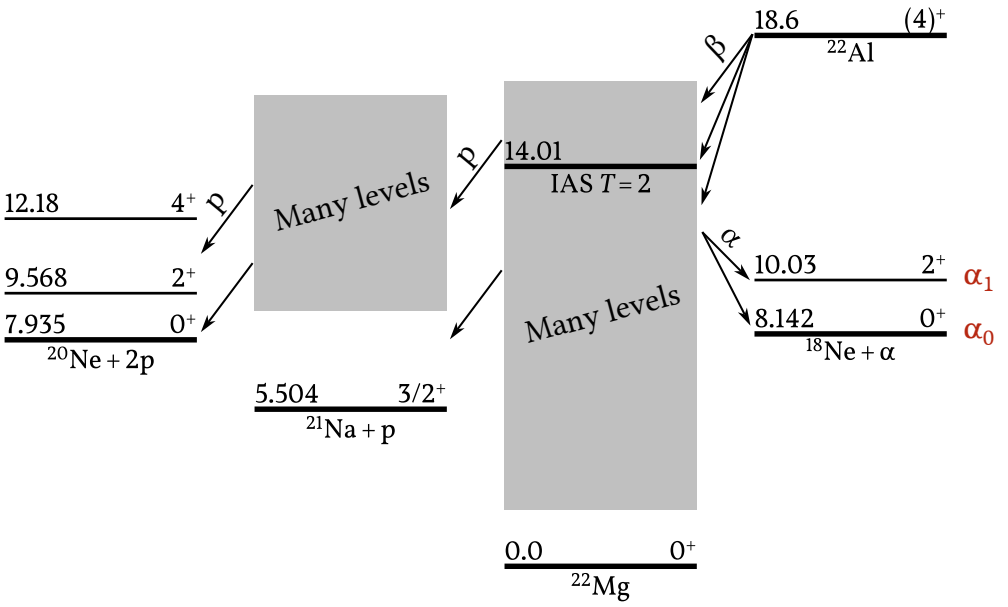

Figure 8.1: Decay scheme of ^{22}Al. All energies are in MeV and are adopted/deduced from AME2020 and ENSDF [Hua+21; Wan+21; Til+95; Til+98; Bas15].

extracted from the thin DSSSDs U1, U2 and U3 above proton punch through threshold are shown. The figure shows the results from all 28 hours of measurement on ^{22}Al and all 24 hours of measurement on ^{26}P as well as a 24-hour background run, for reference. There are some peaks in the background run which are probably due to the implantation of alpha emitters from the 3α calibration source into the surface of the silicon detectors.

From the measurements on ^{22}Al (the left panel in figure 8.3) we observe, for the first time, a transition from the IAS in ^{22}Mg to the 0^+ ground state of ^{18}Ne via the emission of an alpha particle, α_0; see the decay scheme in figure 8.1. The transition from the IAS to the first excited 2^+ state in ^{18}Ne, α_1, was first observed in [Bla+97], and more recently it has also been observed in [Wu+21] by gating on the gamma line in the $2^+ \rightarrow 0^+$ transition. In the literature, the ground state spin of ^{22}Al is assumed to be $J = 4$, while the parity is definitely $\pi = +$. With our observation of the α_0 transition, we can hereby confirm this spin assignment, as the IAS of ^{22}Mg is fed by the Fermi transition from the ground state of ^{22}Al (i.e. both states have the same J^π), and the conservation of angular momentum and parity dictates the emission of α_0 into a space-even

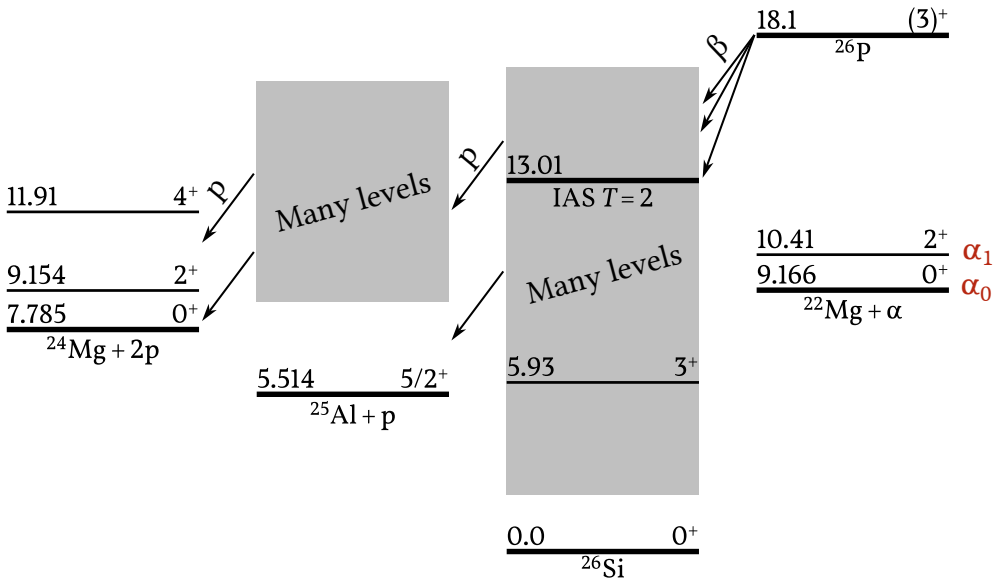

Figure 8.2: Decay scheme of ^{26}P. All energies are in MeV and are adopted/deduced from AME2020 and ENSDF [Hua+21; Wan+21; Bas15; BC22; BH16].

orbit. Smaller or larger spin assignments of even value, $J = 2$ or $J = 6$, are out of the question due to the specific population of intermediate states in ^{21}Na in beta-delayed 2-proton emission.

In the measurements on ^{26}P (the right panel in figure 8.3) we do not see any clear indications of beta-delayed α particles from the IAS. In the literature, the ground state spin of ^{26}P is assumed to be $J = 3$, while the parity is definitely $\pi = +$. The non-observation of α particles from the IAS is consistent with this spin assignment by the same line of reasoning as for ^{22}Al. In the right panel of figure 8.3, the contents of the spectrum up to alpha particle energies of 4 MeV are a bit curious and are not yet understood; further investigations into the nature of this region are required. The contents of the spectrum cannot be produced by (single) protons as the charged particle energies lie above punch through threshold for protons. Hence, the peak at 4.1 MeV, for example, must be produced by an ion that is heavier and/or carries more charge than a proton.

For the case of beta-delayed α emission from the IAS of ^{22}Al, it would be quite interesting to compare with the analogous case of beta-delayed 2-proton emission from the IAS of ^{22}Al. The ground and first excited states of the alpha

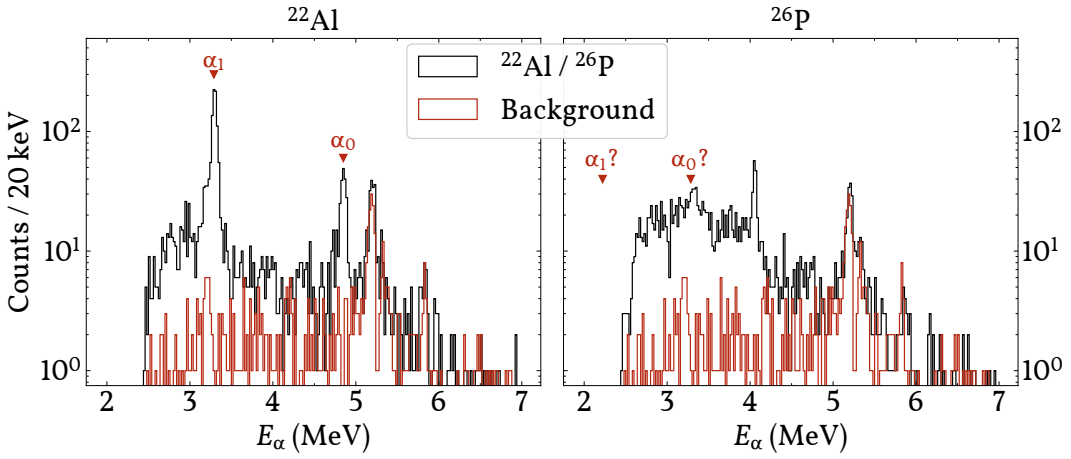

Figure 8.3: Beta-delayed alphas from ^{22}Al (left) and ^{26}P (right). The total measurement time on ^{22}Al is 28 hours, the total measurement time on ^{26}P is 24 hours, and the total measurement time on the background run is 24 hours. The peaks in the background run are assumed to be due to the implantation of alpha emitters from the employed 3α calibration source into the surface of the silicon detectors. The labels α_0 and α_1 indicate where alpha particles emitted from the IAS to the ground and first excited states of ^{22}Al and ^{26}P are expected to appear; see figures 8.1-8.2.

daughter ^{18}Ne and of the 2-proton daughter ^{20}Ne are both 0^+ and 2^+ states. Hence, a comparison of these two decay channels could offer some insights into the differences in ejecting, from the emitter ^{22}Mg, two protons with or without two accompanying neutrons.

8.2 Beta-delayed two-proton emission

In order to study beta-delayed two-proton emission, I first wish to introduce quite the powerful, visual tool, which my co-supervisor Hans Fynbo was the first (as far as I know) to employ in the studies of beta-delayed two-proton emission [Fyn+00]. This visual tool is based on the following ideas. By imposing momentum and energy conservation on the three products (neglecting the beta particle, the neutrino and any recoil imposed by them on the emitter) of beta-delayed two-proton emission – the two protons and the 2-proton daughter – one finds that the Q-value of two-proton emission from a given excited state in the emitter is given by

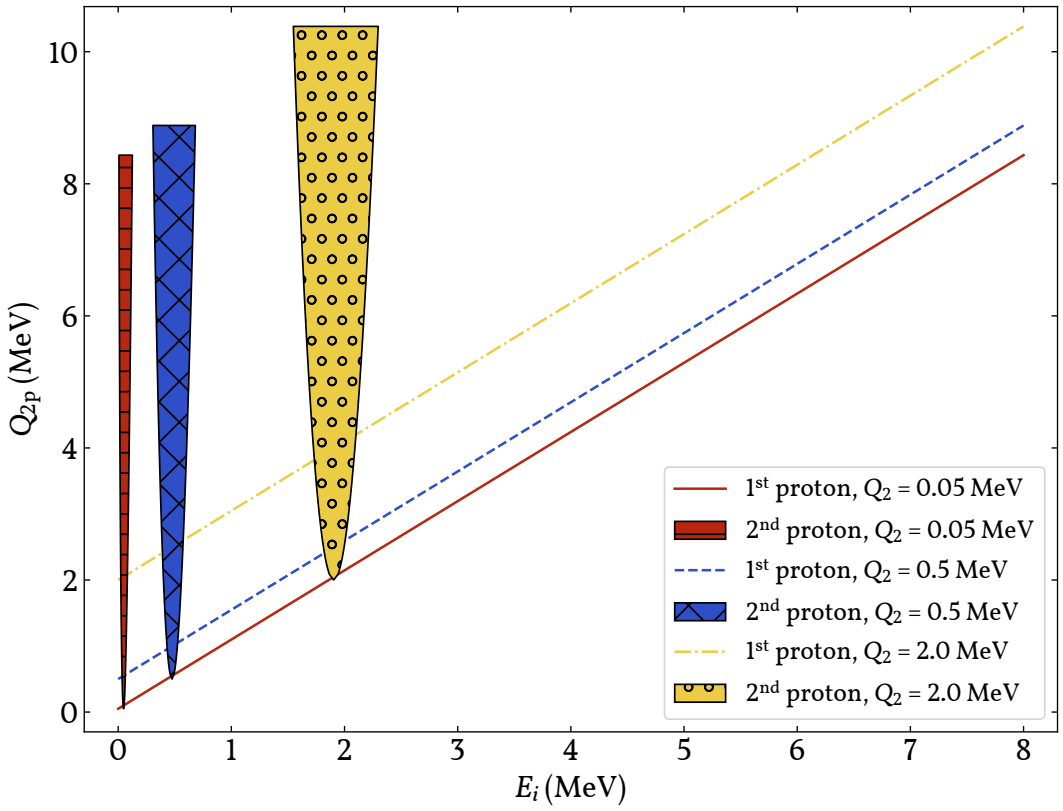

Figure 8.4: Q_{2p} vs. E_i for sequential two-proton emission. The first proton emitted in sequential two-proton emission will, for a given value of Q_{2p}, lie on a straight line which is defined by the mass fraction of the 1-proton daughter and Q_2; see equation (8.2). The second proton emitted in sequential two-proton emission is recoil-broadened; see equation (8.3).

$$Q_{2p} = E_1 + E_2 + \frac{m_p}{M_{2pD}}\left(E_1 + E_2 + 2\sqrt{E_1 E_2}\cos\Theta_{2p}\right) \tag{8.1}$$

where E_1 is the kinetic energy of the first proton, E_2 is the kinetic energy of the second proton, m_p is the proton mass, M_{2pD} is the mass of the 2-proton daughter and Θ_{2p} is the opening angle between the two protons. This relation holds whether the two-proton emission is sequential or direct.

For sequential two-proton emission, the Q-value of two-proton emission, Q_{2p}, can be split into two: Q_1 and Q_2 which are the Q-values of the emissions of the first and second proton, respectively. Q_1 will simply be given by the kinetic energy of the first proton, E_1, and the mass fraction of the 1-proton daughter. For a given value of Q_2, the Q-value of two-proton emission from a given ex-

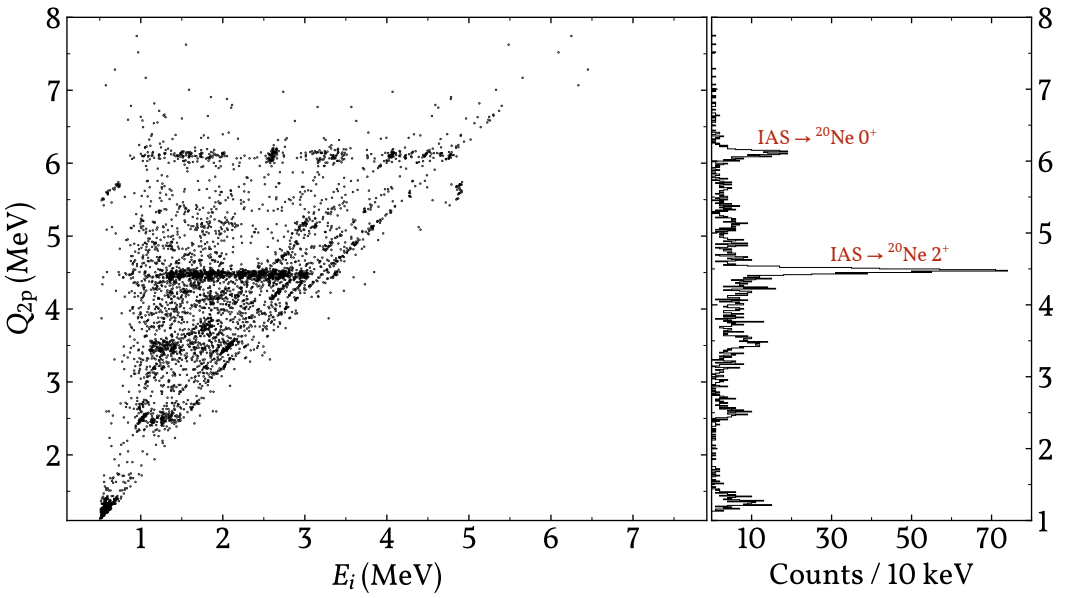

Figure 8.5: Q_{2p} vs. E_i for ^{22}Al. The projection of Q_{2p} is shown to the right. The two most prominent peaks correspond to two-proton emission from the IAS in ^{22}Mg via intermediate states in ^{21}Na to the 0^+ ground state and 2^+ first excited state in ^{20}Ne; see figure 8.1.

cited state in the emitter is then given by

$$\begin{aligned} Q_{2p} &= Q_1 + Q_2 \\ &= \frac{M_{1pD} + m_p}{M_{1pD}} E_1 + Q_2 \end{aligned} \tag{8.2}$$

where M_{1pD} is the mass of the 1-proton daughter. Here, Q_2 depends implicitly on E_1, E_2 and Θ_{2p}. The relation in equation (8.2) is linear in the two proton kinetic energies, E_1 and E_2. Hence, if we were to plot Q_{2p} against the individual proton kinetic energies, $E_i; i = 1, 2$, we would expect (for sequential two-proton emission) the appearance of straight lines with slope given by the mass fraction in front of E_1 in equation (8.2) and with offset given by Q_2. In order to avoid confusion in the following, we shall refer to these straight lines as "diagonals" (their slopes are nearly equal to one). This is exemplified in figure 8.4 where, for each value of Q_{2p}, the two proton kinetic energies E_1 and E_2 will be at the same vertical height. The figure shows the placement of a sample of diagonals with differing values of Q_2.

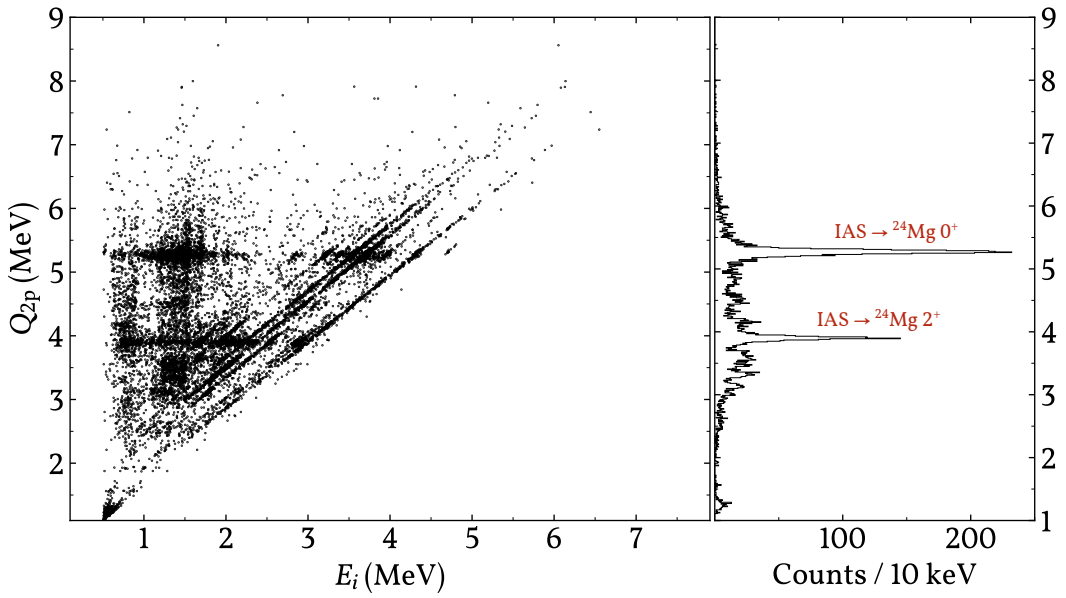

Figure 8.6: Q_{2p} vs. E_i for ^{26}P. The projection of Q_{2p} is shown to the right. The two most prominent peaks correspond to two-proton emission from the IAS in ^{26}Si via intermediate states in ^{25}Al to the 0^+ ground state and 2^+ first excited state in ^{24}Mg; see figure 8.2.

It can be shown that, for sequential two-proton emission, the kinetic energy of the second proton is given by

$$E_2 = E_2' + \left(\frac{m_p}{M_{1pD}}\right)^2 E_1 - 2\frac{m_p}{M_{1pD}}\sqrt{E_1 E_2'}\cos\Theta_{2p} \tag{8.3}$$

where $E_2' = M_{2pD}Q_2/(M_{2pD}+m_p)$. The larger the Q_2, the more recoil-broadened the observed energy distributions of the second proton will be. The opening angle Θ_{2p} between the two protons dictates the placement of E_2 within the shaded regions in figure 8.4.

By plotting Q_{2p} vs. E_i for our experimental data, we can get an immediate visual indication of the presence of sequential beta-delayed two-proton emission in the data. This type of plot is drawn for the cases of ^{22}Al and ^{26}P from the experiment at FRIB in figures 8.5-8.6. In the figures, each two-proton emission event is represented by two points with the exact same value of Q_{2p}. In both figures, diagonals characteristic of sequential decay can be made out. Projections of the Q_{2p} values are also shown in the figures. It is clear that we managed to collect a larger sample of beta-delayed two-proton emission on ^{26}P than we

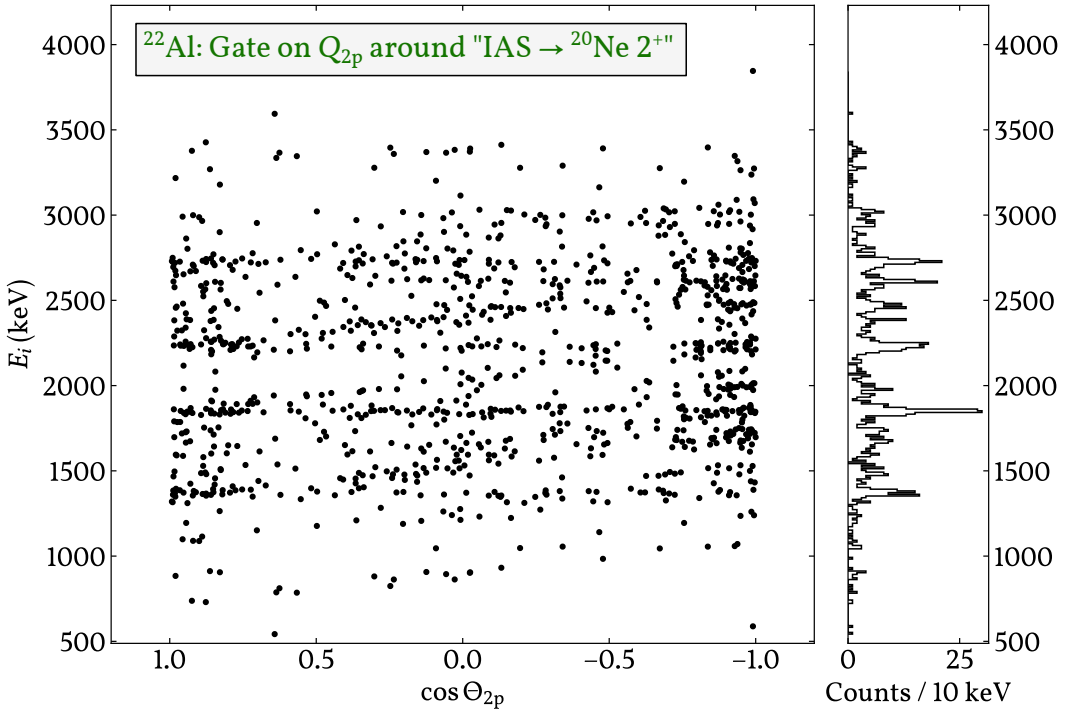

Figure 8.7: E_i vs. cosΘ_{2p} for ^{22}Al. The plot is produced by gating on the most prominent Q_{2p} peak of figure 8.5 labelled "IAS → ^{20}Ne 2^{+}".

did on ^{22}Al in the FRIB experiment; figure 8.5 contains 2,400 events, while figure 8.6 contains 8,000 events. In both figures, the two most prominent peaks in the spectra of Q_{2p} represent two-proton emission from the IAS in the relevant emitter via intermediate states in the corresponding 1-proton daughters to the 0^+ ground state and 2^+ first excited states of the corresponding 2-proton daughters. It is worth noting that deexcitation from ^{21}Na to the 2^+ state in ^{20}Ne is favoured in the decay of ^{22}Al, while the opposite is true of the decay of ^{26}P, where deexcitation from ^{25}Al to the 0^+ state in ^{24}Mg is favoured. Another noteworthy difference in the Q_{2p} vs. E_i plots is that the values E_i seem to be clustered to a larger extent in the decay of ^{26}P than in the decay of ^{22}Al.

Now, returning to equation (8.3), we note that (for sequential two-proton emission) E_2 is linear in cosΘ_{2p}, while E_1 must be independent of Θ_{2p}. We can use this fact to identify the first proton and the second proton in sequential two-proton emission by the method exemplified in figure 8.7. This figure is produced by gating on the most prominent peak in the Q_{2p} spectrum of figure 8.5. In figure 8.7, one can clearly recognise several groups of proton ener-

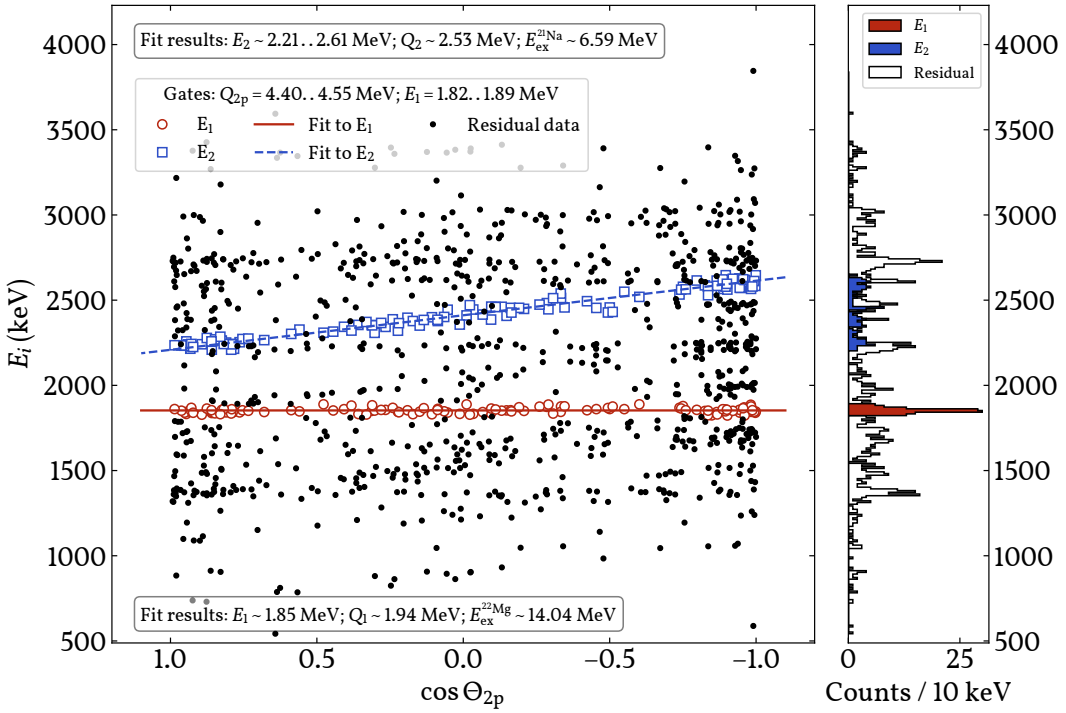

Figure 8.8: E_i vs. cosΘ_{2p} for ^{22}Al with an additional gate. In addition to the gate imposed in figure 8.7, a gate is also imposed on the most prominent peak in the projection of E_i. Based on these gates, estimates of corresponding values of E_1 and E_2 are made, and the excitation energies of intermediate states in ^{22}Mg and ^{21}Na are deduced.

gies E_1, defining horizontal lines in the E_i vs. cosΘ_{2p} plot, as well as groups of proton energies E_2, defining straight lines of slope different from zero. In the projection of E_i values to the right in the figure, the proton energies E_1 stand out as prominent peaks.

Figure 8.8 is a duplicate of figure 8.7, but, in addition to the gate on Q_{2p}, a gate on the most prominent peak in the E_i spectrum is also imposed. Based on this additional gate, a mean value of E_1 is deduced. The corresponding values of E_2 are then fitted to equation (8.3), and the Q-values as well as the relevant excitation energies in the emitter (E_{ex}^{22Mg}) and the 1-proton daughter (E_{ex}^{21Na}) can then be deduced, as is indicated in the figure. The results, $E_{ex}^{22Mg} \sim 14.04$ MeV and $E_{ex}^{21Na} \sim 6.59$ MeV, are calculated based on the mean value of E_1 and the fitted value of E_2 as well as the 2-proton separation energy, S_{2p}, of ^{22}Mg and the excitation energy of the assumed 2^+ final state in ^{20}Ne; see the decay scheme of ^{22}Al in figure 8.1. We see that the derived value of E_{ex}^{22Mg} is consistent with the

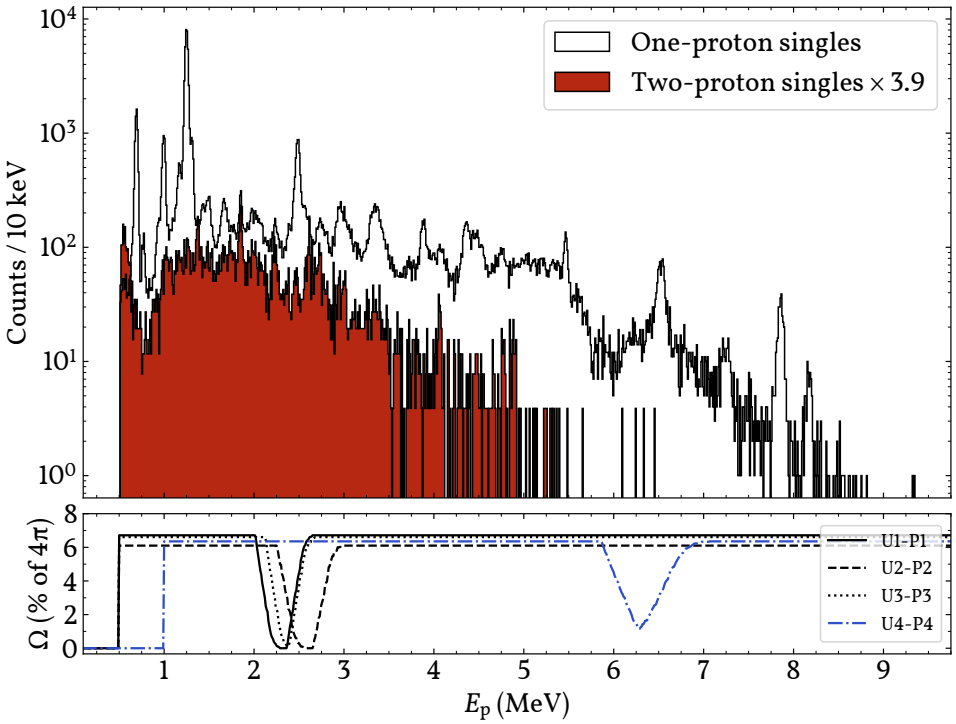

Figure 8.9: Proton singles spectra from the beta decay of ^{22}Al. Both one-proton and two-proton singles spectra are shown. The solid angle coverage Ω is adopted from figure 7.16, and the two-proton singles spectrum is corrected for the summed maximum solid angle coverage of all detector telescopes of 25.7 %.

original identification of proton emission from the IAS. The derived value of $E_{ex}^{^{21}Na} \sim 6.59$ MeV, on the other hand, suggests the population of a state which there may also be weak indications of in figure 4.4 with the gamma gate on the $2^+ \rightarrow 0^+$ transition in ^{20}Ne. The observation of this particular β2p branch is a new discovery; it has not been seen previously e.g. in refs. [Bla+97; Wu+21]. Whether it is also the first time this state in ^{21}Na has been populated by any means requires more scrutiny of the literature, but, at the very least, this state is not well-established in the current literature [Fir15]. The fact that this particular, hitherto unobserved, β2p branch is the most prominent out of all the β2p branches in our measurements of the decay of ^{22}Al suggests that there are many new decay branches to be extracted from the data – this is very exciting.

Based on the methods outlined in this section, it is now possible to map, from the new data recorded at FRIB, the various decay channels of beta-delayed two-proton emission from ^{22}Al and ^{26}P. This work is straightforward, but some

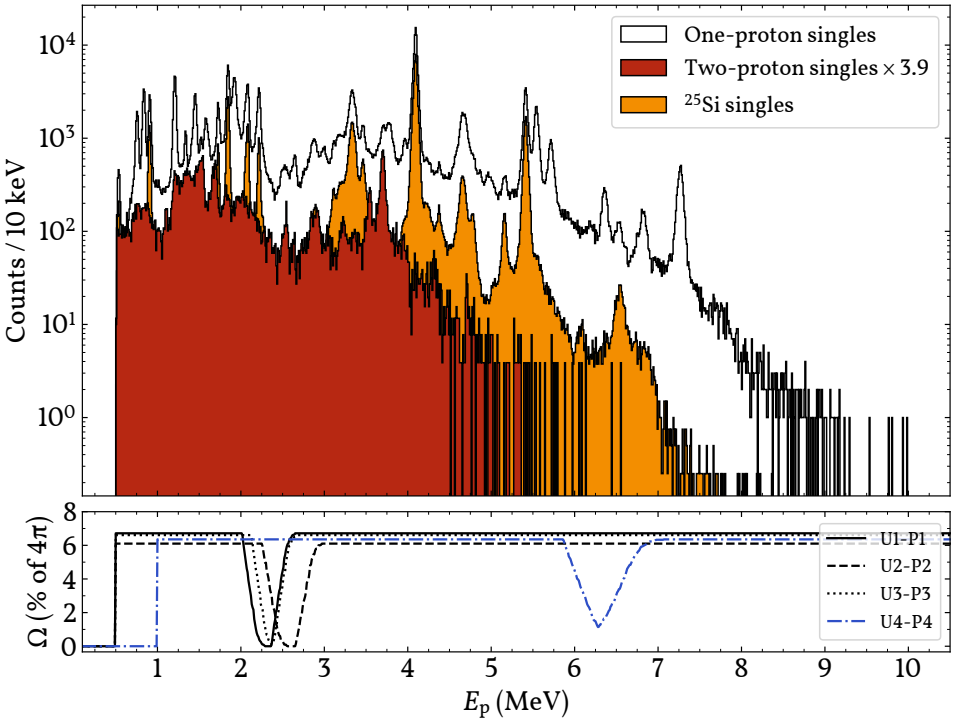

Figure 8.10: Proton singles spectra from the beta decay of ^{26}P. As in figure 8.9, both one-proton and two-proton singles spectra are shown and the detection efficiency of the two-proton singles spectrum is corrected by the solid angle coverage. A singles spectrum from a dedicated measurement on ^{25}Si is also shown; it is clearly seen how many of the peaks of the ^{26}P singles spectrum are due to contamination from ^{25}Si.

care should also be exercised when the various gated spectra are interpreted. It was about when the method of estimating E_1 and E_2 as exemplified in figure 8.8 had been systematised that it was decided to return to the issue of energy calibrations. Systematic deviations in the deduced excitation energies e.g. of ^{22}Mg and ^{21}Na were encountered, and, as was demonstrated in the previous chapter, these deviations were due to the utilisation of energy calibrations based on alpha particle reference energies. In appendix C, figures similar to figure 8.7 are included for the three remaining highlighted peaks in figures 8.5-8.6.

8.3 Beta-delayed one-proton emission

When we are confident that we have identified all the β2p branches contained in our data by employing the methods of the previous section, we can then

move on to identify the βp branches of our data with minimal risk of misidentifying a signal from two-proton emission as that of one-proton emission: When studying the spectra resulting from βp analyses, the individual proton energies of β2p add to the true signals of βp. Our low-energy decay experiment utilising segmented silicon detectors has the advantage that we can extract information on the correlation between two proton signals, as was demonstrated in the previous section, but the solid angle coverage of our 4 DSSSDs amounts to 25.7 % of 4π at best (figure 7.16). Hence, in the majority of β2p events that take place within our experimental setup, there is a bias towards observing just one of the two protons emitted in β2p.

For now, we forego the complete identification of all β2p branches and present proton singles spectra from the decays of ^{22}Al and ^{26}P in figures 8.9-8.10. In both figures, both one-proton singles and two-proton singles spectra are shown; the latter being the complete E_i spectra from the previous section. The two-proton singles spectra are corrected, for all proton energies, by the summed maximum solid angle coverage Ω of all detector telescopes of 25.7 %; i.e. the sum of the four curves of Ω, for example, at $E_\mathrm{p} = 4$ MeV. This correction will, naïvely, compensate for the probability of observing a second proton given that one has already observed the first proton in a given β2p event, and provided there is no preferred spatial distribution of the two protons.

In the case of ^{22}Al, the correction brings some of the peaks around and below 2 MeV of the two-proton singles towards the same intensity as in the one-proton singles spectrum. Our spectrum clarifies some misidentifications of βp and β2p events reported in the study of ^{22}Al at the HIRFL[1] facility [Wu+21] (we use the same proton peak labelling as in the HIRFL paper):

- We see a peak due to β2p between p_8 and p_9 around 1.9 MeV, which is missing in the HIRFL proton singles spectrum.
- p_{10} which is not assigned to either βp or β2p in the HIRFL study seems, in our spectra, to be part of a β2p event.
- p_{22} which is speculated to be due to βp in the HIRFL study seems, in our spectra, to be part of a β2p event.

[1] Heavy Ion Research Facility in Lanzhou, China.

Other indications of disagreements between our spectra and the HIRFL spectra require further investigation.

In the case of ^{26}P, figure 8.10, this kind of comparison is not yet feasible, as the contamination from ^{25}Si complicates the picture. Here, it is particularly advantageous to extract all possible β2p information via the methods presented in the previous section, before trying to characterise the one-proton singles spectra. The β2p spectra of the previous section are "safe", in the sense that, with the event rates of order 1-10 particles per second during the FRIB experiment, the probability of a proton emitted from ^{25}Si to sneak into the β2p spectra is practically zero.

Part III

Taking stock

Chapter 9

Outlook

9.1 Beta-delayed particle emission

Based on the experiments on light proton-rich nuclei presented in this thesis, we are able to explore new avenues in the evolution of nuclear structure far from stability, and we gain new insights into the exotic decay mechanisms that are beta-delayed charged particle emission. A question which has fostered much discussion in the studies of beta-delayed two-proton emission, which we have completely ignored in the material presented thus far, is whether the two-proton emission can proceed in a direct, rather than sequential, fashion by the emission of ^{2}He; see e.g. [Bro90]. As is evident from the data presented on ^{22}Al and ^{26}P in the previous chapter, sequential beta-delayed two-proton emission is prevalent for both nuclides. Whether the signature of direct two-proton emission is present in the data is still too early to tell. The study of the potential competition between sequential and direct two-proton emission was, however, one of the main goals presented in the proposal of the experiment at FRIB; this topic is something to look much deeper into in the future.

The distribution of opening angles Θ_{2p} between the two protons involved in two-proton emission has been suggested as an observable which can clarify the question of sequential vs. direct emission. In figure 9.1, preliminary results of Geant4 simulations of various opening angles Θ_{2p} between two protons are shown. The simulations are carried out using the detector geometry illustrated in figure 7.3. Two protons are emitted in random directions from the catcher

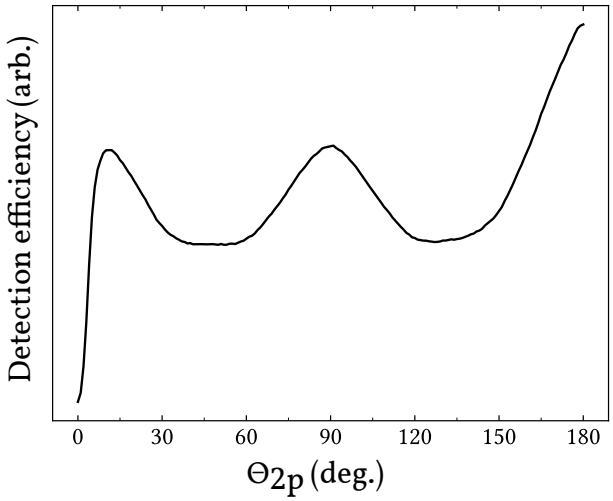

Figure 9.1: Preliminary simulated variation of detection efficiency vs. two-proton opening angle Θ_{2p}. The results of the simulations are based on the detector geometry illustrated in figure 7.3, where two protons are emitted in random directions from the catcher foil, constrained on specific values of Θ_{2p} for the different points in the figure.

foil, but constrained on specific values of Θ_{2p} for the different points in the figure. The variation of detection efficiency for different opening angles is related to the variation of the curve in the figure. As was mentioned in chapter 7, further refinements of the Geant4 simulations are planned in order to improve the geometry description of the detection setup; these refinements will also be highly relevant for the modelling of the detection efficiency distribution as a function of Θ_{2p}. The current simulations do not take detector threshold values and the dead and spurious zones of the detector telescopes into account.

As was mentioned in passing in chapter 6, the characterisation of the astrophysically important 3^+ resonance at 5.93 MeV excitation energy in ^{26}Si is also a main goal of the experiment carried out at FRIB. The proton kinetic energy due to proton emission from this resonance is around 400 keV, and the extraction of these protons from our thin DSSSDs will require some care.

The broad presentation of spectra from ^{22}Al and ^{26}P revealed that there are many new observations contained in these data. Careful mapping of the decay schemes of these two nuclides and their many complex decay paths is another goal for the future. A prevalent alternative to our experimental methods is the implantation of rare ion beams of high energy directly into (stacks of) de-

tector(s). Apart from the larger dispersion of the involved beam particles, this experimental method also has the issue (which can be handled to some extent) of summing of individual particle energies. This leads to the loss of information regarding the correlations between the particles which participate in the multi-particle breakups. We believe that our experimental methods are highly ideal for the consolidation of the decay schemes of ^{22}Al and ^{26}P which are currently established in the literature.

Apart from all of these points, the manuscript included in this thesis on the detailed studies of the decay of ^{21}Mg exemplify very well what else we can do with the new data on ^{22}Al and ^{26}P. When the various decay channels of ^{22}Al and ^{26}P have been properly mapped, we can attempt to extract nuclear structure information based on interference effects between states of shared quantum numbers and penetrability arguments. There is also a link between such penetrability arguments and the nature – sequential vs. direct – of two-proton emission. Finally, we can map the beta strength to the various excited states in the emitters of the decays, we can see how the deduced beta strength compares to the theoretical expectations for the Fermi and Gamow-Teller strengths, and we can look for indications of mirror asymmetry effects by comparing to the nuclei mirror to ^{22}Al and ^{26}P, ^{22}F and ^{26}Na.

9.2 Rare ion beam facilities

The reason why the experiment on ^{22}Al and ^{26}P was carried out at FRIB and not, say, at ISOLDE where our collaboration has carried out many experiments over the years is due to the beam production abilities of the two different facilities. The ISOLDE Yield Database [ISO24] has no records on the two nuclei ^{22}Al and ^{26}P, and these specific nuclei are notoriously difficult to produce with any decent yields with the ISOL method. Broadly speaking, there are two kinds of limitations in the production of rare ion beams:

1. Limitations due to reaction cross sections between primary beam and production target.

2. Limitations due to the chemistry of the production target as well as other

media encountered by the secondary beam along its beam path, after extraction from the production target.

In particular, the limitations due to chemistry are fundamentally very different for ISOL and in-flight facilities. At ISOL facilities, the chemical properties of the rare ions of interest within the production target is the essential element which dictates whether it is feasible, at all, to extract the rare ions of interest from the production target; if the time scales of diffusion, for example, are too long compared to the lifetimes of the rare ions, they will never make it to the experimental setup that requests them. In comparison, in-flight facilities have practically no limitations due to chemistry at the production target. In our experiment on ^{22}Al and ^{26}P, chemistry did become something to consider along the beam line, but this was not until the rare ions reached the Advanced Cryogenic Gas Stopper (ACGS) of the Gas Stopping Area, right before our experimental setup. Compared to the diffusion of rare ions from a thick production target, the extraction time from the ACGS is orders of magnitude faster, diminishing, to a large extent, the concern of the lifetimes of the rare ions.

ISOLDE and FRIB are by no means the only rare ion beam facilities worth noting on a global scale. In the previous section we mentioned the Heavy Ion Research Facility in Lanzhou (HIRFL), China, when comparing our ^{22}Al data to the most recent study of this nuclide. This study was carried out at The Radioactive Ion Beam Line in Lanzhou (RIBLL). Other facilities that spring to mind include the recently commissioned ISOL facility SPIRAL2 at GANIL in France, GSI/FAIR in Germany and the in-flight facility RIBF in Japan. It is by the combined efforts of researchers at all of these facilities (and many more) that our understanding of the nuclear landscape can be expanded ever further.

9.3 Parallels in the proton-rich sd-shell

As a final, brief note, we wish to return to the repeated "IAS complex" structure presented in figure 4.3 in the decay of ^{21}Mg. The difference in intensity of the transitions to the ground and the first excited states cannot be explained by penetrability arguments alone. Furthermore, we have seen indications in the ^{25}Si data from FRIB of the same kind of repeated pattern and of, seem-

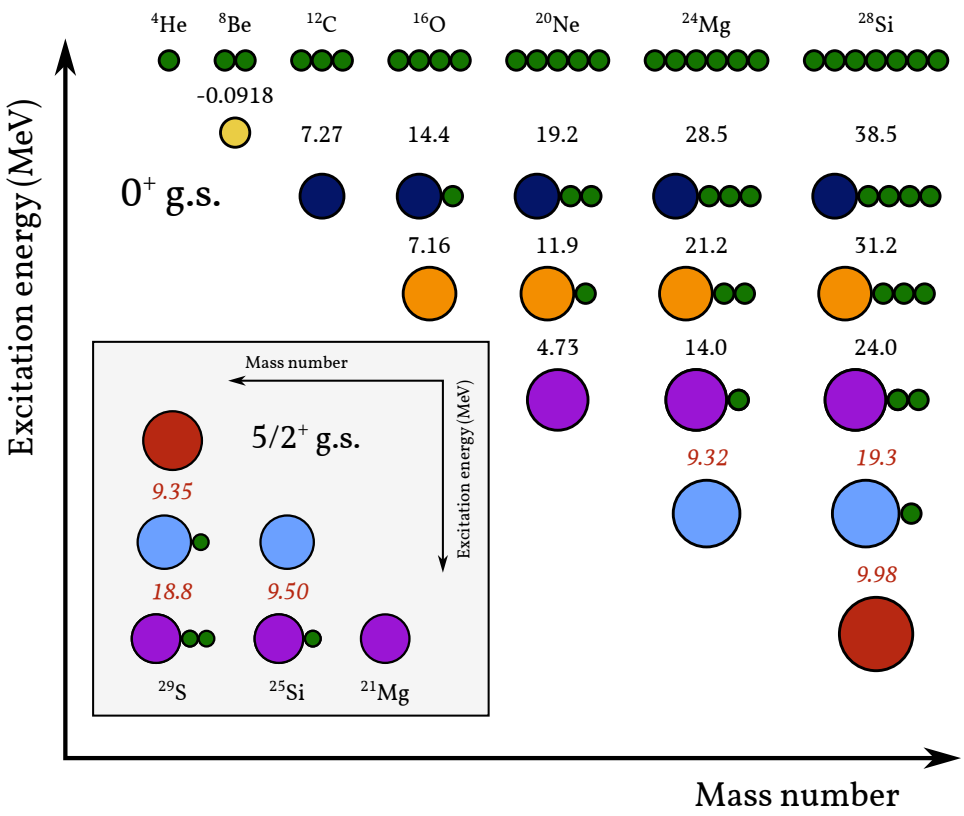

Figure 9.2: Ikeda diagram of the classical ^{4}He-^{8}Be-^{12}C-...-chain and of a potential parallel in the sd-shell nuclei ^{21}Mg, ^{25}Si and ^{29}S. See text.

ingly, similar differences in intensity. Both ^{21}Mg and ^{25}Si have ground state spins and parities of $J^{\pi} = 5/2^{+}$. In figure 9.2 an *Ikeda diagram* [Fre07] is drawn, which is a qualitative illustration of a nuclear structure model in which consecutively heavier nuclei are constructed by adding alpha particles onto lighter nuclei. The inset of the figure shows a more atypical Ikeda diagram in which ^{25}Si and ^{29}S are constructed from ^{21}Mg by adding onto ^{21}Mg one and two alpha particles, respectively. The (likely) inertness of an extra alpha particle in the nuclear potential of ^{21}Mg could be a possible explanation of the similar patterns of the decays of ^{21}Mg and ^{25}Si. ^{21}Mg, ^{25}Si and ^{29}S have the same ground state spins and parities, and we are currently contemplating, in our collaboration, if a study of the similarities in the decays of these three nuclides is worth pursuing. We are also currently working with our colleague Aksel Jensen, a shell model theoretician, in Århus on a possible explanation of the difference in intensities of the "IAS complex" due to shape deformations of the precurs-

ors, emitters and one-proton daughters; i.e. there might be a way to quantify the variations in intensity in terms of the rotational band K quantum number (see e.g. [HM12]).

Appendices

Appendix A

Technical drawings for FRIB experiment

A.1 Silicon detector holder

The silicon detector holder used in the experiment at FRIB consists of 3 pieces: One piece which is to hold the 4 silicon detector telescopes in the horizontal plane, and two identical pieces which can be attached as lids on the top and on the bottom of the first piece. These two lids are each to hold 1 silicon detector telescope.

The technical drawings included on the following pages are designed and drawn by John Erik Vad Andersen from the workshop at the Department of Physics and Astronomy in Århus. All lengths are given in millimeters. The target frame used in the FRIB experiment is also present in the technical drawings.

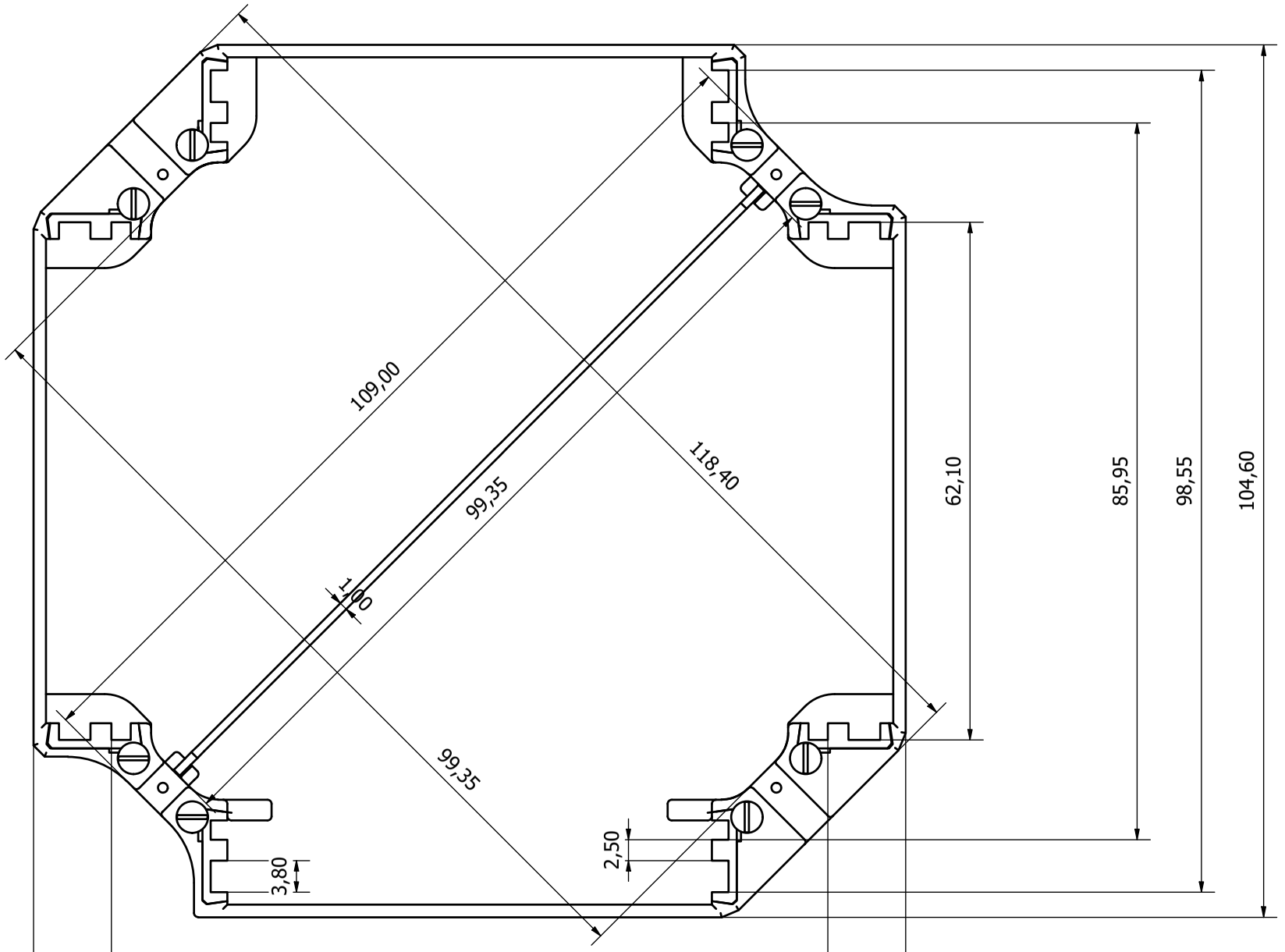

Designed by	Checked by	Approved by	Date		Date	
erik					21/08/2023	

cube-top-down		Edition	Sheet 1 / 1

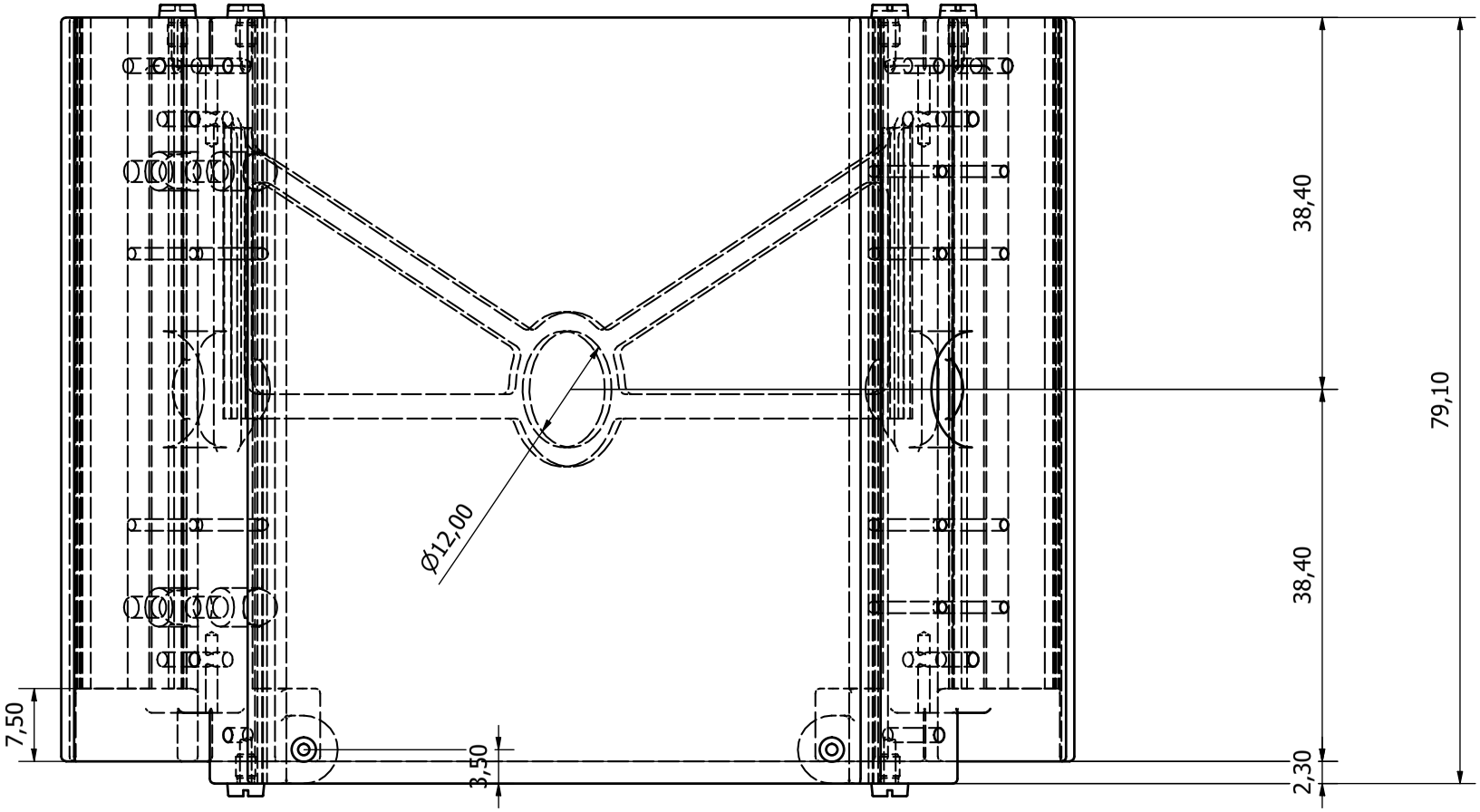

Designed by	Checked by	Approved by	Date		Date	
erik					21/08/2023	

cube-side-on		Edition	Sheet 1 / 1

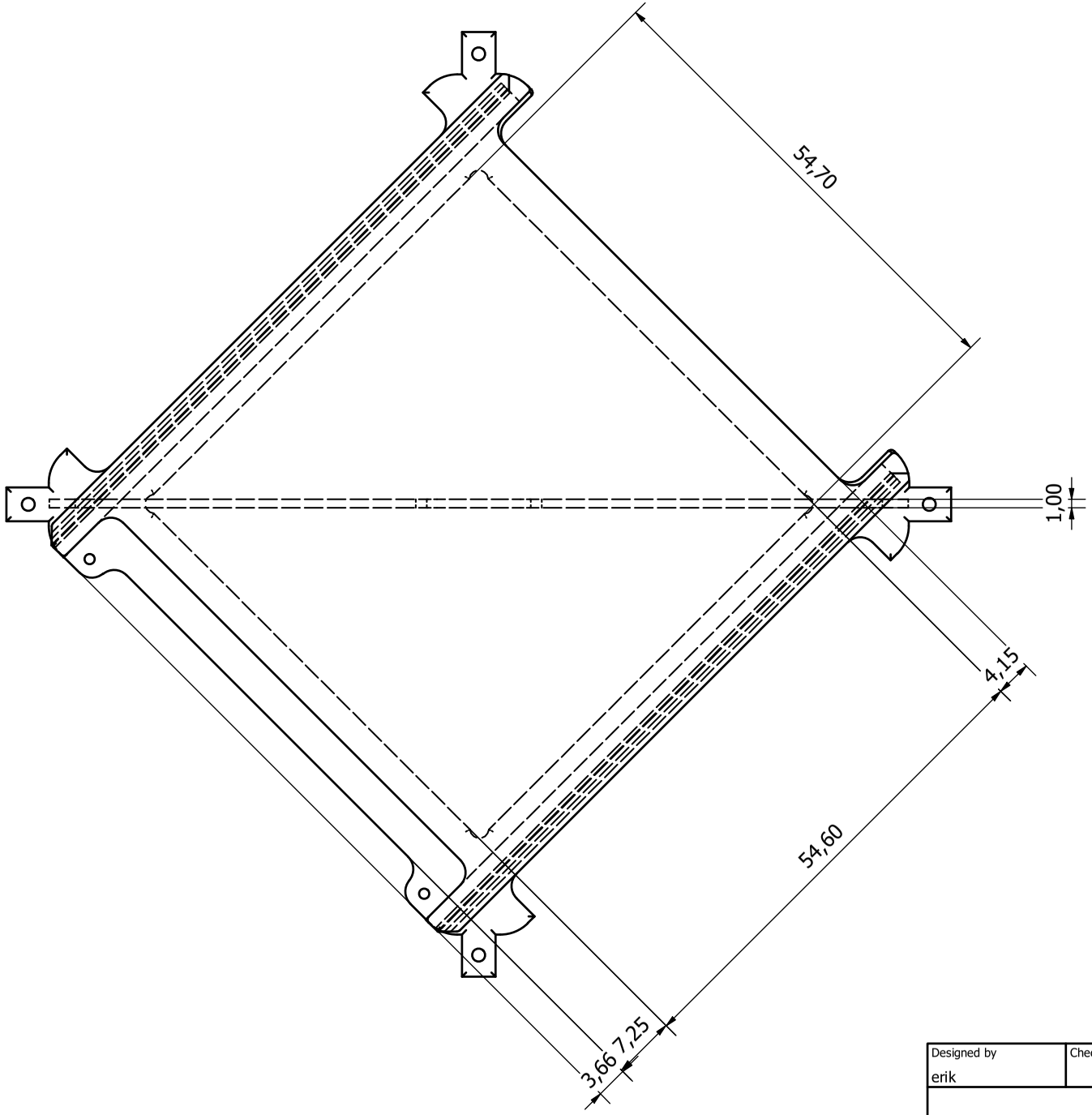

Designed by	Checked by	Approved by	Date		Date	
erik					21/08/2023	

lid-top-down		Edition	Sheet 1 / 1

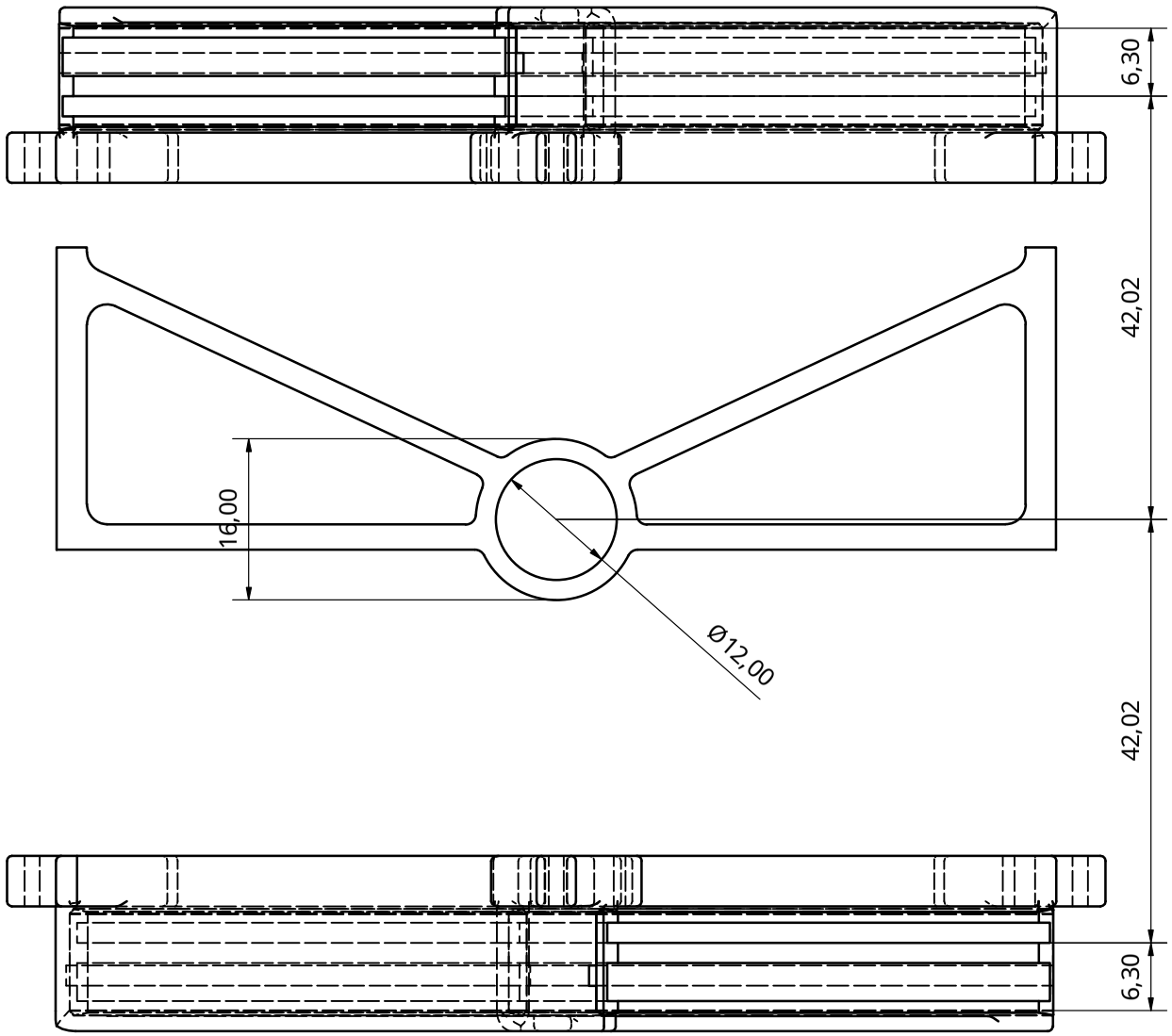

Designed by	Checked by	Approved by	Date		Date	
erik					21/08/2023	

lids-side-on		Edition	Sheet 1 / 1

A.2 Silicon detector PCB

Micron Semiconductor Ltd.'s product catalogue (backed up to our group's wiki page [AUS24]) contains many of the necessary dimensional details of the actual slabs of silicon which make the detectors, but not as many details on the printed circuit boards (PCBs) onto which the slabs of silicon are mounted. In order to be able to describe the placement of our silicon detectors accurately in the geometry of our silicon detector holders, we need these measures as well.

Relevant measures of the PCBs are given in the technical drawing included on the following page. All lengths are given in millimeters.

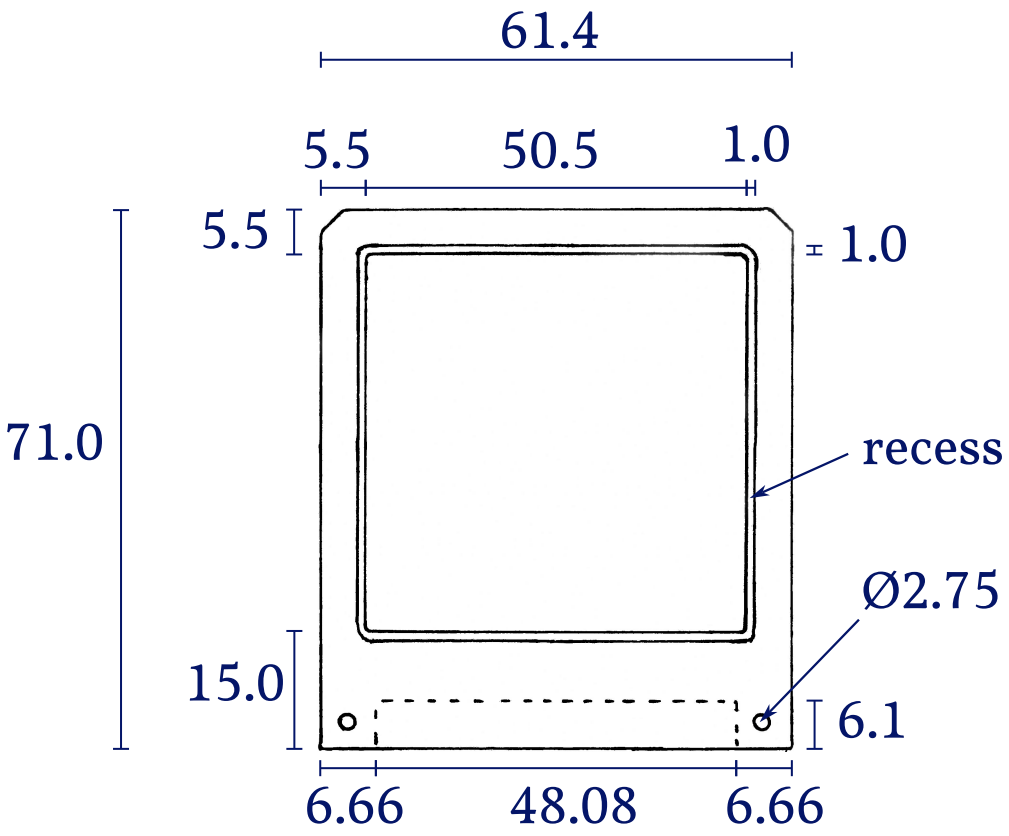

p-side out of page

PADs have indent marked with dashed line

W1's PCB is 1.5 mm thick with 1.0 mm deep recess

PAD's PCB is 3.0 mm thick with 2.0 mm deep recess

A.3 Vacuum chamber and feedthrough with rod

The following technical drawings give some relevant measures in relation to the size of the vacuum chamber and the distances from silicon detector holder to feedthrough flange via the rod on which the silicon detector holder is fixed.

The technical drawings included on the following pages are designed and drawn by John Erik Vad Andersen from the workshop at the Department of Physics and Astronomy in Århus. All lengths are given in millimeters.

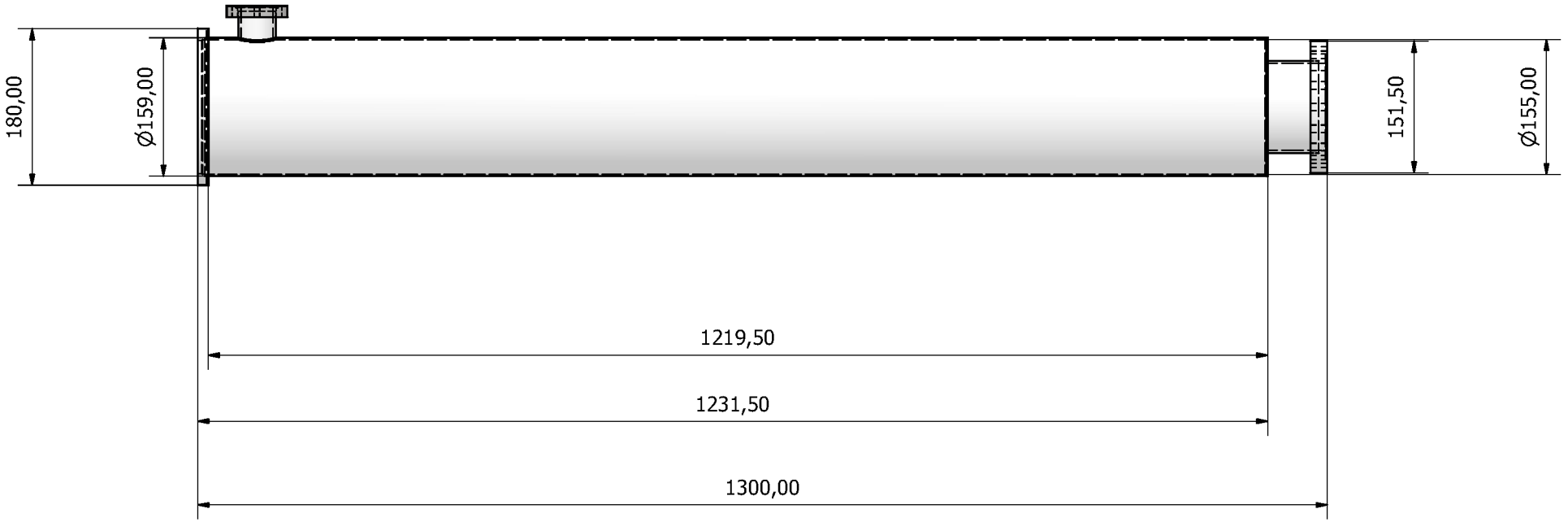

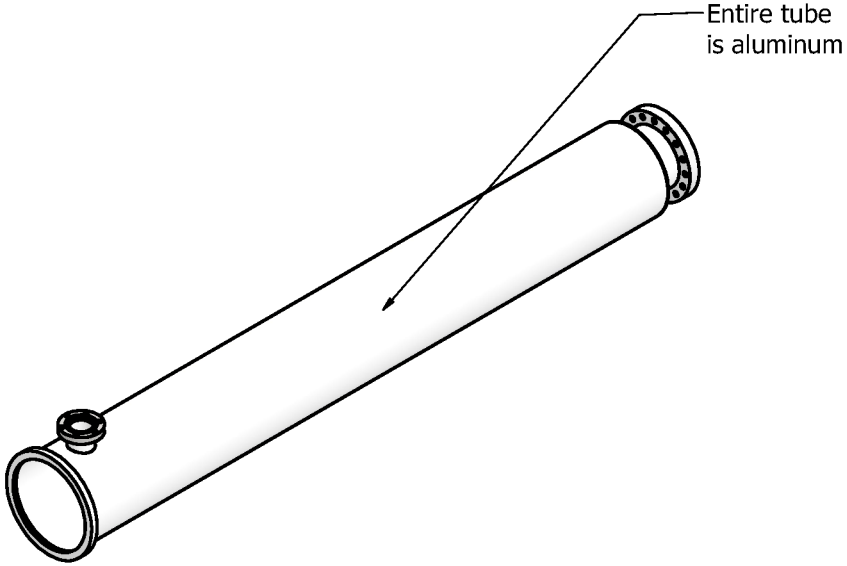

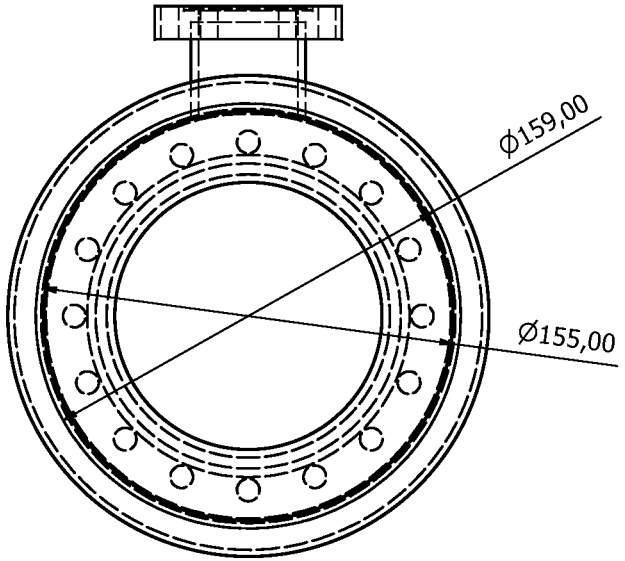

Designed by	Checked by	Approved by	Date		Date	
erik					31/05/2023	

tube		Edition	Sheet 1 / 1

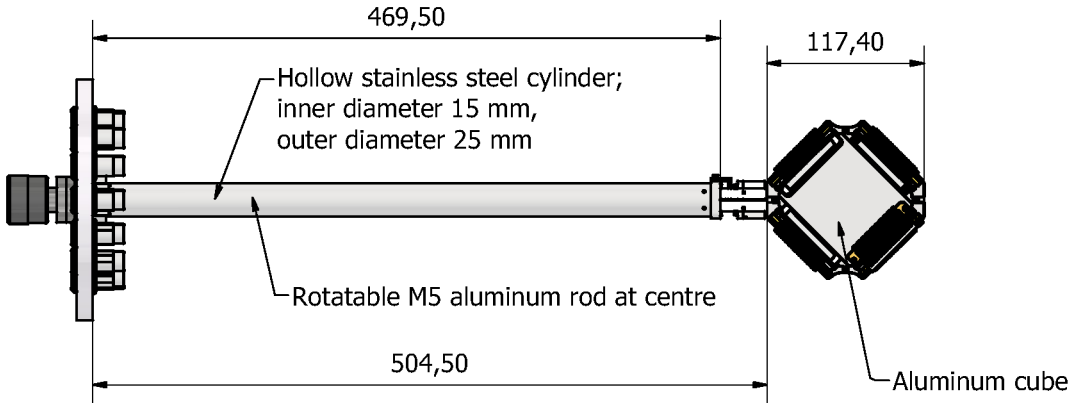

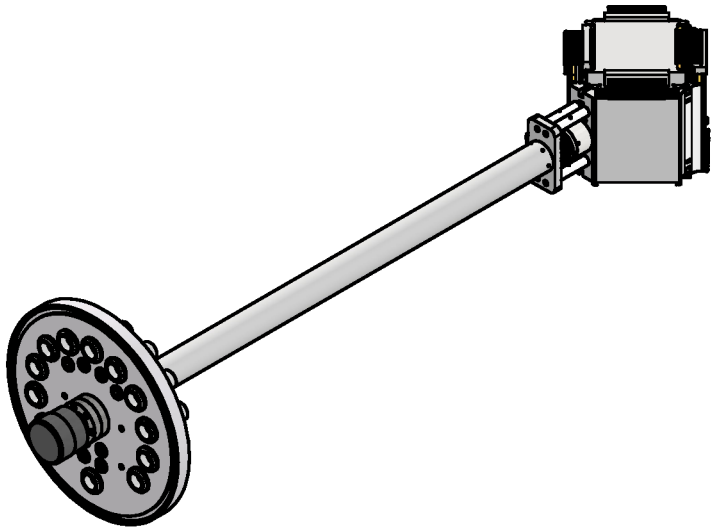

Designed by	Checked by	Approved by	Date		Date	
erik					31/05/2023	

rod		Edition	Sheet 1 / 1

Appendix B

Hardware and software configuration of FRIB experiment

B.1 Trigger and ADC thresholds

Figures B.1 and B.2 illustrate the trigger and ADC thresholds of the individual detector channels of the FRIB experiment. The trigger thresholds were, to a large extent, configured per shaper module, but some individual channels on the p-side of U1 and U2 were optimised in order to expand the dynamic range towards low energy. The ADC thresholds were configured by first disabling the ADC thresholds entirely and then fitting Gaussians, to the resulting pedestal-ridden spectra. 5 times the standard deviation of the fitted Gaussians was added to the mean value of each fitted Gaussian, and the results of this routine define the ADC thresholds of each individual channel. In retrospect, especially the Pads could have benefited from having lower ADC thresholds such that the dead and spurious zones of the detector telescopes would be of smaller extent. As long as true signals in the Pads would rise above the background that is (part of) the pedestals of the ADCs, a lower ADC threshold would have been acceptable, as the higher data throughput of just 5 detector channels would not have over-encumbered the DAQ. Conceivably, employing 3 instead of 5 times the standard deviation in the routine just described would have been just fine.

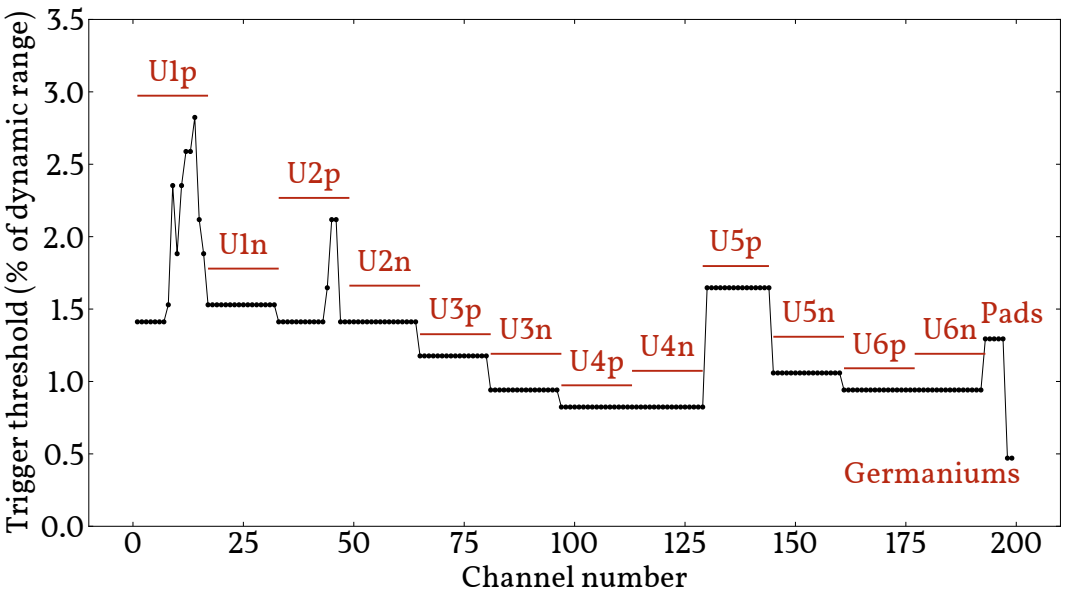

Figure B.1: Trigger thresholds of individual detector channels.

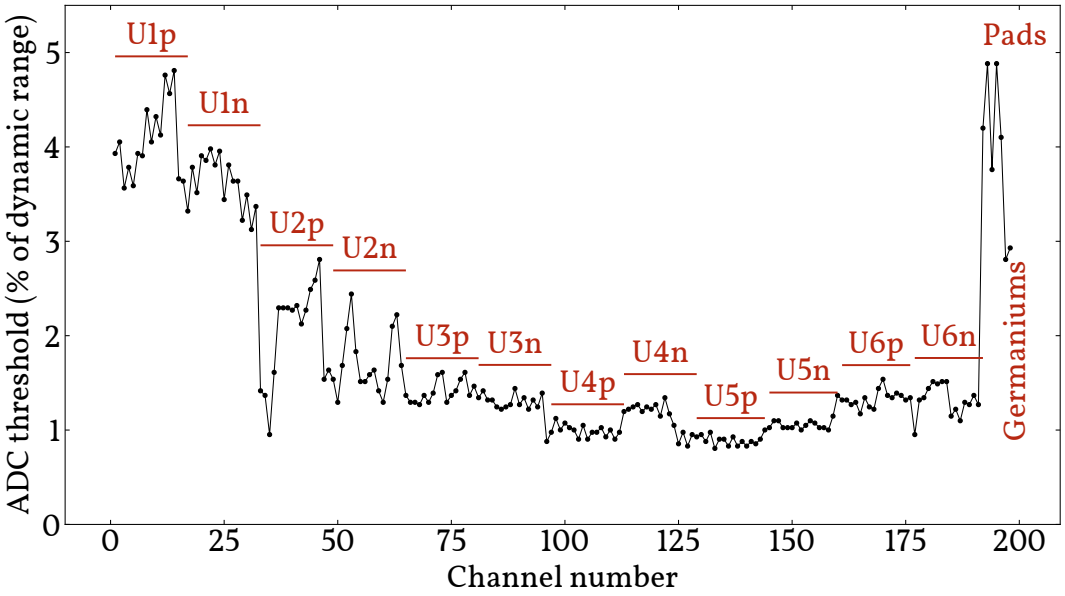

Figure B.2: ADC thresholds of individual detector channels.

B.2 Online access

As mentioned in section 6.3, a link is provided here to a data archive which contains all the hardware and software configuration files that defined the experimental setup at FRIB; this includes the trigger and ADC thresholds depic-

ted in figures B.1 and B.2, the shaping times, pole-zero configurations, etc. of the shaping amplifiers and much more. The iteration of the Git super project called "ausadaq" which was used during the experiment is also part of the data archive, as are the raw, unpacked and calibrated/front-back-matched data from the experiment. Furthermore, the data archive contains files with the employed calibration coefficients of the detector channels, it contains the software which was run on a separate computer to control and monitor the germanium detectors, and it contains log files from the individual pieces of software which were running during data recording. Finally, the data archive also contains a spreadsheet which gives an overview of the conditions of the different runs during the experiment.

The data archive can be found online in the Electronic Research Data Archive (ERDA) at Aarhus University via the following link

`https://anon.erda.au.dk/sharelink/cjzfJWjX4X`

And I am, myself, hosting a mirror of the archive on my own webpage at the following link

`https://www.tenku.dk/files/e21010`

Consult the `README` at the base of the data archive for further information.

The "ausadaq" repository is available at

`https://gitlab.au.dk/ausa/ausadaq/`

Appendix C

Mirror figures

In this appendix, figures that *mirror* other figures presented throughout the thesis are included. The contents of the figures presented here are conceptually similar to specific figures already presented in the main matter of the thesis, but they might illustrate how a conclusion different from the one highlighted in the main matter of the thesis is drawn. For example, a figure in the main matter of the thesis might present a spectrum extracted from a specific detector, and a given mirror figure, presented here, might illustrate the same type of spectrum, but for a different detector. The appendix is organised into sections bearing the same names as the sections in which the original figures first appeared. The figure texts of the figures presented in this appendix reference the figure which they mirror and briefly describe how they differ from it.

C.1 Detector telescope characterisation

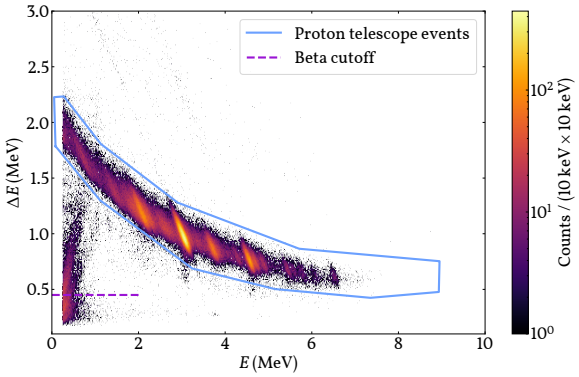

Figure C.1: Mirror of figure 7.14 for the U1-P1 detector telescope.

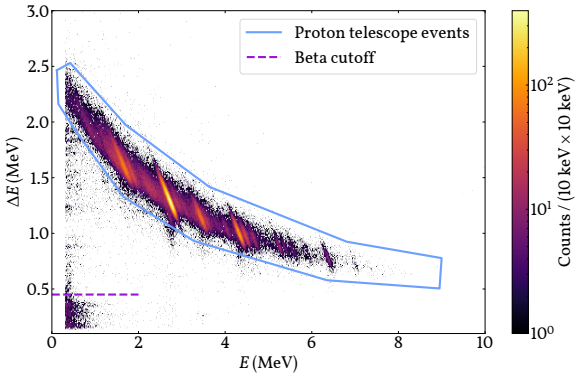

Figure C.2: Mirror of figure 7.14 for the U2-P2 detector telescope.

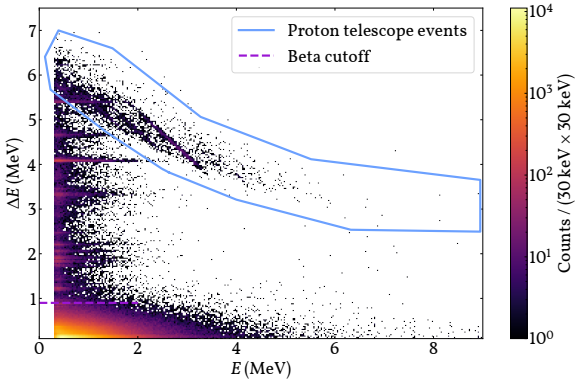

Figure C.3: Mirror of figure 7.14 for the U4-P4 detector telescope.

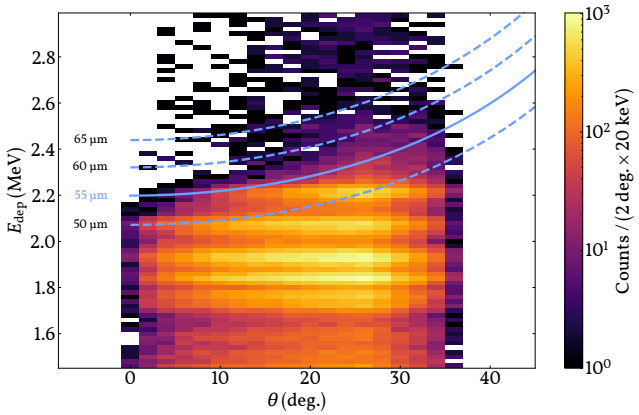

Figure C.4: Mirror of figure 7.15 for the DSSSD U1.

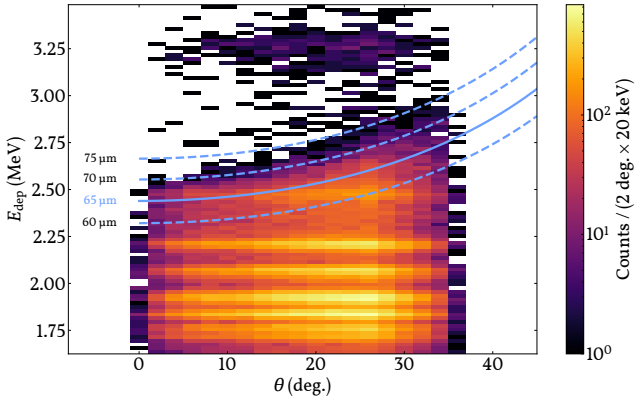

Figure C.5: Mirror of figure 7.15 for the DSSSD U2.

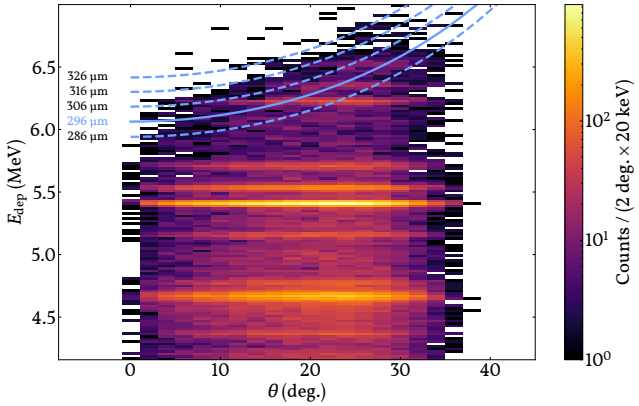

Figure C.6: Mirror of figure 7.15 for the DSSSD U4.

C.2 Beta-delayed two-proton emission

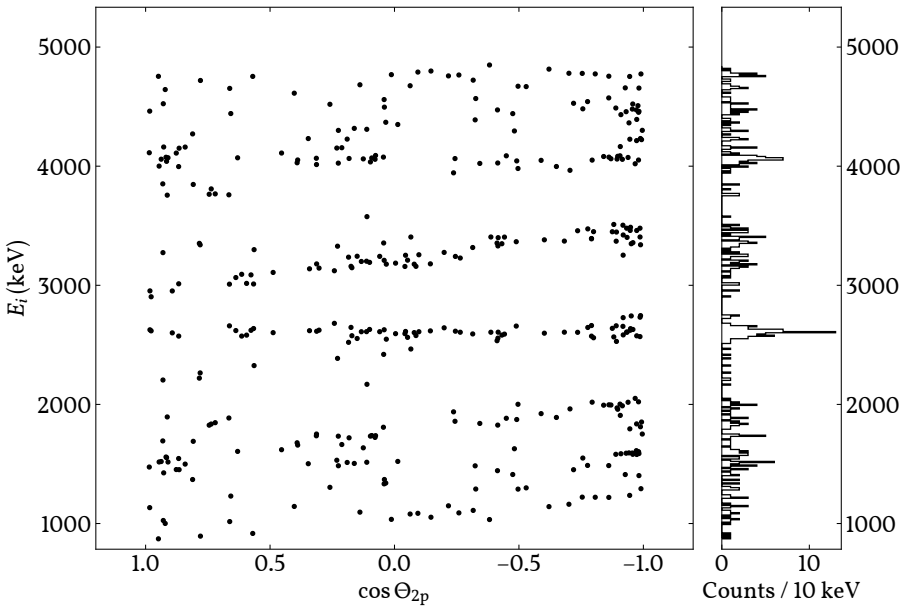

Figure C.7: Mirror of figure 8.7 for a gate on the "IAS $\rightarrow$ ^{20}Ne 0^+" peak.

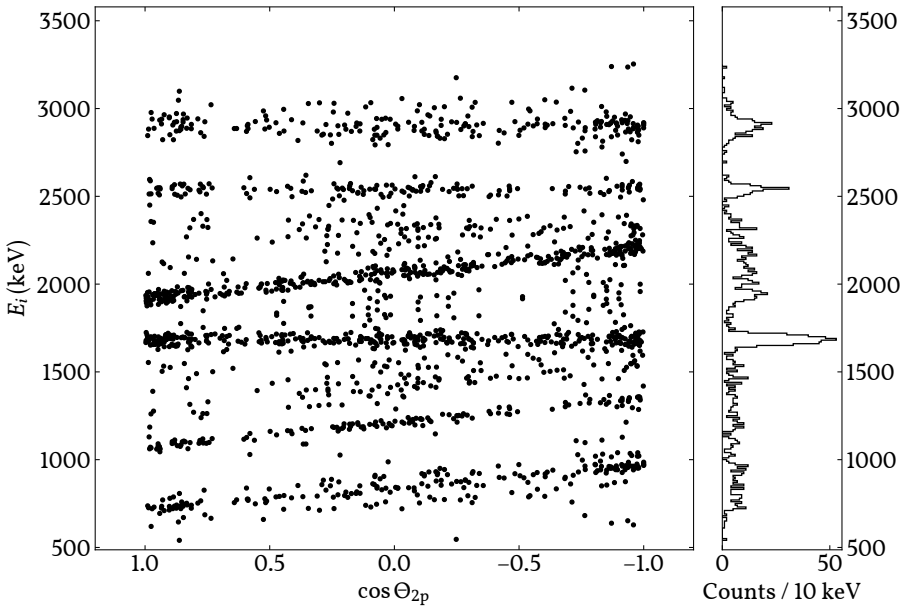

Figure C.8: Mirror of figure 8.7 for a gate on the "IAS $\rightarrow$ ^{24}Mg 2^+" peak.

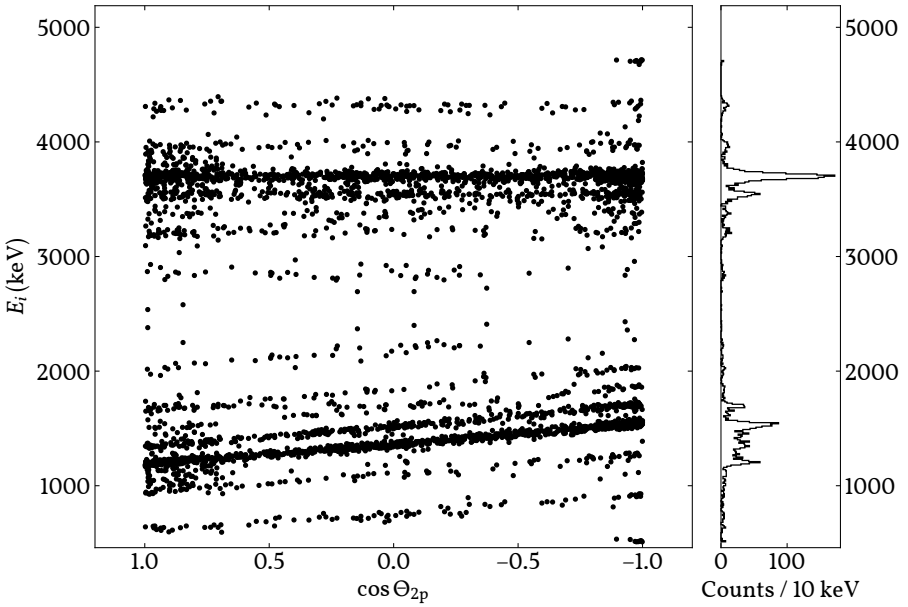

Figure C.9: Mirror of figure 8.7 for a gate on the "IAS $\rightarrow$ ^{24}Mg 0^+" peak.

References

[Ago+03] S. Agostinelli et al. 'Geant4 — a simulation toolkit'. Version 11.2.0. In: *Nuclear Instruments and Methods in Physics Research Section A* 506.3 (2003), p. 250. URL: https : / / geant4 . web . cern . ch/ (visited on 21/02/2023).

[AH13] I. J. R. Aitchison and A. J. G. Hey. *Gauge Theories in Particle Physics: A Practical Introduction*. 4th ed. Vol. 2. CRC Press, 2013. ISBN: 978-1-4665-1299-3.

[Alt18] F. Althausen. *Vollkorn Typeface*. Version 4.105. 9th May 2018. URL: http://vollkorn-typeface.com/#download (visited on 15/12/2023).

[Asv+22] Foteini Asvesta et al. 'High Intensity Studies in the CERN Proton Synchrotron Booster'. In: *JACoW IPAC* 2022 (2022), p. 2056.

[AUS24] AUSA Group. *Wiki - Detectors*. 2024. URL: https://wiki.kern.phys.au.dk/Detectors (visited on 21/02/2024).

[Bad+22] A. Badalà et al. 'Trends in particle and nuclei identification techniques in nuclear physics experiments'. In: *La Rivista del Nuovo Cimento* 45 (2022), p. 189.

[Bas06] M. S. Basunia. 'Nuclear Data Sheets for A = 237'. In: *Nuclear Data Sheets* 107.8 (2006), p. 2323.

[Bas15] M. S. Basunia. 'Nuclear Data Sheets for A = 22'. In: *Nuclear Data Sheets* 127 (2015), p. 69.

[BB08] B. Blank and M. J. G. Borge. 'Nuclear structure at the proton drip line: Advances with nuclear decay studies'. In: *Progress in Particle and Nuclear Physics* 60 (2008), p. 403.

[BC22] M. S. Basunia and A. Chakraborty. 'Nuclear Data Sheets for A = 24'. In: *Nuclear Data Sheets* 186 (2022), p. 3.

[Beh+13] O. Behnke et al., eds. *Data Analysis in High Energy Physics*. John Wiley & Sons, Ltd, 2013. ISBN: 978-3-527-41058-3.

[Bei52] A. Beiser. 'Nuclear Emulsion Technique'. In: *Reviews of Modern Physics* 24.4 (1952), p. 273.

[Ben+00] R. Bennett et al. *Radioactive Nuclear Beam Facilities*. Report. The NuPECC Working Group, 2000.

[Ben05] C. Bentley. *Prince2 Revealed*. 1st ed. Butterworth-Heinemann, 2005. ISBN: 978-0-750-66672-5.

[BH16] M. S. Basunia and A. M. Hurst. 'Nuclear Data Sheets for A = 26'. In: *Nuclear Data Sheets* 134 (2016), p. 1.

[BJ17] M. J. G. Borge and B. Jonson. 'ISOLDE past, present and future'. In: *Journal of Physics G: Nuclear and Particle Physics* 44 (2017), p. 044011.

[Bla+97] B. Blank et al. 'The spectroscopy of 22Al: a βp, β2p and βα emitter'. In: *Nuclear Physics A* 615.1 (1997), p. 52.

[BR97] R. Brun and F. Rademakers. 'ROOT - An Object Oriented Data Analysis Framework'. Version 6.30/02. In: *Nuclear Instruments and Methods in Physics Research Section A* 389 (1997), p. 81. URL: https://root.cern/ (visited on 13/02/2023).

[Bro90] B. Alex Brown. 'Isospin-forbidden β-delayed proton emission'. In: *Physical Review Letters* 65 (22 1990), p. 2753.

[BT14] E. Browne and J. K. Tuli. 'Nuclear Data Sheets for A = 235'. In: *Nuclear Data Sheets* 122 (2014), p. 205.

[CAE24] CAEN S.p.A. *V1190A-2eSST - 128 Channel Multihit TDC (100/200/800 ps) - CAEN - Tools for Discovery*. 2024. URL: https://www.caen.it/products/v1190a-2esst/ (visited on 29/02/2024).

[CER22] CERN. *The accelerator complex | CERN*. 2022. URL: https://www.home.cern/science/accelerators/accelerator-complex (visited on 29/02/2024).

[Chi+08] Jren-Chit Chin et al. 'Accurate localization of low-level radioactive source under noise and measurement errors'. In: *Proceedings of the 6th ACM Conference on Embedded Network Sensor Systems* (Raleigh, NC, USA). SenSys '08. Association for Computing Machinery, 2008, p. 183. URL: https://doi.org/10.1145/1460412.1460431.

[CK23] F. Charette and P. Kime. *CTAN: Package biber*. Version 2.19. 5th Mar. 2023. URL: https://ctan.org/pkg/biber (visited on 15/12/2023).

[Cra+22] H. L. Crawford et al. 'Crossing $N = 28$ Toward the Neutron Drip Line: First Measurement of Half-Lives at FRIB'. In: *Physical Review Letters* 129 (21 2022), p. 212501.

[Fac24a] Facility for Rare Isotope Beams. *FRIB | Facility for Rare Isotope Beams | Michigan State University: Areas and Instruments in Opearation*. 2024. URL: https://frib.msu.edu/users/instruments/operation.html (visited on 18/02/2024).

[Fac24b] Facility for Rare Isotope Beams. *FRIB | Facility for Rare Isotope Beams | Michigan State University: FRIB Fact Sheets*. 2024. URL: https://frib.msu.edu/about/fact-sheets.html (visited on 18/02/2024).

[Fir09] R. B. Firestone. 'Nuclear Data Sheets for A = 25'. In: *Nuclear Data Sheets* 110.8 (2009), p. 1691.

[Fir15] R. B. Firestone. 'Nuclear Data Sheets for A = 21'. In: *Nuclear Data Sheets* 127 (2015), p. 1.

[Fre07] M. Freer. 'The clustered nucleus – cluster structures in stable and unstable nuclei'. In: *Reports on Progress in Physics* 70 (2007), p. 2149.

[Fyn+00] H. O. U. Fynbo et al. 'The β2p decay mechanism of 31Ar'. In: *Nuclear Physics A* 677.1 (2000), p. 38.

[Git24a] Git. *Git*. 2024. URL: https://git-scm.com/ (visited on 29/02/2024).

[Git24b] Git. *Git - gitsubmodules Documentation*. 2024. URL: https://git-scm.com/docs/gitsubmodules (visited on 29/02/2024).

[HM12] I. Hamamoto and B. Mottelson. 'Shape deformations in atomic nuclei'. In: *Scholarpedia* 7.4 (2012), p. 10693.

[HT20] J. C. Hardy and I. S. Towner. 'Superallowed $0^+ \rightarrow 0^+$ nuclear β decays: 2020 critical survey, with implications for V_{ud} and CKM unitarity'. In: *Physical Review C* 102 (2020), p. 045501.

[Hua+21] W. J. Huang et al. 'The AME2020 atomic mass evaluation (I). Evaluation of input data, and adjustment procedures'. In: *Chinese Phys. C* 45.3 (2021), p. 030002. DOI: 10.1088/1674-1137/abddb0.

[Hun07] J. D. Hunter. 'Matplotlib: A 2D graphics environment'. In: *Computing in Science & Engineering* 9.3 (2007), pp. 90–95. DOI: 10.1109/MCSE.2007.55.

[Ili15] C. Iliadis. *Nuclear Physics of Stars*. 2nd ed. Wiley-VCH, 2015. ISBN: 978-3-527-33648-7.

[ISO24] ISOLDE. *ISOLDE Yield Database*. 2024. URL: http://isoyields-classic.web.cern.ch/query_tgt.htm (visited on 29/02/2024).

[Jen+24] E. A. M. Jensen et al. 'Detailed study of the decay of ^{21}Mg'. Submitted to European Physical Journal A. 2024.

[Jen21] E. A. M. Jensen. *Carbon foil floating cookbook*. 2021. URL: https://wiki.kern.phys.au.dk/erik_foil_guide.pdf (visited on 21/02/2024).

[Jen23a] E. A. M. Jensen. *ausadaq · GitLab*. 2023. URL: https://gitlab.au.dk/ausa/ausadaq (visited on 29/02/2024).

[Jen23b] E. A. M. Jensen. *Wiki - Overview of The Aarhus University SubAtomic Group's Data Acquisition System*. 2023. URL: https://wiki.kern.phys.au.dk/DAQ (visited on 29/02/2024).

[JRF23] E. A. M. Jensen, K. Riisager and H. O. U. Fynbo. 'Extracting clean low-energy spectra from silicon strip detector telescopes around punch through energies'. In: *Nuclear Instruments and Methods in Physics Research Section A* 1055 (2023), p. 168531.

[Kew+18] J. Kew et al. *CTAN: Package xetex*. Version 0.999995. 4th Feb. 2018. URL: https://ctan.org/pkg/xetex (visited on 15/12/2023).

[Kir+14] O. S. Kirsebom et al. 'Analysis of the response of silicon detectors to α particles and ^{16}O ions'. In: *Nuclear Instruments and Methods in Physics Research A* 758 (2014), p. 57.

[Kno10] G. F. Knoll. *Radiation Detection and Measurement*. 4th ed. John Wiley & Sons, 2010. ISBN: 978-0-470-13148-0.

[Kon+21] F. G. Kondev et al. 'The NUBASE2020 evaluation of nuclear physics properties'. In: *Chinese Phys. C* 45.3 (2021), p. 030001. DOI: 10.1088/1674-1137/abddae.

[Kow21] M. Kowalska. *The many faces of ISOLDE*. 2021. URL: https://ep-news.web.cern.ch/content/many-faces-isolde (visited on 29/02/2024).

[Len+86] W. N. Lennard et al. 'Nonlinear response of Si detectors for low-Z ions'. In: *Nuclear Instruments and Methods in Physics Research A* 248 (1986), p. 454.

[Lun+15a] M. V. Lund et al. 'Beta-delayed proton emission from ^{21}Mg'. In: *The European Physical Journal A* 51 (2015), p. 113.

[Lun+15b] M. V. Lund et al. 'Systematic trends in beta-delayed particle emitting nuclei: The case of βpα emission from ^{21}Mg'. In: *Physics Letters B* 750 (2015), p. 356.

[Lun+16] M. V. Lund et al. 'Beta-delayed proton emission from ^{20}Mg'. In: *The European Physical Journal A* 52 (2016), p. 304.

[Lun+20] K. R. Lund et al. 'Online tests of the Advanced Cryogenic Gas Stopper at NSCL'. In: *Nuclear Instruments and Methods in Physics Research B* 463 (2020), p. 378.

[Mar67] M. A. Mariscotti. 'A method for automatic identification of peaks in the presence of background and its application to spectrum analysis'. In: *Nuclear Instruments and Methods* 50 (1967), p. 309.

[Mes23] Mesytec GmbH. *mesytec - Detector Readout Systems*. 2023. URL: http://mesytec.com/ (visited on 29/02/2024).

[Mic18] Micron Semiconductor Ltd. *Long Form Catalogue 2018*. 2018. URL: http://www.micronsemiconductor.co.uk/wp-content/uploads/2018/03/2018-Micron-Semiconductor-Ltd-Silicon-Catalogue_Long-Form.pdf (visited on 26/02/2024).

[Mir24] Mirion Technologies, Inc. *XtRa™ Extended Range Coaxial Ge Detectors | Mirion*. 2024. URL: https://www.mirion.com/products/technologies/spectroscopy-scientific-analysis/gamma-spectroscopy/detectors/hpge-detectors-accessories/xtra-extended-range-coaxial-ge-detectors (visited on 21/02/2024).

[MS04] David J. Morrissey and Brad M. Sherrill. 'In-Flight Separation of Projectile Fragments'. In: *Lecture Notes in Physics* 651 (2004), p. 113.

[Mue+01] W. F. Mueller et al. 'Thirty-two-fold segmented germanium detectors to identify ɣ-rays from intermediate-energy exotic beams'. In: *Nuclear Instruments and Methods in Physics Research A* 466 (2001), p. 492.

[Mun18] M. Munch. 'A study of ^{8}Be, ^{12}C and ^{27}Al with state-of-the-art detector arrays'. PhD thesis. Aarhus Universitet, 2018. URL: https://wiki.kern.phys.au.dk/michael.pdf (visited on 27/02/2024).

[Nie16] S. T. Nielsen. 'An Experimental Study of the Decay of ^{21}Mg'. MA thesis. Aarhus Universitet, 2016. URL: https://wiki.kern.phys.au.dk/thesisSTN.pdf (visited on 27/02/2024).

[PGR12] M. Pfützner, L. V. Grigorenko and K. Riisager. 'Radioactive decays at limits of nuclear stability'. In: *Review of Modern Physics* 84 (2012), p. 567.

[Pol12] P. H. Poll. *Linux Libertine*. Version 5.3.0. 6th July 2012. URL: https://libertine-fonts.org/ (visited on 11/02/2024).

[Por+23] M. Portillo et al. 'Commissioning of the Advanced Rare Isotope Separator ARIS at FRIB'. In: *Nuclear Instruments and Methods in Physics Research B* 540 (2023), p. 151.

[Pov+14] B. Povh et al. *Particles and Nuclei: An Introduction to the Physical Concepts*. 7th ed. Springer, 2014. ISBN: 978-3-662-46320-8.

[PR76] D. G. Perry and L. P. Remsberg. 'Particle identification with very thin transmission detectors'. In: *Nuclear Instruments and Methods* 135.1 (1976), p. 103.

[PXC24] PXCT Collaboration. *e21010 [PXCT]*. 2024. URL: https://wikihost.nscl.msu.edu/pxct/doku.php?id=e21010 (visited on 21/02/2024).

[Sal22] F. Salvat. 'Bethe stopping-power formula and its corrections'. In: *Physical Review A* 106.3 (2022), p. 032809.

[SB08] B. Singh and E. Browne. 'Nuclear Data Sheets for A = 240'. In: *Nuclear Data Sheets* 109.10 (2008), p. 2439.

[Sch+87] K.-H. Schmidt et al. 'The momentum-loss achromat — A new method for the isotopical separation of relativistic heavy ions'. In: *Nuclear Instruments and Methods in Physics Research A* 260.2 (1987), p. 287.

[SGC73] R. G. Sextro, R. A. Gough and J. Cerny. 'β^+-Delayed Proton Decay of ^{21}Mg'. In: *Physical Review C* 8 (1973), p. 258.

[She18] Bradley M. Sherrill. 'Future Opportunities at the Facility for Rare Isotope Beams'. In: *European Physical Journal Web of Conferences* 178 (2018), p. 01001.

[Som18] V. Somà. 'From the liquid drop model to lattice QCD'. In: *The European Physical Journal Plus* 133 (2018), p. 434.

[Sor16] E. Sorkin. *Merriweather Sans - Google Fonts*. Version 1.006. 26th Jan. 2016. URL: https://fonts.google.com/specimen/Merriweather+Sans (visited on 15/12/2023).

[Sun+22] L. J. Sun et al. *Application and Extension of the Particle X-ray Coincidence Technique to Astrophysical Reaction Rates*. 2022. URL: https://wikihost.nscl.msu.edu/pxct/lib/exe/fetch.php?media=pxct_lijiesun.pdf (visited on 20/02/2024).

[Ten+04] O. Tengblad et al. 'Novel thin window design for a large-area silicon strip detector'. In: *Nuclear Instruments and Methods in Physics Research A* 525.3 (2004), p. 458.

[The23] The Inkscape Project. *Inkscape*. Version 1.3. 23rd July 2023. URL: https://inkscape.org (visited on 15/12/2023).

[Tho+04] J.-C. Thomas et al. 'Beta-decay properties of ^{25}Si and ^{26}P'. In: *The European Physical Journal A* 21 (2004), p. 419.

[Tho03] J. C. Thomas. 'Spectroscopie des noyaux légers déficients en neutrons'. PhD thesis. Université de Bordeaux, 2003.

[Til+95] D. R. Tilley et al. 'Energy levels of light nuclei A = 18-19'. In: *Nuclear Physics A* 595.1 (1995), p. 1.

[Til+98] D. R. Tilley et al. 'Energy levels of light nuclei, A = 20'. In: *Nuclear Physics A* 636.3 (1998), p. 249.

[Tor+13] D. Torresi et al. 'Influence of the interstrip gap on the response and the efficiency of Double Sided Silicon Strip Detectors'. In: *Nuclear Instruments and Methods in Physics Research A* 713 (2013), p. 11.

[Unk12] Unknown author. *Aozora Mincho*. Version 0.1. 26th Dec. 2012. URL: https://web.archive.org/web/20200321102249/http://blueskis.wktk.so/AozoraMincho/index.html (visited on 23/12/2023).

[Vil+23] A. C. C. Villari et al. 'Gas stopping and reacceleration techniques at the Facility for Rare Isotope Beams (FRIB)'. In: *Nuclear Instruments and Methods in Physics Research B* 541 (2023), p. 350.

[Viñ+21] S. Viñals et al. 'Calibration and response function of a compact silicon-detector set-up for charged-particle spectroscopy using GEANT4'. In: *European Physical Journal A* 57.2 (2021), p. 49.

[Vog68] E. Vogt. 'The statistical theory of nuclear reactions'. In: *Advances in Nuclear Physics* 1 (1968), p. 261.

[WA82] R. C. Weast and M. J. Astle. *CRC Handbook of Chemistry and Physics*. 62nd ed. CRC Press, 1982. ISBN: 0-8493-0462-8.

[Wan+18] Y.-T. Wang et al. 'β-delayed particle emission from ^{21}Mg'. In: *The European Physical Journal A* 54 (2018), p. 107.

[Wan+21] M. Wang et al. 'The AME2020 atomic mass evaluation (II). Tables, graphs and references'. In: *Chinese Phys. C* 45.3 (2021), p. 030003. DOI: 10.1088/1674-1137/abddaf.

[Wei+12] J. G. Weisend II et al. 'Conceptual design of the FRIB cryogenic system'. In: *AIP Conference Proceedings* 1434.1 (2012), p. 94.

[Wei+22] J. Wei et al. 'FRIB Commissioning and Early Operations'. In: *Proc. 13th International Particle Accelerator Conference (IPAC'22)* (Bangkok, Thailand). International Particle Accelerator Conference 13. JACoW Publishing, Geneva, Switzerland, 2022, p. 802.

[Wil+92] J. F. Wilkerson et al. 'Isospin-nonconserving particle decays in light nuclei'. In: *Nuclear Physics A* 549 (1992), p. 223.

[WM74] D. H. Wilkinson and B. E. F. Macefield. 'A Parametrization of the phase space factor for allowed β-decay'. In: *Nuclear Physics A* 232 (1974), p. 58.

[Wor+22] R. L. Workman et al. 'Review of Particle Physics'. In: *Progress of Theoretical and Experimental Physics* 2022 (2022), p. 083C01.

[Wu+21] C. G. Wu et al. 'β-decay spectroscopy of the proton drip-line nucleus ^{22}Al'. In: *Physical Review C* 104.4 (2021), p. 044311.

[XIA24] XIA LLC. *Pixie-16 | XIA*. 2024. URL: https://xia.com/products/pixie-16/ (visited on 27/02/2024).

[ZV17] V. Zelevinsky and A. Volya. *Physics of Atomic Nuclei*. 1st ed. Wiley-VCH, 2017. ISBN: 978-3-527-41350-8.

[ZZB10] J. F. Ziegler, M. D. Ziegler and J. P. Biersack. 'SRIM – The stopping and range of ions in matter (2010)'. In: *Nuclear Instruments and Methods in Physics Research B* 268.11-12 (2010), p. 1818.

List of Figures

List of Tables